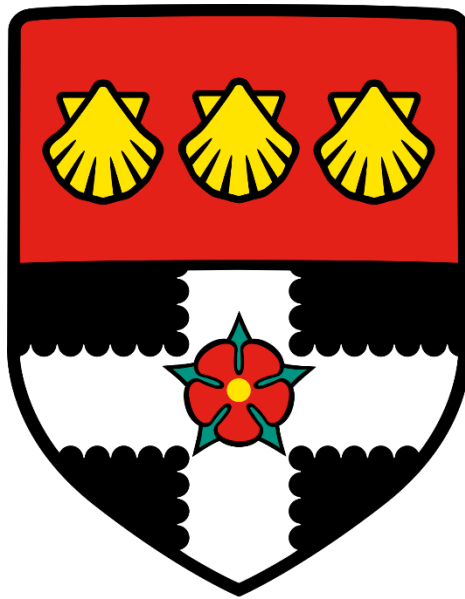


UNIVERSITY OF READING
Department of Meteorology



**Electrical Pre-Conditioning of
Convective Clouds**

James Gilmore

A thesis submitted for the degree of Doctor of Philosophy

July 2019

Declaration

I confirm that this is my own work and the use of all material from other sources has been properly and fully acknowledged.

James Gilmore

Abstract

Lightning presents a substantial hazard. Thunderstorm nowcasting requires a lightning strike to have already occurred, so advance warnings of lightning are currently only possible using numerical weather prediction models. This research aims to identify the processes within cumuliform clouds that can distribute charge prior to the first lightning strike.

Precipitation can influence the potential gradient measured at the surface, masking the charge residing within an overhead cloud. An increase in negative charge was measured with increasing rain rate that was dependent on changes in surface conditions such as wind speed and surface dryness, but not cloud type. A field campaign was set up at Chilbolton Observatory by installing a field mill and Birai thunderstorm detector. Surface atmospheric electricity measurements were analysed for 653 cumuliform clouds observed over two years using a 35 GHz radar. Mixed-phase clouds with a high ice phase moisture content produced the largest electrification with increases in the size, density, and turbulence of the hydrometeors all increased cloud electrification, findings consistent with the relative diffusional growth rate theory. Ten radiosondes were flown from Reading University Atmospheric Observatory to provide in-situ measurements of charge (up to 550 pC m^{-3}), cloud backscatter, turbulence (up to $10^{-1} \text{ m}^2 \text{ s}^{-3}$), and supercooled liquid water (up to 2 g m^{-3}) in cumuliform clouds. These measurements yield consistent findings with those from radar observations. The shallow depth of the charge centres within the cumuliform clouds suggests that the charge was typically insufficiently distributed to allow the required potential gradient enhancement for atmospheric breakdown leading to lightning. This is concluded as the fundamental reason cumuliform clouds in the UK are often charged but rarely produce lightning.

This research could be used to improve probabilistic lightning forecasts and nowcasts through improvements to lightning parametrisation schemes in forecast models and the identification of potential thunderstorms using real-time existing surface- and satellite-based radar networks.

Acknowledgements

I would like to take this opportunity to acknowledge the people and organisations who have helped me in my PhD. I would have not been able to have completed this PhD without the Natural Environment Research Council (NERC) SCENARIO studentship which funded my PhD. Next, I would like to thank my supervisors Giles Harrison, Sue Gray, Keri Nicoll and Alec Bennett (from Biral) who have provided invaluable advice, support and constructive criticism throughout my PhD.

I would also like to thank the meteorology department's technicians who have provided substantial technical support in the design, installation and maintenance of the field campaign at Rutherford Appleton Laboratory's (RAL) Chilbolton Observatory (CO). Specifically, I would like to thank Ian Read, Selena Zito and Rosy Wilson, for their support and sense of humour. I would like to extend my thanks to everyone at CO for their continual support in the very smooth running of the field campaign, specifically Darcy Ladd and Judith Jeffery. Their advice, enthusiasm and kindness made this part of my PhD especially rewarding. I would also like to thank Biral for loaning me their BTD-300 instrument, which was installed at CO.

Next, I would like to thank Graeme Marlton and Martin Airey for their help in both the construction, testing and launching of the radiosondes. Without their knowledge and continued support, I'd still be waiting to launch a radiosonde into charged cumuliform clouds. I would also like to thank the administrators in the meteorology department, particularly Debbie Turner who has helped me on countless occasions, from organising supervisor meetings to booking travel and accommodation at EGU 2018 with such care and patience. I would also like to extend my thanks to Thorwald Stein and Chris Westbrook who have provided invaluable knowledge of the capabilities of the radars at CO along with their limitations. Their support has made it possible to answer the questions of this thesis with greater robustness.

Next, I would like to thank everyone who is/was in 2U06 for their advice and laughs, particularly Lewis Blunn, Will McIntyre, Izzy Capel-Timms, David Meyer (Brian), David Flack (Big Dave), Matt Lang and Mike Goodliff (Chump). I would like to thank my mum for her much-needed support during the highs and lows of this work and for proofreading some of the chapters of this thesis.

Last, but not least, I'd like to thank Jasmine for all of her wonderful effort supporting me and in keeping me sane during this PhD. I wouldn't have been able to complete the thesis without her.

If you want to find the secrets of the universe, think in terms of energy, frequency, and vibration.

Nikola Tesla

Contents

Declaration	II
Abstract	IV
Acknowledgements	V
Contents	VII
Nomenclature.....	XII
List of Acronyms	XVI
1 Introduction.....	1
1.1 The Formation of Convective Clouds	4
1.2 Measurements of Atmospheric Electricity.....	7
1.3 The Electrification of Convective Clouds.....	8
1.4 Thesis Questions.....	12
1.5 Thesis Structure.....	13
2 A review of cloud electrification and the influence of precipitation on the potential gradient	14
2.1 Cloud Electrification Mechanisms.....	14
2.1.1 Ion Capture Mechanism	15
2.1.2 Convective Mechanism	17
2.1.3 Inductive Mechanisms.....	19
2.1.4 Non-Inductive Mechanisms.....	22
2.1.5 Enhancement of the potential gradient.....	29
2.1.6 Cloud Electrification Mechanism Summary	30
2.2 Influence of liquid precipitation on the potential gradient measured at the surface	33
2.2.1 Observing the relationship between precipitation and the potential gradient..	33

2.2.2	The life cycle of falling precipitation and the interaction with the potential gradient	36
2.2.3	Factors that influence the splashing of liquid drops.....	39
2.3	Conclusions	43
3	Instrumentation and Data Processing.....	44
3.1	Field Sites	45
3.1.1	Reading University Atmospheric Observatory.....	47
3.1.2	Chilbolton Observatory	47
3.2	Electrical Instruments	49
3.2.1	Electrostatic Field Mill.....	49
3.2.2	Biral Thunderstorm Detector	53
3.3	Rain Gauge Instruments.....	55
3.3.1	Tipping Buckets	55
3.3.2	Drop Counters	67
3.3.3	Disdrometer	68
3.4	Remote Sensing Instruments	70
3.4.1	Copernicus Radar	71
3.4.2	Ceilometer.....	75
3.4.3	CloudNet	75
3.5	Radiosonde and In Situ Instruments.....	76
3.5.1	Radiosonde Instrument.....	77
3.5.2	Charge Instrument	79
3.5.3	Cloud Instrument	81
3.5.4	Turbulence Instrument	83
3.5.5	Supercooled Liquid Water Instrument.....	83
4	The Effects of Precipitation on the Local Atmospheric Potential Gradient	85
4.1	Introduction	85
4.2	Cloud Identification using Solar Radiation Measurements.....	88

4.3	Case Studies.....	89
4.3.1	Single Rain Event: 2009/11/01	89
4.3.2	Multiple Rain Event: 2016/05/11	93
4.4	Long-Term Statistical Study.....	98
4.4.1	Average Relationship.....	99
4.4.2	Sensitivity and Robustness	102
4.5	Cloud Variations	106
4.6	Surface Conditions.....	110
4.6.1	Definition of a Rain Event.....	110
4.6.2	Determination of the Effect of Surface Splashing	112
4.6.3	Analysis of Surface Conditions	114
4.7	Discussion	118
5	Cloud Electrification Measured at the Surface.....	122
5.1	Introduction.....	122
5.2	Cloud Identification Algorithm using Radar and Ceilometer Data	125
5.3	Classification of Convective Clouds at CO	129
5.4	Case Study Analysis	131
5.4.1	(1) Highly Electrified Cloud	135
5.4.2	(2) Developed Cloud with no Measurable Electrification	139
5.4.3	(3) Cloud Turbulence and Appreciable <i>PG</i> Perturbation.....	144
5.4.4	(4) Negligible Turbulence and Appreciable <i>PG</i> Perturbation	148
5.4.5	Summary of Case Studies	153
5.5	Hypothesis Testing	154
5.5.1	The relationship between cloud electrification and cloud phase and cloud depth 154	
5.5.2	The relationship between cloud electrification and hydrometeor size distribution 159	
5.5.3	The relationship between cloud electrification and turbulence.....	164

5.6	Discussion.....	171
6	Cloud Electrification Measured In Situ.....	175
6.1	Introduction	175
6.2	Launch Criteria	178
6.3	Cloud Identification in One Dimensional Ascent Data.....	181
6.4	Case Studies	182
6.4.1	Overview of Ascents.....	182
6.4.2	Highly Electrified Cloud	187
6.5	Hypothesis Testing.....	192
6.5.1	Relationship between cloud electrification and cloud phase and backscatter	193
6.5.2	Relationship between cloud charge and droplet properties	196
6.5.3	Relationship between cloud electrification and turbulence.....	197
6.5.4	Relationship between space charge and potential gradient	198
6.6	Discussion.....	205
7	Conclusions and Future Work.....	208
7.1	Conclusions	208
7.1.1	The Effects of Precipitation on the Local Atmospheric Potential Gradient	209
7.1.2	Cloud Electrification Measured at the Surface	210
7.1.3	Cloud Electrification Measured In Situ.....	211
7.1.4	Contributions	212
7.2	Limitations.....	214
7.2.1	The Cloud Identification Algorithms	215
7.2.2	Instruments	216
7.3	Implications.....	218
7.3.1	The Effects of Precipitation on the Local Atmospheric Potential Gradient	218
7.3.2	Cloud Electrification Measured at the Surface	219
7.3.3	Cloud Electrification Measured In Situ.....	220
7.4	Future Work	220

Contents

7.5	Closing Remark.....	222
	Appendices.....	223
	Appendix A: Instrument Calibrations.....	224
	Appendix B: Biral Thunderstorm Detector Warning Flags.....	225
	Appendix C: CloudNet Classification Codes.....	226
	Appendix D: Radiosonde Ascent Figures.....	227
	References.....	233

Nomenclature

Generic

<i>Symbol</i>	<i>Definition</i>	<i>Unit</i>
t	Time (in seconds unless stated otherwise)	s
z	Height	m
r	Radius	m
D or d	Diameter	m
m	Mass	kg
A	Area	m ²
v	Velocity	m s ⁻¹
c	Speed of light	299,792,458 m s ⁻¹
p	Momentum	kg m s ⁻¹
ρ_D	Density	kg m ⁻³
γ	Surface tension	N m ⁻¹
ϵ_0	The permittivity of free space	$8.85418782 \times 10^{-12} \text{ m}^{-3} \text{ kg}^{-1} \text{ s}^4 \text{ A}^2$

Meteorology

<i>Symbol</i>	<i>Definition</i>	<i>Unit</i>
T	Temperature	°C
T_p	Parcel temperature	°C
T_e	Environment temperature	°C
P	Atmospheric pressure	hPa
u	Meridional wind	m s ⁻¹
v	Zonal wind	m s ⁻¹
w	Total wind ($\sqrt{u^2 + v^2}$)	m s ⁻¹
RH	Relative humidity	%
RH_W	Relative humidity with respect to water	%

<i>Symbol</i>	<i>Definition</i>	<i>Unit</i>
RH_I	Relative humidity with respect to ice	%
S_g	Global solar irradiance	$W\ m^{-2}$
S_d	Diffuse solar irradiance	$W\ m^{-2}$
DF	Diffuse fraction	-
e	Vapour pressure	hPa
e_s	Saturated vapour pressure	hPa

Electrical

<i>Symbol</i>	<i>Definition</i>	<i>Unit</i>
V	Voltage	V
V_{range}	Voltage difference (max-min)	V
R	Resistance	Ω
Q	Charge on a drop	pC
E	Electric field	$V\ m^{-1}$
E_z	Vertical component of E (positive downwards)	$V\ m^{-1}$
PG	Potential gradient	$V\ m^{-1}$
PG_0	Background PG	$V\ m^{-1}$
PG'	PG time derivative	$V\ m^{-1}\ s^{-1}$
j	Current	pA
J	Current density	$pA\ m^{-2}$
j_C and J_C	Air-Earth conduction current and current density	pA and $pA\ m^{-2}$
j_D and J_D	Displacement current and current density	pA and $pA\ m^{-2}$
j_T and J_T	Turbulent current and current density	pA and $pA\ m^{-2}$
j_P and J_P	Precipitation current and current density	pA and $pA\ m^{-2}$
J_{tot}	Total current measured by BTD-300 ($j_D + j_P + j_T$)	pA
j_s and J_s	Total atmospheric current ($j_C + j_D + j_P + j_T$) and current density	pA and $pA\ m^{-2}$
ρ	Space charge density	$pC\ m^{-3}$

Rain Gauge

<i>Symbol</i>	<i>Definition</i>	<i>Unit</i>
RR	Rain rate	mm h ⁻¹
B	Tipping bucket size	mm
N_D	Number of drops collected by drop counting rain gauge	
ε_d	Drop size used by the drop counting rain gauges	mm
$m_{3.67}$	Moments of order 3.67 used by disdrometer	mm h ⁻¹
N_m	Drop size distribution	
We	Weber number	

Radar

<i>Symbol</i>	<i>Definition</i>	<i>Unit</i>
Z	Radar reflectivity	dBZ
\bar{v}	Doppler velocity	m s ⁻¹
w_z	Vertical air motion	m s ⁻¹
\bar{v}_d	Terminal fall velocity	m s ⁻¹
σ_v	Spectral width	m s ⁻¹
σ_t	The standard deviation of the vertical component of turbulence	m s ⁻¹
σ_b	The standard deviation of the beam broadening	m s ⁻¹
σ_d	The standard deviation of the terminal fall velocity	m s ⁻¹
$\sigma_{\bar{v}}$	The standard deviation of the mean velocity	m s ⁻¹
ε_T	Turbulent kinetic energy dissipation rate	m ² s ⁻³
$\dot{\varepsilon}_T$	Space-time derivative of ε_T	m s ⁻⁴
k	Kolmogorov constant	5/3
L	Length scale	
θ	Beamwidth of the radar	Rad
U	Horizontal wind speed	m s ⁻¹
P_r	Power received by the radar	W
P_t	Power transmitted by radar	W

<i>Symbol</i>	<i>Definition</i>	<i>Unit</i>
τ	Duration of the radar pulse	s
D_a	The diameter of the radar antenna	m
$\ k\ $	The dielectric constant of the target within the atmosphere	Fm^{-1}
λ	The wavelength of the radar pulse	Hz
T	The transmittance of the atmosphere between the radar and the sampling volume	-

Radiosonde

<i>Symbol</i>	<i>Definition</i>	<i>Unit</i>
σ_{acc}	The standard deviation of the acceleration	m s^{-1}
b_o	Weight of the steel wire	g cm^{-1}
F	Frequency	Hz
f_o	The initial frequency of the wire (used in the supercooled liquid water sensor)	Hz
ε_D	Drop collection efficiency	-
A_{eff}	Effective area	m^2
ω	Ascent/descent rate	m s^{-1}
V_C	Charge sensor voltage	V
V_B	Cloud backscatter voltage	V

Statistical

<i>Symbol</i>	<i>Definition</i>	<i>Unit</i>
r	Pearson correlation coefficient	-
R^2	Coefficient of determination	-
p	Probability value	-

List of Acronyms

Acronym	Definition
1R	1:1-line R^2
AC	Alternating Current
AD	Anderson-Darling {Test}
AIC	Akaike Information Criterion
AVHRR	Advanced Very-High-Resolution Radiometer
BTD	Biral Thunderstorm Detector
CAPE	Convective Available Potential Energy ($J\ kg^{-1}$)
CG	Cloud-to-Ground lightning
CI	Cloud Identification {algorithm}
CIN	Convective INhibition
CO	Chilbolton Observatory
DC	Direct Current
DF	Diffuse Fraction
ECMWF	European Centre for Medium-Range Weather Forecasts
EL	Equilibrium Level (m)
EML	Environmental Measurements Limited
<i>ESTOFEX</i>	European STOrM Forecast EXperiment,
FFT	Fast Fourier Transform
FM	Field Mill
GEC	Global Electric Circuit
GFS	Global Forecast System
HR	Huber regression R^2
IC	Intra-Cloud lightning
IR	Infrared

Acronym	Definition
IWC	Ice Water Content (kg m^{-3})
JCI	John Chubb Instrumentation
LCL	Lifting Condensation Level (m)
LED	Light Emitting Diode
LFC	Level of Free Convection (m)
LI	Lifting Index ($^{\circ}\text{C}$)
LNB	Level of Neutral Buoyancy (m)
LR	Least-squares R^2
LWC	Liquid Water Content (kg m^{-3})
MCS	Mesoscale Convective System
METFiDAS	METEorological Fieldsite Data Acquisition System
MSL	Mean Sea Level (m)
MW	Mann-Whitney {Test}
NEODAAS	NERC Earth Observation Data Acquisition and Analysis Service
NERC	Natural Environmental Research Council
NOAA	National Oceanic and Atmospheric Administration
NWP	Numerical Weather Prediction
PANDORA	Programmable ANalogue and Digital Operational Radiosonde Accessory
<i>PG</i>	Potential Gradient (V m^{-1})
PIMS	Programmable Ion Mobility Spectrometer
RAL	Rutherford Appleton Laboratory
RF	Radio Frequency (Hz)
RH	Relative Humidity (%)
RMSD	Root Mean Square Difference
<i>RR</i>	Rain Rate (mm h^{-1})
RUAO	Reading University Atmospheric Observatory
SCENARIO	SCience of the ENvironment: Natural and Anthropogenic pRocesses, Impacts and Opportunities

Acronym	Definition
SI	International System of Units (Système International)
SLW	Supercooled Liquid Water
SLWC	Supercooled Liquid Water Content (g m^{-3})
UK	United Kingdom
UKMO	United Kingdom Met Office
UTC	Universal Time Coordinate
WMO	World Meteorological Organisation
Z	Reflectivity (dBZ)

1 Introduction

All clouds within the atmosphere are charged (Nicoll and Harrison, 2016) but most never produce lightning, particularly in the UK (Anderson and Klugmann, 2014). On average, there are between 840 and 1150 active thunderstorms at any one time, around the globe, which produces 44 ± 5 lightning flashes per second providing a total current of over 700 A (Mezuman et al., 2014; Christian et al., 2003). Figure 1-1 shows the global distribution of lightning as measured by the Lightning Imaging Sensor and Optical Transient Detector satellites (Peterson et al., 2017). In the UK, only around $1 \text{ fl km}^{-1} \text{ yr}^{-1}$ is observed, which is appreciably lower than other areas of the world (e.g. the Congo basin typically has the greatest density of lightning in the world, with $80 \text{ fl km}^{-2} \text{ yr}^{-1}$).

Lightning presents a substantial hazard to both human life and infrastructure. The number of fatalities due to lightning flashes (0.3 deaths per million) has dropped over 95% over the last century (Holle, 2008). The drop in fatalities is mainly caused by increased awareness of the dangers of lightning (Elsom, 2015), the urbanisation of civilisation (United Nations, 2018) and the development of lightning protection systems (Rakov and Uman, 2007). Although the number of fatalities has dropped, more can be done to lower the probability of being struck by lightning. Typically, lightning is produced from cumulonimbus “convective” clouds (MacGorman and Rust,

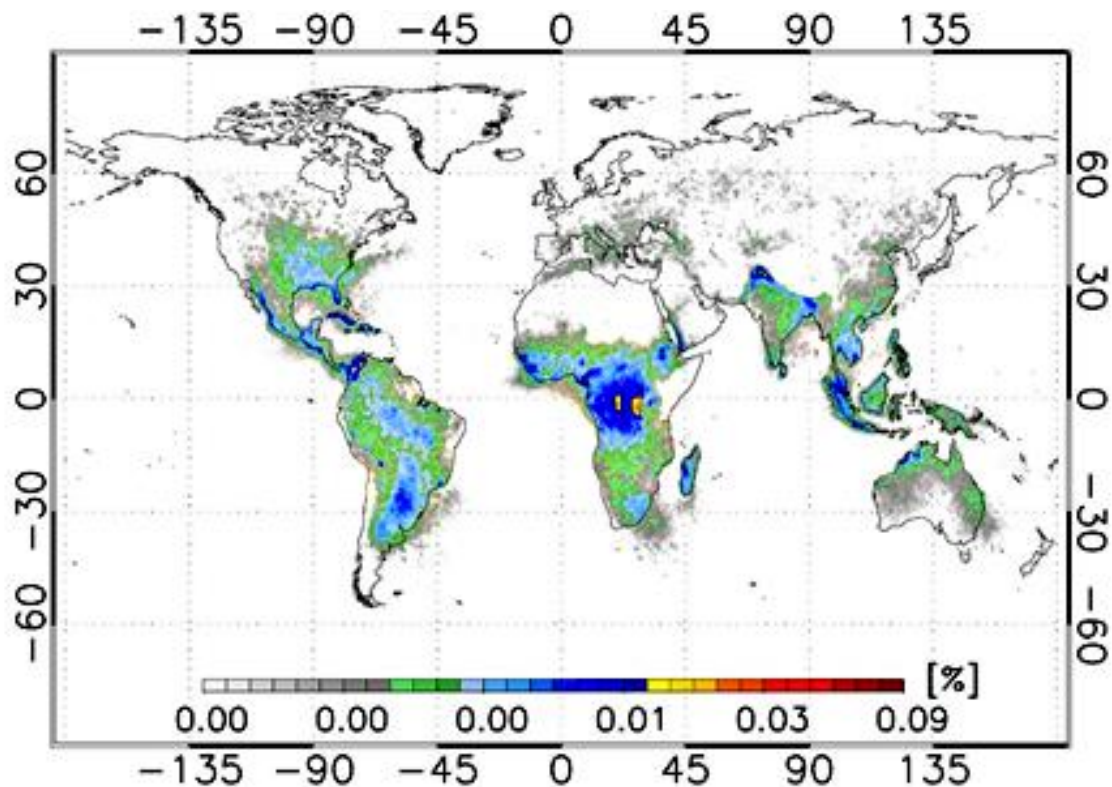


Figure 1-1: The global distribution of total flash rate from the Lightning Imaging Sensor and Optical Transient Detector satellite lightning climatology using data collected between 1997 and 2015 [reproduced by kind permission of Peterson, et al., (2017)].

1998). Although most convective clouds can generate a substantial amount of charge, most convective clouds never produce lightning, particularly in the UK. One of the main issues with thunderstorm detection is that a thunderstorm is only identified once the first lightning strike has occurred. Therefore, no warning for lightning would be possible. In this thesis, the processes needed for a cumuliform cloud to produce lightning are investigated with the aim to improve the forecasts of a thunderstorm before the first lightning flash.

Current methods for forecasting lightning use the outputs from numerical weather prediction (NWP) models (McCaul et al., 2009; Wilkinson and Bornemann, 2014). Although NWP models can provide a forecast for lightning, they often overestimate the spread and intensity of lightning, with high false alarm rates (Wilkinson, 2017). One of the fundamental issues with predicting lightning using NWP models is their ability to resolve convection within these models. As the development of a convective cloud occurs on a smaller scale than the resolution of NWP models, parametrisation is used to model convection (Yano et al., 2018). As NWP models increase their horizontal-grid resolutions, other issues arise when convection is partially resolved. When the coupled processes of the cloud (e.g. updraughts, downdraughts) cannot exist within the same grid cell, inconsistencies arise in the numerical modelling. The issues of partially parametrising convection are known as the grey zone (Yano et al., 2018).

Despite the increased resolution of NWP models in recent years, the number, location, and intensity of convective clouds are still poorly represented in such models. Furthermore, lightning prediction uses the output from NWP models using simple characteristics of the cloud such as graupel mass flux and the concentration of ice (McCaul et al., 2009). Both parameters (graupel mass flux and ice concentration) were chosen due to their strong correlation with the biggest storms within the UK and showed to have a strong linear relationship with maximum flash density (McCaul et al., 2009). Improvements to lightning prediction, which have not been implemented yet, include the identification of rapid growth of the hydrometeor sizes (Courtier et al., 2019). Overall, a better understanding of the convective cloud processes causing electrification can improve the use of NWP model outputs in lightning prediction. For example, looking at the life-stage of a convective cloud using radar and satellite imagery has proved useful in understanding the processes required for sufficient charge separation to occur to produce lightning (Soul et al., 2002).

The development of cloud electrification theory originates from the experiments made in 1746 by two pioneer electricians who noted a similarity between electrical discharges and lightning. John Freke and Johann Heinrich Winkler separately theorized that lightning was electrical

(National Archives, 2017). By 1749, Benjamin Franklin concluded that lightning was electrical after performing similar observations and postulated that thunderstorms were also electrically charged (Priestley, 1767). Thomas-François Dalibard conducted Franklin's proposed kite experiment during May 1752 to observe the electricity within clouds (Figure 1-2). Franklin conducted the same experiment later during June 1752 and was credited for the 'electric fluid' theory despite Dalibard's earlier success.

Soon after Benjamin Franklin's kite experiment, other scientists managed to measure charge during non-thunderstorm events at the surface (Canton, 1753), most notably during fair-weather days. Over a century later, Lord Kelvin designed the first continuous record of atmospheric electricity using a water dropper to measure the electric field strength, recorded using a photographic data logger (Thompson, 1872; Bennett and Harrison, 2007; Aplin and Harrison, 2013). Kelvin showed the electric field was continuous and that the magnitude varied depending on local topography and weather conditions. By the start of the twentieth century, C.T.R. Wilson (1916; 1920; 1929) had developed instrumentation that measured the electric current at the surface. Wilson further developed the understanding of Kelvin's work by concluding that the continuous vertical current, which was measured during fair weather, was part of a larger, global circuit and theorised the existence of the Global Electric Circuit (GEC, see Figure 1-3). In this theory, thunderstorms act as batteries causing the charge they separate to

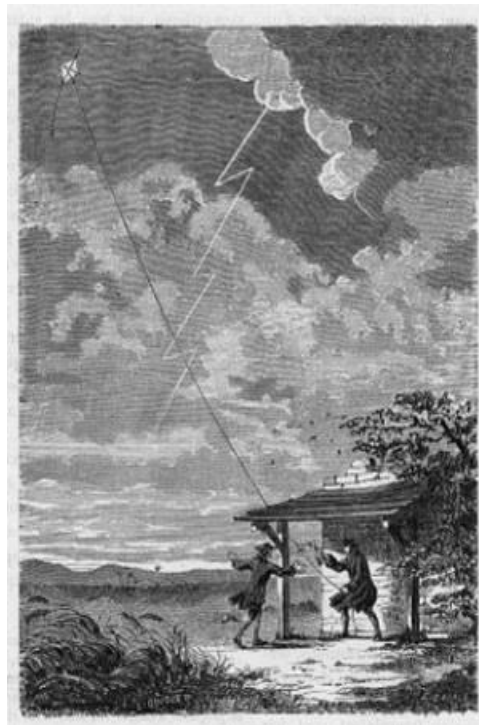


Figure 1-2: Illustration depicting Benjamin Franklin who conducted his famous kite experiment on June 15, 1752, to prove that clouds contain charge [reproduced from Elsom (2015)].

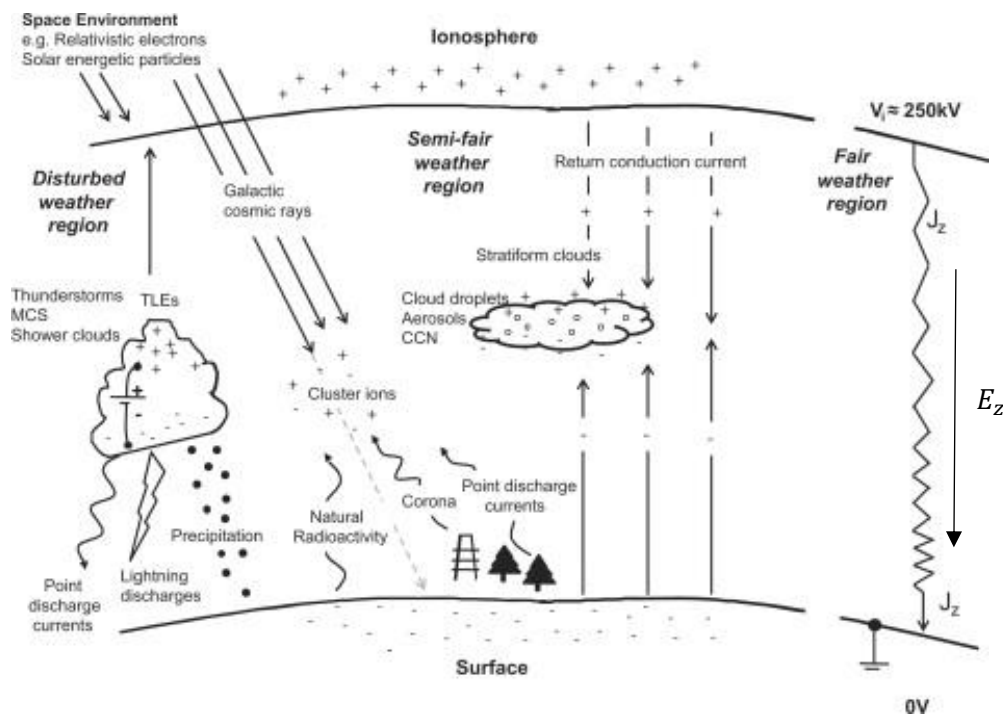


Figure 1-3: The global electric circuit and the relative charging and discharging components. This thesis focuses on understanding the disturbed weather and precipitation region of the GEC [reproduced by kind permission of Rycroft, et al. (2012)].

be distributed globally, forming a circuit with the Earth's surface and the ionosphere, causing a substantial potential difference (250 kV).

Simpson (1909) and other researchers postulated that charge structures existed within a thunderstorm, concluding that there must be at least two oppositely charged regions (Chalmers, 1967). As the electric field is dependent on the distance from a charge source, it is possible to detect multiple charge centres within a cloud as it moves overhead. Wilson (1920) measured changes in the electric field polarity as a charged cloud passed overhead and observed for the first time a dipole charge structure inside a convective cloud. In principle, the magnitude, width and time between polarity peaks from measurements of the electric field can be used to determine the size, velocity, and horizontal displacement of the charge within the cloud.

1.1 The Formation of Convective Clouds

The formation of clouds in the Earth's atmosphere is important for the transport of water (hydrological cycle), aerosols and bacteria around the globe. Clouds are also important for the climate as they can reflect between 50 and 70% of the incoming solar radiation (Eck et al., 1987). The reflectiveness of clouds vary based on the height of the cloud (Eck et al., 1987), particulate concentrations (Twomey et al., 1984) and amount of solar radiation passing through the atmosphere (Elsley et al., 2017). The formation of almost all clouds occurs within the troposphere (Figure 1-4), and the type of clouds that can form depends on the environmental temperature

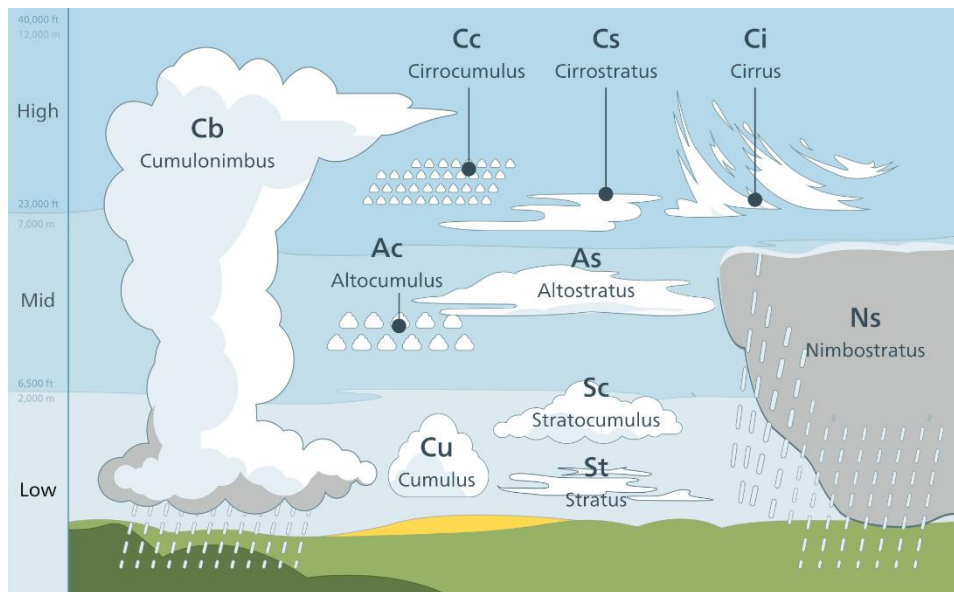


Figure 1-4: The various cloud types that are defined by the WMO (2017) as a function of their height. The low, middle and high represents heights of 0 – 2, 2 – 6 and > 6 km respectively [reproduced by kind permission from Valentin (2012)]

profile of the atmosphere and the amount of moisture (Hakim and Patoux, 2018). The clouds of interest for this thesis are cumulus and cumulonimbus clouds (collectively defined as a cumuliform cloud) as the thermal instabilities within these clouds allow convection; a requirement for the development of thunderstorms.

For a cloud to form, air must be first saturated (relative humidity (RH) = 100%). The saturated air (water vapour) can condense into cloud droplets, most commonly through heterogeneous nucleation (Ambaum, 2010). For heterogeneous nucleation to occur, a solid surface is needed for the water vapour to condense against. Aerosols (e.g. dust, pollen, sea salt) are the most common particle that can be used to condense water vapour within the atmosphere. When water vapour encounters a solid surface (e.g. aerosols), the water vapour can condense. The amount of moisture that an air parcel can hold is dependent on temperature: the greater the temperature, the greater the capacity to hold water. The maximum amount of water that an air parcel can hold is known as the saturated vapour pressure, e_s . For an air parcel to become saturated, either water vapour needs to be evaporated to increase its vapour pressure, e , to match e_s (typically forming fog), or by decreasing the air parcels temperature, T_p (typically forming clouds). Therefore, for clouds to form, parcels of air must be lifted to reduce e_s and allow saturation to occur.

An air parcel near the surface can be heated by solar radiation and the conduction of heat from the surface (Taylor, 2005). An air parcel warmer than the surrounding environmental air is less dense and becomes positively buoyant, allowing the parcel to rise. As the air parcel rises, adiabatic expansion occurs (no heat exchange with the environment) causing the air parcel to

expand to match the environmental pressure. Other processes including turbulent mixing and radiation occur on longer time scales than adiabatic expansion, so these other processes can be considered negligible in the simple case (Hakim and Patoux, 2018). Due to the work of an air parcel expanding, heat energy (temperature) is lost at a faster rate than the environmental temperature, T_e . While $T_p > T_e$, the air parcel stays positively buoyant. If the air parcel is not saturated, the parcel cools at the dry adiabatic lapse rate ($\sim 10 \text{ }^\circ\text{C km}^{-1}$), and the mixing ratio stays constant. As the parcel cools at the dry adiabatic lapse rate, e_s would decrease. Saturation occurs when $e_s = e$ and the parcel can begin to condense. The height when saturation occurs is known as the lifting condensation level (LCL). When the air parcel is saturated and begins to condense, e starts to decrease. While $T_p > T_e$ stays true, the parcel continues to rise and cools now at the moist adiabatic lapse rate ($\sim 6 \text{ }^\circ\text{C km}^{-1}$). When $T_e = T_p$, the parcel is no longer positively buoyant, and the cloud top is reached, a height known as the equilibrium level (EL), also known as the level of neutral buoyancy (LNB).

In many situations, an air parcel's instability is conditional on saturation. For example, the boundary layer is often stable ($T_p \leq T_e$), typically defined by a temperature inversion, which can stop an air parcel from ascending. Above the boundary layer, the atmosphere can be unstable ($T_p > T_e$) for a parcel lifted from the surface. To allow cloud formation, a lifting mechanism must lift an air parcel into the unstable atmosphere (e.g. frontal lifting, orographic lifting, convection). An air parcel forced to rise leads to free convection once $T_p > T_e$ and the height where this occurs is known as the level of free convection (LFC). Past the LFC, no external forces are needed, and buoyancy alone can again lift the air parcel, as long as $T_p > T_e$ holds. The stratosphere (altitude $\sim 12 \text{ km}$) is very stable with a substantial temperature inversion. Cumulonimbus clouds can extend up to the tropopause if $T_p > T_e$ for the entire ascent.

Cumuliform clouds typically have large vertical height covering a large temperature range allowing all hydrometeor phases to exist simultaneously within the cloud. For liquid water, the saturated vapour pressure can be defined even for temperatures below $0 \text{ }^\circ\text{C}$ and this is known as supercooled liquid water (SLW) (Harrison, 2015). SLW exists without freezing as the crystallisation of the liquid must occur (similar to the nucleation of water vapour into cloud droplets), releasing latent heat in the process. Disturbing the structure or flow of a supercooled droplet by colliding with an ice crystal or from deformation can cause the drop to undergo nucleation. Accretion can occur when supercooled drops collide with ice crystals and occur within charged clouds (Grabowska et al., 2017). In the absence of an ice nucleus, supercooled drops can remain in the liquid phase in the atmosphere until homogenous freezing occurs at around -37°C (Murray et al., 2010).

The mixing of these hydrometeors are common methods of cloud electrification as charge can be transferred between colliding particles during the freezing and melting phase transitions (Grabowska et al., 2017; Saunders et al., 2001). Turbulence can occur in cumuliform clouds and is caused by convection which also forms updraught and downdraught regions causing differences in the velocity of the hydrometeors. The strength of an updraught is modulated by the amount of energy that a buoyant air parcel would have with respect to the environment. A buoyant air parcel would rise vertically until $T_e = T_p$ and the energy used to achieve this can be defined as the convective available potential energy (CAPE). As turbulence can cause mixing of the hydrometeors (entrainment), convection which brought warm, moist air parcels from the surface would increase the environmental temperature. Therefore, convection can cause CAPE to reduce over time (Moncrieff and Green, 1972). As these processes continue, subsidence can start to occur leading to the dissipation of the cumuliform cloud.

1.2 Measurements of Atmospheric Electricity

The atmosphere is always charged, everywhere in the world. Charge exists within the atmosphere because of the ionisation of atmospheric gases from radioactive decay and from galactic energetic particle decays (Chalmers, 1967). A global, continuous distribution of active thunderstorms and shower clouds can separate charge which is then transferred downwards to the surface (e.g. lightning flash) and upwards towards the ionosphere which becomes positively charged (Peterson et al., 2017). As the ionosphere (60 – 1000 km altitude) has negligible resistivity, the charge is easily distributed globally, providing a near uniform coverage of charge. As the atmosphere is slightly conductive (2 pA m^{-2}), the charge can flow towards the surface during fair and semi-fair weather conditions via the vertically flowing Air-Earth conduction current, j_c (Harrison and Nicoll, 2018). This hypothetical framework of charge transport is known as the GEC (see Figure 1-3).

The main quantity that can be used to measure the charge within a cloud is the potential gradient (PG). The PG is a widely used quantity in atmospheric electricity (MacGorman and Rust, 1998) used to measure the vertical component of the electric field, E_z ,

$$PG = -E_z. \quad 1-1$$

The PG measured at the surface is sensitive to the magnitude and polarity of charges within the atmosphere. The magnitude of the PG is the superposition of all charges within the atmosphere weighted by the square distance, r between the charge and the observer or instrument. Hence, charges near the surface (e.g. space charge) can be better observed than charges further away, such as charges within the cloud. The PG is positive when a net positive charge exists near the

measuring device, and the PG is negative when a net negative charge exists. During fair weather, the PG has a positive value typically between $50 - 200 \text{ V m}^{-1}$ with a diurnal variation caused by the GEC (Harrison and Nicoll, 2018). The PG is used rather than E_z because of the agreement between charge and PG polarities and because the PG is positive during fair weather. During disturbed weather (e.g. thunderstorms), the PG at the surface is dominated by the charge residing within the cloud, reaching much greater PG values $> \pm 1 \text{ kV m}^{-1}$. As the variability in PG during fair weather is around $5 - 20 \text{ V m}^{-1}$, the PG perturbation caused by a charged cumuliform cloud dominates in comparison (MacGorman and Rust, 1998).

The total flow of charge (current) in a column of the atmosphere moving towards the surface can also be measured. This can be useful in measuring changes in conductivity, charged precipitation and lightning (Bennett, 2018). The total current density, J_s of the atmosphere can be decomposed into four current components:

$$J_s = J_C + J_D + J_T + J_P, \quad 1-2$$

where J_C is the Air-Earth conduction current density, J_D is the displacement current density, J_T is the turbulent current density and J_P is the precipitation current density. J_C is caused by charge within the GEC, flowing from the ionosphere during fair weather. J_D is caused by changes in the PG which induces a current on the measuring sensor. J_T is caused by the transport of space charge from turbulent flows. J_P is caused by charge residing on precipitation, a current that is only observed during precipitation from an appreciably electrified cumuliform cloud (Bennett, 2018). During fair weather, J_s has a typical value of 1 pA m^{-2} , while during disturbed weather, J_s is much greater, reaching values $> \pm 100 \text{ pA m}^{-2}$ (Bennett, 2007). Similarly, the electrical current, j (lowercase J), can be calculated when the surface area of an electrode is known.

The measurements of PG and J_s are useful in measuring the electrical conditions of the atmosphere during the development of a convective cloud prior to lightning. Beyond measuring the charge within the cloud, changes in the PG variability can be used to detect the presence of charged rain and corona, a known pre-requisite of lightning (Bennett, 2018). The instrumentation used to measure the PG and J_s are discussed in §3.2 and are used throughout this thesis.

1.3 The Electrification of Convective Clouds

A basic overview of cloud electrification mechanisms is given in this section, with a review of the published literature given in §2. More detail can be found in several review papers and books,

which provides an overview of the different mechanisms hypothesised to electrify a convective cloud (Chalmers, 1967; MacGorman and Rust, 1998; Saunders, 2008).

For a cumuliform cloud to become charged enough to produce lightning there must be a physical process that can separate or capture charge and then distribute that charge inside the cumuliform cloud (Chalmers, 1967). The prerequisite for charge separation to occur requires convection to supply energy to the hydrometeors (WMO, 2017) within the cloud causing collisions, attachment, or breakup to occur (micro-scale charging). Once the charge has been separated, another process is required to move the charged hydrometeors into distinct regions of the cloud to enhance the *PG* (Beard, 1986). Figure 1-5 shows a conceptual diagram of three types of cloud electrification mechanisms that have been hypothesised in previous studies.

The convective mechanism (Figure 1-5a), uses the principle that the atmosphere contains an abundance of space charge, even during fair weather and was developed by Grenet (1947) and Vonnegut (1953). As a growing convective cloud develops an updraught, space charge beneath the cloud can be brought up into the cloud. The updraught can transport the space charge to the top of the cloud, forming screening layers due to the conductivity gradients between the clear and cloudy air (Rust and Moore, 1974). These screening layers provide charge of opposite polarity to the space charge. Through entrainment, both negative and positive charge can be distributed into the cloud. Experiments by Vonnegut and Moore (1962) showed the polarity of the cloud could be modified by inducing space charge near the surface that was lifted into the cloud, verifying the plausibility of the convective mechanism.

The inductive mechanism (Figure 1-5b), uses the principle of polarised liquid hydrometeors either colliding to separate charge between each other or by the capture of ions and was first theorised by Elster and Geitel (1888). An existing *PG* is needed for a drop to become polarised,

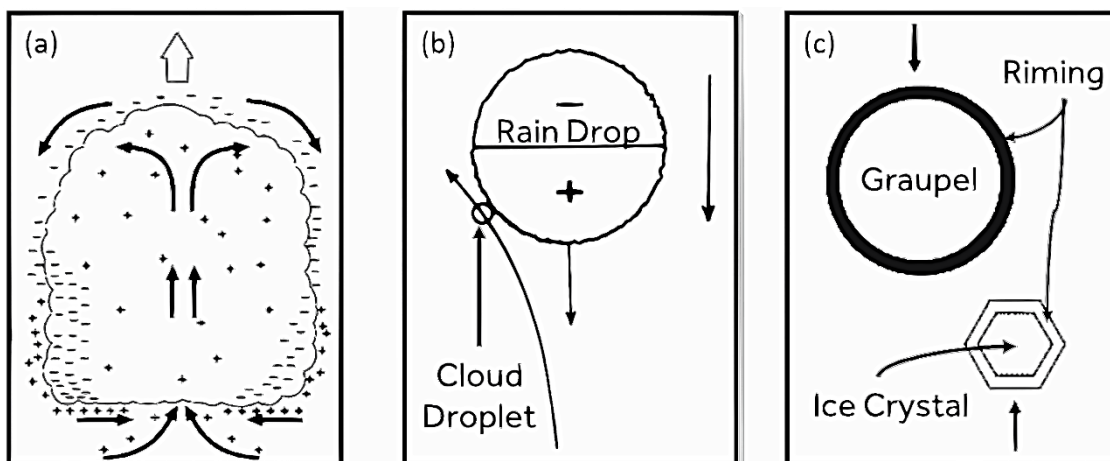


Figure 1-5: Broad classification describing different cloud electrification mechanisms. (a) convective, (b) inductive and (c) non-inductive [reproduced with kind permission from Saunders (2008)].

typically greater than the fair-weather PG . Therefore, another electrification mechanism is needed to increase the PG for the polarisation of drops to occur. A limitation of liquid hydrometeors for charge separation is their tendency to coalesce, stopping the separation of charge. The probability for two liquid drops to coalesce depends on the speed and incident angle of the interacting drop, and the magnitude of the PG (Brazier-Smith et al., 1972). The maximum PG ($\sim 30 \text{ kV m}^{-1}$) that can be observed from the inductive process occurring in an overhead cloud is also another limitation which causes the charge generation to plateau (Jennings, 1975). Mareev and Dementyeva (2017) showed, through modelling, that turbulent mixing can cause synchronisation between the charge and velocity fluctuations of the liquid hydrometeors which can cause the PG observed at the ground to grow exponentially exceeding the breakdown voltage of the atmosphere. When the eddy dissipation rate (ε_T) is greater than $100 \text{ cm}^2\text{s}^{-3}$, the inductive mechanism was found to be more important in producing a strong enough PG for the initiation of lightning compared to the non-inductive mechanism.

The non-inductive mechanism (Figure 1-5c), involves the collision between two or more ice hydrometeors to separate charge. The primary method of non-inductive charge separation depends on the properties of the hydrometeors (e.g. contact potentials, temperature, and relative growth rate) and the cloud environment (e.g. relative humidity, convection) (MacGorman and Rust, 1998). Secondary ice processes, such as ice splintering, can also enhance the non-inductive process, increasing the number of hydrometeors capable of collision (Hallett and Mossop, 1974). Many non-inductive hypotheses suggest that collision between different sized hydrometeors (typically ice crystal and graupel) are needed for charge separation to occur (Beard, 1986). One such hypothesis is the relative diffusional growth rate theory (Emersic and Saunders, 2010) which needs riming to occur on both ice crystals and graupel before they collide. The polarity of charge left on each hydrometeor is dependent on the relative growth rate between hydrometeors, along with the temperature and amount of water vapour in the cloud. Experimental evidence has suggested that the relative diffusional growth rate theory can generate both the charge structure and magnitudes seen in thunderstorms (Emersic and Saunders, 2010). Without enough water vapour for the ice hydrometeors to undergo riming, negligible charge separation can occur.

Once the charge has been separated, the charge needs to be distributed by polarity into different regions of the cloud, forming charge centres containing charge with a single polarity. The development of charge centres is required to enhance the PG , strong enough for atmospheric breakdown to occur, allowing lightning to form. Different methods have been hypothesised to distribute the charge within the cloud. Gravitational separation uses the

principle that the updraught can transport smaller hydrometeors upwards leaving heavier hydrometeors lower in the cloud (Takahashi, 1984). The relative diffusional growth rate theory (Emersic and Saunders, 2010) suggests the temperature and the amount of water content changes the polarity transferred during a collision between two different sized ice hydrometeors. Renzo and Urzay (2018) suggest the importance of turbulence in increasing the rate of collisions at the same time as forming charge centres. The mean size of eddies has been hypothesized by Renzo and Urzay (2018) to determine the size of hydrometeors preferentially captured by those eddies. Hydrometeors greater in size would gain more momentum, from the turbulence, which enables more collisions to occur with the captured hydrometeors. Due to the preferential capture of hydrometeors, charge centres are pre-formed.

A conceptual diagram of the major processes hypothesised for cloud electrification is given in Figure 1-6. The structure of the conceptual diagram is based on a review of the literature (§2) and from observations of charged cumuliform clouds obtained in this thesis (§5). Both liquid and ice hydrometeors are hypothesised to be important for cloud electrification, with neither being likely to generate enough charge for lightning to be produced on their own. The homogenous (updraught) and heterogeneous (turbulence) mixing relate to the transport of charge, forming charge centres needed to enhance the *PG*. Precipitation is the only process in Figure 1-6 which reduces the amount of charge existing within the cloud. Charged rain is a common observation of a developing cumuliform cloud (Bennett, 2018).

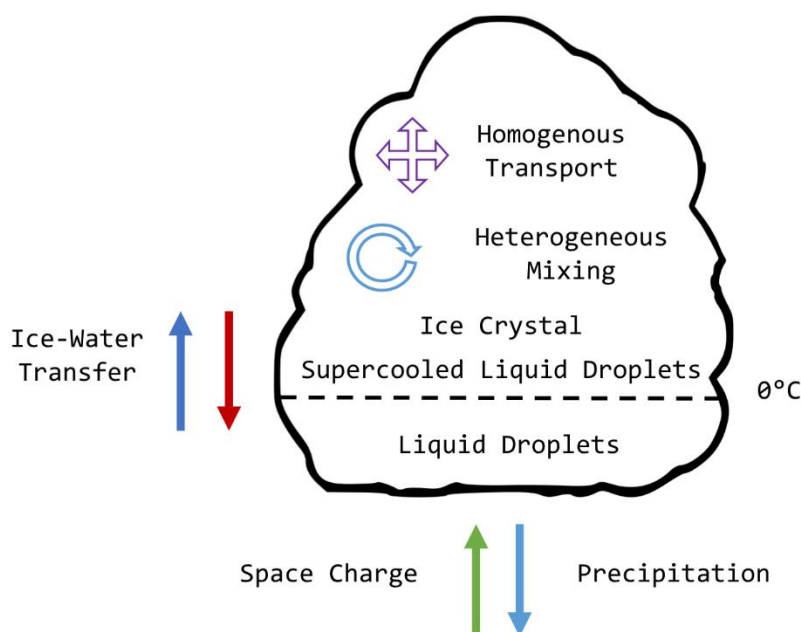


Figure 1-6: A conceptual diagram showing the main processes hypothesised for sufficient cloud electrification for lightning to be produced.

1.4 Thesis Questions

Most cumuliform clouds in the UK are substantially charged, but most would never produce lightning. The UK provides a suitable location for observing charged cumuliform clouds that fail to produce lightning and allows for a better assessment of the important cloud characteristics necessary for lightning to be produced. The cloud characteristics that inhibit the electrification of a cumuliform cloud can also be identified. Overall, this thesis aims to look at the cloud characteristics of cumuliform clouds before, and if, they produce lightning, rather than the forecasting of lightning. The findings in this thesis can be used to build better lightning forecasting algorithms. To increase the understanding of the cloud characteristics needed for cloud electrification, four questions are investigated in this thesis:

1) What are the effects of precipitation on the local potential gradient?

Measuring the PG at the surface provides a convenient way to measure the charge within a cumuliform cloud continuously and remotely. As the magnitude of the PG is dependent on the distance between the charge and the observer (Coulomb's law), the charge existing within a cloud must be substantial enough to be detected above smaller charges closer to the observer. Furthermore, the possible presence of charged rain, corona, and lightning in cumuliform clouds, can greatly influence the PG , making interpretation of the PG difficult. For example, during precipitation, droplets themselves can influence the PG and distort the influence of charge in the clouds being measured at the surface. Therefore, it is important to characterise how precipitation influences the PG at the surface to enable either compensation for this effect when using the PG to diagnose cloud electrification or to determine when PG measurements cannot be accurately used to diagnose cloud electrification. An analysis of rain rate (RR) is compared against the PG along with the local meteorological conditions (e.g. wind speed, surface wetness) to investigate the importance of splashing of the drops against the surface.

2) What are the main processes needed for appreciable electrification of a convective cloud that could lead to lightning?

The microscale electrification processes, such as ice-ice hydrometeor collisions, are well established and have been observed to produce enough charge separation to initiate lightning (Saunders et al., 2001). The processes, such as turbulence, needed to enhance the microscale electrification by distributing the charge by polarity into charge centres of a single polarity are less established. These processes are collectively termed macroscale electrification processes here. Understanding the cloud-scale processes needed for electrification to occur is important to forecast lightning. An analysis of cumuliform clouds at various stages of convective and

electrical development was used to compare measurements of the *PG* at the surface with radar measurements. The size of the cloud, hydrometeor size, and turbulence are compared with the *PG*.

3) How does charge within the cloud relate to the charge measured at the surface?

To use atmospheric electrical measurements to forecast lightning, further understanding of how the charge within the cloud is related to the *PG* at the surface is needed. Using radiosonde measurements of charged cumuliform clouds, a comparison was made to determine the relationship of the vertical charge structure with respect to the *PG* measured at the surface.

4) Why are most convective clouds charged, but rarely produce lightning?

The organisation of charge within a cloud is just as important as generating the charge, as the overall aim is to enhance the *PG* enough to breakdown the atmosphere for lightning to be initiated. For example, all hydrometeors can be charged with an equal number being positively and negatively charged, but if the distribution of the charged hydrometeors is homogenous, no perturbation of the *PG* is possible. Therefore, the charge needs to be distributed by polarity, with enough charge for an atmospheric electrical breakdown. To fulfil the main aim of this thesis, the organisation of charge within the cloud was also analysed using radiosonde measurements of charged clouds.

1.5 Thesis Structure

The questions in §1.4 form the basis of the chapters of this thesis. In chapter 2, existing cloud electrification mechanisms are reviewed and ranked according to their importance in enhancing the *PG* prior to lightning being initiated. The influence of precipitation on the *PG* is also reviewed to rank its importance in enhancing the *PG* when precipitating clouds are overhead. In Chapter 3, the instruments used to gather data are described in detail. In chapter 4, the *PG* is compared to the *RR* (Question 1). In chapter 5, cumuliform clouds are identified and used to compare the *PG* with various cloud characteristics (Question 2 and 4). In chapter 6, radiosondes were flown into cumuliform clouds to provide in situ measurements of cloud charge, allowing further understanding of the cloud characteristics important for cloud electrification (Question 3 and 4). An overview of the findings is presented in chapter 7, along with a discussion of their importance in the wider context. Finally, a discussion of how this work can be continued in the future along with a discussion of the questions that are still unsolved is presented. The appendices include calibration values of the instruments used in this thesis and other supplementary information.

2 A review of cloud electrification and the influence of precipitation on the potential gradient

This chapter consists of two parts. The first part discusses the cloud electrification mechanisms that have been theorised, capable of separating enough charge for lightning to occur along with how these mechanisms can organise the charge within the cloud (§2.1). The second part discusses the influence of precipitation on the potential gradient (PG) at the surface and explores how drops splashing against the surface, can influence the PG (§2.2).

2.1 Cloud Electrification Mechanisms

A discussion of the formation of cumuliform clouds was given in §1.1 and the electrification mechanisms involving cumuliform clouds are now discussed in this section. Since Wilson's (1916; 1920; 1929) and Simpson's (1909) measurement of the PG , when charged clouds were nearby, understanding how the charge structures within cumuliform clouds are formed and how they can create lightning has caused many different hypotheses to be developed. Many of these electrification hypotheses are discussed in the following section as they highlight the micro- and cloud-scale electrical processes that occur prior to lightning. To simplify matters, the mechanisms have been grouped into four classifications (Figure 1-5). The classifications are the ion capture, convective, inductive, and non-inductive mechanisms. Figure 1-5 shows a conceptual diagram of the four electrification mechanisms that are discussed in the following sections. The ion capture and convective mechanism involve the capture and distribution of freely available ions in the atmosphere. The inductive and non-inductive mechanisms involve collisions between hydrometeors that are polarised and unpolarised respectively.

A brief overview of each mechanism was given in §1.3. In this section, each cloud electrification mechanism type is discussed further, detailing the physical conditions required for them to work along with the limitations of each mechanism. As there are so many mechanisms, all of which

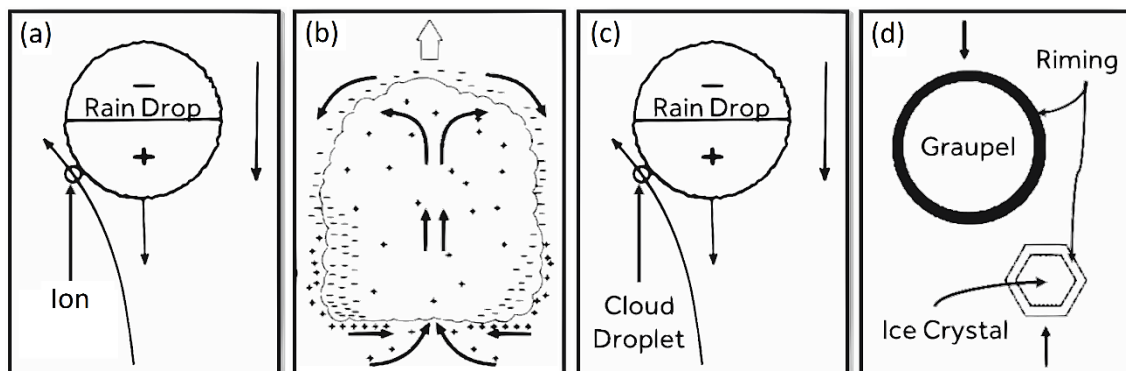


Figure 2-1: Broad classification describing different cloud electrification mechanisms. (a) ion-capture, (b) convective (c) inductive and (d) non-inductive [reproduced with kind permission from Saunders (2008)].

could occur within the lifetime of a cumuliform cloud, a synthesis of these mechanisms is given, narrowing down what are the important cloud characteristics that are thought to be responsible for charge separation (§2.1.6). This electrification synthesis is used to form the hypotheses in the work chapters (§5 and 6) to answer the thesis research questions.

2.1.1 Ion Capture Mechanism

The ion capture mechanisms involve the kinematics and capture of space charge (micro-scale) in the atmosphere (MacGorman and Rust, 1998). There is an abundance of space charge within the atmosphere, even during fair weather, which is created naturally through ionisation from galactic cosmic rays, radioactive decay and corona. Corona only occurs when the ambient PG is very large ($> 4 \text{ kV m}^{-1}$), and typically only occurs when highly charged cumuliform clouds are overhead (MacGorman and Rust, 1998). The rate of surface ionisation can be estimated to be around 11 ion pairs per cubic centimetre per second during fair weather (Saunders, 2008), but this can vary greatly depending on the wind speed, overhead cloud type (e.g. stratiform, cumuliform), and the geographic location (due to variations in surface radioactivity).

Wilson (1929) proposed that in the presence of a substantial PG , ions can be captured by liquid drops as they fall through the cloud because of electrostatic attraction. The drops need to be polarised before they can selectively capture ions. A drop of a certain size can be polarised by the PG if the strength of the PG is strong enough. For example, if the PG is positive, positive ions would reside on the underside of a drop (see Figure 2-1a). For a drop to gain a net charge, the speed difference between drop and ion must be small enough to avoid the capture of positive ions on the top side of a drop. This theory is known as the selective ion capture mechanism.

A theoretical treatment of the ideas proposed by Wilson (1929) was fully developed by Whipple and Chalmers (1944) who took the strength of the PG , the size of the drop and the viscosity of the air into consideration. The relative velocity between a drop and an ion must be fast enough for the ion to be captured. From Whipple and Chalmers (1944) a relationship was found between the charge on the drop, Q , the PG and the drop radius r ;

$$Q = \begin{cases} 3 \cdot PG \cdot r^2 & -ve \text{ ions} \\ -3 \cdot PG \cdot r^2 & +ve \text{ ions} \\ 0.55 \cdot PG \cdot r^2 & +ve \text{ and } -ve \text{ ions} \end{cases} \quad 2-1$$

In the experimental analysis by Abbas and Latham (1967), polarised liquid drops preferentially captured ions of the same polarity to the PG . Figure 2-2a shows the empirical relationship of the charge acquired by a drop with a constant radius ($r = 0.145 \text{ cm}$) that has been exposed to both

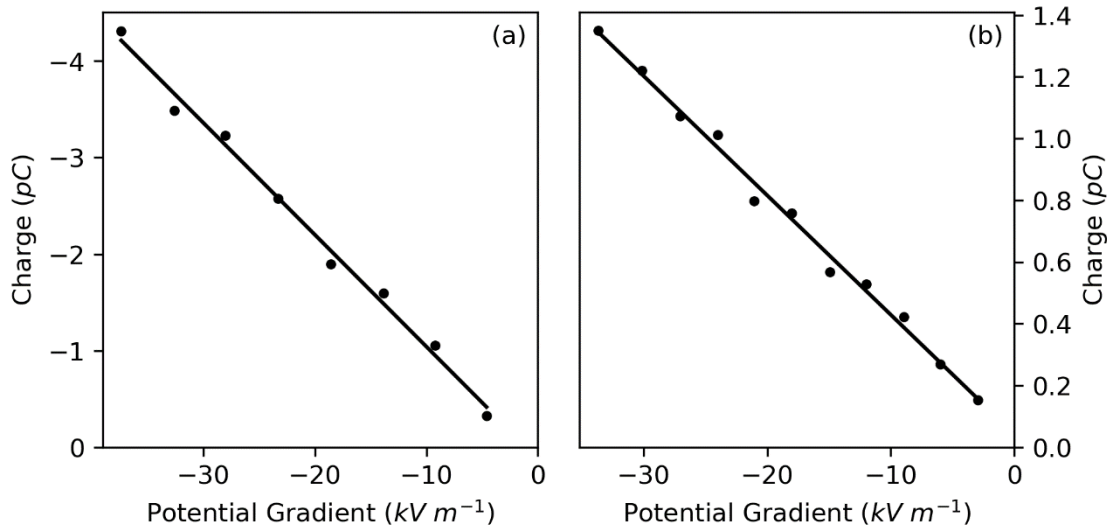


Figure 2-2: (a) The charge, Q captured by an uncharged suspended liquid drop ($r = 0.145$ cm), which has been polarised by an ambient PG . Positive, and negative ions were injected into the environment with the suspended drop. (b) The charge, Q captured by an uncharged ice sphere ($r = 0.111$ cm) of irregular surface structure which has been polarised by an ambient PG . Positive ions were injected into the environment with the ice sphere [reproduced and converted to SI units with kind permission from Abbas and Latham (1967)].

positive and negative ions. Despite equal amounts of ion concentrations, the drop increases its negative charge consistent with the theory by Whipple and Chalmers.

Despite the experimental evidence supporting the selective ion capture mechanism, two fundamental limitations can be considered. First, as a drop continues to capture charge of a single polarity, its electrostatic attraction to oppositely charged ions would increase exponentially, thereby limiting the amount of charge that can be captured (Abbas and Latham, 1967). Second, the total electrification of any cloud is limited by the amount of available space charge. Once all the ions in the cloud have been captured, the electrical growth of the cloud would stall. Either a substantial influx of ions is required from outside of the cloud (see §2.1.2) or another electrification mechanism is needed to further enhance the PG (see §2.1.3 and 2.1.4).

Wilson's ion capture theory can be extended to polarised ice spheres which have been shown to capture ions in a similar way to liquid drops (Abbas and Latham, 1967). Whipple and Chalmers (1944) quantitative treatment of how ions are captured from polarised water drops also holds for ice spheres that are riming. In Figure 2-2b, the total charge on a drop matches the relationship defined by Whipple and Chalmers (1944) for fast moving positive ions ($Q = +3 \cdot PG \cdot r^2$) to within 5%. Abbas and Latham (1967) showed the surface smoothness had very little influence on the total amount of charge that an ice sphere can capture. The amount of charge that can be captured was also found to be related to the strength of the ambient PG under experimental conditions (Figure 2-2b). The polarity of the ion captured is controlled by the polarity of the ambient PG , similar to the drops in the Wilson theory. The influence of both

polarised liquid and ice hydrometeors are important in the development of cloud electrification which can occur in the full depth of the cloud.

The capture of ions does not necessarily require the hydrometeor to be polarised. Unpolarised liquid drops in ionised air have been shown to acquire negative space charge preferentially over positive space charge (Wormell, 1953). Frenkel (1947) suggested that water drops would become stable after becoming negatively charged. The remaining positive ions are unaffected by water drops and both polarities are separated under gravitational separation enhancing the *PG*. Gravitational separation (cloud-scale) occurs when hydrometeors of different sizes fall at different rates through the cloud, thereby increasing the distance between charges. If an updraught exists then smaller hydrometeors can ascend while larger hydrometeors continue to descend. The kinematics of a hydrometeor depends strongly on its size distribution and the strength of the updraught.

The difference between the Frenkel and the Wilson theory involves the water drops being polarised. No experimental evidence has been found to agree with Frenkel's unpolarised ion capture mechanism though. According to Frenkel (1947), the capture of negative ions is dependent on drop size and *PG* strength. For example, for a drop size of 50 μm , the *PG* must be less than 100 V m^{-1} . For larger drop sizes or an increase in *PG*, a polarised drop is needed (Wormell, 1953). Despite the Frenkel (1947) mechanism not being very effective in capturing charge, Wormell (1953) suggests, with caution, that this mechanism might be responsible for determining the polarity of the cumuliform cloud.

An overview of the ion-capture mechanisms is given in Table 2-1. This highlights the micro- and cloud-scale processes for each mechanism and the cloud and hydrometeor properties that are important for the mechanisms to function.

2.1.2 Convective Mechanism

Similar to the ion capture mechanism, the convective mechanism is also concerned with space charge. During the initial development of a cumulus cloud, space charge can be lifted from the surface into the cloud along an updraught according to the theory developed by Grenet (1947) and Vonnegut (1953). As the space charge enters the cloud, screening layers are induced at the cloud boundary collecting charge of opposite polarity at the clear-air—cloud interface. Screening layers are caused by a difference in conductivity between the clear-air—cloud interfaces and the strength of the screening layer is dependent on the growth rate of a cumulus cloud in the early development stage (Rust and Moore, 1974). The space charge, brought into the cloud by the updraught, is then captured by liquid and frozen drops as described by the

Table 2-1: A summary of the ion-capture mechanisms that can occur within cumuliform clouds with the micro-scale and cloud-scale features. The cloud and hydrometeor properties that each mechanism are dependent on are given along with a qualitative rank of how each mechanism can organise the charge [adapted from Beard (1986) with additions from Chalmers (1967), MacGorman and Rust (1998) and Saunders (2001)].

<i>Mechanism</i>	Micro-scale Processes	Cloud-scale Processes	Charge Organisation	Cloud and Hydrometeor Properties
<i>Breaking Drop Theory (Lenard, 1892)</i>	Charge transfer between polarized particles	Sedimentation	Small	Surface tension; Relative Drop Size
<i>Wilson Ion Capture (Wilson, 1929)</i>		Sedimentation	Small	Relative Drop Velocity
<i>Unpolarised Ion Capture (Frenkel, 1947)</i>	Charge transfer between unpolarized particles	Sedimentation	Small	Drop Size; PG strength

Wilson (1929) and Frenkel (1947) mechanisms. The updraughts within the cloud cause the charge to be lifted to the top of the cloud creating a secondary charging layer at the cloud top.

In the theory by Grenet (1947) and Vonnegut (1953), the cloud boundaries are treated as rigid surfaces rather than diffuse edges. The screening layer at the top of the cloud induces a charge of opposite polarity along the cloud edge. Downdraughts near the top of the cloud cause the charge to flow around the cloud boundary through entrainment as described by Squires (1958). The process of entrainment only occurs after the cumulus cloud has a substantial vertical depth (> 4 km). Squires (1958) also noted that, during the development of a cumulus cloud, dry air must mix with condensation nuclei to account for the steep lapse rates typically found. The downdraughts of air caused by evaporative cooling coincide with the theory that space charge can be transported into the cloud from space charge created solely from galactic cosmic ray ionisation above the cloud (Pruppacher, 1963).

Experimental investigations of the convective mechanism were designed to show the interaction of space charge on developing cumulus clouds by deliberately releasing space charge from the surface using a 14 km long fine wire (Vonnegut and Moore, 1962). At the same time, PG measurements were made simultaneously at the surface and aloft above the cloud top. Figure 2-3 shows the influence of positive space charge being advected aloft by thermal gradients and

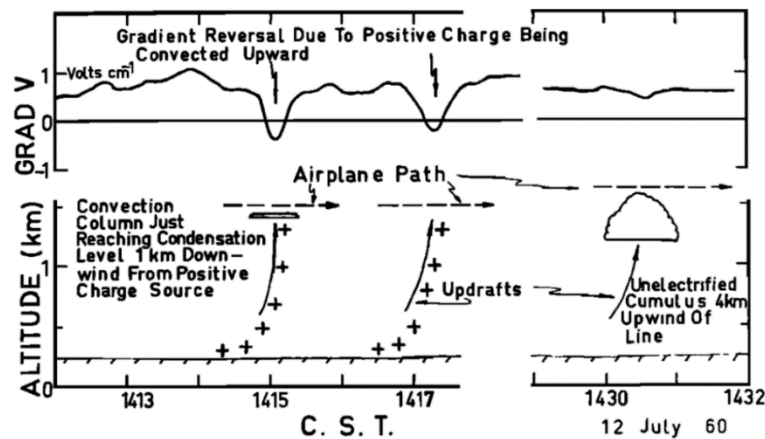


Figure 2-3: A time series (C.S.T = Central Standard Time = UTC – 6) of the potential gradient measured aloft when positive space charge was released from a 14 km fine wire. The potential gradient was also measured when a non-electrified cumulus cloud was overhead [reproduced with kind permission from Vonnegut and Moore (1962)].

shows a reversal in the *PG* measured aloft. The induced space charge was also lifted into a nearby developing cumulus cloud along its updraft. The dominant polarity of a charging cumulus cloud could be modulated by the polarity of the space charge. Changing the induced space charge polarity at the surface flipped the polarity of the charge within the overhead cumulus cloud. The influence of space charge on a developing cumulus cloud highlights the importance of charge separation.

The advection of space charge using the convective mechanism is beneficial for the ion-capture mechanism. Additional space charge supplied by the convective mechanism allows liquid drops to continuously capture ions within the cloud. As there is a limited amount of space charge beneath the cloud, the convective mechanism and ion-capture mechanisms are not sufficient to enhance the *PG* to cause a breakdown of the atmosphere for lightning to be produced (Saunders, 1992). An overview of the convective mechanism is given in Table 2-2. As with Table 2-1, this highlights the micro- and cloud-scale processes for the convective mechanism and the cloud and hydrometeor properties that are important for the mechanism to function.

2.1.3 Inductive Mechanisms

The inductive mechanism requires the collision of hydrometeors that have been polarised by the *PG* (micro-scale) and was first theorised by Elster and Geitel (1888). This is different from the ion-capture mechanism, which is a passive charging mechanism, as the inductive mechanism causes charge to be separated between hydrometeors (an active mechanism). The ability of a drop to become polarised is a function of the ambient *PG*, temperature, relaxation time and radius of a drop (Singh and Singh, 2004). An increase in temperature increases the polarizability of a drop because of the increased thermodynamic energy available to organise the positive and negative charge within the drop. Figure 2-4 shows the relationship between the radius of a drop

Table 2-2: Same as Table 2-1 but for the convective mechanism.

<i>Mechanism</i>	Micro-scale Processes	Cloud-scale Processes	Charge Organisation	Cloud and Hydrometeor Properties
<i>Convective Mechanism (Vonnegut, 1953)</i>	Space charge production, ion capture in drift currents	Convection	Large	Temperature

and the applied *PG* required for polarisation to occur. As an existing *PG* is required, a separate electrification mechanism must exist beforehand to strengthen the *PG* sufficiently. Therefore, the inductive mechanism is likely only important in the advanced stages of a cumuliform cloud.

Once the charge has been separated, after a collision between hydrometeors, the *PG* is enhanced through gravitational separation (Illingworth and Caranti, 1985). In general, for the charge to be transferred under the inductive mechanism, two conditions are required. First, an electrical conductivity high enough for the hydrometeor to be polarised. Second, the collision time must be longer than the electrical relaxation time for the charge to be transferred between colliding particles (Saunders, 2008).

There are four types of interactions that can occur when two liquid drops collide: (1) bouncing, (2) permanent coalescence, (3) partial coalescence and (4) coalescence with smaller droplets being ejected (Brazier-Smith et al., 1972). For the charge to separate, a colliding drop must initially coalesce and then detach, leaving the droplet with a net charge. For drop-drop interactions, collision often leads to permanent coalescence (Levin and Machnes, 1977). The

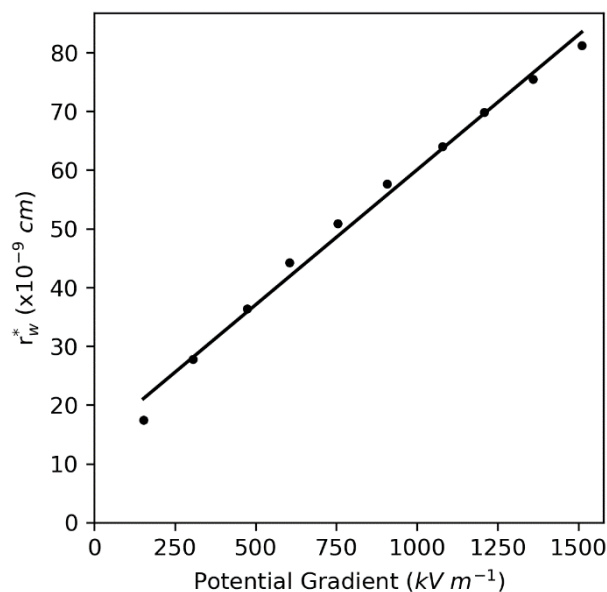


Figure 2-4: The critical polarisation radius of liquid water drop, r_w^* as a function of the *PG* for a constant temperature (263 K) [reproduced and converted to SI units with kind permission from Singh and Singh (2004)].

four interaction types are strongly dependent on the relative drop size, relative velocity, external PG and the charge present on the drop (Jennings, 1975; Levin and Machnes, 1977). Although the permanent coalescence efficiency is typically high ($> 80\%$), under certain conditions the partial coalescence efficiency can be maximised. For drop-drop collisions, a large enough difference in drop-drop sizes and an incident angle between $45-67.5^\circ$ has been observed to provide partial coalescence efficiencies of up to 25% (Levin and Machnes, 1977).

Ice crystals and graupel have a high enough electrical conductivity for polarisation to occur, but for unpolluted ice crystals, the efficiency of ice-ice collisions to separate charge has a nearly zero efficiency. Illingworth and Caranti (1985) discovered that the finite conductivity of ice was not sufficient to inductively separate charge. Charge separation can occur by increasing the conductivity of ice and was achieved by adding Sodium Chloride (NaCl) to the ice structure. NaCl has been used to accelerate droplet nucleation to enable clouds to prematurely precipitate (i.e. cloud seeding) (Langmuir, 1951). The amount of NaCl used to activate charge separation in ice-ice collisions was 10^{-2} mol/L but the amount of NaCl found in the atmosphere is not sufficient for charge to be separated inductively, even in highly polluted areas.

The collisions between riming ice and supercooled liquid drops have been shown to separate charge with a higher efficiency under a strong enough PG (> 10 kV m^{-1}) (Aufdermaur and Johnson, 1972). For the charge to be separated, a supercooled liquid drop must collide and rebound from the ice sphere. The supercooled drop must collide with the ice at a very shallow angle which would gently graze the ice. Even though the collision efficiency of these events is very low ($0.01 - 0.1\%$), the amount of charge released ($2 - 30$ fC) and the rate of collisions was found to be sufficient enough to cause the electrification observed in thunderstorms (Gaskell, 1981). Collisions between riming ice and supercooled drops have a higher conductivity and are less prone to permanent coalescence. Another advantage is that charge resides on the rime of an ice sphere which would increase the charge separation after the collision. The polarity of charge residing on rimed ice is largely controlled by the temperature and liquid water content (Saunders et al., 1985)

Another issue to consider is that the PG can increase the coalescence efficiency of cloud droplets (Freier, 1960). Jennings (1975) suggested a PG greater than 30 kV m^{-1} would cause permanent coalescence after their results showed the charge separation efficiency rate decreased with increasing PG strength. As the drops are polarised, they would travel along the electric field lines gaining momentum. For a PG greater than 30 kV m^{-1} , the drops increase their effective radius improving the drops ability to attract nearby droplets and coalesce.

The rate of nucleation (both condensation and ice) is dependent on the strength of the PG (Pruppacher, 1963; Singh and Singh, 2004). The PG induces polarisation charges within the drop which causes deformation. As deformation of a drop occurs, energy is given to the system leading to nucleation. This process could further reduce the relevance of the inductive mechanism in developing cumuliform clouds as pure ice-ice collisions have an insufficient electrical conductivity to induce a charge.

As discussed, the inductive mechanism has two fundamental limitations that limit its ability for the electrification of a cumuliform cloud. The inductive mechanism requires a large enough PG to polarise drops but small enough to stop permanent coalescence of the drops. The hydrometeor type is also important in separating charge as the collision between all hydrometeor combinations (e.g. liquid-liquid, ice-liquid and ice-ice) have fundamental limitations that only allow charge to separate under specific conditions. Therefore, this mechanism can only be considered plausible within a finite region of the development of a cumuliform cloud. Nevertheless, this mechanism can still be useful for the enhancement of the PG if it coincides with another electrification mechanism (e.g. non-inductive).

An overview of the inductive mechanism is given in Table 2-3. As with Table 2-1, this highlights the micro- and cloud-scale processes for the inductive mechanism and the cloud and hydrometeor properties that are important for the mechanism to function.

2.1.4 Non-Inductive Mechanisms

The non-inductive mechanism involves the collision between two unpolarised hydrometeors (micro-scale) and does not require an ambient PG for charge separation to occur (MacGorman and Rust, 1998). The intensification of the PG after charge separation varies between hypotheses but typically depends on the characteristics of the cloud (e.g. temperature and moisture), which influence the polarity of charge being separated (cloud-scale). These characteristics provide an inherent spatial variability in the charge structure (Emersic and

Table 2-3: Same as Table 2-1 but for the inductive mechanism.

<i>Mechanism</i>	Micro-scale Processes	Cloud-scale Processes	Charge Organisation	Cloud and Hydrometeor Properties
<i>Particle-Particle collisions (Sartor, 1954; Elster and Geitel, 1913)</i>	Charge transfer between polarized particles	Sedimentation	Small	Relative Drop Size; Impurities

Saunders, 2010). Intensification by gravitational separation is a fundamental requirement for certain mechanisms such as the melting ice mechanism (Dinger and Gunn, 1946).

Most charge separation hypotheses developed can be considered non-inductive and are reviewed in detail in several articles and books (Chalmers, 1967; Saunders, 1992; MacGorman and Rust, 1998; Saunders, 2008). The underlying physical processes of the non-inductive mechanisms are discussed in this section, focusing on the spatial and temporal limitations underpinning the development of a cumuliform cloud. The main methods of charge separation occur through (1) contact potentials, (2) splashing, (3) ice splintering, (4) convection, (5) temperature variations and (6) relative growth rate.

Contact Potentials

A contact potential exists between two substances (e.g. ice-air, liquid-air) and is caused by the orientation of the molecules within each substance. A contact potential creates an electric double layer¹ at the interface between the two substances (Dinger and Gunn, 1946; Grahame, 1947; Stojek, 2010). The contact potential typically intensifies (order of 10 V) during the freezing phase transition of pure liquid drops. A contact potential has been observed during the freezing of liquid drops (Dinger and Gunn, 1946) and the freezing of supercooled drops on ice particles (Caranti and Illingworth, 1980), also known as riming. The contact potential could account for charges being induced on the hydrometeors during their phase transition. Laboratory studies have found that the net polarity on ice hydrometeors depends on the temperature and effective water content² of the cloud, with the contact potential being unaffected (Saunders, 2008).

Droplet Splashing

The contact potential mechanism can be extended further when taking into account the splashing of supercooled drops on ice particles which can release negative charge (Workman and Reynolds, 1950). The separation of charge from droplet splashing on ice is limited to regions of the cloud with temperatures < -10 °C, thereby limiting the spatial and temporal³ potential for this mechanism considerably. The splashing of drops is similar to the observations made by Lenard (1892) where negative space charge was measured near waterfalls (a complete discussion of droplet splashing is given in §2.2). This mechanism is inefficient at separating

¹ A double layer consists of a thin layer of positive and negative charge stacked on top of each other and is found at the boundaries between the water and air interfaces. This combination of charged layers is only present when an object is wet and the disruption of such a layer causes the charges to be separated rather than discharged straight to the object (Levin and Hobbs, 1971).

² The effective water content can be defined as the liquid water content multiplied by the liquid water path. Physically this is the amount of water available for an ice particle to grow from diffusion.

³ The development of the cloud must be sufficient for an ice phase to exist below -10°C.

charge and would not produce enough charge to cause atmospheric breakdown within the typical lifetime of a cloud (Caranti and Illingworth, 1983). This is in agreement with observations of the small amount of charge released by splashing at the surface, relative to the charge required for lightning to occur (Levin and Hobbs, 1971). Nevertheless, the release of negative space charge into the cloud can be used by the Wilson (1929) and Frenkel (1947) mechanisms to further enhance the *PG*.

Ice Splintering

Ice splintering can occur during the freezing of supercooled liquid water on ice hydrometeors between a temperature of -3 and -8 °C travelling at a relative velocity between 0.15 and 2.1 m s⁻¹ (Latham and Mason, 1961; Saunders, 2008). During the ice splintering process, a net charge is gained on the primary and secondary ice hydrometeors. The net polarity on each ice hydrometeor was found to depend on the growth rate of the primary ice hydrometeor (Hallett and Saunders, 1979). Charge measurements were conducted by Hallett and Mossop (1974) during the ice multiplication processes and concluded that the number of secondary ice hydrometeors produced was small and does not account for the number of ice hydrometeors observed in natural clouds. The amount of charge found per fragment was on the order of 10⁻¹⁶ C, and was found to not account for the rate of electrification observed within measured thunderstorms (Saunders, 2008). Nevertheless, despite the narrow region of the cloud that the ice splintering mechanism can operate, the production of secondary ice hydrometeors can allow a chain reaction to occur as long as enough moisture is supplied to that region. This mechanism can possibly feed into other non-inductive mechanisms that require the collision between hydrometeors to separate charge, reducing the risk for a cumuliform cloud to stop its electrification.

Convection

Convection within melting ice particles was found to produce negatively charged droplets caused by the bursting of air bubbles (Saunders, 2008). Dinger and Gunn (1946) measured on average -4.17×10^{-10} C ml⁻¹ of charge acquired by the air and $+4.17 \times 10^{-10}$ C ml⁻¹ was acquired by melting ice. The rate at which the ice melts is directly related to the amount of charge transferred. As a liquid drop freezes, dissolved gases can form bubbles that reach the ice-air interface. During the subsequent melting, these air bubbles can burst caused by convection (Kochin, 2001). Under the same principle, as defined by Lenard (1892), the bursting of the air bubbles can release negative ions within the cloud. The charge transfer is weakened if the ice contains impurities (e.g. sodium hydroxide (NaOH)) and under sufficient concentrations can completely suppress the electrification mechanism. The melting mechanism is important in

defining the lower positive charge centre, important in the development of cloud-to-ground lightning, and for the development of charged precipitation during substantially developed cumuliform clouds. The evolution of precipitation after being ejected from the cloud is discussed in detail in §2.2.2.

Temperature Variations and Relative Growth Rates

An important process for charge separation involves the relative growth rates of ice hydrometeors which are controlled by the supersaturation of the cloud itself. Ice growing by vapour diffusion is typically positively charged, with sublimation being negatively charged (Dash et al., 2001). Experimental evidence of ice-ice collisions in cloud chambers showed a strong dependence between the relative growth and the polarity of charge which is transferred (Saunders et al., 2001). The experiments showed that the faster-growing ice particle would become positively charged while the slower-growing ice particle would become negatively charged. During the collision, mass is transferred between ice particles and the charge present on the particle's surface is transferred to the neighbouring particle. The discussion by Dinger and Gunn (1946) and Caranti (1991) showed that negative charge would reside on an ice particle's liquid-air interface; the fast-growing particle would have a greater negative charge present on its interface. During an ice-ice collision, greater negative charge can be transferred, providing a net positive charge on the faster-growing ice particle. This mechanism is called the relative diffusional growth rate theory (Emersic and Saunders, 2010).

During a graupel-crystal collision, the polarity of charge separated was found to be strongly related to the temperature and effective water content within the cloud (Emersic and Saunders, 2010). Figure 2-5 shows the polarity of charge gained after a collision between graupel and ice crystals dependent upon the cloud temperature and the effective water content (Emersic and Saunders, 2010). The relevance of temperature and effective water content relates to the supersaturated vapour pressure required for ice particles to grow. Similar to the coalescence and growth of liquid droplets, there is a size dependence on the growth rate. Smaller particles tend to grow at a faster rate at the expense of supercooled droplets (Dominguez, 2011). Two factors strongly influence the rate and structure of a cloud charging, (1) the greater the supersaturation, the greater the rate of electrification and (2) a greater mixing of hydrometeors, the stronger the temperature dependence (Twomey, 1956). The relative diffusional growth rate theory is typically regarded, in the literature, as the main mechanism responsible for the charge observed in a thunderstorm.

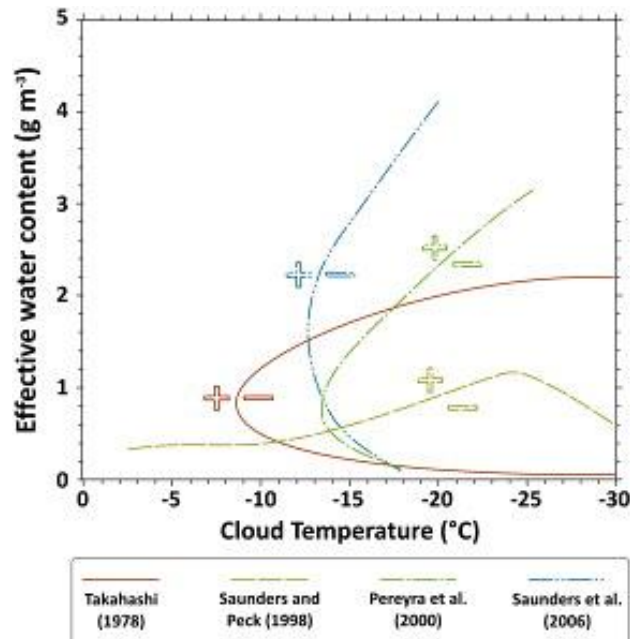


Figure 2-5: The charge gained by graupel after collision with an ice crystal by varying the effective water content and cloud temperature [reproduced with kind permission from Emersic and Saunders (2010)].

As discussed, the non-inductive charging mechanism is a viable candidate for the dominant electrification mechanism in a cumuliform cloud as the amount of charge that can be separated through these processes are consistent with the charge observed in thunderstorms. There are many physical processes which have been hypothesised to occur during a collision between ice and supercooled particles, but these vary in the amount of charge that can be separated and when the process can occur within the development of the cloud. The melting mechanism, for example, provides a useful method for charged precipitation and the development of a lower positive charge centre. The melting mechanism would only occur during the later stages of the development of a cumuliform cloud when downdraughts are capable of descending ice into the warm region of the cloud ($> 0^{\circ}\text{C}$). The relative diffusional growth rate theory shows a good example of how the charged layers are created without the dependence on gravitational separation. Furthermore, the rate of electrification is dependent on the physical properties of the cloud such as the effective water content of the ice phase which is maintained by an influx of supercooled water from the warm region of the cloud.

An overview of the non-inductive mechanisms is given in Table 2-4. As with Table 2-1, this highlights the micro- and cloud-scale processes for the mechanisms and the cloud and hydrometeor properties that are important for the mechanism to function. There are common properties between many non-inductive mechanisms. These commonalities between mechanisms are discussed in §2.1.6 and form the basis for analysing cumuliform clouds in §5 and 6.

Table 2-4: Same as Table 2-1 but for the non-inductive mechanism.

<i>Mechanism</i>	Micro-scale Processes	Cloud-scale Processes	Charge Organisation	Cloud and Hydrometeor Properties
<i>Graupel-Ice (GI) collisions (Reynolds et al., 1957)</i>	Charge transfer between particles of differing growth rates and temperature	Sedimentation	Large	Temperature; Effective Water Content
<i>Williams GI (Williams et al., 1991)</i>	Charge transfer between particles of differing growth rates	Sedimentation	Large	Effective Water Content; Growth and Sublimation Rates
<i>Caranti GI (Caranti et al., 1991)</i>	Charge transfer between particles of differing temperature	Sedimentation	Large	Temperature; Growth and Sublimation Rates
<i>Baker GI (Baker and Dash, 1994)</i>	Charge transfer between particles transferring liquids on contact	Sedimentation	Large	Effective Water Content; Relative Mass Transfer;
<i>Illingworth GI (Illingworth, 1985)</i>	Charge from non-uniform ice growth	Sedimentation	Large	Temperature; Growth and Sublimation Rates
<i>Temperature Gradients in Ice (Keith and Saunders, 1990)</i>	Charge transfer between particles of differing temperature	Sedimentation	Large	Temperature; Sublimation Rates
<i>Screening Layer (Rust and Moore, 1974)</i>	Ion capture by changes in conductivity	Conductivity	Small	Temperature; Conductivity

<i>Mechanism</i>	Micro-scale Processes	Cloud-scale Processes	Charge Organisation	Cloud and Hydrometeor Properties
<i>Freezing Potentials (Workman and Reynolds, 1950)</i>	Charge transfer between particles involving contact potentials	Sedimentation	Very Small	Temperature
<i>Contact Potential (Caranti and Illingworth, 1980)</i>	Charge transfer between particles involving contact potentials	Sedimentation	Medium	Relative Drop Size; Relative Mass Transfer
<i>Melting Effects (Dinger and Gunn, 1946)</i>	Breakup of water from melting ice	Drift Currents	Medium	Impurities
<i>Ice Splintering (Latham and Mason, 1961; Hallett and Mossop, 1974)</i>	Shattering of ice on freezing	Sedimentation	Medium	Effective Water Content
<i>Relative Diffusional Growth (Dash et al., 2001; Reynolds et al., 1957; Mason and Dash, 2000; Saunders et al., 2001)</i>	Charge transfer between particles transferring liquids on contact	Temperature and Effective Water Content	Large	Temperature; Effective Water Content; Relative Mass Transfer; Impurities

2.1.5 Enhancement of the Potential Gradient

Once charge has been either separated or captured by the hydrometeors, it is necessary to organise the charge, by polarity, into separate regions of the cloud. Transporting a single polarity of charge allows the formation of charge centres within the cumuliform cloud and allows the enhancement of the *PG*. Without the enhancement of the *PG*, no electrical breakdown of the atmosphere would be possible and therefore, no lightning would be produced from a cumuliform cloud (MacGorman and Rust, 1998).

Some of the methods used to organise hydrometeors, with a net charge, have already been discussed. One method to organise the charge within the cloud is gravitational separation. As most electrification mechanisms state that there is a difference in hydrometeor sizes that gain a net positive and net negative charge, convection can be used to split the different sized hydrometeors (Saunders, 2008). Under ideal circumstances, an updraught can lift the smaller, lighter hydrometeors into the higher region of the cumuliform cloud, leaving behind larger, heavier hydrometeors. As long as there is a substantial movement of net negative or positive charge, away from the opposite polarity, then the *PG* would be enhanced. Depending on the separation distance and the magnitude of the newly formed charge centres, an atmospheric breakdown can occur forming lightning. As there is a balancing of forces, between updraught speed and gravitational acceleration, it is difficult to assume that the hydrometeors with a particular net polarity could become organised sufficiently using gravitational separation alone after the charge has been separated. The Wilson (1929) ion-capture mechanism only works because of gravitational separation, causing larger, heavier hydrometeors to fall, capturing ions that are smaller than the drops.

Some of the electrification mechanisms already pre-organise their charge within a cumuliform cloud, forming charge centres. For example, the relative diffusional growth rate theory states the net charge on graupel and ice crystals after colliding is dependent on the temperature and moisture within the cloud (Emersic and Saunders, 2010). As the temperature of a cloud decreases with height, it is possible to form vertical charge structures.

Lesser known methods to organise the charge within a cumuliform cloud involve turbulence. Renzo and Urzay (2018) theorised turbulence could be used to preferentially capture hydrometeors of a certain size into a finite region of the cloud (Figure 2-6). The size of the hydrometeors that are captured is based on the mean eddy size. Larger hydrometeors would not be captured but instead, gain momentum from the turbulence. An increase in velocity of the larger hydrometeors would increase the rate of collisions with the smaller, captured

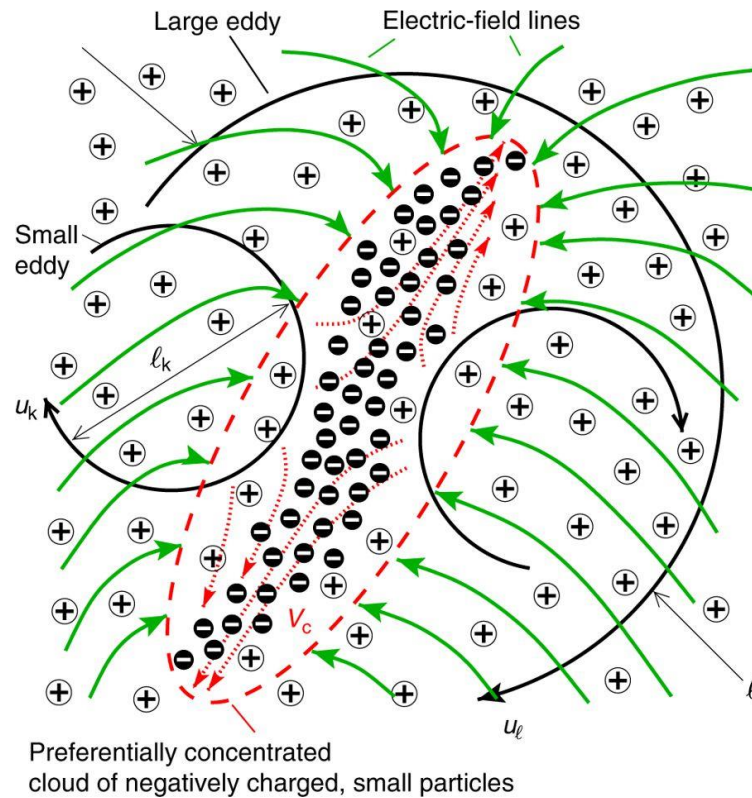


Figure 2-6: The enhancement of charge separation caused by the preferential capture of smaller hydrometeors, with the size of captured hydrometeors dependent on the mean eddy size of turbulence [reproduced with kind permission of Renzo and Urzay (2018)].

hydrometeors. If enough hydrometeors are captured by the turbulence, then a net region of charge would be formed; a charge centre. Using the processes from other mechanisms such as the relative diffusional growth rate theory, the amount of available moisture and the temperature of the cloud would control the polarity that the captured hydrometeors would gain. If the turbulence within the cloud is heterogeneous, then multiple charge centres could be formed. Recent theoretical modelling of thunderstorm electrification suggests the importance of turbulence for charge separation for both inductive and non-inductive mechanisms (Helsdon et al., 2002; Mareev and Dementyeva, 2017). Under a strong eddy dissipation rate, $\epsilon_T (> 10^{-2} \text{ m}^2 \text{ s}^{-3})$, the inductive mechanism was found to reach the breakdown voltage before the non-inductive mechanism. For the inductive mechanisms, the synchronisation between charge and relative velocity fluctuations cause the PG to grow exponentially in time. Meanwhile, with the aid of turbulence, the non-inductive mechanism would only cause the PG to grow linearly in time (Dementyeva and Mareev, 2018).

2.1.6 Cloud Electrification Mechanism Summary

There are two common processes for how clouds become electrified; ion-capturing and hydrometeor collisions. Hydrometeors either capture the available charge within the cloud or

they transfer their own charge from a collision which can transfer both mass and charge between each other (Saunders, 2008).

There are many proposed mechanisms for how a cloud can separate charge (see Table 2-1, Table 2-2, Table 2-3 and Table 2-4). There is a wide range of cloud and hydrometeor properties thought to be important for cloud electrification, with multiple properties likely to be required to produce the charge observed in thunderstorms. Many mechanisms are also limited in both the region of the cloud that they can occur or the total amount of charge that can be separated within the lifetime of a cumuloform cloud.

As discussed so far, many of the charging mechanisms are closely related to each other. The most notable example is the requirement of the convective mechanism by Grenet (1947) and Vonnegut (1953) that would transport space charge into a developing cloud. An abundance of space charge can be captured by polarised and unpolarised hydrometeors as defined by Wilson (1929) and Frenkel (1947) respectively. The Workman and Reynolds (1950) and Dinger and Gunn (1946) mechanisms also provided a flux of space charge from the splashing and bursting of drops providing an internal source of charge, increasing the efficiency of the Wilson and Frenkel mechanisms.

The electrification of a cloud can be thought of in terms of the convective development of a thunderstorm starting from the fair-weather stage (Figure 2-7). Many mechanisms typically occur at the same time in the development of the cloud, but during the small cumulus and growing cumulus stages (when an ice phase exists), the only mechanisms that are active include the convective and Frenkel mechanisms. These mechanisms are not very capable of enhancing the electrification in the cloud and the other mechanisms require an ice phase to develop sufficiently (e.g. relative diffusional growth rate theory requires graupel to form).

Overall, there are six fundamental physical properties that appear to control the rate of electrification: (1) cloud temperature, (2) moisture, (3) relative growth rate, (4) relative hydrometeor size, (5) relative hydrometeor velocity and (6) hydrometeor impurities. These fundamental properties are used to provide the necessary pre-conditions before lightning can occur. The fundamental properties (3), (4) and (5) are consistent with the collision integral of the Boltzmann transport equation, which describes the statistical behaviour of particles not in a state of equilibrium (Lieberman and Lichtenberg, 2005). For a particle $f_i(\mathbf{v}, \mathbf{p}, \mathbf{r}, t)$ which has a velocity, \mathbf{v} , momentum \mathbf{p} and radius, \mathbf{r} , the collision integral, per unit time, t , can be defined as,

$$\left(\frac{df}{dt}\right)_{coll} = \int d^3v_2 \int_0^{2\pi} d\vartheta_1 \int_0^\pi (f'_1 f'_2 - f_1 f_2) |\mathbf{v}_1 - \mathbf{v}_2| I \sin\theta_1 d\theta_1, \quad 2-2$$

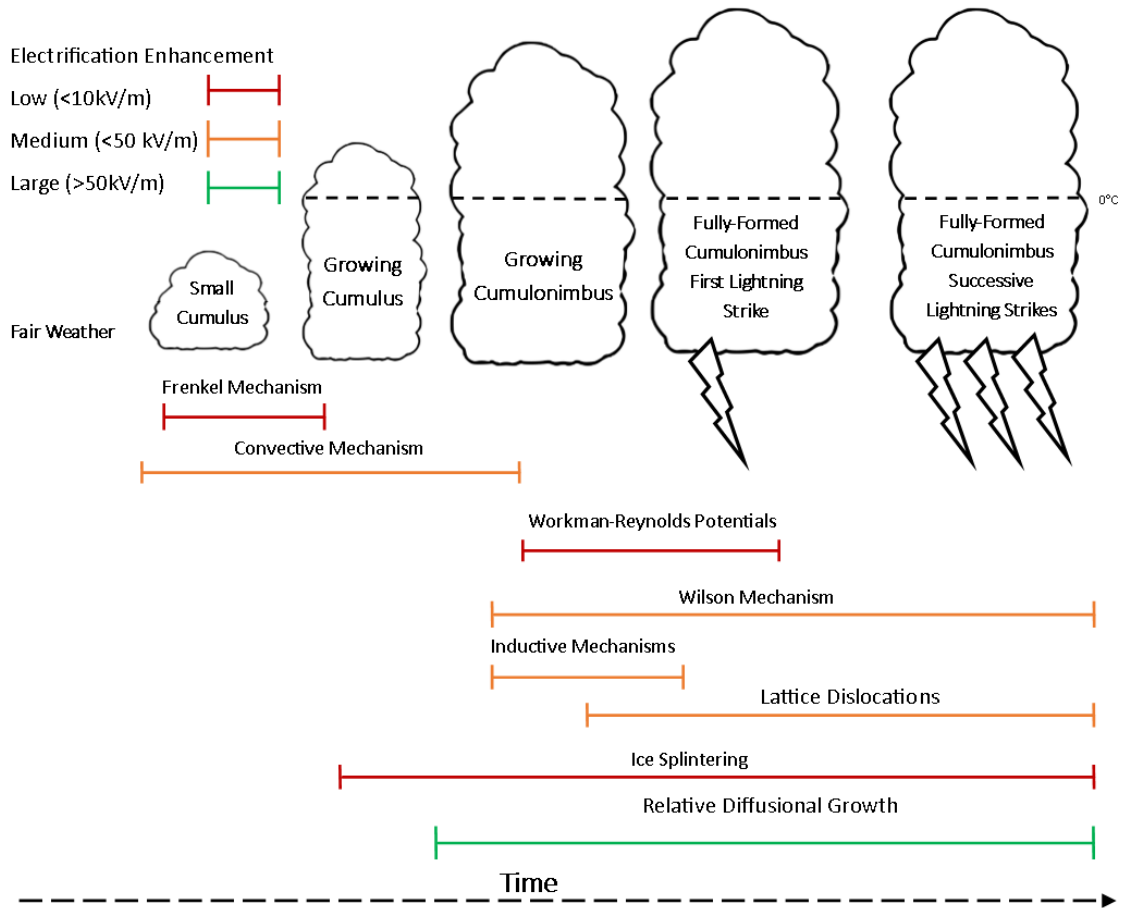


Figure 2-7: A simplistic schematic of the development of various charge separation mechanisms. The time when each mechanism occurs in the lifecycle of a thunderstorm is estimated. A broad estimate on the enhancement of the PG is shown.

where f_i and f_i' are the particle distributions before and after the collision respectively, with indices 1 and 2 being the labels of the two colliding particles. I is the differential cross section of the collision through the solid angle $\Omega(\theta_1, \vartheta_1)$. The other properties (1, 2 and 6) are specific to the cloud, which have been found to be necessary for charge separation within cumuliform clouds.

In this thesis, the charge within a cumuliform cloud is measured using electrical instruments at the surface (see §3.2 for a description of these instruments). Even though the charge within the cloud can be substantial, perturbing the PG over several $kV m^{-1}$, the charge from nearby sources such as precipitation, space charge and corona can also perturb the PG appreciably (Standler and Winn, 1979). As cumuliform clouds produce precipitation, the influence of the charge from both the cloud and precipitation on the PG occurs simultaneously. The next section discusses how precipitation can influence the PG . This knowledge is used in §4 of the thesis to further characterise the PG variability and to understand how much charge within the cloud is required before it can be detected above precipitation.

2.2 Influence of liquid precipitation on the potential gradient measured at the surface

The interaction between water and the PG measured at the surface was first measured by Lenard (1892) who measured an abundance of negative space charge near areas of falling water; waterfalls and fountains. The Lenard effect can be applied to precipitation falling from clouds and how rain can influence the PG measured near the surface (Smith, 1951). Many researchers have detailed the importance of turbulence, atmospheric pressure and the breakup of drops in the formation of space charge (Lüttgens et al., 2015; Zilch et al., 2008; Levin and Hobbs, 1971). In this section, the influence of precipitation on the PG measured at the surface is discussed. The terms 'drop' and 'droplet' have a specific definition in this section. A drop is defined as the precipitation falling from the cloud, before reaching the surface. A droplet is defined as the liquid being ejected from the parent drop either caused by deformation of the drop or from splashing.

2.2.1 Observing the relationship between precipitation and the potential gradient

The influence of precipitation on the PG has been previously studied by comparing the PG with the precipitation current, j_p . Definitive experimental evidence of drop splashing on the PG was often masked by the variability of the charge within the overhead cloud (Harrison et al., 2017). Simpson (1909) measured j_p and observed that precipitation was positively charged. The positive charge would be transferred to the surface while negative ions would be released into the atmosphere from the breakup of large drops, which ionises the atmosphere (critical threshold of 5.5 mm diameter). The initial charge on a drop is independent of the final charge on the drop after breakup and would gain the same charge as the ambient PG . Simpson (1949) postulated that the air motion in the upper atmosphere is the direct cause for the charge to flow through the atmosphere and the PG is not directly related to the rain rate (RR). Other hypotheses have been developed to understand the influence of precipitation on the PG which involved sparks (Adkins, 1959) or corona (Chalmers, 1967; Scrase, 1938; Ramsay and Chalmers, 1960) being produced from the breakup of the drops; either from the drop being too large or from the splashing of the drops at the surface (Smith, 1951). The influence of rain splashing on the PG has been thought to be small (Simpson, 1909) which would only be observed during high RR s ($> 10 \text{ mm h}^{-1}$).

Ogawa (1960) suggested the effects of splashing can only become relevant once the background PG is small enough ($< 1 \text{ kV m}^{-1}$) suggesting the charge within the cloud would stop the relationship between PG and j_p from being detected, where any evidence of splashing was extremely difficult to determine. Simpson (1949) observed a negative linear relationship

between PG and j_p , but when splashing was observed the relationship between PG (units = $V\ m^{-1}$) and j_p (units = A) became positively correlated. This led to the following empirical relationship between j_p and RR (units = $mm\ h^{-1}$),

$$j_p = -4 \times 10^{-7} PG \cdot RR + 1.6 \times 10^{-6} RR. \quad 2-3$$

This relationship is bounded for RR s between 0- and 40- $mm\ h^{-1}$ according to Simpson (1949). The first term relates to the charging of the precipitation itself and the second term relates to the drop splashing. In the original analysis, the coefficients for each term were presented without errors. This led to a difference in values when Ogawa (1960) compared their results to Simpson (1949) which would have been possible if a confidence interval was given. Soula and Chauzy (1997) made measurements of the j_p and PG near and above the surface (44 m) and found a similar mirror-image relationship with RR that was found by Simpson (1949). The dominant electric charge on drops was negative and correlated with the dominant charge polarity in the overhead cloud.

The relationship found by Ogawa and Simpson does not take into account the effects of positive ions being released from splashing that can occur when enough water resides on the surface (Levin and Hobbs, 1971). Many observations have shown that negative ions are released from the expulsion of smaller droplets caused by the breakup of the original drop but positive ions have been observed when larger droplets are released (Takahashi and Fullerton, 1972). Specifically, Levin and Hobbs (1971) and Hao (2017) showed the shape of the drop would change dependent on the impact speed and the amount of water that collides with the drop. The charge within a drop can redistribute itself under deformation (Zilch et al., 2008) making negative charge preferential in being ejected from the crown upon splashing. The positive charge is transferred to the surface.

Measurements of the ion mobilities⁴ and concentrations during rainfall supports the findings that negative charge increases during rainfall (Harrison and Aplin, 2007). Harrison and Aplin (2007) made measurements using a Programmable Ion Mobility Spectrometer (PIMS) during precipitation that occurred at the Reading University Atmospheric Observatory (RUAO⁵) over a 20-day period. The relationship between ion mobilities and concentrations were compared for precipitation and non-precipitation events (Figure 2-8). The maximum RR measured during the sampling period was 13 $mm\ h^{-1}$. An asymmetry was found between two ion polarities during

⁴ Ion mobility is the velocity that an ion gains within the PG , and is inversely proportional to the mass of the ion.

⁵ Location: 51.44142°, -0.93776°, Elevation: 63.3 m above MSL

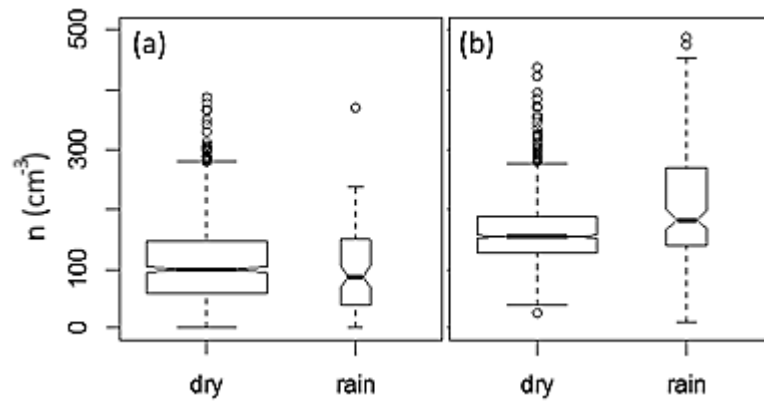


Figure 2-8: Box-Whisker plot showing a 20-day sample of ion number concentrations during precipitation and non-precipitation events measured by the PIMS instrument at the RUAO, (a) positive polarity ions, (b) negative polarity ions [reproduced with kind permission of Harrison, R. G.].

precipitation as the concentration was greater for negative ions over positive ions, but the mobilities remained constant (within sampling errors).

Lane-Smith (1969) was able to measure the precipitation and displacement currents from observations in Freetown, Sierra Leone during a series of tropical thunderstorms. Analysis of the precipitation data using various models (Whipple-Chalmers, Droplet Diffusion and Droplet Blanket) showed that the influence of rain on the PG must take into account j_p , the displacement current, j_D and the electrical double layer (referred to as the droplet blanket). Measurements of the charge created from drop splashing were performed by measuring the ejected droplets after the initial collision. The net contribution from splashing from their experiments was found to be nearly zero and thus negligible.

Scrase (1938) made measurements of the charge on raindrops at Kew Observatory, London. Measurements of RR and charge (number, polarity and magnitude) on the drops were made using an underground rain gauge which was electrically shielded. This also helped to minimise effects on the instrument (e.g. wind). Precipitation was collected through a funnel and an ammeter was used to measure the polarity and magnitude of the drop charge. A tipping bucket was used to calculate the RR . The experiment range covered a single year between 1935 and 1936. Scrase (1938) noticed that for small RR s ($< 10 \text{ mm h}^{-1}$), the majority of the drops were positively charged with a small number being negatively charged. These measurements are consistent with observations made by Simpson (1909). For larger RR s, the number of drops being negatively charged increased but was still less than the number of positively charged drops. The relationship of charge polarities with RR is similar to the results found in laboratory experiments (Levin and Hobbs, 1971; Liu et al., 2010; Shewchuk and Iribarne, 1970).

2.2.2 The life cycle of falling precipitation and the interaction with the potential gradient

Understanding the life of a drop falling from a cloud is required to fully account for how precipitation influences the PG measured at the surface. The ways in which precipitation can influence the PG include,

1. The initial state of the drop falling from the cloud, being either charged or uncharged (neutral);
2. The deformation, breakup and coalescence of the drop as it falls and reaches terminal velocity;
3. The collection or loss of charge from a collision due to differential fall speeds or from the capture of space charge;
4. The splashing of a drop upon the surface;
5. The surface properties which the drop lands on (e.g. temperature, wetness and roughness of the surface itself).

These aspects are discussed in the following section with an emphasis on the conditions at the surface. The initial state of the drop was discussed in §2.1 as the charge separation that occurs within the cloud can strongly influence the precipitation. As the interaction of the drop with the surface has the greatest value to this thesis, a discussion of how drops splash is also given.

Drop Deformation

A drop falling through the atmosphere typically undergoes deformation and eventually breaks up into smaller droplets either due to gravitational effects or from turbulence (D'Adderio et al., 2015; Blanchard, 1950; Cotton and Gokhale, 1967). A drop falling through the atmosphere naturally oscillates and any disturbance to the flow of the drop can cause deformation. Blanchard (1950) experimented with falling drops inside a bespoke wind tunnel, purposely designed to control the effects of turbulence on the drops. Drops bigger than 5.5 mm were found to be unstable and would break up, while the addition of turbulence would cause an explosion of droplets causing them to scatter (Lenard, 1904). Increasing the air flow rapidly would increase the deformation of drops (analogous to an updraught) while decreasing the air flow rapidly would reduce the deformation of the drops (analogous to a downdraught). The change in air flow velocity would alter the pressure applied to the drop and the surface tension can redistribute the liquid to provide maximum stability. Adding air inside a drop can stabilise itself from deformation and breakup substantially. Even under the presence of turbulence, the internal pressure applied by a bubble of air would substantially reduce the chance for the drop to break up (Blanchard, 1948).

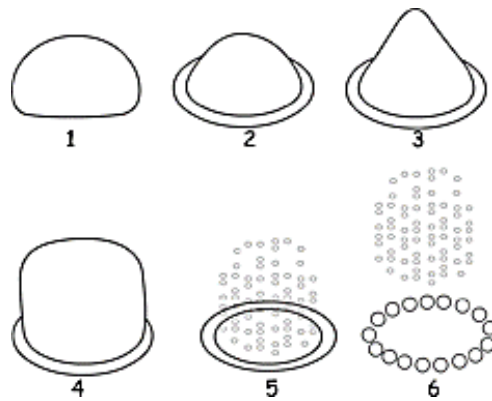


Figure 2-9: Common scenarios for (a) drops undergoing deformation and breakup along with (b) charge separation that can occur within neutral drops (from Lüttgens, et al. (2015)).

Drop Breakup

In Figure 2-9a, several scenarios for drop deformation highlights the complex but common dynamics that a descending drop encounters (Lüttgens et al., 2015). During the drop's breakup, Zilch, et al. (2008) measured the residual charge using an image charge detection mass spectrometer. The results showed, after the breakup, larger drops would be positively charged while the smaller droplets would be negatively charged. These results are similar to the charge on drops after splashing with the surface (Levin and Hobbs, 1971). According to Lüttgens, et al. (2015) neutral drops don't experience triboelectric charging when they fall through the atmosphere but under a strong enough turbulent flow, negative ions can be ejected from the neutral drop (Zeleny, 1933).

Drop Coalescence

The most common method for droplet growth is caused by the direct capture of other droplets (Cotton and Gokhale, 1967). Smaller droplets ($< 10 \mu\text{m}$) are more likely to undergo coalescence compared to larger droplets. The greater the size of the droplet, the lower the probability of coalescence, plateauing to 50% for drops up to 5 mm in diameter. The lower collection efficiency of larger drops is related to the higher surface tension (Tolman, 1949). When a large and small droplet interacts, the small droplet can roll around the larger droplet and continue along its trajectory; highlighting differential fall speeds. This interaction between different sized droplets is a requirement for certain charge separation mechanisms and is most efficient if the droplets have been polarised by the ambient PG (Sartor, 1954; Elster and Geitel, 1913).

The PG has been found to increase the stability, to avoid a breakup, of drops both inside a cumuliform cloud and falling towards the surface (Moore et al., 1962). The PG was found to increase the coalescence probability of cloud drops near the lightning channel as the drops became polarised. The drops would become electrostatically attracted to drops perpendicular to the electric field lines (Eow and Ghadiri, 2003). Colgate (1967) suggested that charged drops

would be accelerated (up to 15g) along the electric field lines in opposite directions depending on the polarity. This was found to rapidly increase the coalescence of drops. The experimental findings by Freier (1960) are consistent with Colgate (1967) and Sartor (1960). Freier (1960) observations highlighted that unpolarised and uncharged drops are also influenced by the *PG*. Blanchard (1948) showed that the natural drop oscillations can also increase the efficiency of coalescence even without a strong *PG*.

Levin and Ziv (1974) showed that the enhanced *PG* produced by the overhead cloud can reduce the fall speed of drops to the point of levitation if the *PG* is strong enough. Case studies of thunderstorms showed that once a lightning strike had occurred, there was a sudden increase in *RR* measured at the surface momentarily afterwards (Jayaratne and Saunders, 1984). A sudden increase in *RR* after a lightning strike is known as a rain gush. Once a lightning strike has occurred, the *PG* slowly recovers, plateauing to the pre-lightning magnitude. During this process, the *RR* slowly decreases, roughly at the same rate the *PG* plateaus to its pre-lightning magnitude. Figure 2-10 shows an example of a rain gush during two lightning strikes highlighting the relationship between the *PG* and *RR*.

Splashing of a drop against the surface

There are two distinct shapes that a splashing drop can create. The first, and most common, is the ejection of water from the base of the drop, forming a crown around the drop itself. Instabilities in the crown cause the presence of smaller jets at the peripheries which can break away and release droplets which are negatively charged (corona splashing). The other shape adds a single large jet forming at the centre of the impact zone which moves perpendicular to

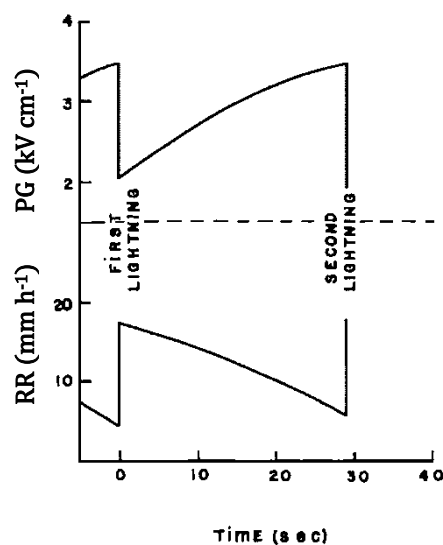


Figure 2-10: The variation in the *PG* and *RR* during two lightning strikes (0.5 and 40 C discharges respectively) observed from model outputs during simulations of thunderstorm development [reproduced with kind permission from Levin and Ziv (1974)].

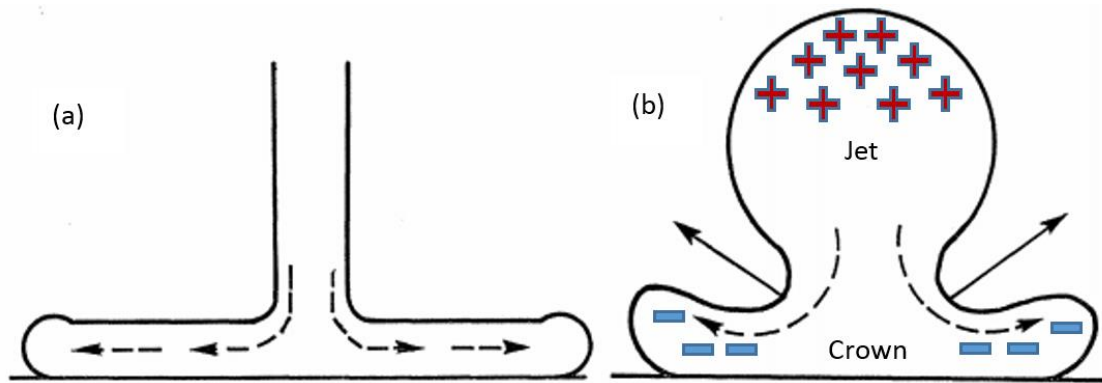


Figure 2-11: The shape of a drop after the collision with its incident surface. (a) The radial flow of water from a constant stream of water and (b) the flow due to a splash of a drop against a solid surface. The common charges on the splashing of the drop are also labelled accordingly [reproduced with kind permission from Levin and Hobbs (1971)].

the surface (prompt splashing). This large jet can break away from the main splash and release positive ions (Figure 2-11).

Lenard (1892) first measured the expulsion of negatively charged ions from water drops caused by the collision of the drop with a wet surface. The mechanism associated with this effect is attributed to the mechanical breakdown of the drops membrane (surface tension) from the deformation of its structure on contact with the surface (Smith, 1951). The tendency of ions to be released from a drop is caused by the disruption of the electrical double layer (Stojek, 2010; Grahame, 1947). In the presence of a wind field, the ions can be transferred to the atmosphere which would enhance the PG near the surface. The release of ions can be approximated using the Rayleigh criterion assuming that the drops are spherical (Taflin et al., 1989).

The shape and structure of a drop as it splashes are dependent on several factors which change the amount of charge transferred between contact points (i.e. between drop and surface). The main factors include, (1) impact speed; (2) surface water content; (3) surface roughness; (4) applied PG ; (5) impurities, (6) size of drop and (7) air pressure (Levin and Hobbs, 1971; Liu et al., 2010; Xu et al., 2007). These factors are discussed in more detail in the next section.

2.2.3 Factors that Influence the Splashing of Liquid Drops

For analysing a drops interaction with the environment (both interaction with other drops and the surface), the Weber number is often used to characterise the drop's splashing ability (Riboux and Gordillo, 2016). The Weber number is used to define the density, ρ_D , velocity, v , surface tension, γ and the diameter of a drop, d ,

$$We = \frac{\rho_D v^2 d}{\gamma}. \quad 2-4$$

In principle, the larger the Weber number the greater the mass of liquid water ejected from the drop. Riboux and Gordillo (2016) showed that a Weber number of ≈ 50 was the critical splashing limit for a drop.

Impact Speed and Drop Size

The impact speed and size of a drop can increase the amount of charge released upon splashing. This is caused by greater momentum on the drop causing the expulsion of more liquid water (Liu et al., 2010; Stow and Stainer, 1977). The breaking of a drop's surface tension is essential to the release of space charge into the atmosphere. For a drop to release its charge, the strength of the drop's surface tension (e.g. air pressure) and what controls the breakup of the surface tension (e.g. impact speed) needs to be known. Stow and Stainer (1977) measured the splashing of drops under various conditions based on the work by Levin and Hobbs (1971). They found that for splashing to occur, on a flat surface, drops must have a minimum radius of 0.75 mm. Under atmospheric conditions, the velocity of the drop would be limited by its terminal velocity and would not gain enough energy to break the surface tension of the drop. The surface tension is proportional to the drop size as the curvature is greater for smaller drops providing a smaller internal pressure for the drop (Tolman, 1949). The relationship of drop size with surface tension can be defined using the Young-Laplace equation,

$$\Delta p = \gamma \left(\frac{1}{a} - \frac{1}{b} \right), \quad 2-5$$

where Δp is the difference in pressure between the two fluids (e.g. atmosphere and the drop), γ is the surface tension and a, b are the semi-major and semi-minor lengths of the drop.

Drop Impurities

Adding impurities to a drop can inhibit charge from being released during splashing. This was observed for varying impact velocities, drop sizes, surface roughnesses and temperatures (Shewchuk and Iribarne, 1970; Levin and Hobbs, 1971). This is because the conductivity of the drop increases with impurities, providing a stronger bond between ions, which under splashing are more resilient to being ejected from the drop. Impurities within the drop can greatly reduce a drop's ability to splash. For example, $2 \times 10^{-4} \text{ mol l}^{-1}$ of sodium chloride (NaCl) can reduce the release of ions by a factor of 0.75 (Shewchuk and Iribarne, 1970).

Surface Roughness

Surface roughness can appreciably influence the number of subsequent droplets released from a drop splashing as well as the size of each new droplet (Stow and Stainer, 1977). Surface roughness causes a frictional force to act on rain-sized drops due to their size. This friction is

necessary to initiate the formation of a crown on splashing which is responsible for most of the charge to be released (Levin and Hobbs, 1971). Increasing the surface roughness increases the number of droplets ejected from the parent drop and increases the distribution of droplet sizes. In the opposite situation, a smooth surface (e.g. flat steel surfaces) would reduce the number of droplets released during splashing (Hao, 2017).

Applied Electric Field

In an applied *PG*, a drop splashing against a wet surface would release charge of the same polarity (Levin and Hobbs, 1971; Lane-Smith, 1969). Levin and Hobbs (1971) experimented with an applied *PG* by varying the impact speed of drops and by changing the magnitude and polarity of the *PG*. Figure 2-12 shows the mean charge transferred from a 2.5 mm diameter drop for different impact speeds and *PG* strengths. For an impact speed of 4 m s^{-1} , the maximum amount of charge that was released from splashing was found, invariant to the *PG* strength or polarity. A possible explanation for why an impact speed of 4 m s^{-1} provides the greatest charge released from splashing relates to the contact time of the drop and the relaxation time of the charge carriers. A greater amount of charge can be separated for a longer contact time (slower impact speed) but the amount of charge is controlled by the time difference between the contact time and relaxation time (i.e. contact time \gg relaxation time). The non-uniformity in the contact and relaxation times causes a maximum to be formed at $\sim 4 \text{ m/s}$ for a drop size of 2.5mm.

The structure of the drop and wetness of the impact surface is also important in the presence of an applied *PG*. Figure 2-12 shows that in the absence of a *PG*, the amount of charge transferred by splashing was only measurable for large impact speeds ($> 1.5 \text{ m s}^{-1}$). The shape of a drop splashing is also important when a *PG* is applied. A wet (or rough) surface is required for the formation of a crown and was found to contain mainly negative charge on the ejected

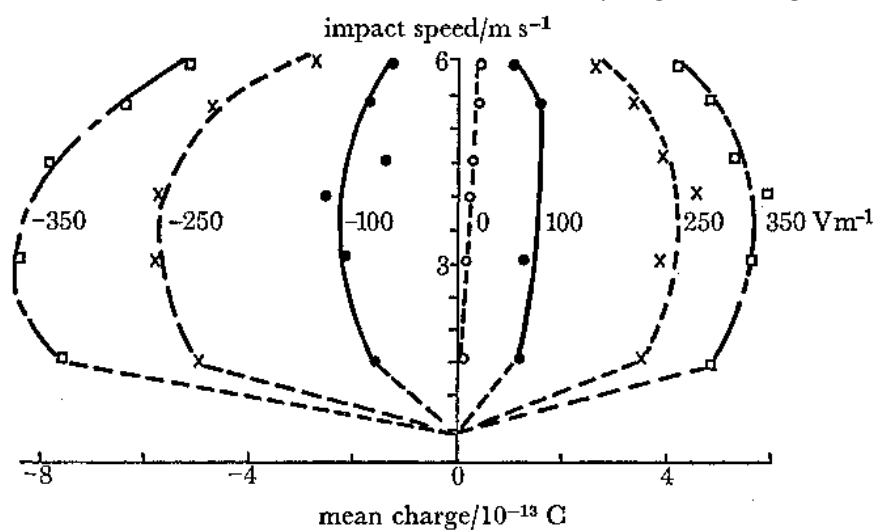


Figure 2-12: The mean charge transferred from a 2.5mm diameter drop splashing at different impact speeds onto a conducting sphere in the presence of an applied *PG* [reproduced with kind permission from Levin and Hobbs (1971)].

droplets. In an applied PG , the contact time of these droplets is small in comparison with the relaxation time of the charge carriers. Therefore, less negative charge can be released into the atmosphere (Stow and Stainer, 1977). An increase in RR can be loosely related to both an increase in drop size distribution and the fall velocity (Kingsmill et al., 2006; Ochou et al., 2007). Precipitation from highly charged clouds has been shown to produce positive corona (independent of applied PG) from the central jet of a splashing drop. (Phelps et al., 1973). The PG was found to be greater than 180 kV m^{-1} before corona is activated for a drop with a diameter of 3 mm. The strength of the PG is extremely high, even for the most intense thunderstorms (MacGorman and Rust, 1998). Therefore, corona is unlikely to occur for precipitation splashing against the surface.

Atmospheric Pressure

The atmospheric pressure can also substantially influence the structure of a drop after collision (Wu and Cao, 2017; Liu et al., 2010). Liu, et al. (2010) experimented with the splashing of perfluorohexane (C_6F_{14}) drops and showed that at standard atmospheric pressure (1 atm) no crown was formed when collided with a dry surface. At higher pressures (2-6 atm) a crown was formed after the collision and the velocity and angle of the crown increased appreciably with pressure. From the previous discussion on the influence of an applied PG to the charge released from splashing, it can be inferred that higher pressures would release less charge as the contact angle and velocity would reduce the contact time with the surface.

Wu and Cao (2017) and Xu, et al. (2005) both experimented with ethanol liquid drops in reduced pressure chambers and concluded that splashing can be completely suppressed by reducing the pressure by an arbitrary amount. The critical pressure for a splash not to occur was found to be directly correlated with the impact speed, molecular weight and viscosity of the drop. In terms of the atmospheric pressures typically observed (950-1050 hPa) the variations in drop splashing structure would be small. Observations by Liu, et al. (2010) suggest that the critical threshold for a drop to develop a crown after a collision is near 1000 hPa. Variations in drop sizes and surface roughness mainly controls whether a drop would produce a crown, but no experimental evidence showing the influence of the atmospheric pressure on precipitation is known.

Surface Water Content

As discussed previously, for the Lenard (1892) effect to exist, the surface that a drop collides with needs to be wet for a splash to occur. The depth of water required for a drop to splash was approximated by Levin and Hobbs (1971). They examined the effects of drop splashing and the distribution of charge being released was found to be a function of the surface wetness with a

water depth minimum of 0.5 mm being required in order to release any charge. Adkins (1959) also observed the effect that precipitation had on the *PG*. He stated that the release of ions must be caused by the splashing of drops as no ions were observed when the surface was dry and corona had no effect on the charge released. In Adkin's experiments, he only saw the effects of the charge being released—from the splashing—during heavy rainfall events ($> 15 \text{ mm h}^{-1}$). The influence of surface wetness and its relationship to meteorological factors is an important aspect of the splashing of drops which remains poorly understood.

2.3 Conclusions

In this chapter, the different cloud electrification mechanisms have been examined, and the limitations of each mechanism discussed. Four electrification mechanism types were examined (ion-capture, convective, inductive, non-inductive) with the non-inductive mechanism likely to provide the greatest amount of electrification. The other mechanisms are likely to occur during the development of a cumuliform cloud and are useful in maintaining the continued electrification of the cloud. The organisation of the charge within the cumuliform cloud was also examined. Certain mechanisms such as the Wilson (1929) ion-capture and relative diffusional growth rate theory showed how the charge generation and charge organisation could occur simultaneously. A lesser known method for charge organisation involves turbulence, which can preferentially capture small hydrometeors and increases the momentum of larger hydrometeors (Renzo and Urzay, 2018). This would increase the collision rates of inductive and non-inductive mechanisms and allow the formation of charge mechanisms at the same time. Overall, there are six fundamental physical properties that were shown to be important for the electrification of a cumuliform cloud. The properties are (1) cloud temperature, (2) moisture, (3) relative growth rate, (4) relative hydrometeor size, (5) relative hydrometeor velocity, and (6) hydrometeor impurities. These properties are used to help answer the research questions for this thesis.

The influence of precipitation on the *PG* measured at the surface has also been examined. There are many stages in the lifecycle of a falling drop, from its initial charge after leaving the cloud, to the breakup and deformation of the drop during descent along with the drops interaction with the surface. As well as the contribution of other charges (e.g. cloud charge), the influence of precipitation on the *PG* is complex. It is apparent though, that the splashing of the drop against the surface would add charge, most likely negative charge, into the atmosphere. From the literature, the amount of charge that can be released from splashing and the minimum *RR* required for this to occur is unclear.

3 Instrumentation and Data Processing

This chapter examines the instrumentation and data processing methods used throughout this thesis. Seven instruments were used for primary data collection and nine instruments were used for secondary data collection. The data were used to investigate the processes required for cumuliform clouds to separate charge before lightning can be produced. This chapter consists of five parts which examine four types of instrumentation and the data processing methods used to quality control the data before any analysis is performed from two field sites (see §4–6). The first part discusses the Reading University Atmospheric Observatory (RUAO) and Chilbolton Observatory (CO) where the sixteen instruments are located (§3.1). The second part discusses two electrical instruments; the electric field mill (FM) and Biral thunderstorm detector (BTD) (§3.2). The third part discusses seven rain gauges: three tipping buckets, three drop counters and one disdrometer (§3.3). The fourth part discusses two remote sensing instruments: a 35 GHz radar and a ceilometer (§3.4). The fifth part discusses four in-situ instruments used on board a radiosonde: charge, cloud backscatter, turbulence and supercooled liquid water instruments (§3.5). As multiple instruments are used in multiple chapters, an overview of all instruments

Table 3-1: All the instruments used for data analysis in this thesis, grouped by instrument type. The location of each instrument and the chapter the instrument is used for data analysis is also given. * defines instruments used for primary data collection.

Instrument Type	Instrument	Location	Chapter Used
Electrical	JCI 131 Electric Field Mill *	RUAO and CO	4, 5 and 6
	Biral Thunderstorm Detector 300*	CO	5
Rain Gauge	Delta-T Tipping Bucket	RUAO	4
	EML SPS-500 Tipping Bucket		
	Munro Tipping Bucket		
	RAL rapid response drop counter A	CO	
	RAL rapid response drop counter B		
	RAL rapid response drop counter C		
	Distromet RD-80 disdrometer		
Remote Sensing	35 GHz “Copernicus” Doppler Radar		4, 5 and 6
	Vaisala CT75K Ceilometer		5
In Situ	Vaisala RS92 radiosonde *	RUAO	6
	Charge Instrument *		
	Cloud Optical Thickness Instrument *		
	Turbulence Instrument *		
	Liquid Water Instrument *		

used throughout this thesis is given in Table 3-1. Details on how the data collected by the instruments were used to answer the thesis questions (§1.4) are given in the individual chapters (4–6).

3.1 Field Sites

Two field sites (RUAO⁶ and CO⁷) were used to take measurements of the atmosphere to answer all the questions discussed for this thesis (§1.4). At the RUAO, automatic measurements from a FM and two tipping buckets have been recorded since 2005. Although the RUAO can measure the overhead cloud base using a Vaisala CL31 ceilometer, the RUAO does not have any instruments for measuring the full structure of a cumuliform cloud, such as a radar. Therefore, a field campaign was set-up at CO to make use of their remote sensing instruments, particularly their radar.

Figure 3-1 shows the location of the RUAO and CO within the South of England with an inset map showing the entire UK. The distance between the two observatories is 48.0 km making them useful for cross comparisons when synoptic-scale weather patterns move over the UK. The

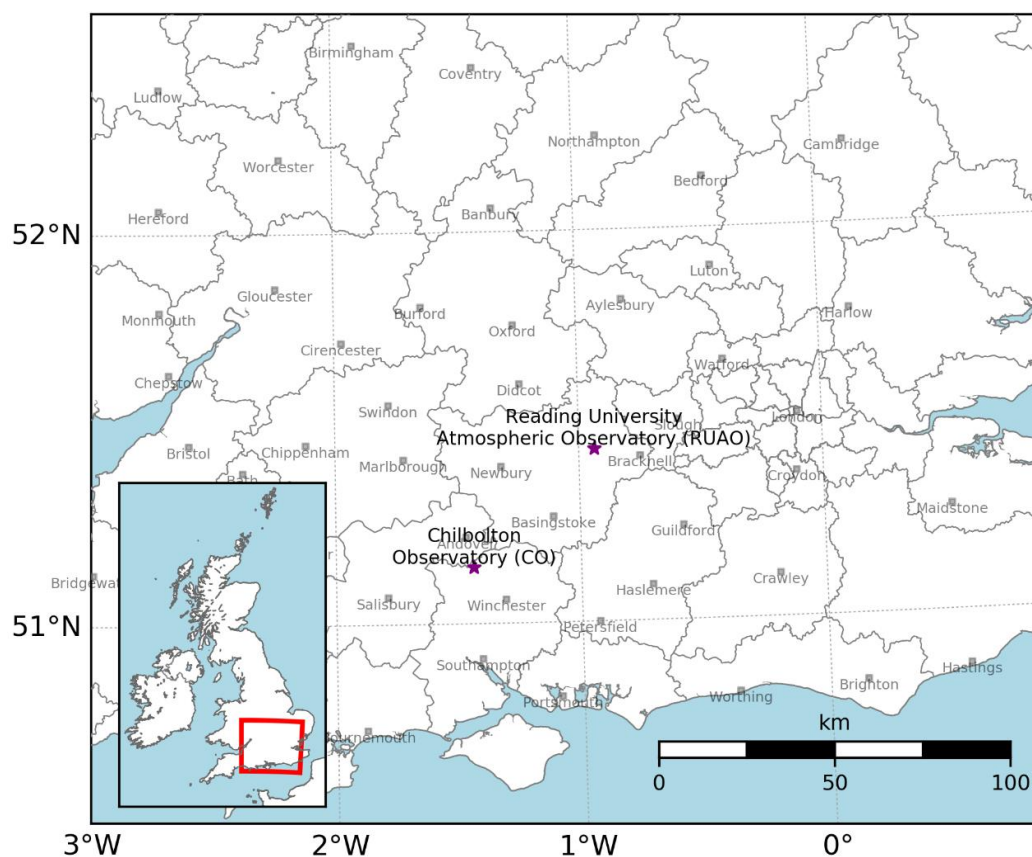


Figure 3-1: A map of South-East England showing the location of the Reading University Atmospheric Observatory (RUAO) and Chilbolton Observatory (CO). The grey boundaries define the postcode regions.

⁶ Location: 51.44142°, -0.93776°, Elevation: 63.3m above MSL

⁷ Location: 51.144701°, -1.439097°, Elevation: 84.0m above MSL

Table 3-2: Availability of each instrument type at the RUAO and CO.

	Manual Rain Gauge	Tipping Bucket	Drop Counter	Disdrometer	Radar	Ceilometer	Solar Radiation
RUAO	Yes	Yes	No	No	No	Yes	Yes
CO	No	Yes	Yes	Yes	Yes	Yes	Yes

synoptic-scale events typically originate from the North Atlantic, brought over to the UK by the jet stream (Slingo et al., 2014). Perturbations of the jet stream can often bring disturbed weather to the UK, leading to more frequent rain events of greater intensity, while mesoscale convective systems would provide appreciable variations between sites, caused by local heating of the air near the surface. Overall, the data collected at the RUAO and CO spanned over 13 years (2006 – 2018) and the availability of each instrument installed at the RUAO and CO is given in Figure 3-2.

The type of instruments that were available at the RUAO and CO is also given in Table 3-2. The lack of a manual rain gauge with a routine observer taking standard measurements at 0900 UTC meant the rain gauges at CO could not be tested for their accuracy as a measure of precipitation. Only CO has an operational radar installed providing valuable information about the cloud structure, useful for comparison with the precipitation type. The following sections discuss the

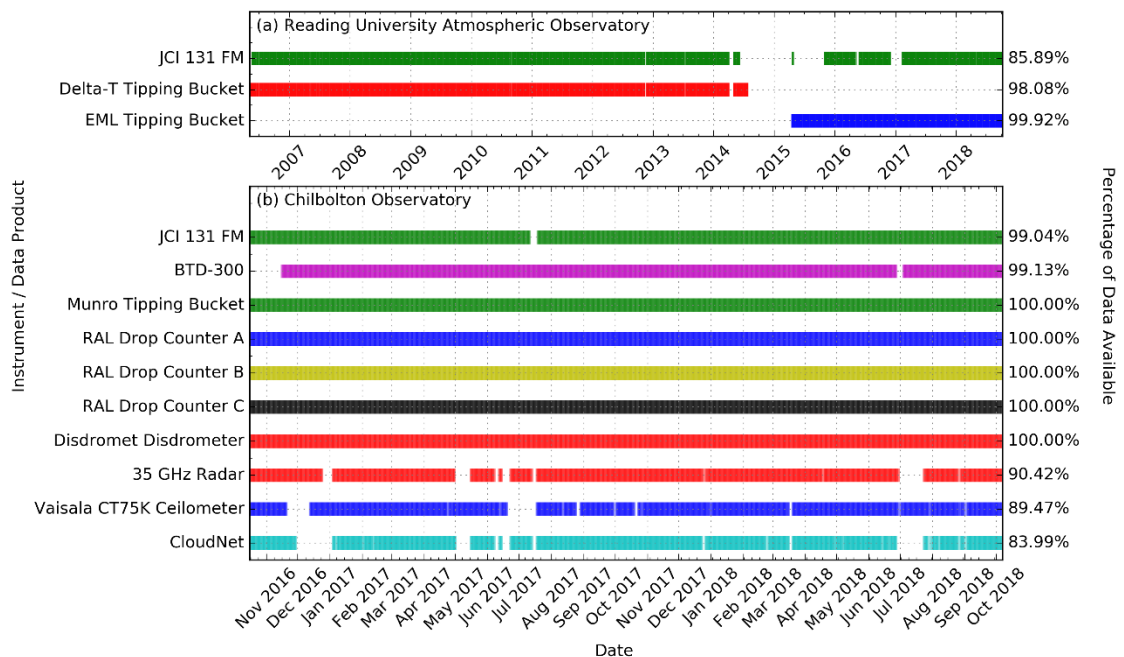


Figure 3-2: The availability of data from all continuously measuring instruments at the RUAO between 06/05/2016 and 06/10/2018 (a) and CO between 06/10/2016 and 06/10/2018 (b). Each data available percentages (secondary y-axis) are calculated from the installation date of each instrument or from the installation of the FM for the CO instruments (except the BTD). CO CloudNet is a derived data product using the 35 GHz radar (see §3.4.3).

site characteristics of the RUAO and CO, highlighting any issues with the instruments at these sites.

3.1.1 Reading University Atmospheric Observatory

The RUAO (Figure 3-3) has been collecting routine meteorological data since 1901 (Brugge and Burt, 2015) using manual observations, while automatic observations have been collected almost continuously since 1997. Several data logging systems have been implemented since 1997 with the latest being METFiDAS-3⁸. The potential gradient (*PG*) and precipitation measurements used for this thesis were collected by METFiDAS-I and METFiDAS-3 since 2006 (Table 3-3).

The temporal resolution for all instruments used at the RUAO was 1 Hz. The high temporal resolution was needed to resolve the small-scale variability in the *PG*, typically caused by precipitation (see §4). For the purposes of answering thesis question (1), measurements from the RUAO were used after May 2006 to avoid the initial data issues of the FM when logging with METFiDAS. There were two versions of METFiDAS, which have been implemented at the RUAO since 2005, which used different logging systems to record the data from various instruments. Table 3-3 describes the different logging system implementations, including the date of operation and the data acquisition method used. METFiDAS I was only able to measure analogue voltages, which caused an issue when recording the digital outputs from the Delta-T tipping bucket rain gauge. These issues are discussed in detail in §3.3.1.

3.1.2 Chilbolton Observatory

A field campaign was set-up at CO (Figure 3-4) to compare surface electrical measurements with the structure of charged cumuliform clouds, using the 35 GHz “Copernicus” radar. All instruments at CO, not installed as part of this field campaign, are run by the Chilbolton group of the space science and technology department at Rutherford Appleton Laboratory (RAL). For this field campaign, another FM was installed at CO to measure the *PG*, the same FM design

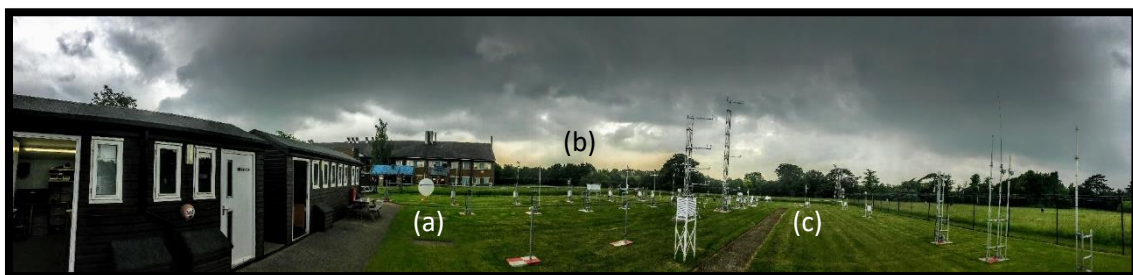


Figure 3-3: Panorama of the RUAO showing the various instruments located at the observatory including (a) Vaisala RS92 radiosonde, (b) EML tipping bucket and (c) FM.

⁸ METeorological Fieldsite Data Acquisition System (METFiDAS)

Table 3-3: The automatic data logging systems implemented at the RUAO since August 2005. N.B. METFiDAS II (2) was not an active logging system and only used as a backup for METFiDAS I near the end of its lifetime.

Logging System	Active Dates	Logger
Corrdisp	01/01/1997 to 11/01/2009	Keithley Metrabyte 12-bit logging cards installed in a DOS PC
METFiDAS I	08/08/2005 to 27/07/2014	Amplicon 12-bit logging cards and Windows NT PC (Amplicon, 2018)
METFiDAS 3	30/08/2014 to present	Campbell Scientific CR9000X data logger (Campbell Sci., 2018)

used in the RUAO (JCI, 2006). The data from the FM is recorded at 1 Hz (10 Hz sampling), matching the resolution of the FM at the RUAO, using a Campbell CR1000 data logger (Campbell Sci., 2019a). The data is transmitted back to a local computer at the University of Reading using a Campbell CELL215 cellular module (Campbell Sci., 2019b). The BTM was also installed as part of this field campaign and measures the displacement, j_D , precipitation, j_P and turbulent, j_T currents. The data measured by the BTM-300 was transmitted using serial communication to a laptop situated at CO. Bespoke software for the BTM-300 was used to record both 0.5 and 100 Hz data simultaneously (Biral, 2018). Table 3-4 provides the installation dates and the temporal resolution of the FM and BTM.

Five rain gauges were also present at CO; a Munro tipping bucket rain gauge (Munro Instruments, 2015), three RAL rapid response drop counting rain gauges (Norbury and White, 1971) and a Distromet RD-80 “Joss-Waldvogel” disdrometer (Distromet, 2012). Four radars are located at CO, which operates at different frequencies (1.275, 3, 35, and 94 GHz). The 35 GHz “Copernicus” radar (Rutherford Appleton Laboratory, 2016) is well suited to measuring mixed phased clouds and is capable of measuring graupel-sized hydrometeors up to 5 mm in diameter. During the set-up of the field campaign, the 35 GHz radar was the only radar measuring the atmosphere continuously and provided the most reliable measurements. Figure 3-5 shows the location of the electrical, rain gauge and remote sensing instruments installed at CO. The FM



Figure 3-4: A panorama image of the field site housing the BTM (a), FM (b) and 3 GHz CAMRa radar instruments situated along the 500 m range between the transmit and receive cabins (taken on 25/04/2018).

Table 3-4: Description of the electrical instruments installed at CO as part of the field campaign set-up for this thesis.

Instrument	Installation Date	Time Resolution (Hz) / Sampling Rate (Hz)	Electric Quantity Measured
JCI 131 Electrostatic Field Mill (FM)	06/10/2016	1 / 10	Potential Gradient (PG)
Biral Thunderstorm Detector (BTD) 300	16/11/2016	0.5 / 100	Displacement Current (j_D), Precipitation Current (j_p) and Turbulence Current (j_T)

was installed 100 m away from the rain gauges north of their location and 250 m away from the remote sensing instruments.

3.2 Electrical Instruments

This section discusses two electrical instruments used in this thesis. The first is the Chubb JCI 131 electric FM (Chilworth, 2016) and the second is the BTD (Biral, 2018). A description of how these instruments measure the electrical properties of the atmosphere is given along with the data processing methods used to quality control the data.

3.2.1 Electrostatic Field Mill

The FM used in this thesis measures the PG using a rotational shutter design, where an electrode is exposed to the atmosphere facing vertically upwards, causing charge to be induced by the

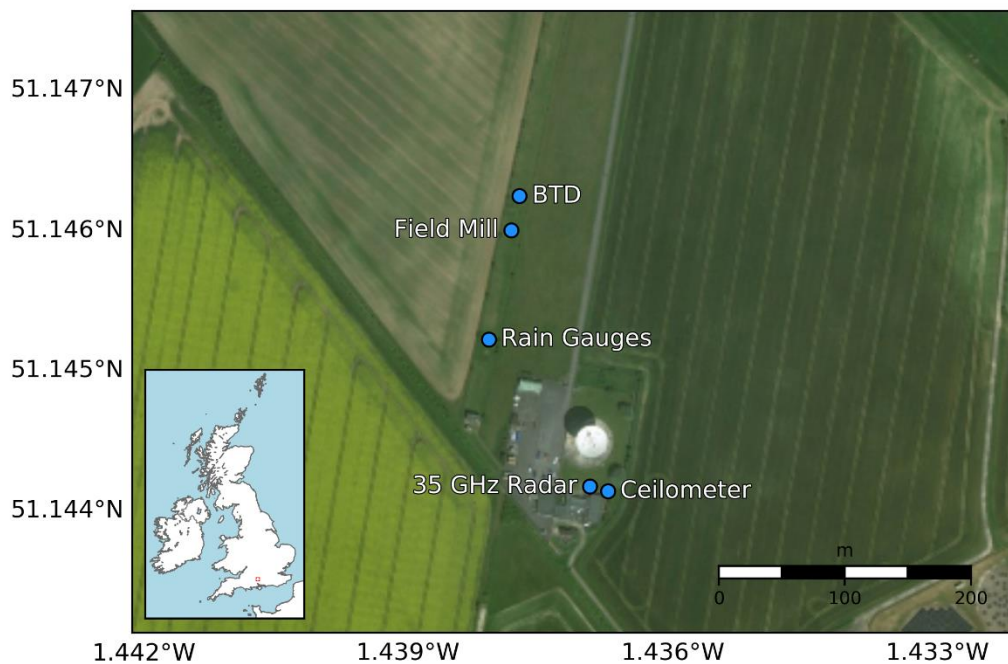


Figure 3-5: A map of Chilbolton Observatory showing the location of the electrical, rain gauge and remote sensing instruments [Sources: Esri, DigitalGlobe, GeoEye, i-cubed, USDA FSA, USGS, AEX, Getmapping, Aerogrid, IGN, IGP, swisstopo, and the GIS User Community].

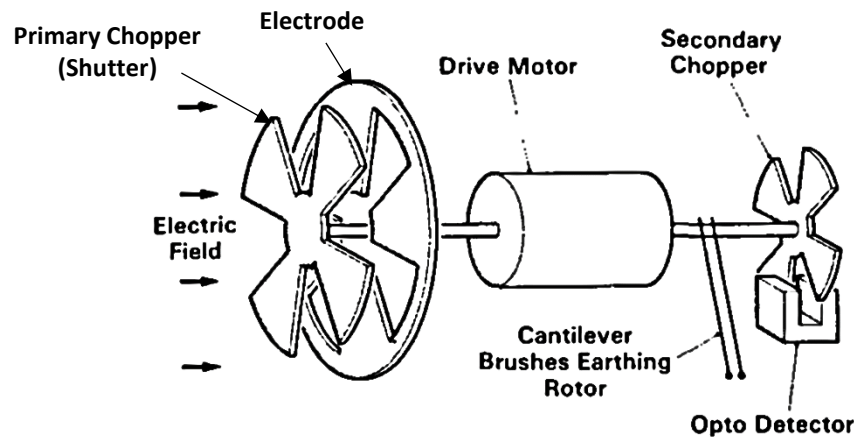


Figure 3-6: Standard electrostatic FM design using a variable shielded electrode [reproduced with kind permission from Chubb (1990)].

ambient PG (Figure 3-6). A rotating shutter, which is grounded, covers the electrode causing the charge to dissipate. As the shutter causes the electrode to be exposed to the atmosphere periodically, an alternating current is produced which is proportional to the PG . The FM has a high accuracy (1% full-scale deflection), small temporal drifts ($\pm 5 \text{ V m}^{-1}$) and is resilient to highly disturbed weather conditions including thunderstorms and temperature extremes (JCI, 2006). The FM's resilience is caused by the large gaps between the rotating shutter and the outer casing and drainage holes at the bottom of the outer case, which minimises short-circuiting of the electrode caused by precipitation.

The measurement range for the FM positioned at the RUAO was $\pm 1 \text{ kV m}^{-1}$, which is typically used for studying fair weather conditions (Bennett, 2007). The smaller range increases the resolution of the FM and is useful for resolving small-scale variations in the PG . At CO, the measurement range was increased to $\pm 10 \text{ kV m}^{-1}$ to allow measurements of highly charged clouds. Both FMs are mounted on a cylindrical metal pole, positioned three metres above the surface, allowing enough clearance from the surface to minimise electrical distortions of the surface (Figure 3-7).

The FM can be calibrated using both laboratory tests and the passive wire method. Calibrating the FM also takes into account the PG distortion of the instrument and the 3 metre metallic pole that the FM is installed on (Bennett, 2007; Bennett and Harrison, 2006). The calibration of the RUAO FM has been performed on three separate occasions between 2006 and 2009 (Appendix A). These repeated calibrations increase the reliability of the PG measurements being made at the RUAO and reduce the instrument errors in the analysis.

The CO FM was calibrated by initially installing the instrument at the RUAO so comparisons could be made with the RUAO FM over a period of several weeks. The FMs were positioned 17 metres apart at the same altitude (63.3 m above MSL) with both FMs positioned away from any ground

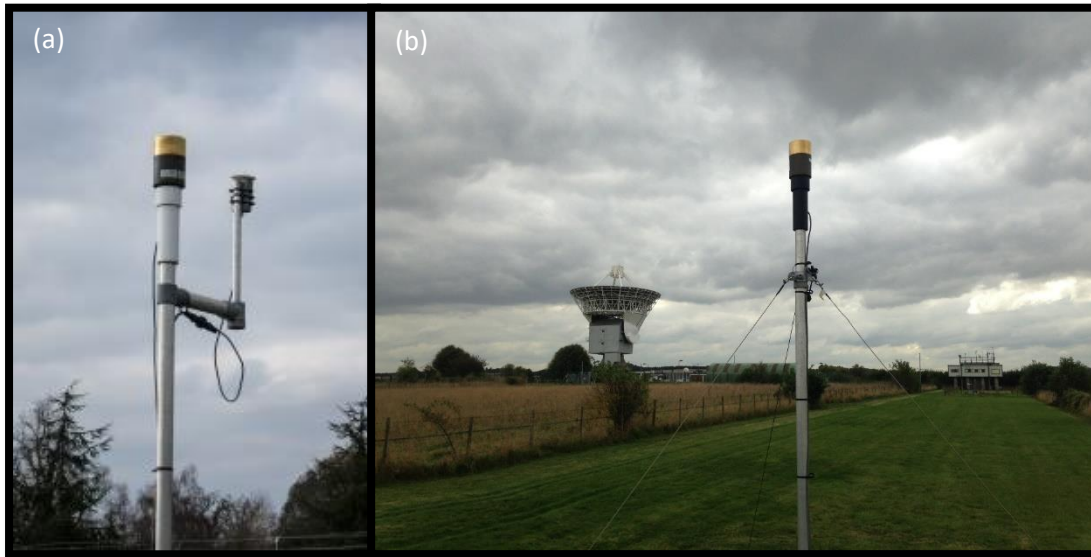


Figure 3-7: The FM installed at the RUAO (a) and CO (b). In (b) the 3 GHz CAMRa radar is shown in the background of the figure.

clutter that could distort the PG . The statistical relationship between FMs was very strong ($R^2 > 0.99$) with the remaining variance attributed to local effects such as local variations in space charge (Chubb and Pavey, 2009). The details of the calibration and the operating range of both RUAO and Chilbolton FMs can be found in Appendix A.

As the RUAO FM uses the fair-weather range ($\pm 1 \text{ kV m}^{-1}$) to measure the PG , there were many occasions when saturation occurred at both positive and negative polarities. The PG saturation occurs exclusively during disturbed weather events in the UK unless there was an instrument fault. In this thesis, two processing methods were applied to the FM to remove undesirable data to increase the comparability of the surface PG with precipitation to answer thesis question (1) (see §4). The method involved the detection of electrical discharges and PG anomalies. Depending on the distance and magnitude of the flash, the PG can change in the order of kVs per second increasing the variability of the PG . Even though a typical lightning flash can occur for only 200 ms, on average, it can affect the measurement of the PG on a temporal scale a few orders of magnitude larger than its occurrence (up to tens of seconds). After a lightning strike, the PG slowly plateaus back to its pre-lightning strike state (MacGorman and Rust, 1998).

The method used to detect a lightning flash was based on the criterion that the PG time derivative (defined as PG') must be above a certain threshold and was designed as part of this thesis. PG' is defined as the change in PG over one second. The PG' associated with a lightning discharge occurs within a single second and the magnitude of the time derivative is directly related to the distance of the flash and the amount of charge transferred. Figure 3-8 shows the distribution of PG' for a sample dataset from the RUAO FM between 2006 and 2018. Most of the PG' distribution occurs below $750 \text{ V m}^{-1} \text{ s}^{-1}$ and is difficult to distinguish between lightning

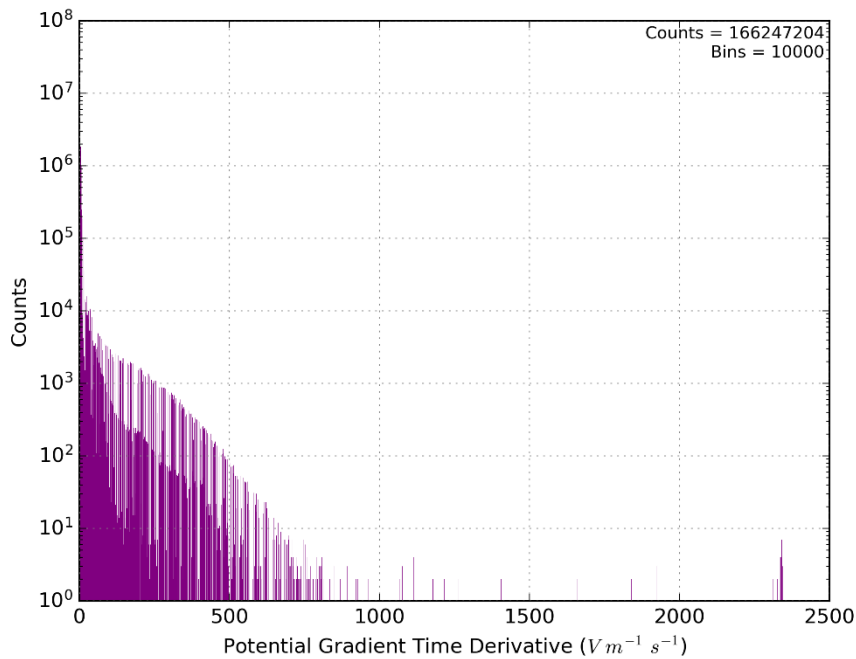


Figure 3-8: A histogram of PG' values between 2006 and 2018 for days when precipitation was measured (≥ 0.2 mm day $^{-1}$). The stated instrument range was set to ± 1 kV m $^{-1}$. $PG' > 2$ kV m $^{-1}$ s $^{-1}$ are saturated values. The number of counts is 166,247,204 with a bin width of 0.36 V m $^{-1}$.

and non-lightning events below this threshold. For values above this threshold, the distribution becomes fragmented caused by breaks in the histogram resulting in fast changes in the PG exclusively caused by lightning flashes at variable distances and intensities. Below 750 V m $^{-1}$ s $^{-1}$, the histogram increases in density, but the fragmented nature still exists to a smaller extent. Lightning flashes have been observed in the PG data for PG' much less than 750 V m $^{-1}$ s $^{-1}$ caused by distant (> 20 km) flashes. Any distant lightning flashes that cause the PG to change less than 500 V m $^{-1}$ s $^{-1}$ were not removed from the data to minimise the number of false positives. Despite the FM being capable of detecting lightning flashes directly, the FM is poor at differentiating between other sources of electrical disturbances (e.g. charged rain and corona).

The saturation of the FM can occur when nearby clouds are appreciably charged which can often saturate the FM at both polarities for a single cloud. These saturated values must be removed from further processing. Figure 3-9 shows a histogram of PG values measured between 2006 and 2018 for days when precipitation was measured (≥ 0.2 mm). The global maximum in the histogram is in the fair-weather region ($50 - 200$ V m $^{-1}$). The distribution of PG values is non-symmetrical around the fair-weather region with negative PG values more likely than positive PG values. At the edges of the histogram, there are several noticeable peaks highlighting when the data has been truncated. These peaks are caused by changes in the calibration that were performed on the FM between 2006 and 2009. Therefore, a threshold for removing saturated

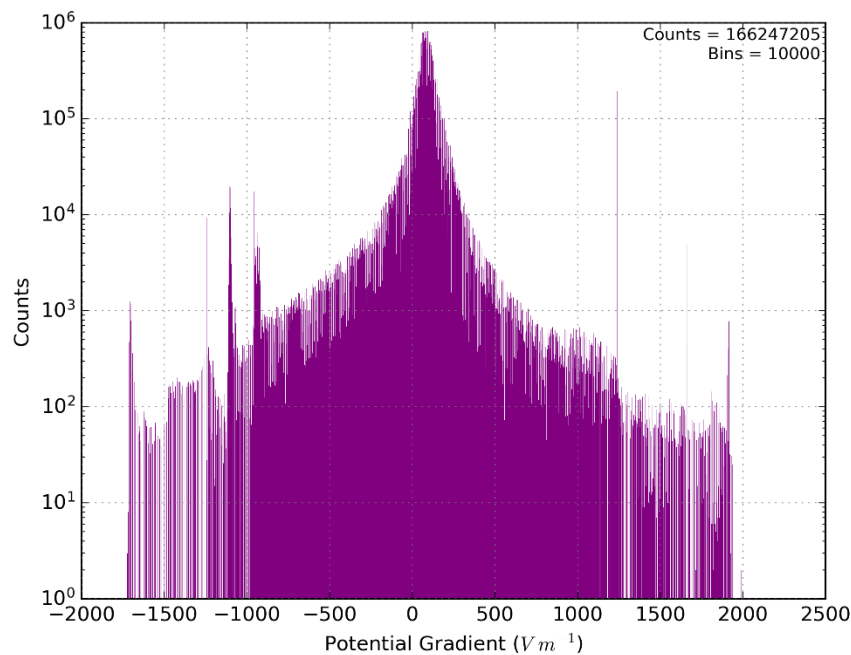


Figure 3-9: Same as Figure 3-8, but for PG.

values was calculated using the raw *PG* voltages, before the voltage was calibrated to V m^{-1} . This stops the need for multiple threshold values, dependent on the calibration dates.

3.2.2 Biral Thunderstorm Detector

The BTD (Biral, 2018) consists of three electrodes; one spherical (primary) and two toroidal (secondary and tertiary), which exists at a lower height (Figure 3-10). The BTD uses quasi-electrostatics⁹ to measure the electrical current, j , to detect lightning strikes with a near zero false alarm rate (0.3%) and a high spatial resolution (0.01 km). The BTD can detect lightning up to 100 km away and can measure the variability in the *PG* (j_D), charged rain (j_P) and corona (j_T) through inductive contact with the electrodes. The primary electrode is the most sensitive electrode as it has the greatest distance from the surface providing the greatest signal-to-noise ratio. Changes in the *PG* are band-pass filtered (1 – 47 Hz) to remove the noise caused by the mains electricity power at CO (110 V, 5A, 50/60 Hz) and to avoid direct sampling of the DC currents (< 1 Hz). Measuring the *PG* between 1 and 47 Hz along with using three electrodes allows for the high detection rate for lightning (Bennett, 2016). Another benefit of removing slow variations of the DC currents (< 1 Hz) is removing the contributions of the conduction current (j_c) caused by the flow of charge through the global electric circuit (GEC) (Bennett and Harrison, 2008). As the current flowing through the GEC has a diurnal pattern, the removal of j_c

⁹ Quasi-electrostatics can be defined as approximating a dynamical system as static. Although the charge within the atmosphere is moving, treating the atmosphere as static eliminates the need to account for the magnetic field that is produced as a result of moving charges (Griffiths, 1999a).

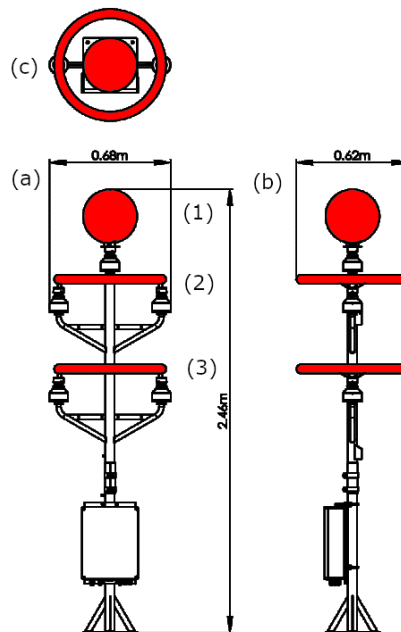


Figure 3-10: BTD-300 schematic for front view (a), side view (b) and top-down view (c). Red sections are the primary (1), secondary (2) and tertiary (3) electrodes [reproduced with kind permission of Biral].

normalises the measurements taken by the BTD across the entire day. As the BTD measures multiple currents, the combination of currents, j_D , j_P and j_T measured by the BTD can be defined as the total current, j_{tot} .

As the BTD uses three electrodes, charged precipitation that would land on a single electrode can be differentiated from other atmospheric electrical features (such as space charge and lightning), which would induce a current on all three electrodes simultaneously. The detection of charged rain at the surface acts as an early warning indicator of lightning emanating from the overhead cloud (Bennett, 2018). The magnitude and polarity of charged rain can be calculated from the covariance between the primary and secondary sensors as precipitation should only be measured on a single sensor at any one time. The melting ice mechanism (§2.1.4) is the proposed cause of charged precipitation. This mechanism typically requires the generation of a convective downdraught. Therefore, the presence of a downdraught with charged rain is a strong indicator that the cumulonimbus cloud overhead is strongly electrified, potentially leading to lightning (Dinger and Gunn, 1946).

The BTD can also measure corona, also known as a point discharge, which can be considered as the first stage¹⁰ of the electrical breakdown of the atmosphere where the air fails as an insulator and can begin to conduct from ionisation. The electrical breakdown occurs when the PG is above what is known as the activation limit, E_{on} (MacGorman and Rust, 1998). This typically occurs

¹⁰ The later stages included sparks and lightning, which typically require much greater PG for these phenomena to occur, thus acting as a natural progression.

around pointed objects, which act as a conductor, increasing the PG above E_{on} . In localised regions, corona can lead to the production of space charge once the corona is advected. Therefore, the greater the curvature of a pointed object, the greater the electric field density, which in turn can increase the rate that corona is produced. A needle is fitted to the side of the BTD to help induce corona once the PG is above E_{on} .

A background zeroing is performed by the BTD automatically by looking at the site characteristics of the environment. The variability of the PG changes is measured to detect anomalies at the site that can be used to offset the measurements for all three electrodes. The calibration, which takes 30 seconds, was performed during undisturbed weather conditions when no precipitation, charged clouds, nor people were influencing the instrument. The BTD has a sampling resolution of 100 Hz, which can be used to measure the fast-varying changes in the PG from the three sensors. The automatic detection of charged rain, corona, enhanced PG , and lightning is provided at a resolution of 0.5 Hz and is sampled from the 100 Hz data. These detections are categorised as warning flags and a description of each warning flag is provided in Appendix B.

3.3 Rain Gauge Instruments

This section discusses seven rain gauge instruments used in this thesis, specifically for use in §4. Due to the substantial number of rain gauges used for analysis, this section is subset by the rain gauge class (tipping bucket, drop counter, and disdrometer) as the instruments are similar in these classes. The methods used to measure precipitation are discussed along with how the data were processed to ensure data quality were controlled.

3.3.1 Tipping Buckets

Three tipping bucket rain gauges are used in this thesis (see Table 3-5) located at the RUAO and CO. Each tipping bucket works using the same principle of collecting precipitation in a bucket with a capacity of 0.2 mm (equivalent to a rain height of 0.2 mm). Once the bucket reaches capacity, the bucket is emptied automatically (tip) and the time at which the bucket tips are recorded. Once two or more tips have occurred, it is possible to calculate the rain rate (RR). The calculation of the RR (units = mm h⁻¹) is made based on the bucket size, B used to collect precipitation with respect to the time difference between tips, Δt ,

$$RR = \frac{B}{\Delta t}. \quad 3-1$$

For the Munro tipping bucket, the data are quality controlled by checking for anomalous tips with respect to the other rain gauges. The output for this tipping bucket was recorded at a

Table 3-5: The specifications for each tipping bucket rain gauges used at the RUAO and CO for comparison with the FM.

Instrument	Operational Date	Location	Data Type	Resolution (Hz)
Delta-T Tipping Bucket (Delta-T, 2016)	08/08/2005 to 27/07/2014	RUAO	Analogue	1
EML SPS-500 Tipping Bucket (Environmental Measurements Limited, 2018)	30/08/2014 to present	RUAO	Digital	1
Munro Tipping Bucket (Munro Instruments, 2015)	01/01/2001 to present	CO	Digital	0.1

resolution of 0.1 Hz, compared to both RUAO tipping buckets at a resolution of 1 Hz. One of the limitations of a tipping bucket is the near-discrete variable resolution of the instrument. For small *RRs*, the spacing between successive *RR* bins was negligible, but for larger *RRs* this issue is appreciable. The smaller time resolution of the Munro tipping bucket emphasised this issue further as the data was recorded every 10 seconds. Only 8640 different *RRs* could be measured per day unlike the tipping buckets at the RUAO, which had ten times the resolution.

There are some key differences between the tipping bucket rain gauges used (Table 3-5). Both Munro and EML tipping bucket measurements are recorded as a digital signal (1 for a tip, 0 otherwise), but the Delta-T tipping bucket measurements are recorded as an analogue voltage to represent when a tip has occurred. At the start of a single day, the voltage would be reset to 0 V. After a tip had occurred, the voltage output would increase by a small step voltage¹¹ and would remain at that voltage until either another tip occurred or until the end of the day when the voltage was reset. Random noise was a major problem within the tipping bucket dataset and often obscured the tips within the data, thereby identifying the number and time of tips was difficult.

Figure 3-11 shows the raw voltage output for a rainy day on 03/03/2009 measured by the Delta-T tipping bucket. Each step increment marks a tip occurring in the rain gauge (example tip is highlighted by a red circle in Figure 3-11a), but between increments, there is appreciable variability which is not constant in time (Figure 3-11a). Another issue is the increment marking a tip is not constant either (Figure 3-11b). For each tip, the voltage should increase by either

¹¹ The step voltage increased between 20 and 40 mV during the lifetime of the Delta-T tipping bucket to improve the signal-to-noise ratio of the instrument. See Appendix A for details of when the Delta-T tipping bucket step voltage was changed.

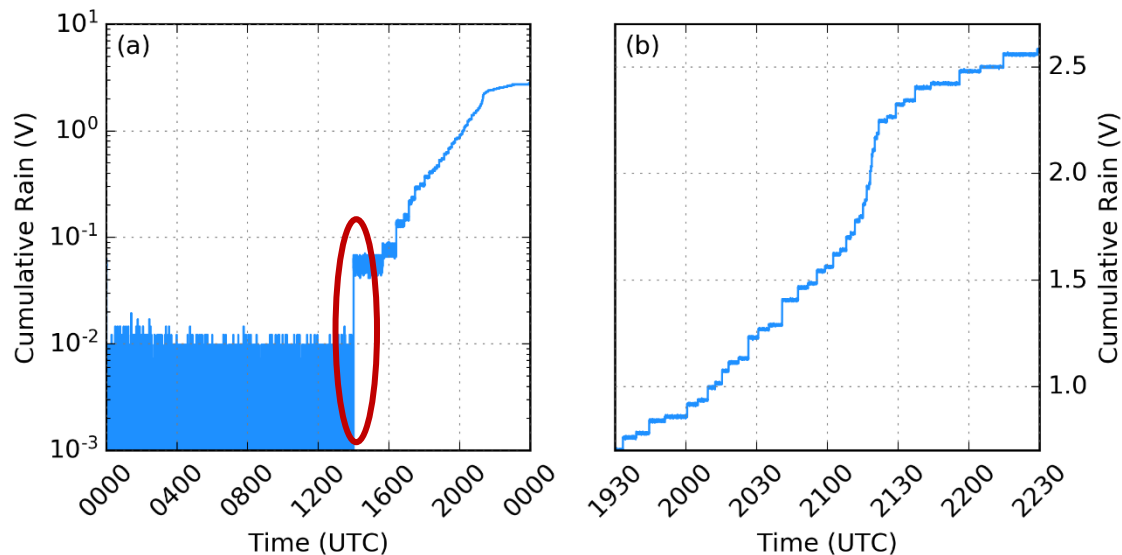


Figure 3-11: A time series of voltage measured from the Delta-T tipping bucket rain gauge on 03/03/2009 for (a) the entire 24 hours and (b) between 1930 and 2230 UTC during a rain event. Each step change in the data marks a tip of the tipping bucket rain gauge (red circle shows example).

exactly 20, 30 or 40 mV depending on the calibration used (see Appendix A for calibration dates and voltages used). The analysis of the data can be simplified as only positive increases in voltage signify a tip. Simply using 20, 30 or 40 mV as a threshold to identify the position of the tips has a high false positive and negative ratio. To identify the time of the tips within the dataset, a bespoke algorithm was designed to minimise the number of false positives and negatives and increase the detection efficiency. To test the efficiency of the tip detection algorithm, a series of methods were conducted to analyse the Delta-T tipping bucket rain gauge measurements. The following methods were performed on the Delta-T tipping bucket and are discussed in more detail:

- Details of the top-down tip detection algorithm designed for this thesis,
- Testing of the algorithm's robustness using pseudo-random data with tips and noise added to the data,
- Calculation of the noise embedded inside the rain gauge measurements and comparing these results with the pseudo-random data,
- Comparison of rainfall between the tipping bucket rain gauge and a manual rain gauge using the tip detection algorithm,
- Removal of *RR* anomalies and correction of tips due to floating point errors.

The Top-Down Tip Detection Algorithm

The top-down tip detection algorithm was designed to accurately detect the number and time of tips within a tipping bucket timeseries dataset. The top-down algorithm is based on the principle that averaging can improve the signal-to-noise ratio of the dependent variable at the

cost of degrading the resolution of the independent variable. Using 24 hours of tipping bucket data, the data is split into two, 12-hour subsets. The mean of each subset is calculated and the difference between subsets is found. The difference in mean is tested against a threshold value. The threshold for identifying tips in the tipping bucket rain gauge was set to 40 mV as this was the voltage that was expected to be added per tip. As shown in Figure 3-11, the absolute size of the step jumps was not constant even during a single day. There is a very small probability that multiple tips occur within the same second as this would equate to a RR of 720 mm h^{-1} , an unlikely rain intensity anywhere in the world.

The number of tips that occurred within a subset is unknown as the temporal resolution has been reduced by averaging. To improve the temporal resolution, each subset identified as significant (greater than the threshold) is split up into two equal-sized subsets (i.e. 6-hour subsets). The significance tests are repeated for these smaller subsets thereby increasing the temporal resolution and accuracy of the tips being identified. This process is then repeated until the subsets only contained single values and the system became degenerate (i.e. in our case 1-second resolution). Repeating the process of subsetting and testing the data, each unsuccessful identification would be eliminated from further testing (i.e. no tips are present in that subset). Eliminating subsets from being tested again would minimise the noise in the data and avoid degrading the tip detection as false positives would often occur as the noise was not static. Overall, this algorithm can minimise the noise within a dataset without sacrificing the temporal resolution using standard averaging techniques. The flow diagram of the process is given in Figure 3-12.

Identifying tips in an analogue tipping bucket

To test the capabilities of the top-down algorithm for detecting the exact timing of tips within a timeseries, test data was created with a random number of tips added to the data. For consistency with how the tipping bucket rain gauge is stored, the length of the data was kept constant at 86400 spanning between 0 and 24 hours to simulate the hours of the day as a fractional hour. Gaussian noise was added to the data before a random number of tips were added at random times. The standard deviation of the noise was varied between 0.0001 and 0.1 V, 50 times, spaced using a logarithmic scale to emphasis small noise scales. In addition, 20 ensemble members were used to calculate the confidence intervals of the algorithm's detection ability.

To provide some perspective on the algorithms ability to detect tips, three other algorithms were also tested (Table 3-6). The threshold algorithm has been previously discussed and defines

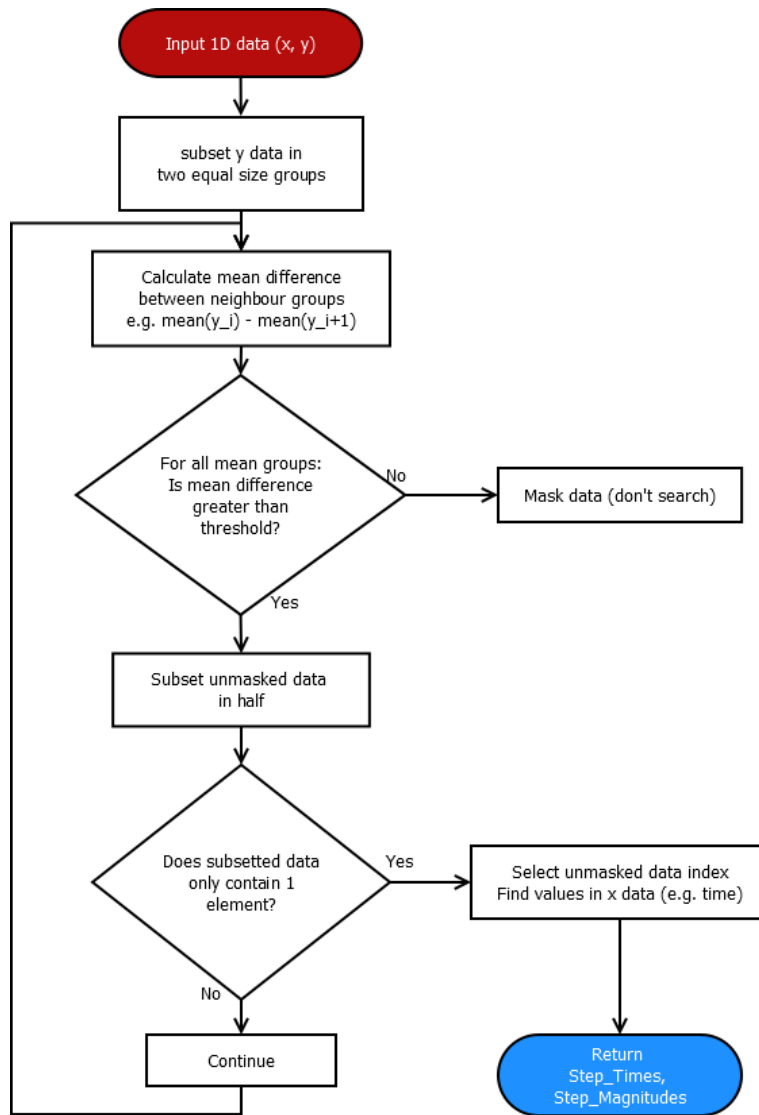


Figure 3-12: Flow diagram of top-down tip detection algorithm used to identify the tips in a tipping bucket rain gauge that outputs an analogue voltage.

any change in voltage ≥ 40 mV as a tip. The converger algorithm uses the voltage at the end of the day to estimate the number of tips expected. The threshold value of 40 mV is perturbed in increments until the number of tips can be found within the data. The Mallat-Zhong (1992) is a third-party step detection algorithm that uses an edge-preserving smoothing function to increase the contrast of the tips within the data (Kahn, 2016).

To test each algorithm's ability to identify tips within the pseudo-random data, the detection, false negative and false positive ratios were calculated,

$$\text{Detection Ratio} = \frac{CT}{N}, \quad 3-2$$

$$\text{False Positive Ratio} = \frac{FT - CT}{N}, \quad 3-3$$

$$\text{False Negative Ratio} = \frac{N - CT}{N}, \quad 3-4$$

Table 3-6: Descriptive details of the four tip-detection algorithms used to determine the tip times from a tipping bucket rain gauge.

Algorithm	Method	Pro/Cons
Threshold	Constant Threshold	<p>Pro: Simple construction and proves reliable if the noise is always less than step sizes.</p> <p>Con: Susceptible to noise and difficult to find an acceptable threshold value.</p>
Converger	Variable Threshold	<p>Pro: Less susceptible to noise as the number of tips expected could be determined prior to testing.</p> <p>Con: Detection was still an issue most of the time due to varying differences from expected.</p> <p>Con: Extremely slow performance ($\sim 5 - 500 \text{ s day}^{-1}$) due to the method of convergence which is a function of noise levels.</p>
Mallat-Zhong	Edge Preserving Smoothing and Threshold Test	<p>Pro: Fast computational speeds ($\sim 0.4 \text{ s day}^{-1}$).</p> <p>Con: Has exceptionally large false positive errors and misses some tips.</p>
Top-Down	Mean sub-setting and threshold testing	<p>Pro: Fast computational speeds ($\sim 1 \text{ s day}^{-1}$).</p> <p>Pro: Robust to increasing and random changes in noise.</p> <p>Con: Boundary effects exist in this algorithm which on occasions can fail to predict tips near the boundary.</p>

where CT is the number of correctly identified tips, FT is the number of tips identified and N is the number of tips added to the dataset being tested. Figure 3-13 shows the detection ratio and false positive ratio for all four tip detection algorithms. The top-down algorithm provides the greatest detection ratio for noise levels $> 0.015 V$, while the threshold algorithm is better for smaller noise levels. When comparing the results with the false positive ratio (Figure 3-13b), the top-down algorithm has a consistently low ratio ($< 10^{-4}$), unlike the other algorithms. The false positive ratio of the threshold algorithm, for example, misidentified up to 100 extra tips within the dataset. In comparison, the converger and Mallat-Zhong algorithms both perform worse than the top-down algorithm for noise $> 10 \text{ mV}$. Overall, the top-down algorithm is more resilient to noise than the other algorithms.

Tipping Bucket Noise

One of the concerns when designing a tip-detection algorithm was its ability to handle variations in anomalous data. Figure 3-14 shows the daily standard deviation of the Delta-T tipping bucket

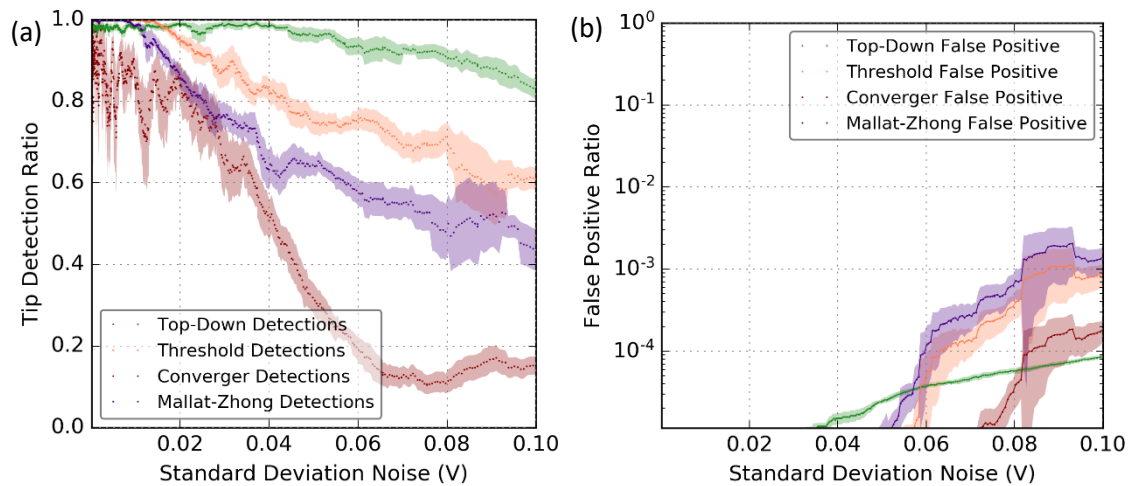


Figure 3-13: (a) Tip detection ratio and (b) false positive ratio for the top-down (green), threshold (orange), converger (red) and Mallat-Zhong (purple) tip detection algorithms applied to pseudo-random data (see text for description of data used). For each algorithm, the detection ratio and false positive ratio have been averaged (solid points) with the 95% confidence intervals (shading) provided.

rain gauge between 2006 and 2014 for zero-tip days (i.e. no precipitation). The raw voltages were used to estimate the variance of the instrument over time. Over eight years, the rain gauge showed a strong day-day variability with no obvious seasonal or annual pattern. During 2013, there was a substantial reduction in the variability of the tipping bucket. A cause for the decrease in variability does not coincide with the increase in voltage-per-tip increments that occurred in 2006 and 2007. What can be noted during the 2013 period is the high number of data logger failures that occurred (> 50%).

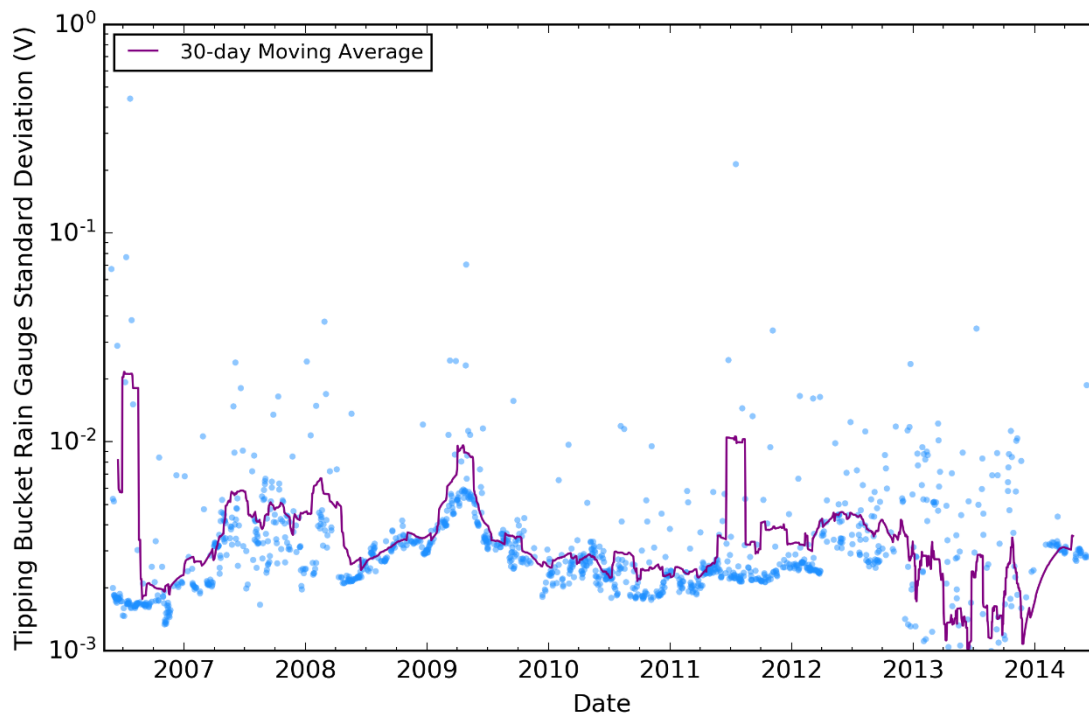


Figure 3-14: The daily standard deviation (blue points) for zero-tip days for the Delta-T tipping bucket at the RUAO between 2006 and 2014. A 30-day moving average (purple line) was applied to the data.

Table 3-7: The predicted efficiency of each tip-detection algorithm with respect to the full range of standard deviation values measured by the tipping bucket rain gauge during zero-tip days.

Tip-Detection Algorithm	Detection Ratio	False Positive Ratio	False Negative Ratio
Top-Down	$0.975^{+0.002}_{-0.141}$	$0.000^{+0.0001}_{-0.0000}$	$0.000^{+0.000}_{-0.000}$
Threshold	$0.999^{+0.001}_{-0.390}$	$0.000^{+0.0009}_{-0.0000}$	$0.947^{+0.053}_{-0.947}$
Converger	$1.000^{+0.000}_{-0.563}$	$0.000^{+0.0002}_{-0.0000}$	$0.000^{+0.054}_{-0.00}$
Mallat-Zhong	$0.761^{+0.163}_{-0.607}$	$0.000^{+0.0014}_{-0.0000}$	$0.000^{+0.053}_{-0.00}$

The range of variability of the rain gauge covered three orders of magnitude with a mean of 3.74 mV and the 95th percentile range of 7.37 mV. The efficiency of the tip-detection algorithms is given in Table 3-7, giving the detection, false positive and false negative ratios based on the testing performed in Figure 3-13. The converger algorithm had the greatest detection ratio of the mean noise contained within the tipping bucket measurements. The top-down had the smallest variation of all algorithms for the detection, false positive and false negative ratios, despite not detecting all tips in the test data.

Comparison of Rainfall from Tipping Bucket and Manual Rain Gauge

One of the main concerns when understanding the accuracy of measuring precipitation relates to the disagreements between different rain gauges. The error associated with any rain gauge is related to the design of the instrument (Lanza et al., 2005; Goodison et al., 1998). Influences such as wind velocity, temperature, bucket size, bucket materials, and the height of the rain gauge are the many reasons for the errors in rainfall amount (Pollock et al., 2018). Another error is introduced when working with tipping buckets caused by the time taken for the bucket to empty when it has reached its capacity (0.2 mm). This error is negligible during small *RRs* but can be appreciable for larger *RRs* when the time taken to empty the bucket and to start collecting precipitation again is proportional to the amount of precipitation lost (Marsalek, 1981). Therefore, testing the robustness of a tipping bucket against standard rain gauges can be useful in assessing the ability of the tipping bucket rain gauge.

The Delta-T tipping bucket data was compared to standard rain gauge observations made at the RUAO at 0900 UTC each day. An ordinary least-squares and an ordinary Huber¹² linear regression model was fitted to the relationship of daily rainfall amounts between the standard rain gauge and the four tip detection algorithms (Figure 3-15). A Huber regression model is used to adjust

¹² The Huber (1973) linear regression model is robust to the outliers within the dataset, specifically the dependent variable. Huber model uses a maximum likelihood function to optimise the loss function with a dataset containing up to 50% outliers.

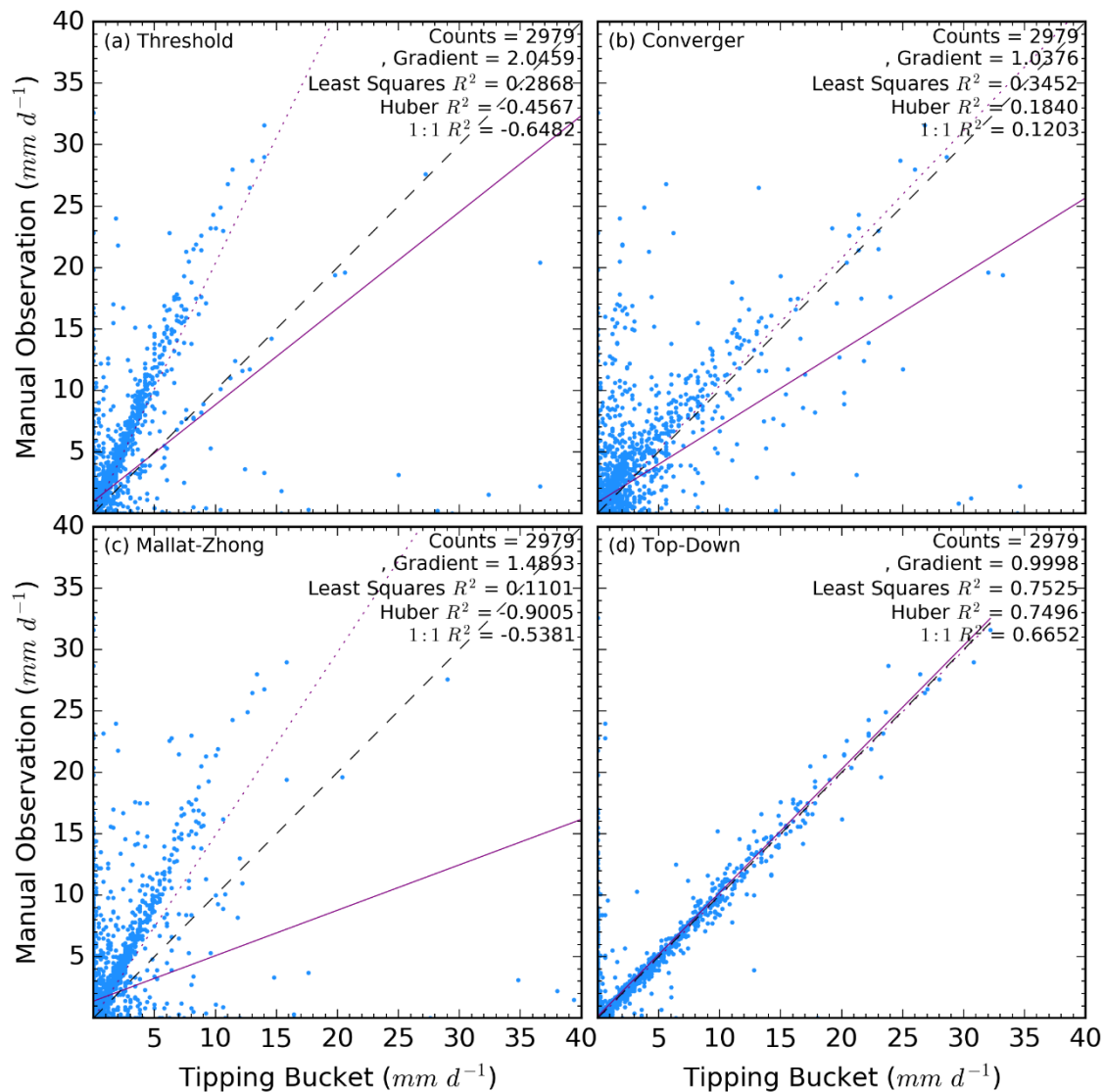


Figure 3-15: A comparison of daily rain totals between manual observations and tipping bucket for all rain days between 2006 and 2014. All 4 tip-detection algorithms were used for determining the rain totals, (a) threshold, (b) converger, (c) Mallat-Zhong and (d) top-down. The least squares (purple line) and Huber (1973) (purple dotted line) linear regression models were fitted to the data to account for significant outliers in the data. A 1:1 line (black dashed) represents the line of best fit for a tip-detection algorithm.

for outliers within the data between the two rain gauges. The gradient, least squares R^2 (LR), Huber R^2 (HR) and 1:1-line R^2 (1R) was used to compare each tip-detection algorithms' ability to detect the correct number of tips in the dataset. This test assumes that both the standard rain gauge and tipping bucket received equal amounts of precipitation, which is not accurate due to the limitations of both rain gauges previously discussed. Nevertheless, this test provides a reasonable guess on the amount of precipitation that was received at the RUAO each day. The 1R is closely related to the root mean square difference (RMSD). To calculate the 1R, the residuals between the total rainfall measured by the tipping bucket and the observations are compared. For a model f (e.g. tipping bucket), and the associated data y (e.g. observer) the R^2 can be calculated using,

$$R^2 = 1 - \frac{\sum_i (y_i - f_i)^2}{\sum_i (y_i - \bar{y})^2} \quad 3-5$$

where \bar{y} is the geometric mean of y . The range of values that can be observed for R^2 is $(\infty, 1]$ with 1 being a perfect agreement between the model, f and the data y . If the manual observations act as a true representation of the total rainfall, a comparison between the tipping bucket and observer provides a useful comparison against the LR. Having a LR equal to 1 does not necessarily mean that the two rain gauges agree—only when LR and 1R both equal 1.

The linear relationships for all algorithms were statistically significant but from comparisons of their LR, only the top-down algorithm had an acceptable relationship (LR = 0.7525). The top-down algorithm also returned the highest 1R and HR value (1R = 0.6652, HR = 0.7496). According to the least-squares regression, there was a small tendency for the tipping bucket to underestimate the amount of rain. This could potentially be corrected by considering the time for the tipping bucket to empty itself after saturation. However, determining the correction factor can also introduce varying degrees of error as the exact timing of emptying can vary over large temporal scales and temperatures (Marsalek, 1981). The negative 1R values for the threshold and Mallat-Zhong algorithms can be attributed to the extremely large outliers present in certain rain days, which had a significant influence over the least squares fitting. Hence why the linear regression has a substantial difference with the Huber regression. For example, the threshold algorithm detected 120 mm d⁻¹ during a single day while the manual observation detected a dry day (0 mm d⁻¹). Observations of the Cook distances¹³ for each data point confirmed the strong influence that these data points had upon the linear regression models.

Along with the ordinary least-squares linear regression model, the Huber (1973) linear regression model was fitted to the data (dotted purple line in Figure 3-15). The Huber (1973) model can identify outliers in the data by optimising the square loss of the data¹⁴. This model was used here, as it provided one of the best linear regression models for dealing with outliers, particularly useful for dealing with the outliers present in Figure 3-15. The Huber regression model struggled to minimise the outliers in the data for the threshold, converger, and Mallat-Zhong algorithms. An issue with the robust regression models (such as the Huber model) is the

¹³ Cook distance is a statistical diagnostic used to determine the influence that each residual has upon a least-squares linear regression model. Residuals with largest Cook distances have the greatest influence on the regression and can be used to indicate regions in the data space where the values are anomalous with respect to the trend of the data (Fox, 1991).

¹⁴ The loss function is defined as the normalised difference between the predicated value and the true value. The Huber model attempts to minimise the loss function below some threshold, thus providing a linear regression that captures the majority of the data.

critical limit for the number of outliers. The breakdown point is less than 50% of the dataset, as it would be impossible to detect which data were the outliers (Huber, 1984). Despite the large outliers in the threshold and Mallat-Zhong algorithms, the Huber calculated a near-perfect relationship between the top-down algorithm and the manual rain gauge (gradient = 0.9998). As the Huber regression model struggled with the anomalous data, the threshold and Mallat-Zhong algorithms can be considered unstable for use with real-world data. The substantial variation between daily rainfall amounts calculated using the converger algorithm suggests that it too is not suitable for use with real-world data.

Comparing the tipping bucket with the manual observations further, the maximum cumulative output voltage for each day was divided by the applied step voltage for each tip¹⁵ to represent the expected amount of rain that occurred during the day. The analysis between rain gauges was limited to days with more than 1 mm of rain to avoid the unambiguity of manual records defining a *trace* indicator for any day. A relationship was found between rain gauges to be statistically significant (LR = $R^2 = 0.8696$, $p < 0.001$) but the gradient in the relationship was not 1 and an offset was needed for all rain totals. Due to the limited size of the bucket, the tipping bucket could underestimate the daily amount of rain measured by ± 0.2 mm. By adjusting the R^2 value, assuming the linear relationship should follow a 1:1 line, a weaker relationship was found between the rain gauges ($1R = 0.3964$).

The difference between rain gauges is threefold. First, the error associated with the tipping bucket caused by the time delay between the bucket saturation and the bucket emptying time. Second, the error in the manual observation readings. Third, the error caused by the wind and drop splashing causing variability in the precipitation entering the rain gauge. Despite this, the error in the manual observation can become quite significant and is often dependant on the measuring device characteristics (Ying et al., 2006). Therefore, despite the requirement of an offset to show statistical significance with the manual observations, the fact that they have a small p -value for any arbitrary difference suggests the tipping bucket has a strong ability to measure precipitation accurately and consistently.

It must be noted that the detection ratios shown in Table 3-7 are based on when the algorithm found a perfect match. An algorithm can detect all tips within a dataset, but if the timestamps do not match up (even a one-second difference), then this 'tip' is assumed to be an incorrect identification, increasing the false positive and negative ratios. This double penalty is an

¹⁵ This method is useful to determine the overall effectiveness of the tipping bucket rain gauge but does not consider when the tips occurred during the day.

appreciable issue for the top-down algorithm, but as shown in Figure 3-15d changes to the number and timing of the tips are negligible for small errors. A small error in the timing of the tip (< 5 seconds) is better than incorrect or miss identification of a tip which can change both the *RR* and the *PG* being averaged. The false positives and false negatives ratios are more important in the evaluation of the tip-detection algorithm's performance. Overall, the tipping bucket was fairly stable in its operation leading to a small underestimation in the total rainfall when compared to manual observations. The top-down algorithm provided the best detection of tips from the tipping bucket rain gauge with a near-perfect relationship with the manual rain gauge (Figure 3-15d).

Post Processing of Rain Rates

Errors caused by high *RRs* can be derived from the tipping bucket and the tip-detection algorithm (Habib et al., 2001). The tipping bucket can measure low rain intensities accurately as the time for the precipitation to funnel into the gauge and the time for the bucket to tip are negligible (Marsalek, 1981). As the *RR* increases, these timing issues become an appreciable issue and can cause a systematic bias in the *RR*.

The comparison of rainfall totals of the tipping bucket and standard rain gauge (Figure 3-15) shows the tipping bucket was, on average, underestimating the amount of precipitation. The underestimation increased with daily rainfall total. This underestimation was caused by the tipping bucket design, which cannot be easily fixed post-measurement. Another source of error comes from the accuracy of the tip detection algorithm. Tip detection methods, including the top-down algorithm, have a small probability of not resolving the exact time when a tip occurred. For most rain days, at least one tip would be identified twice, first at the start of the rising edge and second, at the end of the rising edge between voltage increments. This led to small times between tips (1-10 seconds) and if not removed would result in *RRs* between 72- and 720-mm h⁻¹ which are exceedingly rare intensities to observe, anywhere in the world. These *RRs* are likely to be anomalies and were removed from any further analysis. A histogram of all the *RRs* detected at the RUAO between 2006 and 2018 are shown in Figure 3-16. The histogram shows a minimum in *RRs* at 10 mm h⁻¹ with the highest concentration for *RRs* less than 10 mm h⁻¹ (84.5%) with no more than 200 counts per *RR* after 10 mm h⁻¹. The minimum at 10 mm h⁻¹ provides a threshold between stratiform and cumuliform rainfall types.

When processing the precipitation data, considerations were made to compensate for the floating-point precision limits native to all binary computer systems. When using non-exact

timestamps in any measurement record¹⁶ (e.g. using floating-points), the errors, although small, are compounded when used in calculations. When calculating the *RR* for a tipping bucket (equation 3-1), the subtraction, and the division of two timestamps can lead to a small difference from the correct *RR*. To correct the *RRs*, the data was adjusted into the nearest acceptable *RR*. Figure 3-16 shows the *RRs* after the correction. All histogram lines (purple) match directly with the possible *RRs* available using equation 3-1 (grey).

3.3.2 Drop Counters

Three RAL rapid response drop counters (Norbury and White, 1971) located at CO were used for this thesis. The drop counters measure precipitation by first collecting the hydrometeors in a reservoir and then releasing the collection in the form of droplets at a constant volume. The droplets are then detected using an optical sensor. The reservoir is kept at a constant level inside the instrument, primed for when precipitation is collected. Using a reservoir decreases the response time of the instrument as droplets can be released from the reservoir the moment precipitation enters the drop counter. The droplets are formed using a precision tube when the pressure of additional water from incoming precipitation increases past a threshold.

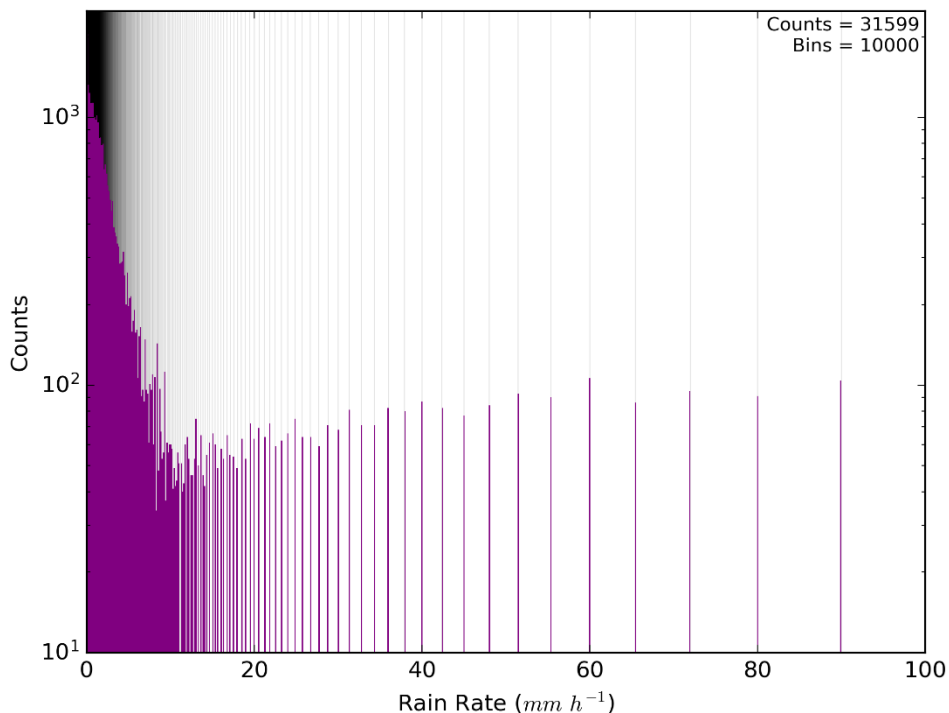


Figure 3-16: A histogram (purple) of all the *RR* detected between 2006 and 2018 for *RRs* between 0-100 mm h^{-1} . The grey vertical lines represent the *RR* values that are possible using equation 3-1 (see text for their importance).

¹⁶ METFiDAS I used fractional hours, to four decimal places, to record each new measurement despite being recorded at 1 second increments. As $1/3600 \approx 0.0002\bar{7}$ is an irrational number, errors would start to occur if the fractional time stamps are used directly. The errors are compounded when used with any other data containing error.

A single drop is equivalent to 0.0033 ± 0.0003 mm for the two low-resolution drop counters (A and B) and 0.00189 ± 0.00019 mm for one high-resolution drop counter (C). The calculation of the RR using a drop counter differs from the tipping bucket slightly,

$$RR = \frac{N_D \cdot \varepsilon_d}{\Delta t}, \quad 3-6$$

where N_D is the number of droplets collected during the collection time, Δt and ε_d is the size of the droplets.

In comparison with the tipping bucket, ε_d influences the resolution of the RR . For a ten second sample (0.1 Hz), the minimum RR possible is 1.188- and 0.68-mm h⁻¹ for the low- and high-resolution drop counters respectively. These high minimum RR s are problematic for understanding the relationship with PG for small RR s. Another difference of the drop counter is the RR resolution is constant for all RR s. The resolution is equal to the minimum RR possible. In our example, using a sample of ten seconds was too coarse for an accurate comparison with the PG . A solution for improving the RR resolution was to increase the sample time, but at the cost of reducing the temporal resolution of the instrument. Decreasing the temporal resolution of the drop counters would also impact the relationship with the PG that varies on much smaller timescales. Therefore, the classic uncertainty principle occurs,

$$\Delta RR \cdot \Delta t \propto \varepsilon, \quad 3-7$$

which is directly proportional to the size of the drop used to measure the rainfall (i.e. you cannot have an infinite RR and t resolution simultaneously). To accommodate these issues discussed, a Δt of 1 minute was used for calculating the RR in equation 3-6.

3.3.3 Disdrometer

For this thesis, a Distromet RD-80 disdrometer (Distromet, 2012) located at CO was used. The disdrometer is a similar instrument to the drop counter but rather than artificially creating droplets of a fixed size from the accumulating precipitation, the droplets are measured in situ as they interact with the sensor. The precipitation droplets interact with the disdrometer by landing on an electromechanical pressure plate made from Styrofoam. The mechanical impulse of the drop produces a force, which is proportional to its size. Only a single drop can be measured at any one time, but the relaxation time of the instrument is negligible with respect to the time of any subsequent drop landing on the pressure plate. This means that the disdrometer is capable of measuring precipitation instantaneously and can respond to changes in droplet size and intensity almost instantly.

Due to the disdrometer's extremely high sensitivity, several signal processing methods are required to interpret any mechanical impulse detected by the instrument. This minimises the number of false positives that would occur, such as insects, birds, and debris landing on the pressure plate. Despite the use of signal processing, there has never been a single day on record when a single "drop" was not detected. Simple methods to determine the legitimacy of the detected drop can include cross-comparing with radar or lidar data at CO to determine whether a cloud was measured overhead. A second method requires multiple droplets to be detected over a short time length (e.g. 10 seconds). For this thesis, a minimum of 10 drops was required within 1 minute before the *RR* was calculated to minimise the amount of anomalous data.

The disdrometer has a temporal resolution of 0.1 Hz and a central drop diameter resolution ranging between 0.313 and 5.145 mm with a drop size uncertainty of $\pm 5\%$ of the measured diameter. Figure 3-17 shows the variation in bin width against the central drop diameter, which is grouped into 127 bins. The non-linear distribution of the central drop diameter is clear when compared with their bin width, which is non-monotonic.

Calculating the *RR* for the disdrometer is more complex in comparison to the tipping bucket and drop counters. The shape of the drop impacting the pressure plate of the disdrometer must be taken into account when determining the volume of water impacting the instrument. Islam (2012) showed that the *RR* is derived from the moments of order 3.67, $m_{3.67}$,

$$RR = 3.78 \cdot \frac{\pi}{6} \cdot m_{3.67}. \quad 3-8$$

The moments of order can be defined as,

$$m_{3.67} = \sum_{i=1}^n d_i^{3.67} \cdot N_m(d_i, t) \cdot \Delta d_i \quad 3-9$$

where d is the central drop diameter (in mm), Δd is the drop diameter width (in mm) defined as,

$$\Delta d_i = (d_{i+1} - d_i) + (d_i - d_{i-1}). \quad 3-10$$

The drop size distribution, N_m , can be calculated using the time invariant form,

$$N_m(d_i, t) = \frac{n_i}{A \cdot \Delta t \cdot v_i \cdot \Delta d_i}, \quad 3-11$$

where n_i is number of droplets detected in the central drop diameter bin, i , while A is the area of the sensor area (in m^2), Δt is the time interval between samples (in s) and v_i is the terminal fall velocity (in $m \text{ s}^{-1}$) of the drop defined as,

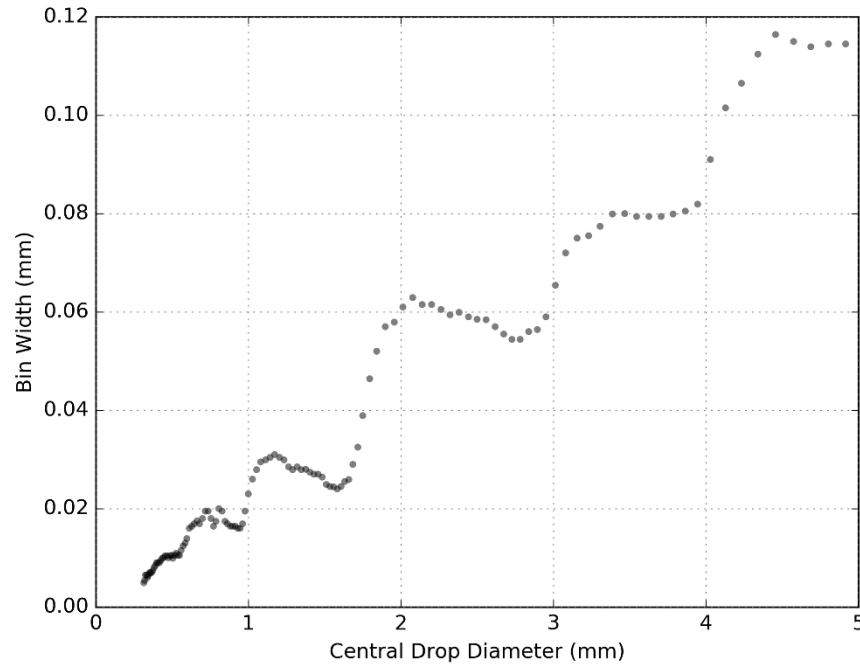


Figure 3-17: Disdromet RD-80 disdrometer central drop diameter comparison with the bin width. Number of size bins is 127.

$$v_i = 3.78 \cdot d_i^{0.67}. \quad 3-12$$

The relationship between the disdrometer derived RR , calculated using equation 3-8, and the drop counting rain gauge has a very high correlation ($r = 0.89 - 0.99$) when measured over hourly periods (Islam et al., 2012). The remaining variance is caused by the local variations between rain gauges. As the disdrometer has extremely high precision, any difference in RR s between rain gauges at CO is not negligible and cannot be associated with the error of the individual instruments. One of the main advantages of the disdrometer is the extremely high RR resolution when compared with the tipping bucket and drop counters. The tipping bucket and drop counters have 8640 RR bins (86400 for the RUAO tipping buckets), but the disdrometer has 9.22×10^9 RR bins¹⁷ over a 24-hour period, even at a 0.1 Hz temporal resolution. This provides a much greater resolution when compared with measurements taken from the CO FM.

3.4 Remote Sensing Instruments

Two remote sensing instruments were used in this thesis, both located at CO, the 35GHz “Copernicus” Doppler radar (henceforth ‘radar’) (Rutherford Appleton Laboratory, 2016) and the Vaisala CT75K Ceilometer (henceforth ‘ceilometer’) (Rutherford Appleton Laboratory, 2002). The following subsections discuss how the radar (§3.4.1) and ceilometer (§3.4.2) work along with the measurements that can be taken from both instruments, along with details of CloudNet

¹⁷ Each of the 127 central drop diameter bins can measure up to 8400 droplets every 10 seconds. Therefore, the total number of RR bins can be computed as $127 \times 8400 \times \frac{86400s}{10s} = 9.22 \times 10^9$

(2005) which derives extra information from the radar data (e.g. ice water content) useful for this thesis (§3.4.3).

3.4.1 Copernicus Radar

The radar was used in this thesis to provide a near-continuous measurement of the atmosphere overhead up to a height of 13.8 km (Rutherford Appleton Laboratory, 2016). The radar has a height of three metres above the surface, pointing vertically and scans the atmosphere continuously at 34.960 GHz with a pulse rate of 5500 Hz. As the radar is a static instrument¹⁸, the only free variables are height and time. The width of the cloud can be calculated from the time taken for the cloud to pass overhead together with a speed estimate. However, only a single vertical slice of the cloud can be measured at a single point in the evolution of the cloud.

As the radar was shared with other researchers, the temporal resolution of the instrument varies day-to-day (30 – 180 s), resulting in some clouds being poorly resolved. The height resolution is kept constant with 460 height levels between 0 and 13760 m with a constant spacing of 30 m. Although the radar can measure the size, number concentration, and velocity of the hydrometeors within the full height of the cloud with minimal attenuation (relative to a horizontally pointing radar), the cloud base is often masked by precipitation and boundary layer aerosols.

There are three main quantities that can be determined from a Doppler radar: The Reflectivity (Z), Doppler Velocity (\bar{v}) and Spectral Width (σ_v). These quantities are often described as the zeroth, first and second Doppler moments as they are all related by the magnitude and phase of the radar's return signal and are now described in turn (Fabry, 2015a).

Radar Reflectivity

In general, Z (units = dBZ) can be calculated from the return power of the electromagnetic pulse that a radar emits. As a pulse travels through the atmosphere it is reflected from various targets—the most important being hydrometeors—and is scattered isotropically with a reduced signal returning to the radar. The efficiency of Z can be characterised using the radar equation (Fabry, 2015a),

$$P_r = \underbrace{\frac{1.22^2 0.55^2 10^{-18} \pi^7 c P_t \tau D_a^2}{1024 \log_e 2}}_{\text{Constants}} \underbrace{\lambda^4}_{\text{Radar parameter}} \underbrace{\frac{T(0, r)^2}{r^2}}_{\text{Path}} \underbrace{\|k\|^2 Z}_{\text{Target properties}}, \quad 3-13$$

¹⁸ The radar measures the atmosphere continuously, pointed vertically, and does not move from this position.

where P_t, P_r is the power of the transmitted and received pulse, c is the speed of light, τ is the duration of the pulse, D_a is the diameter of the antenna, $\|k\|^2$ is the dielectric constant of the target, λ is the wavelength of the radar and $T(0, r)$ is the transmittance of the atmosphere between the radar and the sampling volume, r .

Certain assumptions must be made to estimate, $T, \|k\|^2$ and r as they can all vary dependent upon the target's physical characteristics, size, shape, orientation and composition. This can lead to variations in the dielectric constant, absorption, transmittance and the position of each target. Therefore, assumptions must be made to generalise the conditions of the atmosphere, although these can greatly oversimplify the dynamics and variations of a typical cloud structure:

- A beam must travel at the original angle after reflection;
- Targets absorb little to no radar energy;
- Targets must be smaller than the radar wavelength and should be represented as homogeneous spheres;
- Targets should only be liquid or frozen and not both; and
- Targets are uniformly distributed through the sample volume.

The importance of target sizes being much smaller than the radar wavelength is to be able to approximate the hydrometeors using Raleigh scattering. As the target sizes increase, the targets begin to behave according to Mie scattering. The radar—wavelength of 8.58 mm—would struggle to calculate the Z of large hydrometeors such as hail—diameter of ~ 10 mm—and typically underestimates their size. For smaller hydrometeors, it is possible to calculate the Z using the Raleigh scattering approximation,

$$Z = \int_0^{\infty} N(D)D^6 dD, \quad 3-14$$

where $N(D)$ is the is the number of hydrometeors as a function of their diameter, D .

In equation 3-14, the magnitude of Z is directly proportional to the density and size of the hydrometeors. The shape of the target though is still important. A strong relationship of Z with droplet size has led to the correlation of RR with Z (Marshall and Palmer, 1948). The strong relationship between Z and RR was possible as there is a strong correlation between droplet size and RR discovered from independent studies (Harikumar et al., 2010). Even though ice crystals, graupel and aggregate all have a larger diameter than cloud droplets on average, their Z would typically be lower due to their shape being able to scatter less radiation. For an ice particle of the same diameter as a cloud droplet, the cloud droplet Z is 7 dBZ greater than the ice particle

on average. An example of how the different hydrometeor types are measured by the radar is seen at the freezing level. At the freezing level, Z increases uniformly with height and this increase is known as the bright band. This enhanced Z is caused by ice crystals falling into the warm sector of the cloud, causing them to melt. As ice crystals melt, they can scatter more radiation due to the greater size of an ice crystal compared to a liquid drop and the increased reflectiveness of liquid water. As the size of the ice crystal is typically larger than a cloud droplet, Z substantially increases when ice sublimates. Overall, the largest drop sizes have the greatest effect on Z where the variations in hydrometeor density have a negligible effect in the measured Z . Measurements of the rate of change in Z can highlight the evolution of the hydrometeors between radar scans and can be used to estimate the dynamics and possibly the charge separation inside a cloud.

There are several limitations involved when measuring Z , which relate to the unphysical descriptions set out by the approximations of equation 3-13. Attenuation of a signal can occur when the absorption of passing targets is large overall causing degradation in the measurement efficiency of the cloud further away from the radar. This effect can be seen during thunderstorm events when the density of hydrometeors is greatest, and the radar pulse must travel through a greater mass. Temperature inversions and sharp moisture gradients can refract the radar pulse caused by the change in the dielectric of the different air masses. This is less noticeable for vertically scanning radars compared with horizontally scanning radars, but a divergence or convergence of pulses as a cloud system passes can cause an offset towards the conditions measured at the surface. Attenuation can be reduced by using radars with longer wavelengths. For example, the 35 GHz radar is more resilient to attenuation than the 94 GHz “Galileo” radar also located at CO.

For each volume that is sampled, there are a variety of objects moving with different velocities (i.e. hydrometeors, aerosols, insects, etc.) which can affect the magnitude of \bar{v} (Bhatnagar et al., 2003). The distribution of velocities in each sampling area can be measured yielding the mean of the distribution (\bar{v}) and the width of the distribution (σ_v). The velocity of the hydrometeors is discussed in the next sections.

Doppler Velocity

The Doppler velocity, \bar{v} (units = m s^{-1}) is derived using the Doppler effect, where the frequency and wavelength of a distant object can change dependent on the velocity relative to an observer. For a radar, \bar{v} is calculated using the relative phase difference of the transmitted and received microwave pulses rather than using the change in frequency (Fabry, 2015b). Using a phase shift

to calculate \bar{v} is used to emphasise the radial velocity of a distant object. As the velocity of an air mass or hydrometeor within a cloud is relatively small ($< 5 \text{ m s}^{-1}$), the change in frequency is small relative to the other effects such as signal attenuation which can also modify the return pulse (NETPDTC, 2011). Overall, it is possible to identify the presence of updraughts and downdraughts within the cloud. As \bar{v} is weighted by the largest hydrometeors, only once \bar{v} is large enough (e.g. $> 5 \text{ m s}^{-1}$) consistently through a column of the cloud can an updraught be identified with any accuracy.

The magnitude of \bar{v} can be split into two components, w_z , the vertical air motion and \bar{v}_d , the mean Z-weighted terminal fall velocity (O'Connor et al., 2005),

$$\bar{v} = w_z + \bar{v}_d. \quad 3-15$$

The terminal fall velocity can be related to Z using a power law, similar to the Z-RR relationship discussed earlier (Protat et al., 2004; Protat et al., 2003),

$$\bar{v}_d = 1.56 \cdot Z^{0.202}. \quad 3-16$$

Consequently, w_z can be calculated using measurements of \bar{v} .

Spectral Width

The spectral width, σ_v (units = m s^{-1}) is the Z-weighted standard deviation of velocities measured by the radar. The standard deviation of velocities is related to the individual velocity of all particles in the atmosphere. For example, σ_v can increase when the hydrometeors experience turbulent motions. For a radar with a finite beamwidth (0.25° for the 35 GHz radar), the horizontal wind component, σ_b can also increase σ_v . If the turbulence component, σ_t is small, the terminal velocity of the hydrometeors, σ_d can also increase σ_v . These three components can be considered the main contributions to σ_v for a cloud (O'Connor et al., 2005),

$$\sigma_v^2 = \sigma_t^2 + \sigma_b^2 + \sigma_d^2. \quad 3-17$$

As defined by O'Connor, et al. (2005), σ_b can be defined as,

$$\sigma_b = \frac{U \cdot \theta}{4 \cdot \ln 2}, \quad 3-18$$

where U is the horizontal wind speed (m s^{-1}) and θ is the beamwidth of the radar (radians). The turbulent component takes into account the length scale, L , of the turbulence:

$$\sigma_t = \sqrt{\sigma_v^2 \frac{L_s^{2/3}}{L_l^{2/3} - L_s^{2/3}}}, \quad 3-19$$

where σ_v is the standard deviation of mean velocity and L can be defined as,

$$L = Ut + 2z \cdot \sin \frac{\theta}{2}, \quad 3-20$$

where z is the height of the horizontal wind speed observation and t is observation time which is 1 and 30 s for L_s and L_l respectively. Consequently, σ_d can be calculated as,

$$\sigma_d = \sqrt{\sigma_v^2 - \sigma_t^2 - \sigma_b^2}. \quad 3-21$$

As σ_t only represents the vertical component of turbulence, Bouniol et al. (2003) used the horizontal wind speed to determine a two-dimensional turbulence estimate of the atmosphere, the eddy dissipation rate, ε_T :

$$\varepsilon_T = \left(\frac{2}{3a}\right)^{3/2} k \cdot \sigma_v^3, \quad 3-22$$

where a is the Kolmogorov constant with a value of 5/3 (Sreenivasan, 1995), and k is the wavenumber which is a function of the horizontal wind velocity.

3.4.2 Ceilometer

The ceilometer (Rutherford Appleton Laboratory, 2002) is used to identify the presence and height of the cloud base. The ceilometer is similar in design to the radar but emits a much shorter wavelength pulse at 905 nm (the radar's wavelength is 8.6×10^6 nm). The shorter wavelength is extremely sensitive to the cloud base as the size of hydrometeors is typically much greater than the pulse length. A disadvantage of the wavelength used by the ceilometer is the reflection of the signal caused by liquid water. The reflection is beneficial for accurate detection of the cloud base but means that the ceilometer cannot be used for measuring the interior of the cloud unless the optical thickness of the cloud is very small. The raw attenuated backscatter received by the ceilometer is used to identify a high Z band, typically signifying a cloud base.

3.4.3 CloudNet

CloudNet provides derived products using radar, ceilometer, and microwave radiometer data (CloudNet, 2005). The products provided by CloudNet include liquid (LWC) and ice (IWC) water content, target classification, turbulent kinetic energy eddy dissipation rate (ε_T) and model outputs from the ECMWF Integrated Forecast System, which are interpolated allowing CO to reside within the centre of the grid cell. These products are used in this thesis to determine the presence of supercooled liquid water and the relationship of turbulence with the electrification of a cumuliform cloud (§5). For this thesis, the ε_T values and the target classification are used to answer thesis question (2) and (3) and so are discussed in more detail.

The turbulent kinetic energy eddy dissipation rate, ε_T as defined in equation 3-22 suggests how variable the motion of the hydrometeors are with respect to each other. A useful quantity used in this thesis was to examine the height (z) – time (t) derivative of ε_T , which is defined as,

$$\dot{\varepsilon}_T = \frac{d^2\varepsilon_T}{dt dz}. \quad 3-23$$

For this thesis, $\dot{\varepsilon}_T$ is interpreted as the size of the turbulent variations observed within the cloud over both spatial and temporal dimensions. Higher values indicate greater fluctuations in turbulence.

The hydrometeor classification (Donovan et al., 2002) from CloudNet estimates the target type within radar data and is derived using these data and additional measurements from lidar and microwave radiometer instruments. The classification can differentiate between hydrometeors, aerosols, and even insects. The classification is particularly useful for defining the freezing level and providing an estimate of the amount of supercooled liquid water. A caveat for the identification of supercooled liquid water was the high false negative ratio (Donovan et al., 2002). Supercooled liquid water was determined using measurements from the ceilometer as liquid water is highly reflective at the wavelength used by the instrument (905 nm). As discussed earlier, the ceilometer beam is easily attenuated and absorbed by the cloud droplets. Although the ceilometer can penetrate into the cloud, the depth of penetration is inversely related to the optical thickness of the cloud. The optical thickness typically observed in cumuliform clouds is high, resulting in many instances when measurements of the ice phase are poor or impossible. Nevertheless, as the identified clouds often have a wide area, multiple measurements of the cloud were taken to reduce the chance that a cloud with a high moisture content would not be observed. In contrast, the false positive rates for supercooled liquid water identification was found to be low (Hogan et al., 2003), increasing the reliability for when supercooled liquid water is found in the ice phase. A full list of the classifications is given in Table 3-8.

3.5 Radiosonde and In Situ Instruments

In this section, four bespoke instruments (Figure 3-18) are described that were built to measure, in situ, the structure of charged cumuliform clouds on board a standard Vaisala RS92 radiosonde (henceforth ‘radiosonde’) (Vaisala, 2013). The four instruments measure turbulence, charge, cloud backscatter, and supercooled liquid water content (SLWC). The design and processing of these four instruments are discussed in turn after a description of the main radiosonde instrument package.

Table 3-8: A list of target classification codes used in radar data, (provided by CloudNet (2004)).

Classification Code	Description
00	Clear sky
01	Cloud liquid droplets only
02	Drizzle or rain
03	Drizzle or rain coexisting with cloud liquid droplets
04	Ice particles
05	Ice coexisting with supercooled liquid droplets
06	Melting ice particles
07	Melting ice particles coexisting with cloud liquid droplets
08	Aerosol particles, no cloud or precipitation
09	Insects, no cloud or precipitation
10	Aerosol coexisting with insects, no cloud or precipitation

3.5.1 Radiosonde Instrument

The radiosonde contains standard meteorological instruments capable of measuring common atmospheric characteristics (e.g. temperature, pressure, humidity, wind). The radiosonde provides a high temporal (1 Hz) resolution with high precision for all meteorological instruments with the uncertainties for these sensors within acceptable limits to answer the questions for this thesis.

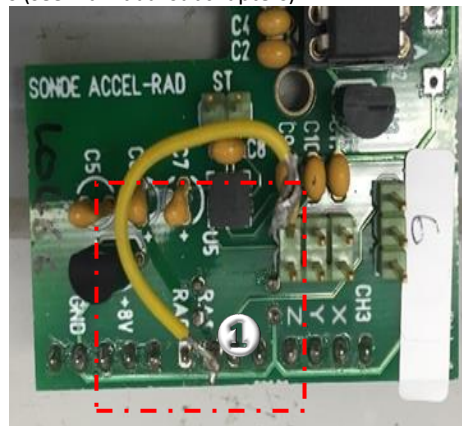
The four bespoke instruments all communicated with the radiosonde using a novel in-house data system known as PANDORA (Programmable ANalogue and Digital Operational Radiosonde Accessory) which supports four analogue input channels (16-bits each, totalling 64-bit data stream) and two digital input channels (Harrison et al., 2012). The voltage communicated by each instrument was converted to counts using an analogue-to-digital converter, which was then communicated with the radiosonde. All data, radiosonde and bespoke, are communicated using radio frequency to a receiving station, at the RUAO, which records the data on a hard disk. The bespoke instrumentation and PANDORA were housed within 3D printed plastic boxes providing some shelter from water short-circuiting the instruments as the radiosonde ascended through the atmosphere.

Both cloud and charge instruments contain multiple sensors and due to the limitations of the PANDORA data system, which could only send 64-bits of data per second, not all instruments could be used concurrently (e.g. orange and infrared cloud sensor). Each sensor had to share the available bandwidth of the PANDORA data system resulting in a reduction to the resolution

Figure 3-18: Circuit board snapshots for each sensor used within this thesis. The circuit schematics of each instrument can be found in the relevant technical papers (see individual subchapters).

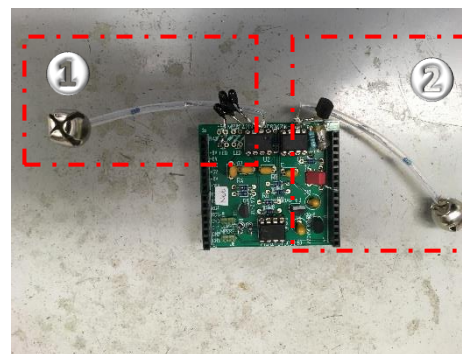
Turbulence Instrument

- ① z-direction



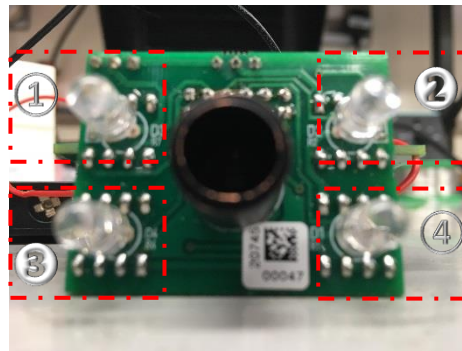
Charge Instrument

- ① Log
- ② Linear



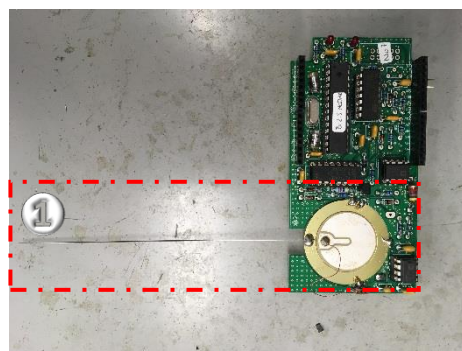
Cloud Instrument

- ① Cyan
- ② Orange (Not Used)
- ③ Infrared (Not Used)
- ④ Infrared



Liquid Water Instrument

- ① Vibrating Wire



of each instrument. To resolve the bandwidth issue, three considerations were used when combining the instruments for each radiosonde ascent. First, the number of sensors providing measurements, second, the temporal resolution of the measurements and third, the precision of the measurements. A reduction in one of these considerations would allow an improvement

in the other.

After each radiosonde flight into a charged cumuliform cloud, the measured data were quality controlled and processed to remove any anomalous values and the data were converted into physical units. The measurements from each bespoke sensor were recorded as a count after being passed through an analogue-to-digital converter. Storing the measurements in count form was beneficial to maximise the available data bandwidth on PANDORA. An intermediate step was required to convert the counts back into the raw voltage, V , before further conversion into physical units. Conversion between counts and volts is related to the voltage range, V_{range} of the instrument (5 V for this thesis) and the number of values that can be stored within that voltage range:

$$V = \frac{V_{range}}{2^n}, \quad 3-24$$

where n is the number of bits (either 12 or 16 in this thesis, see Table 6-1 for the number of bits used for each radiosonde flight).

3.5.2 Charge Instrument

The charge instrument is based on the design by Nicoll (2013) and Harrison et al. (2017) which uses two electrical sensors, measuring charge over linear and logarithmic scales. Two small metallic bells (12 mm diameter) were used as a sensing electrode for the two sensors, which responded to displacement and impact¹⁹ currents. The linear sensor uses a series of resistors in a T-network configuration and the current is passed through a linear amplifier to increase the sensitivity to the current measured.

The logarithmic sensor uses four blacked-out green light emitting diodes (LEDs) wired in inverse parallel. The configuration of the LEDs allows for the measurement of the current in both polarities. The current received by the logarithmic sensor is passed through a logarithmic amplifier to provide a wide range of current measurements over six orders of magnitude (pA to μ A). A major issue with the logarithmic sensor is temperature dependence, which is difficult to resolve. A solution to overcome the temperature dependence was to provide a relative calibration with the linear sensor when the linear sensor was not saturated (Harrison et al., 2017).

¹⁹ Impact currents are caused by charged particles impacting the sensing electrode.

Space charge density and electrical current were derived from the measurements taken by both the linear and logarithmic charge sensors. An analytical relationship can be used to relate the sensor to the electrical current, j using the principles of Ohm's law (Nicoll, 2010):

$$j = -\frac{V_c - \bar{V}_c}{R}, \quad 3-25$$

where V_c is the voltage from the sensor, \bar{V}_c is the median voltage from the sensor and R is the size of the gain resistor within the circuit (in this thesis, $R = 2.4 \times 10^{11} \Omega$). As many electronic components within the charge instrument can have a large uncertainty (e.g. gain resistor = $\pm 5\%$), a more accurate and precise estimate of the current would be advantageous.

The electrical current was found through calibration of both linear and logarithmic charge sensors. The calibration was conducted in laboratory conditions and was achieved by applying a known current directly into each sensor. By changing the current over small interval steps, the relationship between input current and output voltage for both linear and logarithmic sensors could be estimated. Figure 3-19 shows the calibration of the linear and logarithmic sensors for all ten radiosondes. There is a substantial variation between sensors, particularly near both extrema, beyond the 95% confidence levels. Comparison between package three and four (extreme cases) has a substantial root mean square difference (RMSD) of 0.5866 V (11.7% of V_{range}) and 0.0587 V (0.012% of V_{range}) for the linear and log sensors respectively. The

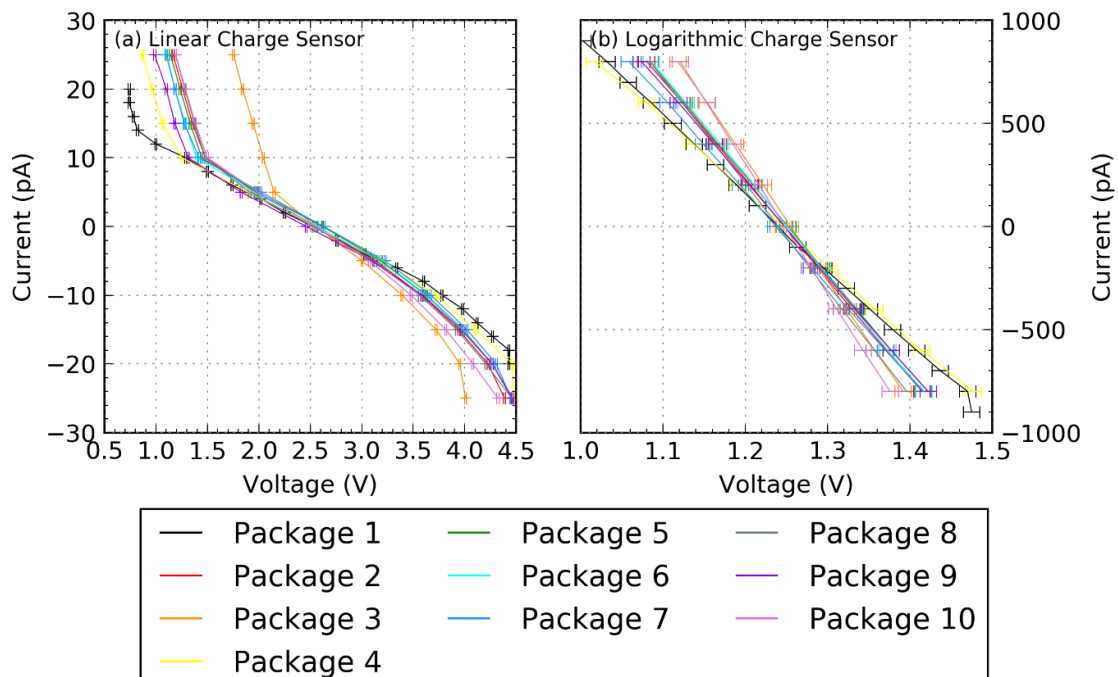


Figure 3-19: The calibration of the linear and logarithmic charge sensors for all ten radiosondes flown during this thesis. The error bars for each data point represent the 95% confidence limits (1.96-sigma).

appreciable RMSD, particularly for the linear charge sensor, emphasises the use of calibrating these sensors before use.

The space charge density, ρ can be calculated from the electrical current defined in equation 3-25,

$$\rho = -\frac{j}{A_{\text{eff}} \cdot \omega}, \quad 3-26$$

where A_{eff} is the effective area of the electrode ($A_{\text{eff}} = 0.0196 \text{ m}^2$ as defined by Nicoll, et al. (2018)) and ω is the ascent rate of the radiosonde (units = m s^{-1}). For this thesis, a series of small metallic bells were used for the electrode (see Figure 3-18). The purpose of having both linear and logarithmic sensors was to provide a wide range of charge detection capabilities. As the logarithmic sensor has a substantial temperature drift, the linear sensor was used to provide a relative calibration of the logarithmic sensor. Therefore, when the linear sensor becomes saturated, the logarithmic sensor can extend the measurement of charge.

The relative calibration of the logarithmic sensor is performed in five parts (see Figure 3-20 for an overview). First, the data is subset every 1 km in height, providing enough data points to be sampled. Second, the data is further subset into two groups: when the linear current is positive and negative. This is required as the electronic circuit controlling the measurement of the positive and negative logarithmic sensor respond separately. Third, the subsetted data is then binned into six equal element voltage bins and averaged to minimise the variations in the data. This is required as the linear and logarithmic sensors have different time responses when measuring charge. Fourth, two inverse one-standard error weighted least-squares linear regression models are calculated using the averaged data for both positive and negative subsetted datasets. Fifth, the coefficients from the regression model are then used to calibrate the positive and negative subsetted logarithmic charge sensor data. This process is repeated for each 1 km subsets of the charge sensor data. The addition of the logarithmic sensor was especially useful for ascents through charged cumuliform clouds, which typically saturated the linear sensor through the majority of the cloud (see §6.4 for examples).

3.5.3 Cloud Instrument

The cloud instrument is based on the design by Harrison and Nicoll (2014) which consists of four ultra-bright (100 cd) LEDs of different wavelengths along with a photodiode (VTB8440B, 580 nm peak response). The four LEDs consist of one cyan ((505 ± 5) nm), one yellow-orange ((590 ± 5) nm), and two infrared ((850 ± 5) nm) LEDs. The instrument works based on the backscatter. The light emitted from the four LEDs are reflected, from atmospheric particles or otherwise, and are

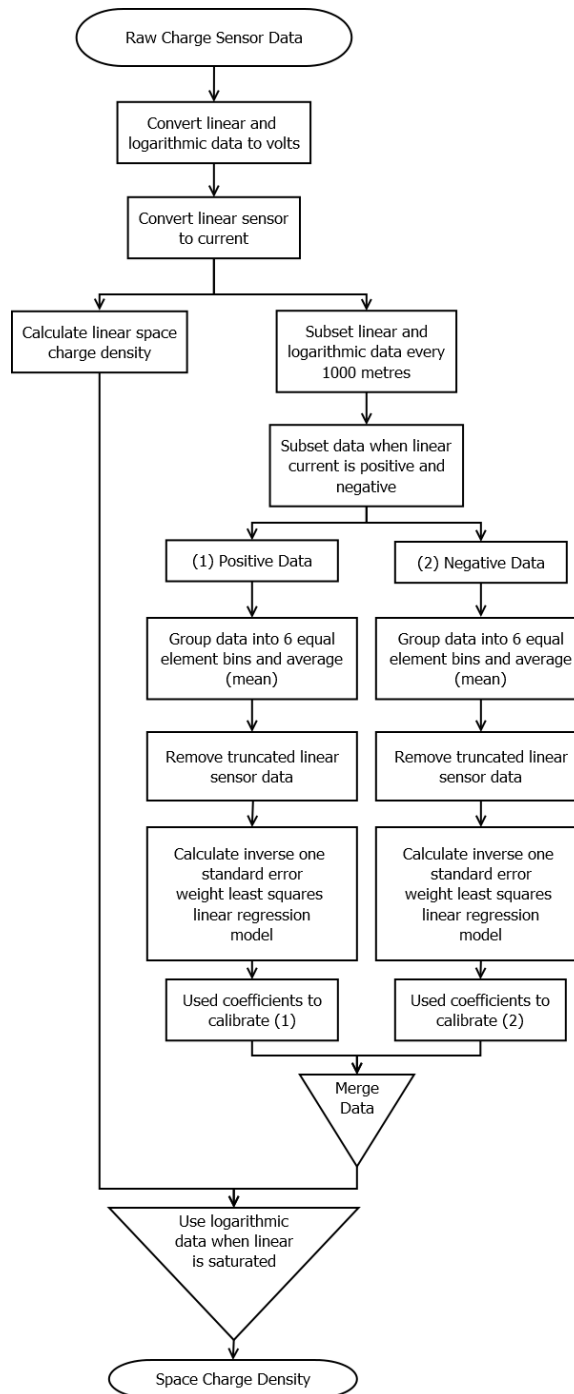


Figure 3-20: A flow diagram detailing the methods designed and used in this thesis to convert the raw charge sensor data to space charge density combining the linear and logarithmic charge sensors. The methods are based on the methods defined by Harrison et al (2017).

measured by a photodiode. As the size of the hydrometeor is sensitive to wavelength, the four LEDs can sample the hydrometeors, within the atmosphere, at distinct parts of the size distribution. For example, infrared is sensitive to smaller hydrometeors, while cyan is sensitive to larger hydrometeors.

The principle of this instrument is similar to both Radar and Lidar implementations, which works on the principle of backscatter, through Rayleigh and Mie scattering processes (Fabry, 2015a).

The backscatter is proportional to both the number concentration and size of the hydrometeors. Ultimately, it should be possible to derive the size and number concentration distributions with other sensors, but this is not within the scope of this thesis and is a task for future work. Therefore, only the backscatter (raw) voltage is used in this thesis and no processing was done to convert the data into physical units. Furthermore, only the infrared sensor is used as this uses the brightest LED and therefore produces the largest signal.

3.5.4 Turbulence Instrument

The turbulence instrument uses an ADXL325B accelerometer to measure movements in all three spatial dimensions (x, y, z) (Analog Devices, 2009). The accelerometer has an accuracy of $\pm 1\%$ and provides a typical measurement range of ± 5 g with a high resolution (5.75×10^{-3} g mV⁻¹) for observing turbulence within charged cumuliform clouds. This instrument has previously been used in several studies to observe turbulence within frontal clouds (Marlton, 2016). Only a single coordinate axis of the accelerometer was used to compensate for the low bandwidth of the radiosonde. The vertical dimension, z, was used as this dimension provided the greatest sensitivity to turbulent motions.

Calibration of the accelerometer was performed using the methods defined by Marlton (2016),

$$Acc_z = \frac{1}{95} (837 - 500 \cdot V_{z-axis}), \quad 3-27$$

where V_{z-axis} is the voltage from the z-axis of the accelerometer (units = V) and Acc_z is the acceleration along the z-axis (units = g) normalised by the standard acceleration of gravity (9.80665 ms⁻²).

An estimate of the turbulent kinetic energy eddy dissipation rate (ϵ_T) was made by Marlton, et al. (2015) using measurements of the accelerometer with respect to a lidar-derived ϵ_T . A linear regression model was derived from the relationship between the lidar and accelerometer,

$$\log_{10} \epsilon_T = (0.424 \pm 0.147) \cdot \sigma_{acc} - (3.73 \pm 0.357), \quad 3-28$$

where σ_{acc} is the standard deviation of the acceleration in the z-axis as defined by equation 3-27. To provide a suitable sample size, the standard deviation was calculated for each 200 m height subsets.

3.5.5 Supercooled Liquid Water Instrument

The supercooled liquid water (SLW) instrument is based on the design by Airey et al. (2017) and consists of a freely exposed vibrating wire (120 mm x 0.5 mm) controlled by a piezo transducer ((24 ± 2) Hz). The instrument works on the principle that any accumulation of mass on the

vibrating wire causes a reduction in the frequency of the oscillation. The rate of change in frequency is directly proportional to the amount of mass collected on the wire. The purpose of the instrument within this thesis was to detect the presence of SLW, which on contact with the vibrating wire freezes instantly causing the wire to rime (Mason and Dash, 2000). A phase-locked loop method was used to measure the frequency of the vibrating wire. The principle of this SLW instrument has been tested, showing an accurate determination of the amount of supercooled liquid water within mixed phased clouds (Serke et al., 2014).

A physical description relating the change in the vibrating frequency of the wire to the SLWC was defined by Serke et al. (2014) as,

$$\text{SLWC} = -\frac{2b_0f_0^2}{\epsilon_D D w f^3} \frac{df}{dt} \quad 3-29$$

where b_0 is the weight of the steel wire per unit length (units = g cm^{-1}), f_0 is the initial frequency of the wire before launch (units = s^{-1}), ϵ_D is the drop collection efficiency (unitless), D is the wire diameter (units = cm), w is the wind speed measured by the radiosonde (units = cm s^{-1}), f is the frequency of the wire (units = s^{-1}) and t is the time of each measurement (units = s). From equation 3-29, the SLWC is given in units of g cm^{-3} .

Most quantities in equation 3-29 can be determined from the dimensions of the wire (b_0 , D), the vibration of the wire (f_0 , f) and the measurements from the radiosonde (w , df/dt). The drop collection efficiency, ϵ_D is a function of the hydrometeor size and its mean velocity relative to the vibrating wire. For small droplet sizes ($< 20 \mu\text{m}$) and small mean velocities ($< 2 \text{ m s}^{-1}$), ϵ_D has a large rate of change (Lozowski et al., 1983). For larger droplet sizes and velocities, ϵ_D can be assumed constant. For this thesis, as the average radiosonde ascent speeds were around 5 m s^{-1} and the droplet sizes can be considered larger than $20 \mu\text{m}$ on average within a cumuliform cloud, ϵ_D can be assumed to be constant with a value set at 0.95 (Serke et al., 2014).

4 The Effects of Precipitation on the Local Atmospheric Potential Gradient

This chapter consists of seven parts. First, a discussion of the hypotheses is explored with the importance of understanding the influence of precipitation on the local potential gradient (PG) (§4.1). Second, the methods used to identify the overhead cloud type using solar radiation data is explored (§4.2). Third, two case study examples of how rain rate (RR) influences the PG at the surface and how the PG varies depending on the cloud type (§4.3). Fourth, the average relationship between RR and the PG , with sensitivity and robustness tests conducted on the relationship (§4.4). Fifth, to understand the variability between the PG and RR , the relationship was decomposed by cloud type to understand the importance of the cloud itself and the clouds influence on precipitation (§4.5). Sixth, the dependence of the surface conditions is examined to see if splashing at the surface is a primary source of space charge (§4.6). Seventh, a summary of all the results that have been shown (§4.7).

4.1 Introduction

In this chapter, the influence of precipitation on the PG near the surface was analysed to answer thesis question (1) discussed in §1.4. It is important to characterise the variability of the surface PG during precipitation, as precipitation can mask the influence of charge within the cloud. Another reason is to understand how precipitation relates to the development of a cumuliform cloud, which is useful for the prediction of lightning. On average, precipitation, charged precipitation, and corona are useful predictors for lightning (Bennett, 2018).

For this study, earlier research on the influence of precipitation discussed in §2.2 was used to form three hypotheses. From these hypotheses, further understanding of how precipitation influences the PG with the mechanisms that cause the PG perturbation was achieved. This study was used to answer the first question for this PhD, discussed in §1.4,

What are the effects of precipitation on the local potential gradient?

The RR was used in this chapter as it defines a flux of drops reaching the surface. Therefore, a relationship can be found to determine whether changes in precipitation influence the PG directly. The relationship between RR and the PG can be considered in three parts. First, how the drops can become charged from the cloud which they were precipitated. Second, the washout of radon by precipitation, bringing negative charge towards the surface. Third, the release of ions from the splashing of the drops against the surface. In the latter case, the drops can be considered either charged or uncharged (neutral), but in both situations, the force

applied to the drop once it encounters another object (i.e. the surface) can enable the release of ions into the atmosphere (Smith, 1951). The release of ions into the atmosphere can form space charge, ρ once attachment with atmospheric gases and aerosols occurs. The three hypotheses were developed to explore the variability of the influence of precipitation on the local PG and the mechanisms causing the perturbation:

1 The rain rate has an inverse relationship with the potential gradient measured at the surface

The charge present on precipitation is useful to characterise the amount of charge being transferred between the cloud and the surface. The amount of charge transferred was particularly useful for actively charging clouds such as cumulus and cumulonimbus (Ramsay and Chalmers, 1960). The relationship between precipitation and the PG were thought to be related by the intensity of rainfall (i.e. RR), but the mechanism of how the PG can be influenced by precipitation is not fully understood. Previous research has shown an inverse relationship between the PG and precipitation for RR s up to 40 mm h^{-1} (Simpson, 1949; Ogawa, 1960).

Decoupling the influence of precipitation on the PG has been a challenging area of research caused by the high variability of charge during precipitation, both within the cloud and near the surface. The lack of long datasets covering many rain events has been the main reason for the uncertainties in how precipitation influences the PG .

2 The cloud type has a negligible influence on the average relationship between rain rate and the potential gradient measured at the surface

Although the magnitude of the PG can be perturbed by the charge within the cloud, the higher frequency ($> 0.1 \text{ Hz}$) variability in PG is caused by charge closer to the surface (MacGorman and Rust, 1998). The main cause of PG variability includes variations in space charge and the ionisation of the surrounding air caused by corona and radioactive decay (Rycroft et al., 2012). The splashing of rain at the surface would also increase the PG variability. The PG variability caused by rain splashing is due to the proximity of the released ions with the surface, the variability in the advection of newly created space charge and the variability in RR in both time and space. To determine whether the cloud type is independent on the relationship between PG and RR , the data was subset into rain events, and each rain event was classified into broad cloud types (e.g. stratiform, cumuliform). These broad classifications increase the contrast between actively charging clouds

(cumuliform) and passively charging clouds (stratiform) from the conduction currents within the atmosphere (Nicoll and Harrison, 2016).

3 The relationship between rain rate and the potential gradient is dependent on the local meteorological and the dryness of the surface

The earliest research on how rainfall might influence the *PG* was related to the splashing of droplets against the surface, which tended to release negative ions into the atmosphere (Lenard, 1892). The splashing of rain droplets against the surface is hypothesised to influence on the *PG* at the surface, caused by the increased amount of space charge entering the atmosphere. An increase in space charge, caused by droplet splashing, could influence the *PG* near the surface due to its proximity. The proximity of space charge near the surface is related to the inverse square law applied to electric charges as defined by Coulomb's law (Chalmers, 1967; Griffiths, 1999b). Coupled with the creation of space charge caused by droplet splashing, the density of charge would be greater near the surface until another mechanism could disperse or neutralise the charge (e.g. wind).

Further research by Levin and Hobbs (1971), Ogawa (1960) and Smith (1955) has shown the charge released from splashing is dependent on the properties of the atmosphere and the surface. Changes in the *PG*, wind speed and impurities of the drop have all been observed to change both the polarity and magnitude of charge released from splashing. Other properties such as the low atmospheric pressure have been found to suppress the splashing process (Liu et al., 2010). The depth of water residing on the splashing surface was found to both suppress any splashing (< 0.5 mm) and allow positive charge, along with negative charge, to be released once the depth of water increased passed an undefined threshold (Harrison, 2013). The variations in meteorological and surface conditions are hypothesised to exist during precipitation.

In this chapter, precipitation data were collected from seven rain gauges from the Reading University Atmospheric Observatory (RUAO) and Chilbolton Observatory (CO) and *PG* data were provided by two JCI 131 electric field mills (FM) (Chilworth, 2016). Overall, 3 tipping buckets, 3 drop counters and 1 disdrometer were used to measure the relationship between *RR* and the *PG*. Further details are given in §3 on these instruments used in this chapter along with the data processing methods used to ensure the quality of the data was controlled. The longest available precipitation data, measured from a Delta-T tipping bucket located at the RUAO, was recorded as an analogue voltage rather than in a digital format. A top-down tip detection algorithm was designed for this thesis to interpret the Delta-T tipping bucket data and to retrieve the number

and timing of the tips within the dataset due to appreciable noise in the data. Sensitivity and robustness tests were used to ensure a valid relationship existed between the PG and RR (§4.4.2). The next section looks at cloud identification using solar radiation measurements, which was required to test hypothesis (2).

4.2 Cloud Identification using Solar Radiation Measurements

To identify the cloud type causing the precipitation measured at the surface, the Harrison et al. (2008) cloud identification (CI) algorithm was used as the cloud identification research was conducted at the RUAO. The method can differentiate between both stratiform and cumuliform cloud types and only requires a single measurement input (Figure 4-1). The CI algorithm uses solar radiation measurements to characterise the presence and thickness of a cloud overhead. During a cloudless fair-weather day, the global shortwave irradiance, S_g would only be attenuated by atmospheric gases and aerosols as solar radiation from the top of the atmosphere reached the surface. When a cloud is present, the path through the atmosphere is restricted, causing the solar radiation to scatter, reducing S_g . The diffuse solar irradiance, S_d increases with the amount of cloud covering the sky. The combination of S_d and S_g was used to estimate the amount and depth of the cloud. The CI algorithm uses the mean and standard deviation of the diffuse fraction, DF defined as

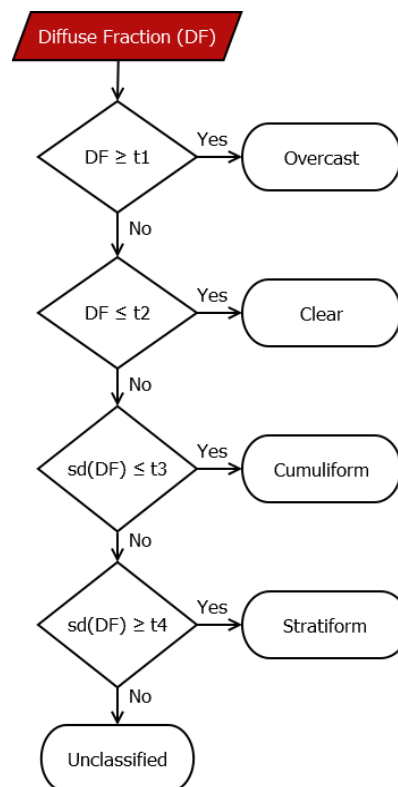


Figure 4-1: A flow diagram depicting the cloud identification algorithm. The magnitude of the diffuse fraction (DF) defines the amount of cloud within the vicinity of the detector. The variability of DF defines the height of the cloud allowing a distinction between cumuliform and stratiform clouds. Threshold values for each decision block are $t_1=0.9$, $t_2=0.3$, $t_3=0.05$ and $t_4=0.1$ (adapted from Harrison, et al., 2008).

$$DF = \frac{S_g}{S_d}. \quad 4-1$$

One of the main differences between cumuliform and stratiform clouds is their physical dimensions. In relative terms, stratiform has a large swath and small depth; cumuliform has a small swath and a large depth. Therefore, under these broad classifications of cloud type, it was possible to identify the overhead cloud type.

The CI algorithm needs a fifteen-minute sample to provide enough data to calculate the mean and standard deviation statistics. The algorithm can classify the clouds into five groups; clear, overcast, stratiform, cumuliform and unclassified. When the diffuse fraction is between 0.3 and 0.9 the depth of the cloud was used to specify whether the cloud is stratiform or cumuliform. Otherwise, only broader assumptions about the amount of cloud can be made. The methods used to define a stratiform and cumuliform cloud are broad and only provides an estimate of the cloud type. Another limitation of the CI algorithm is the Sun needs to be above a certain elevation angle (8.3° for the RUAO), above the horizon, before enough global and diffuse radiation could be measured. These limitations were considered for the analysis conducted in this study. The next section looks at two case study examples of rain events, highlighting the changes in the *PG* coupled with the synoptic-scale meteorology.

4.3 Case Studies

To understand how the *PG* varies during a rain event, two case studies were examined showing the differences between stratiform and cumuliform precipitation along with the capabilities of the CI algorithm.

4.3.1 Single Rain Event: 2009/11/01

The first case study examines a single rain event that occurred on 2009/11/01. The surface pressure analysis (Figure 4-2a) showed a low-pressure system moving across the UK on the morning of 2009/11/01 moving along an easterly trajectory. The low-pressure system (980 hPa) brought three frontal systems (warm, upper-level occlusion and a cold front), with its trajectory favourable for comparing observations between the RUAO and CO which are 48.0 km apart. A satellite image of Western Europe (Figure 4-2b) was taken at 0912 UTC using the advanced very-high-resolution radiometer (AVHRR) aboard the NOAA-17 satellite (NOAA, 2017). The near-infrared (0.725-1.100 μm) satellite image shows a large band of cloud covering the entire UK

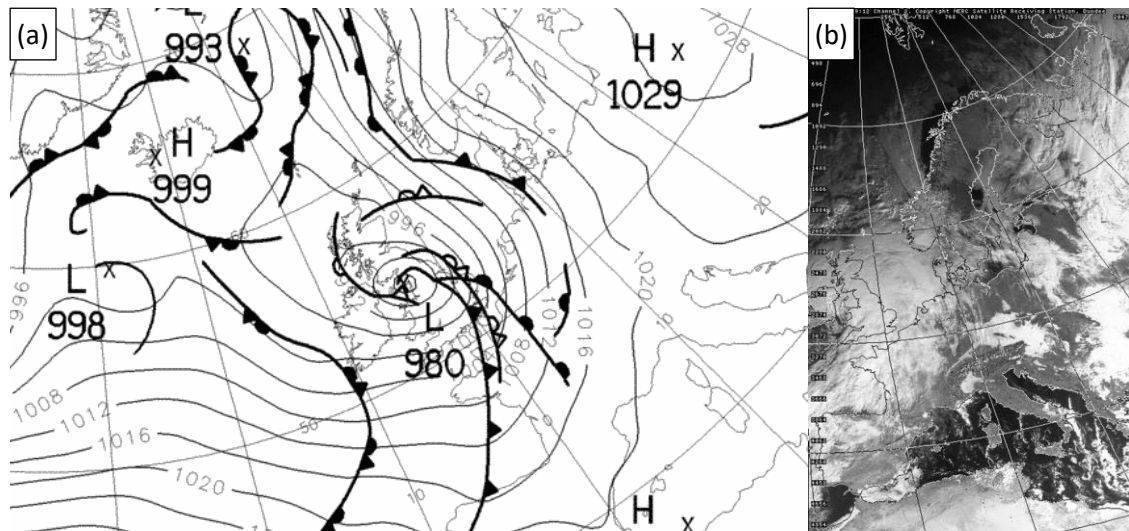


Figure 4-2: The synoptic conditions during the cases study on 2009/11/01. (a) The United Kingdom Met Office (UKMO) surface pressure analysis charts on 2009/11/01 1200 UTC (courtesy of www.wetter3.de/fax). (b) A near-infrared (0.725-1.100 μm) satellite image was taken at 2009/11/01 0912 UTC over western Europe. The image was taken using the advanced very-high-resolution radiometer (AVHRR) aboard the NOAA-17 satellite [courtesy of NERC Satellite Receiving Station, Dundee University, Scotland (NEODAAS-Dundee, 2018)].

consistent with the surface pressure analysis. The homogenous covering of the cloud in the satellite image²⁰ suggests the cloud depth was uniform over Reading, UK.

The radar reflectivity (Z) measured at CO was consistent with the observations by the satellite (Figure 4-3). The cloud top as measured by the radar was around 11 km and was mostly uniform for the entire passing of the low-pressure system, agreeing with the satellite measurements. Three distinct regions of high Z (> 20 dBZ) were observed below the freezing level (3.3 km). The three regions of high Z (0500-0630 UTC, 0700-0900 UTC and 0930-1130 UTC) coincides with the RR measured by the disdrometer at CO. The same grouping of RR was seen at the RUAO (0600-0730 UTC, 0800-0930 UTC, and 1000-1200UTC) between 30 and 60 minutes after being measured at CO. The time delay suggests the movement of the cloud followed a westerly trajectory, typical of Atlantic weather systems, consistent with the surface pressure analysis given in Figure 4-2a.

Figure 4-4 shows a timeseries of the PG and times the tipping bucket tipped (a) along with the cloud type detected using the CI algorithm (b). Overall, 10.2 mm of precipitation (51 tips) was measured from the Delta-T tipping bucket rain gauge (using the top-down algorithm) over a period of 6 hours between 0400 and 1200 UTC (Figure 4-4a). There were noticeable negative perturbations on the PG during the rain event with a single polarity inversion at 1000 UTC. The polarity inversion at 1000 UTC is a common feature in the PG defined by the passing of a charged

²⁰ Homogenous cloud cover is represented by negligible changes in the near infrared. In Figure 4-2b, the colour of the pixels does not change for most of the UK. A noticeable exception is over South-East Wales where the cloud appears darker suggesting shallower cloud.

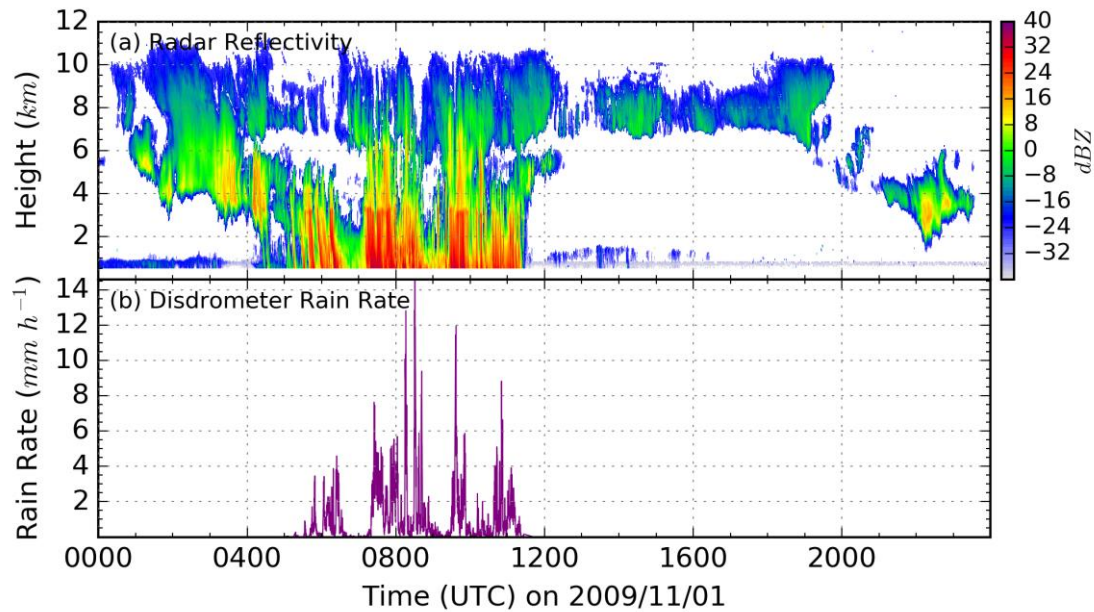


Figure 4-3: The radar reflectivity (a) from the 35 GHz Copernicus radar and the Disdrometer (b) located at Chilbolton Observatory, UK on 2009/11/01.

convective cloud (in this case, a negative dipole), while the negative perturbations were caused by the abundance of negative space charge closer to the surface. Before 0600 UTC, the PG resembled the characteristics of a fair-weather day, with little perturbation from its idle state ($\approx 100 \text{ V m}^{-1}$). There was a transition in the PG at the time of the first tip (0611 UTC) where the PG decreased steadily, passing zero until the rainfall intensity increased at 0753 UTC. As the rainfall intensity increased after 0753 UTC, the PG decreased further, and the PG variability increased. The rainfall intensity decreased again at 0900 UTC, coinciding with the PG increasing and the PG variability decreasing. After the polarity inversion caused by the charged cloud at 1000 UTC, the rainfall intensity became less varied, as does the variability in the PG . The few dips in the PG at 1105 and 1148 UTC could be caused by sudden changes in RR , wind speed or wind direction. At 1157 UTC the last tip was detected, but the PG carried on increasing steadily until 1300 UTC when the magnitude and variability resembled the fair-weather like state again.

The sunset and sunrise occurred at 0657 and 1637 UTC, respectively (vertical dashed blue lines in Figure 4-4b). The first two tips were measured before sunrise and no identification of the cloud type was possible. After sunrise, the CI algorithm initially detected clear skies. As the identification occurred only 15 minutes after sunrise, the sun was too close to the horizon and ground clutter (e.g. trees, buildings) blocked direct measurement of the sun. After the first clear-sky identification, stratiform clouds followed by overcast conditions were identified. The overcast conditions were caused by a stratiform cloud covering the entire sky. The polarity inversion at 1000 UTC indicates charge-separating permitting convection occurred during the rain event.

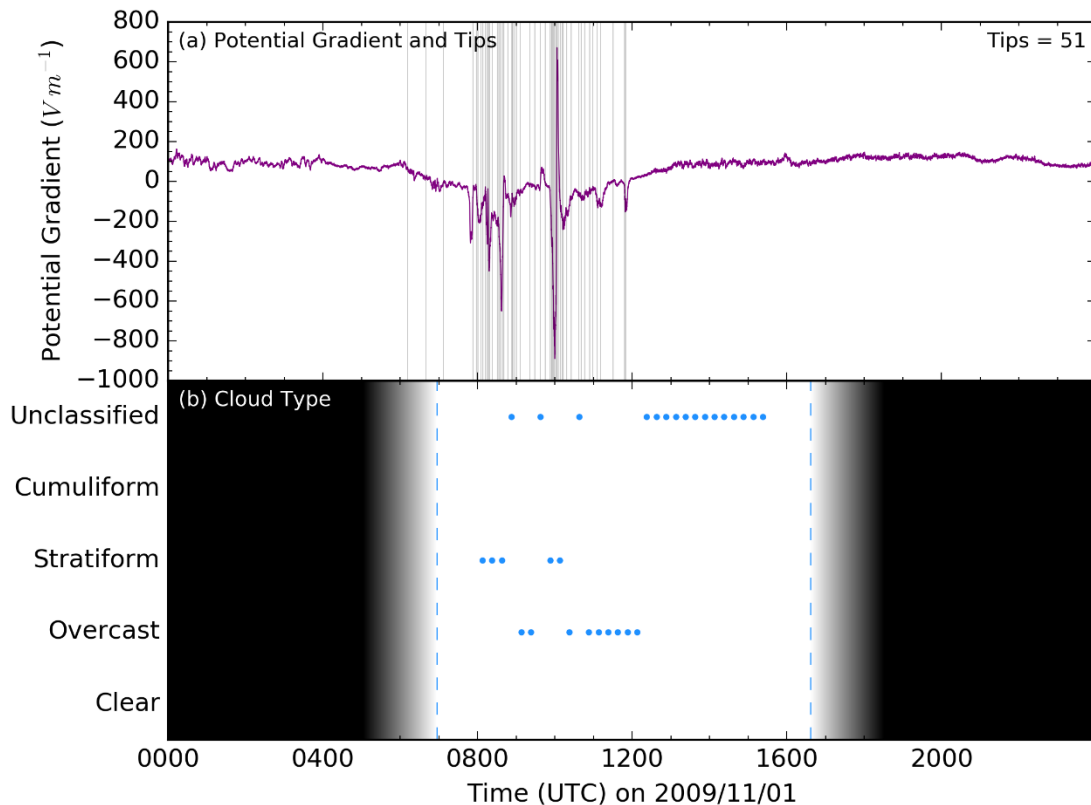


Figure 4-4: A time-series of (a) the PG (purple), tipping bucket tip times (grey) and (b) the cloud type (blue points) measured at the RUAO using CI algorithm on 2009/11/01 with the solar cycle (black shading). Each cloud type point occurs every fifteen minutes. The sunrise and sunset times (blue dashed line) occurred at 0657 and 1637 UTC, respectively.

Figure 4-5 shows a scatterplot of the relationship between PG and RR . The median PG was calculated between each tip of the tipping bucket rain gauge and compared with the RR calculated between each tip. During the rain event, 51 tips were found with RR s between 0.26- and 14.7- mm h^{-1} . There was a weak negative trend in the PG with respect to the RR ($r = -0.388$) consistent with the observations from Figure 4-4. An ordinary least-squares linear regression model and a lowess²¹ function (Cleveland, 1993) were calculated using the data in Figure 4-5. The linear regression showed a weak statistically significant negative relationship ($p = 0.0053$, $SE = 8.9369$). The lowess function is consistent that a negative trend exists, which for low RR s ($< 5 \text{ mm h}^{-1}$) is linear. For most RR s, even close to zero, the PG remained negative. The single outlier with a PG of 550 V m^{-1} captured the charged cloud at 1000 UTC, which caused a polarity inversion in the PG . The relationship is also heteroskedastic²² as the variability in PG increases with RR . Using the Goldfeld-Quandt test, the null hypothesis that the relationship was homoscedastic could be rejected ($F = 20.09310$, $p < 0.001$). This suggests the relationship is not

²¹ The lowess function is a locally weighted smoothing function, which use non-parametric regression models to smooth the data. Lowess is useful for seeing trends in highly scattered data.

²² Heteroskedastic is defined as when the variance is a function of the independent variable (i.e. the variance increases with RR).

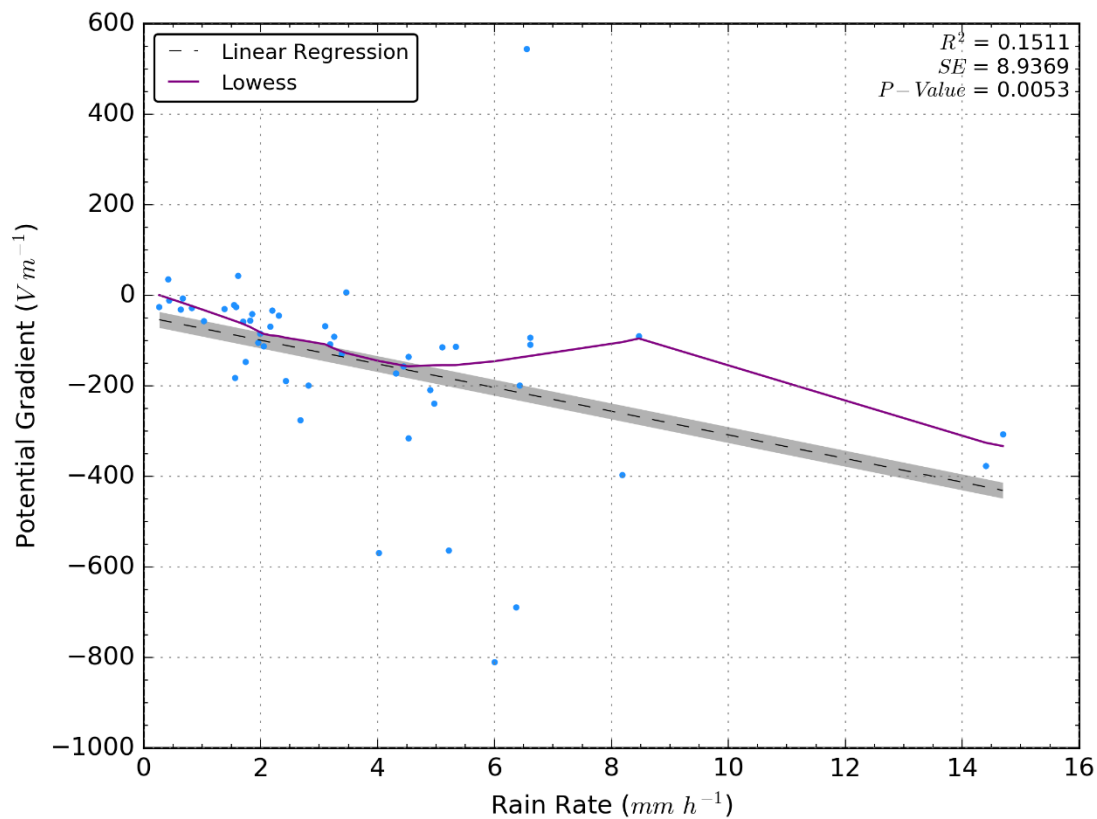


Figure 4-5: The relationship between the potential gradient and rain rate measured at the RUAO on 2009/11/01. The linear regression (black dashed line), 95% confidence interval (grey), and the lowess function (purple) have been calculated for the relationship.

causal and dependent on other conditions, such as the charge in the cloud. The non-causality of the relationship between PG and RR is evaluated in §4.5 and §4.6.

Overall, a decrease in PG , from its fair-weather state, was seen when precipitation was measured at the surface (Figure 4-4). The magnitude and variability of the PG are closely related to the intensity of precipitation measured at the surface. As the RR increases, the PG was found to decrease, below 0 V m^{-1} , and the variability in the PG also increases substantially once the RR passes a critical threshold.

4.3.2 Multiple Rain Event: 2016/05/11

The second case study examines four rain events that occurred during a single day at the RUAO on 2016/05/11. Comparisons of the surface pressure analysis (Figure 4-6), satellite images (Figure 4-7) and Z measured at CO (Figure 4-8) showed several occluded and warm fronts passing over the RUAO and CO between 0030 and 1230 UTC. Figure 4-9 shows a timeseries of the PG and times the tipping bucket tipped (a) along with the cloud type detected using the CI algorithm (b). Overall, 22.4 mm of precipitation (112 tips) was measured by the EML tipping bucket rain gauge over a period of 16 hours between 0100 and 1700 UTC. Four separate rain events were identified from the rain gauge data (0050 – 0734 UTC, 1138 – 1249 UTC, 1412 – 1427 UTC, and

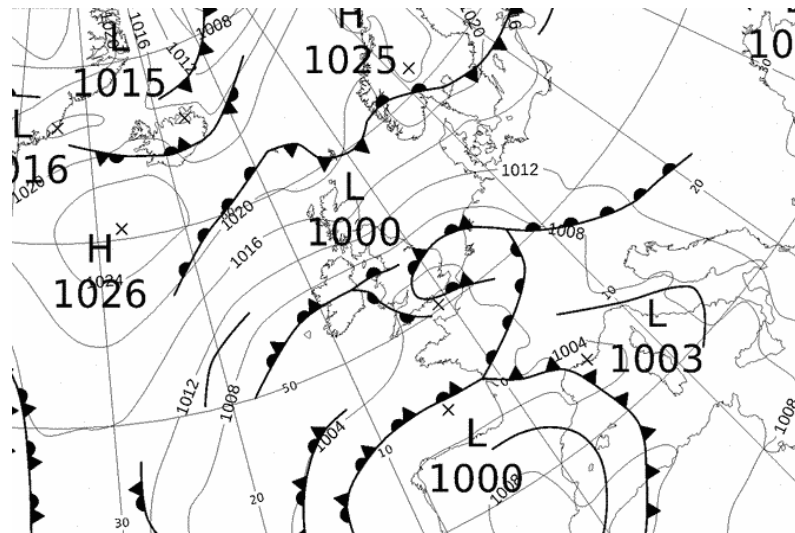


Figure 4-6: Same as Figure 4-2a but on 2016/05/11 0600 UTC.

1629 – 1657 UTC), which were caused by different synoptic scale features leading to different meteorological conditions at the surface. Appreciable cloud electrification within these fronts would cause the *PG* perturbations observed at the RUAO.

The first rain event (0050 – 0734 UTC) has a complex *PG* structure causing the FM to saturate at the negative polarity. The length of the rain event (404 minutes) coincided with a frontal system (Figure 4-6), like the earlier case study discussed (Figure 4-4). The *RR* varied substantially during the rain event with the boundaries of the frontal system having the greatest *RR*. The complex structure of the *PG* highlights the difficulty in decoupling the influence of precipitation on the *PG*. Here the charge within the cloud is the primary influence on the *PG*.

The second rain event (1138 – 1249 UTC) has a simpler *PG* structure and the strong perturbations were caused by the electrification of the overhead cloud. The satellite image in Figure 4-7a provides the most comparable conditions to the second rain event. As the thermal-infrared wavelength is sensitive to cloud depth²³, the two clear bands in Figure 4-7a show clouds with distinctly different cloud depths. A consistent observation was seen in *Z* measured at CO, with a clear distinction between clouds at 0930 UTC caused by the differences in cloud depth (Figure 4-8). Despite the small distances between the RUAO and CO, there were appreciable differences in meteorology seen between the two locations caused by the angular trajectories of the synoptic meteorology.

The third rain event (1412 – 1427 UTC) was the smallest event in this case study and consisted of a single *PG* perturbation caused by a charged cumulus cloud. The radar observations at CO

²³ The depth of the cloud is proportional to the strength of the return signal, so the brighter the pixels in the image, the greater the depth of the cloud.

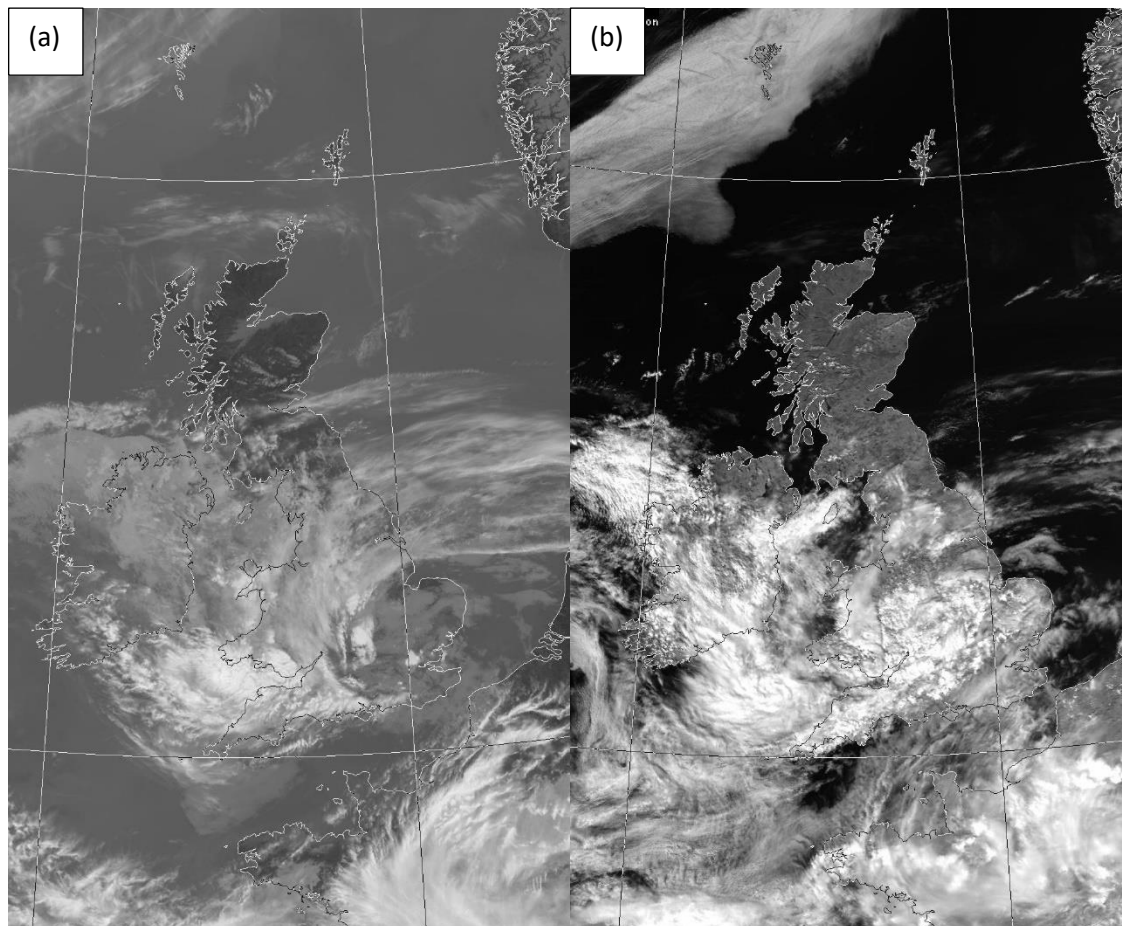


Figure 4-7: Same as Figure 4-2b but for (a) thermal-infrared ($10.3\text{--}11.3\ \mu\text{m}$) taken at 1011 UTC and (b) near-infrared ($0.725\text{--}1.100\ \mu\text{m}$) taken at 1434 UTC.

showed a series of small cumulus clouds passing overhead during the early afternoon, with evidence of convection during the early afternoon. The satellite image shown in Figure 4-7b shows a heterogeneous layout in the cloud structure, with groups of clouds being banded together in the Southeast of England. The *RR* being measured at the RUAO and CO is characteristic of convective rainfall. Convection was weak in the Southeast ($\text{CAPE} = 33.41\ \text{J kg}^{-1}$, $\text{CIN} = -8.72\ \text{J kg}^{-1}$, $\text{LI} = 1.18\ ^\circ\text{C}$)²⁴ as measured by the Larkhill radiosonde station (03743) at 0900 UTC (University of Wyoming, 2018). A lifting index²⁵ (LI) below $0\ ^\circ\text{C}$ is typically needed for convective clouds to develop. CAPE below $100\ \text{J kg}^{-1}$ would be unable to lift moist surface parcels to a high altitude before reaching the equilibrium temperature of the atmosphere. Although convection was seen in the radar data, the *RR* was below $1\ \text{mm h}^{-1}$. Low *RR* suggests the cloud was not in its mature life stage despite the large *PG* perturbations measured for these clouds.

²⁴ CAPE = Convective Available Potential Energy, CIN = Convective Inhibition, LI = Lifting Index.

²⁵ The lifting index defines the atmospheric instability. It is calculated by finding the temperature difference between the environment and an air parcel lifted adiabatically from the surface to 500 hPa. Temperatures less than $0\ ^\circ\text{C}$ are considered unstable with colder temperatures increasing the probability for thunderstorms to occur.

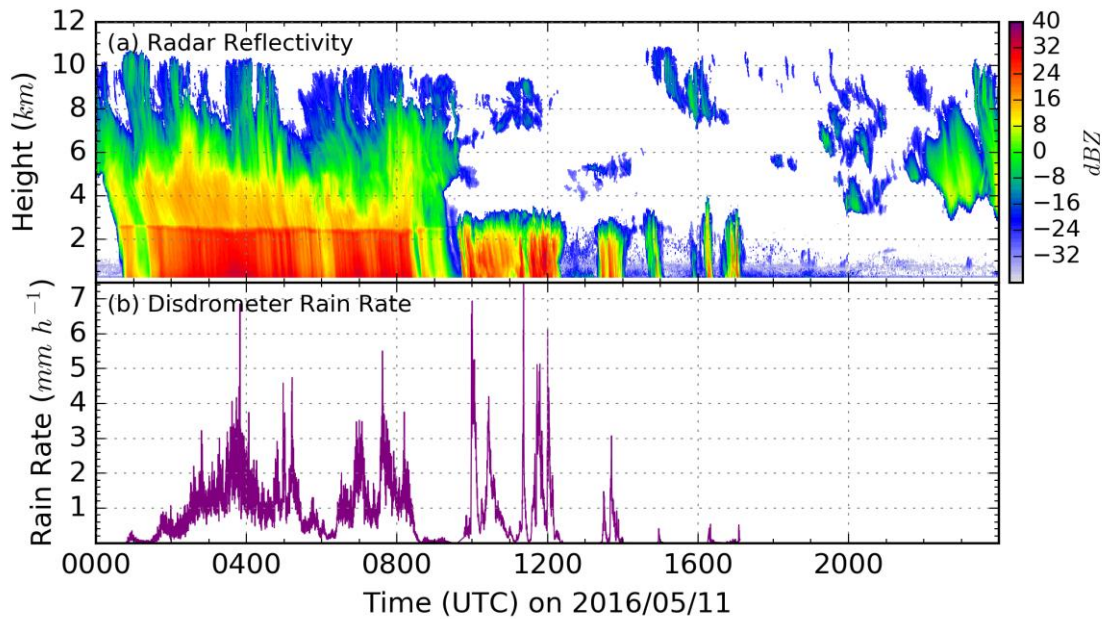


Figure 4-8: Same as Figure 4-3 but on 2016/05/11.

The fourth rain event (1629 – 1657 UTC) was comparable to the third rain event with a single charged convective cloud being measured. The RR for this event was much greater (32.1 mm h^{-1}) and the influence of precipitation was more pronounced in the PG at the RUAO. A closer inspection of the PG between the third and fourth rain events (Figure 4-10) shows a similar PG perturbation caused by the charged cloud overhead, but differences in the small-scale variability. After the positive peak in PG (Figure 4-10b), the falling edge consisted of small PG perturbations related to the time of intense precipitation measured by the EML tipping bucket. The PG perturbations caused by the smaller RR s observed in the third rain event was negligible compared to the perturbation of the cloud.

The high-frequency perturbations caused by precipitation are often masked by the charge within the cloud. When the PG is substantially perturbed by the charge within the overhead cloud, the influence of the precipitation can only be observed near the turning points in the PG . At the turning points, the influence of the charge within the cloud on the PG reaches a minimum and the smaller and faster-varying charge closer to the surface (e.g. space charge, corona) can influence the PG again. This was seen in rain events three and four at 1420 and 1630 UTC respectively (Figure 4-10).

The cloud type identified by the CI algorithm suggested overcast conditions occurred for most of the day with the exception of clear skies between 0500 and 0900 UTC. The satellite images from Figure 4-7 shows appreciable cloud cover over the UK for most of the day. The CI algorithm was unable to decouple the cloud type (stratiform or cumuliform) from the overcast conditions with frontal and cumulus clouds being identified as overcast. Both cloud types have vastly

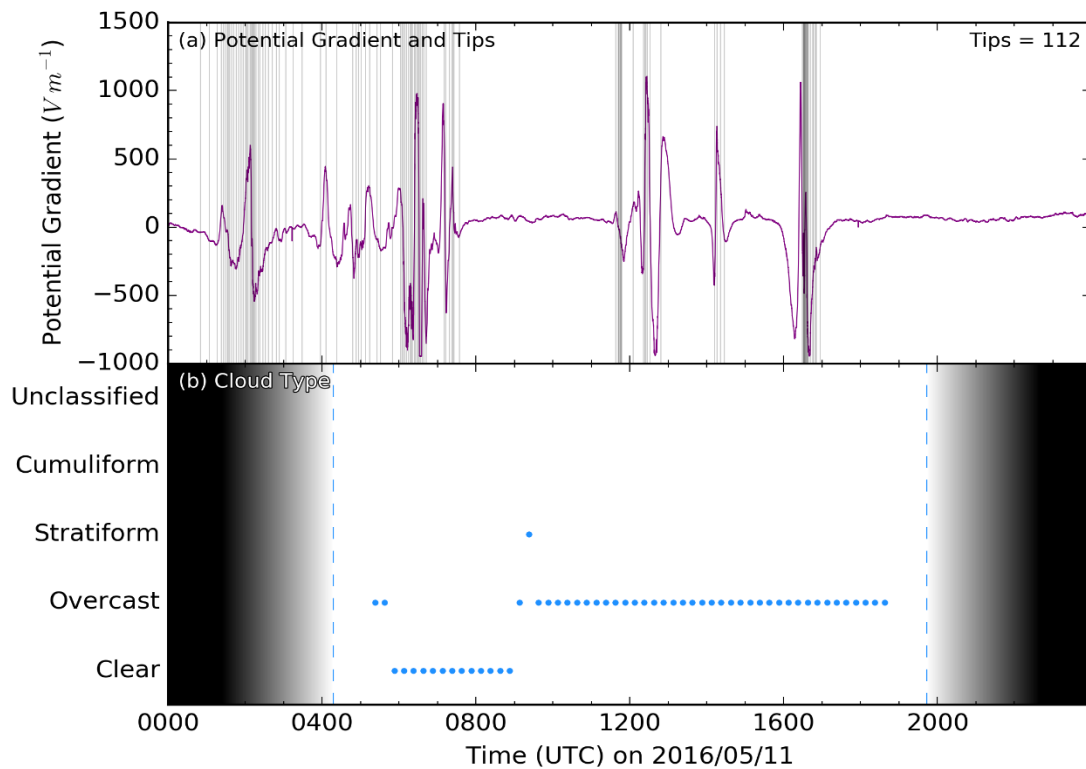


Figure 4-9: Same as Figure 4-4 but on 2016/05/11 with sunrise and sunset times occurring at 0417 and 1944 UTC respectively. The time of the four rain events analysed are 0050 – 0734 UTC, 1138 – 1249 UTC, 1412 – 1427 UTC, and 1629 – 1657 UTC.

different geometries and influence the *PG* differently. Cumuliform clouds can perturb the *PG* much greater than stratiform clouds, on average, and are usually well defined by the *PG*. Frontal clouds typically have a wide horizontal and vertical extent and are often homogenous in depth, *Z* and *RR*. The influence of frontal clouds on the *PG* is often more complex than from single-celled cumuliform clouds. The complex structure can be seen for rain event 1 compared to a cumulus cloud in rain event 3 (Figure 4-9).

Figure 4-11 shows a scatterplot of the relationship between *PG* and *RR*. The same methods were used to average the *PG* from the earlier case study (§4.3.1). In this case study, a greater number

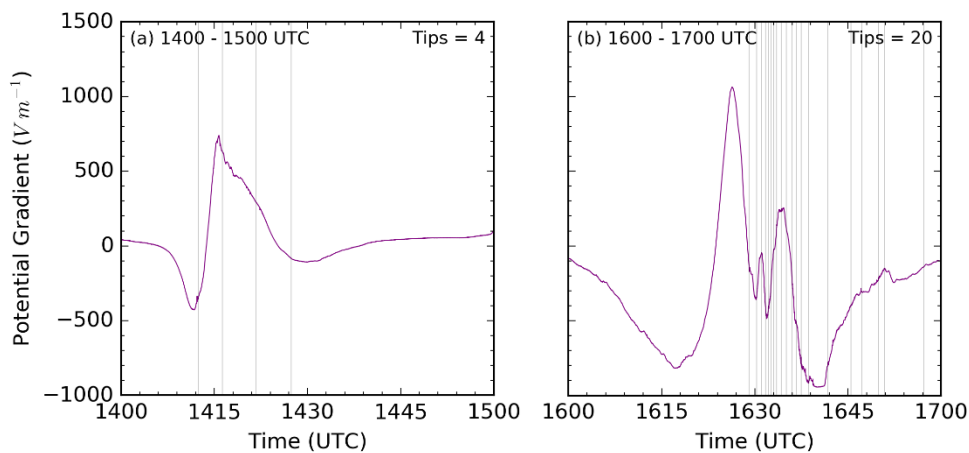


Figure 4-10: A zoomed in time-series of the PG (purple) and, tipping bucket tip times (grey) between (a) 1400-1500 UTC and (b) 1600-1700 UTC.

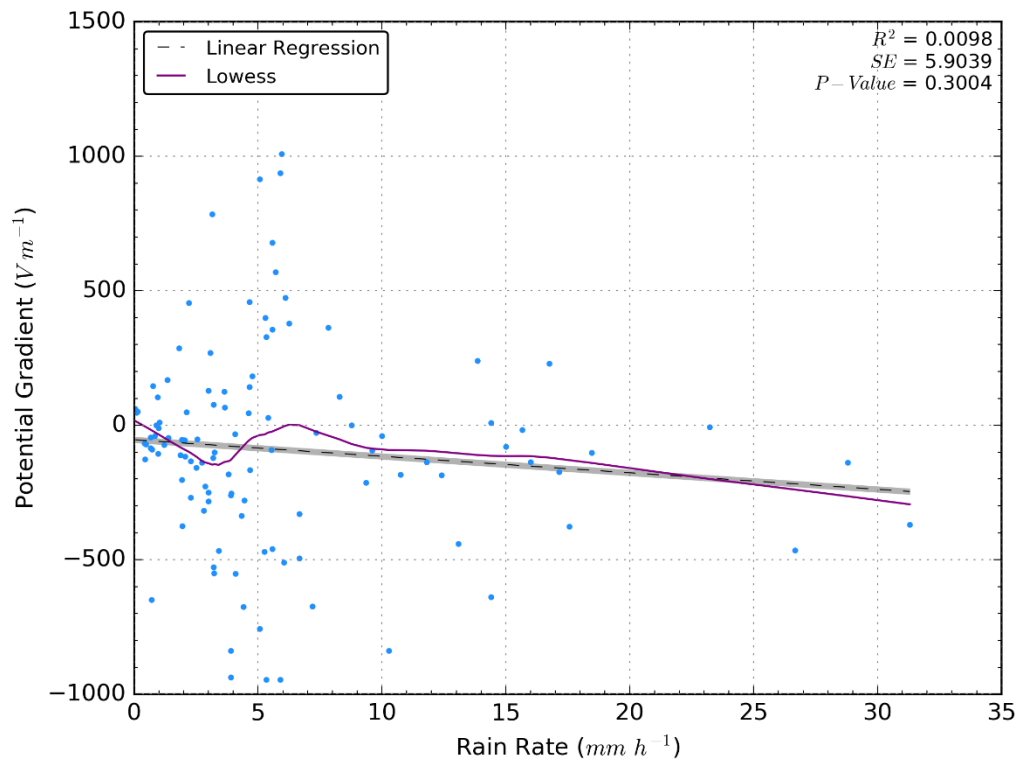


Figure 4-11: Same as Figure 4-5 but on 2016/05/11.

of data points were available for comparison (112 tips), but the spread of the scatterplot was much greater reaching $\pm 1 \text{ kV m}^{-1}$ (maximum range of FM). The range of RR s measured during this case study was also much greater ($0.049 - 31.2 \text{ mm h}^{-1}$) which provides a good predictor for charged cumuliform clouds (Bennett, 2018). An ordinary least-squares linear regression model and lowess function were calculated between PG and RR and showed a negative trend for all RR s. The regression model suggested the relationship was not statistically significant ($p = 0.300$, $r = 0.099$) as the scatter was caused by the charge within the clouds perturbing the PG at the surface. RR s less than 8 mm h^{-1} showed the greatest variability in the relationship. The relationship was found to be heteroskedastic using the Goldfeld-Quandt test ($F = 2.75334$, $p < 0.001$). The heteroskedastic relationship is a result of charged convective clouds, which produce higher RR s while uncharged stratiform clouds produce smaller RR s. Therefore, the heteroskedastic part of the PG and RR relationship is not causal and is an artefact of the cloud type, consistent with observations given in this case study.

4.4 Long-Term Statistical Study

The two case studies (§4.3) showed a negative relationship existed between PG and RR on average. Each case study showed substantial variability in their relationship, which can be attributed mainly to the charge present within overhead cumuliform clouds. A method to understand the direct influence of precipitation on the PG was to combine multiple rain events

together to average out the variability caused by any charged clouds. All the data available for each instrument at the RUAO and CO were used to represent the average relationship between *PG* and *RR* (see Figure 3-2 for data availability).

4.4.1 Average Relationship

A moving median was used to estimate the relationship between *PG* and *RR* to minimise the variability caused by charged clouds. A moving median improves the resolution of the relationship, minimises variability and is less susceptible to extreme values in the data. Figure 4-12 shows the median relationship between the *PG* and *RR* for seven rain gauges from the RUAO and CO²⁶. The two tipping buckets at the RUAO were combined due to their similar design, as well as neither instrument existed concurrently. The relationship was comparable for all rain gauges with the *PG* decreasing for small *RRs* ($< 5 \text{ mm h}^{-1}$) with the lowest *PG* found to exist between 4- and 6- mm h^{-1} . The relationship between the *PG* and *RR* for all rain gauges is non-linear and has a similar structure, particularly for the tipping buckets and disdrometer, coinciding within the 95% confidence limits of each rain gauge. The confidence limits for the CO rain gauges were weaker than the RUAO rain gauges caused by the smaller number of data points available. There is approximately a 5:1 ratio in the length of data available. The wide confidence limits were prominent in the CO tipping bucket but showed a comparable relationship observed by the RUAO tipping bucket.

The influence of precipitation on the *PG* is relative to the fair-weather *PG* value at the RUAO and CO. As the fair-weather *PG* between the RUAO ($(85.7 \pm 0.009) \text{ V m}^{-1}$) and CO ($(91.5 \pm 0.024) \text{ V m}^{-1}$) differs, an offset was required for a fair comparison between the different rain gauges. The difference in fair-weather *PG* was associated with differences in the environment between the RUAO and CO as both FMs are identical in design and were calibrated with respect to each other. At CO, the topography is extremely flat ($< 0.5 \text{ m}$ elevation change) while at the RUAO the instrument is located on a small hill ($> 3 \text{ m}$ elevation change). Other causes for the difference in *PG* include natural (e.g. trees), and artificial obstructions (e.g. fences, buildings). At the RUAO, the FM is located near barbed-wire fences at a height of 3 metres with other instruments nearby; the most noticeable is the 10-metre mast for measuring wind speed. At CO, there were fewer instruments acting as obstructions, but greater natural obstructions such as small trees and shrubs.

²⁶ For the Delta-T tipping bucket, the top-down algorithm was used to determine the timing of the tips in the data. Further tests using the Delta-T tipping bucket data is conducted to ensure validity in their results. This was achieved through comparison of the relationship between the *PG* and *RR* using the other six rain gauges.

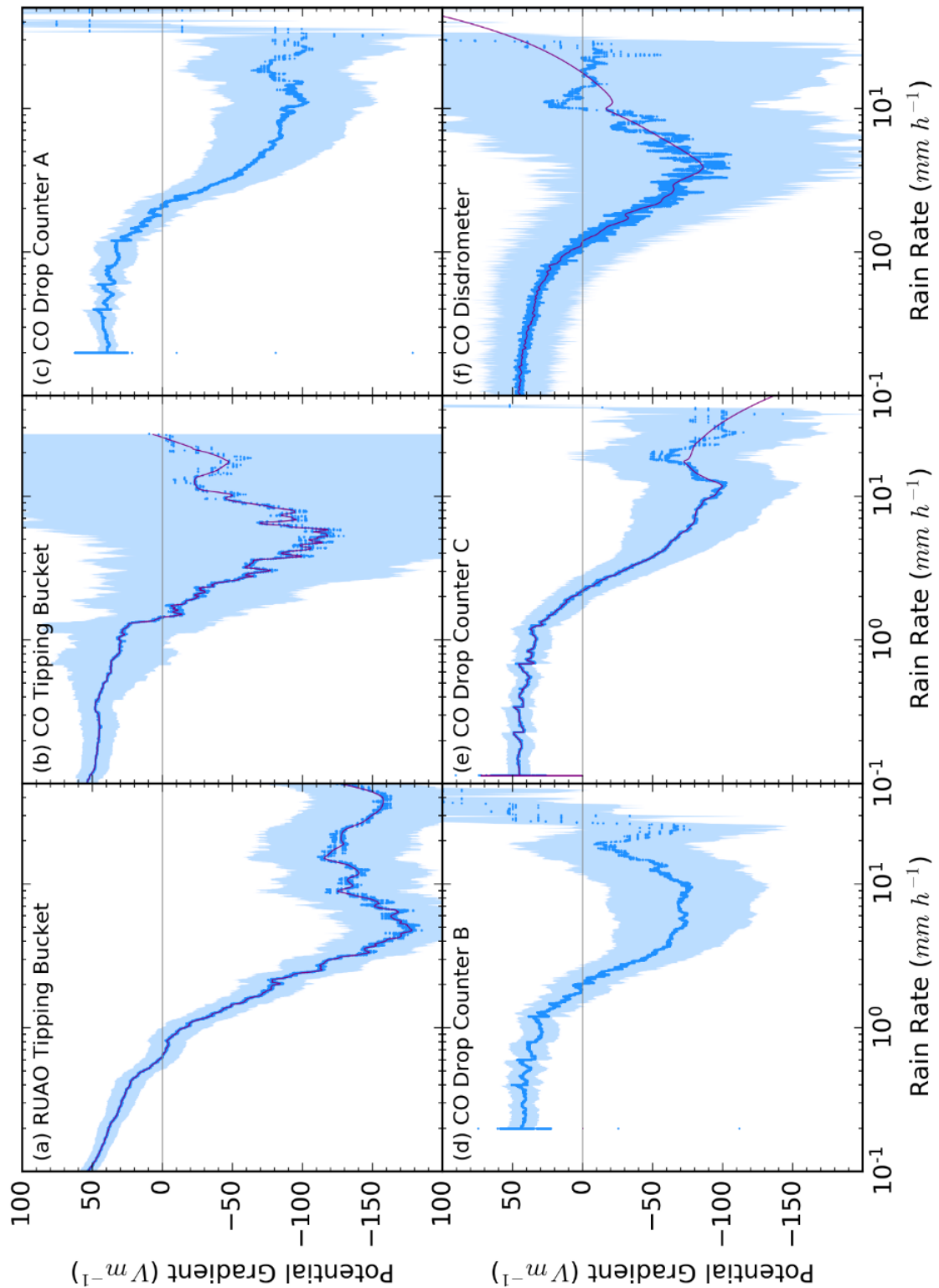


Figure 4-12: A moving median (blue points) between the PG and RR for all seven rain gauges at the RUAO and CO. The rain gauges were (a) RUAO tipping bucket, (b) CO tipping bucket, (c) CO drop counter A, (d) CO drop counter B, (e) CO drop counter C and (f) CO disdrometer. The data from the Delta-T and EML tipping buckets were combined in (a). The 95% confidence intervals (blue shading) and lowess (purple solid line) were added to the data. The zero lines (grey) were added to emphasise the polarities of charge.

In Table 4-1, the details of the relationship between the *PG* and *RR* for all seven rain gauges are given. For all rain gauges, the minimum *PG* was comparable ($-168.5 - -75.4 \text{ V m}^{-1}$) along with the *RR* at the minimum *PG* ($3.9 - 5.8 \text{ mm h}^{-1}$) assuming drop counters A and C were outliers. The initial rate of change ($< 5 \text{ mm h}^{-1}$) represents the increase of negative charge with respect to the *RR*. All rain gauges are comparable on the initial rate of change, ranging from -45.7 to $-28.8 \text{ V m}^{-1}/\text{mm h}^{-1}$. After the turning point (around 5 mm h^{-1}), there was a steady increase in the *PG*, common for most rain gauges, ranging between 0.1 and $3.6 \text{ V m}^{-1}/\text{mm h}^{-1}$. An ordinary least-squares linear regression model was used to calculate the rate of change for each rain gauge and was found to be statistically significant throughout ($p < 0.0001$).

Overall, for light precipitation ($< 5 \text{ mm h}^{-1}$) a negative perturbation of the *PG* was observed suggesting negative charge was dominant near the surface, while for heavier precipitation ($> 5 \text{ mm h}^{-1}$) the perturbation decreases, caused by either an increase of positive charge into the atmosphere, or from the washout of negative charge. These hypotheses are consistent with previous research on drop dynamics and the dependencies of the surface (Smith, 1955; Scrase, 1938; Ogawa, 1960). The summary statistics about the rain patterns and associated *PG*, which were observed at the RUAO between 2006 and 2018, can be found in Table 4-2.

Table 4-1: Details of the relationship between the *PG* and *RR* for all seven rain gauges at the RUAO and CO

Location	Rain Gauge	<i>PG</i> at 0 <i>RR</i> (V m^{-1})	Minimum <i>PG</i> (V m^{-1})	<i>RR</i> at Minimum <i>PG</i> (mm h^{-1})	Initial Rate of Change ($< 5 \text{ mm h}^{-1}$; $\text{V m}^{-1}/\text{mm h}^{-1}$)	Final Rate of Change ($> 5 \text{ mm h}^{-1}$; $\text{V m}^{-1}/\text{mm h}^{-1}$)
RUAO	<i>Tipping Bucket</i>	65.7 ± 6.0	-165.1 ± 55.5	4.6 ± 0.0	-45.7 ± 0.1	1.3 ± 0.0
	<i>Tipping Bucket</i>	86.0 ± 1.5	-168.5 ± 223.9	5.8 ± 0.0	-42.2 ± 0.3	3.6 ± 0.3
CO	<i>Drop Counter A</i>	62.6 ± 3.4	-101.7 ± 56.0	11.0 ± 0.0	-32.5 ± 0.1	2.3 ± 0.1
	<i>Drop Counter B</i>	62.8 ± 3.2	-75.4 ± 39.2	3.9 ± 0.0	-31.1 ± 0.1	2.8 ± 0.1
	<i>Drop Counter C</i>	61.3 ± 0.6	-93.3 ± 57.4	10.8 ± 0.0	-28.8 ± 0.0	2.9 ± 0.3
	<i>Disdrometer</i>	55.9 ± 0.3	-94.1 ± 51.6	4.1 ± 0.0	-42.7 ± 0.0	0.1 ± 0.2

4.4.2 Sensitivity and Robustness

To test the reliability of the relationship between the *PG* and *RR*, a series of sensitivity and robustness tests were conducted on the data. The RUAO tipping bucket data was used for this analysis as the RUAO provided the longest dataset. Using the RUAO data, the efficiency of the top-down algorithm was evaluated to understand how sensitive the precise timing and number of tips affected the relationship between the *PG* and *RR*.

Perturbation of the number of tips detected

The first method to test the sensitivity of the relationship between *PG* and *RR* involved changing the number of tips that were detected by the top-down algorithm. The sensitivity test was completed in three parts. First, a known percentage of tips were removed (at random) from the analysis. Second, a known percentage of tips were added with unique timestamps provided at random. Third, the first and second process was repeated, with the same perturbation distribution, for several iterations to improve the sampling, making an error analysis possible.

Table 4-2: Summary statistics of the *PG* and *RR* observed at the RUAO and CO.

	RUAO	CO				
	Tipping Bucket	Tipping Bucket	Drop Counter A	Drop Counter B	Drop Counter C	Disdrometer
#Tips/Counts	31486	7553	88743	79337	79010	881711
#Rain Days	681	202	N/A	N/A	N/A	N/A
#Stratiform Days	186	6	N/A	N/A	N/A	N/A
#Cumuliform Days	80	0	N/A	N/A	N/A	N/A
#Unclassified Cloud Days	415	196	N/A	N/A	N/A	N/A
Mean Rain Length (h)	8.99	2.16	N/A	N/A	N/A	N/A
Mean Daily Rainfall (mm)	4.40	4.23	2.28	2.48	3.22	2.37
Mean Rain Rate (mm h⁻¹)	6.76	3.89	1.27	1.33	1.31	0.47
Mean <i>PG</i> during Rainfall (V m⁻¹)	-93.16	-26.85	-15.13	-18.01	-8.73	6.74

For each perturbed dataset, the median relationship between the PG and RR was calculated consistent with Figure 4-12. The percentage of tips added or removed was incremented over a logarithmic scale, providing a finer resolution for smaller perturbations, around the control relationship between the PG and RR (Figure 4-12a). Each perturbed relationship between the PG and RR was compared against the control relationship between PG and RR using the root mean square difference (RMSD). Use of standard statistical tests (e.g. Anderson-Darling) became redundant for this analysis as any small differences between perturbed and control relationship between the PG and RR were seen as statistically different due to a large number of data points used in the analysis. The RMSD was used instead, as the metric provided a better estimate of the differences in units of PG .

For this analysis, 1000 datasets were created from 50 different tip perturbations ranging between 13% and 200% of the total number of tips detected from the control relationship (i.e. 20 datasets per tip perturbation). In Figure 4-13a, the 50 perturbed relationships between the PG and RR shows a tight spread around the control relationship given in red. A minimum PG around 4 mm h^{-1} was consistent for all 50 relationships, although the variance in PG was greatest at this point. The RMSD between the 50 perturbed relationships (Figure 4-13b) with respect to the control is well defined as the percentage of detected tips increased from the control. For 15% of the originally detected tips, there was a 50 V m^{-1} RMSD while for twice as many tips (200%) there was a 30 V m^{-1} RMSD. The tight spread in the perturbed relationships indicates the stability of the relationship between the PG and RR using the top-down algorithm.

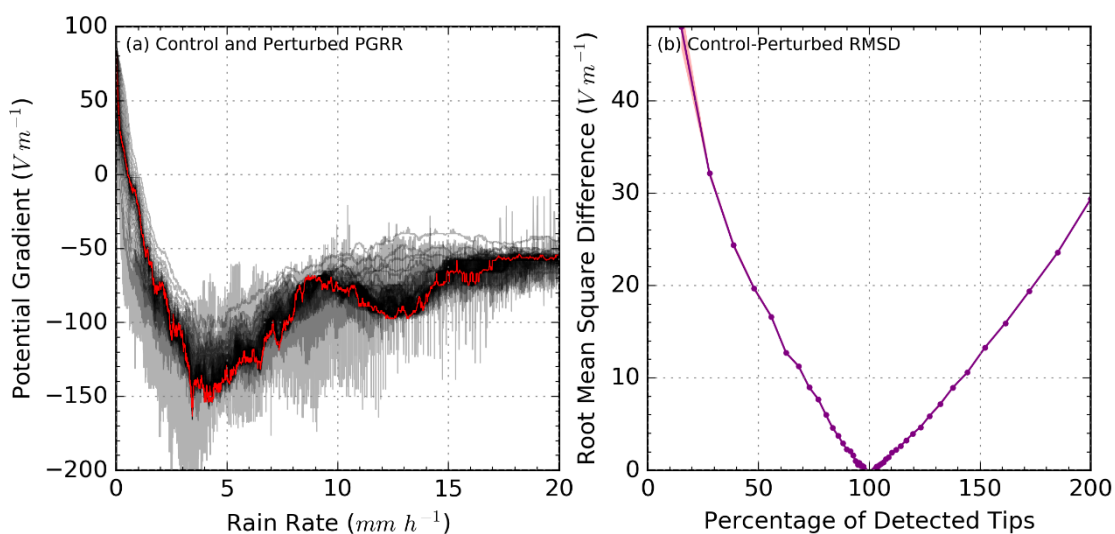


Figure 4-13: The sensitivity of the relationship between PG and RR using the RUAO tipping bucket dataset. (a) 1000 perturbed relationship between PG and RR s (grey lines) with various tip percentages against the control relationship between PG and RR (red). (b) The root-mean-square error (purple points) for each perturbed relationship between PG and RR with respects to the control relationship. The 95% confidence limits were also calculated for each perturbation (purple shading).

Tip-Detection Variations

The second method to test the sensitivity of the relationship was to compare the differences between the various tip-detection algorithms used to derive the correct number and timing of tips from the Delta-T tipping bucket. The algorithms used for testing were the threshold, converger, Mallat-Zhong, and top-down. The relationship between the *PG* and *RR* was calculated for all tip-detection algorithms using the Delta-T tipping bucket rain gauge during the METFIDAS 1 era (2006-2014).

In Figure 4-14, all tip-detection algorithms showed a decrease in *PG* for small *RR*s (1 mm h^{-1}) but the minimum *PG*—the point at which rainfall had the greatest influence on the *PG*—varied between algorithms. For the threshold and Mallat-Zhong algorithms, the minimum occurred around 1 mm h^{-1} , much earlier than for the top-down algorithm with a minimum around 4 mm h^{-1} . The minimum for the threshold, converger and Mallat-Zhong algorithms are different

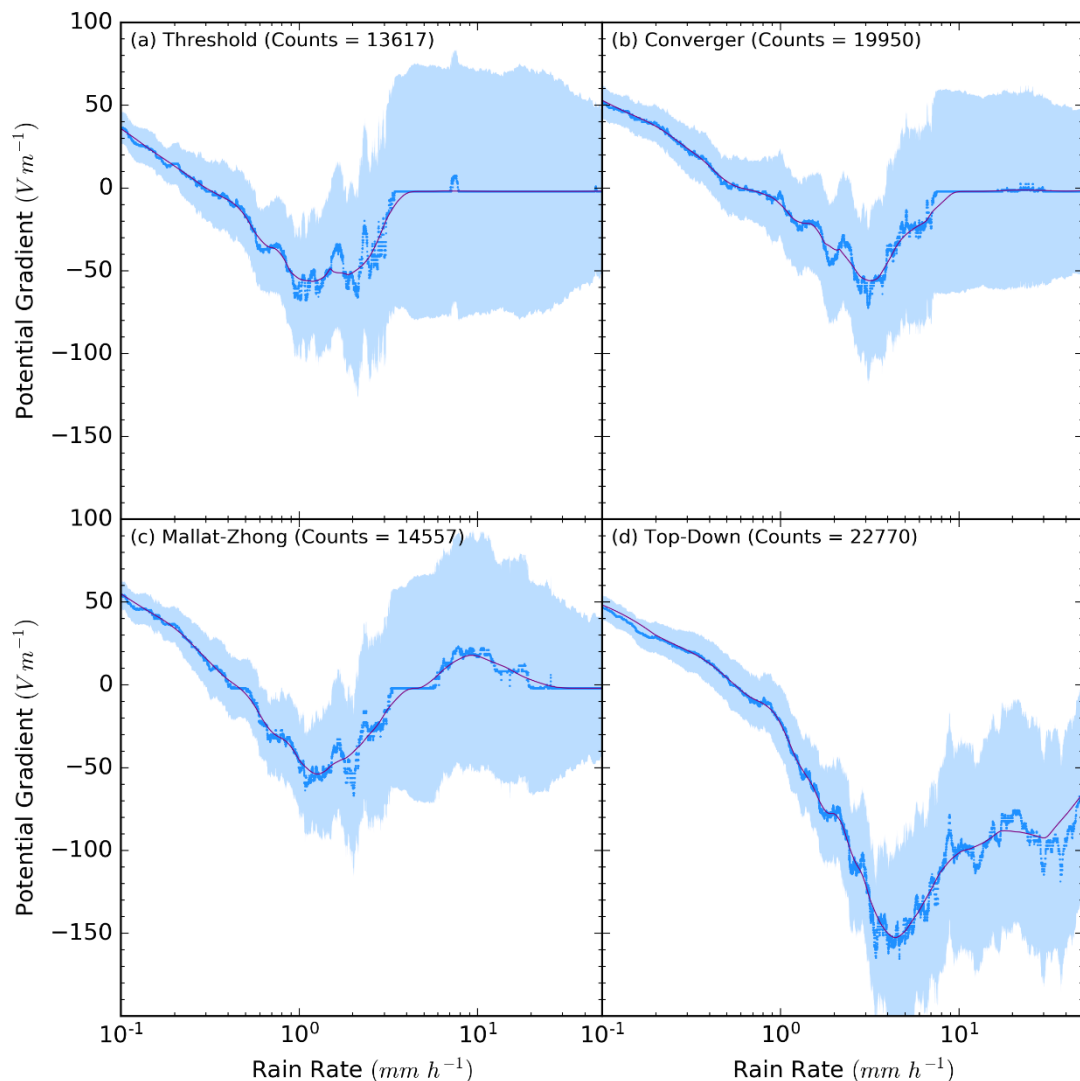


Figure 4-14: The median relationship between *PG* and *RR* (blue points) for different tip-detection algorithms, (a) threshold, (b) converger, (c) Mallat-Zhong and (d) top-down. The 95% confidence limits (blue shading) and lowest function (purple solid lines) were calculated for each algorithm.

from the rain gauges at CO, which also had a common minimum at around 4 mm h^{-1} . After the minimum PG , all algorithms increased in PG with all but the top-down algorithm increasing above zero PG . Only the disdrometer at CO increased in PG above zero at 12.5 mm h^{-1} .

Overall, the threshold, converger, and Mallat-Zhong algorithms gave appreciably different relationships between the PG and RR , although all algorithms agree that the PG is negative for small RR s ($< 4 \text{ mm h}^{-1}$). As the top-down algorithm was shown to be the only algorithm closely comparable to the manual rain gauge at the RUAO and the other five rain gauges at CO, the top-down can be assumed to provide an accurate method for detecting tips within the Delta-T tipping bucket rain gauge.

METFiDAS Variations

The final method to test the sensitivity of the relationship between PG and RR involved decoupling the relationship for the different rain gauges used at the RUAO. Specifically, a single rain gauge was used during each METFiDAS logging system, making decoupling the relationship for different rain gauges synonymous with each METFiDAS system.

Figure 4-15 shows the relationship between the PG and RR for the Delta-T tipping bucket (METFiDAS 1) and for the EML tipping bucket (METFiDAS 3). The Delta-T tipping bucket had the longest dataset with 22770 tips detected by the top-down algorithm compared with the EML tipping bucket with only 8716 tips. There was a significant difference between the relationships for both rain gauges with no turning point visible in the EML tipping bucket. A turning point (or minimum PG) had been observed in all other rain gauges in this study.

As the data collected for the EML tipping bucket coincided with the data collected at CO, there was little evidence to suggest the difference in relationships was climate related. Therefore, the difference must be caused by either an issue with the FM or the rain gauge. The average yearly rainfall (disregarding data losses) for the Delta-T and EML rain gauges was 91.4 and 74.9% of the 1981-2010 climatology respectively (UKMO, 2018). Although both rain gauges were below the 635.4 mm yearly rainfall climatology, the EML rain gauge was substantially worse.

As stated in §3.3.1, the EML rain gauge outputted a digital signal when the instrument collected 0.2 mm of rainfall stating a tip had occurred at a specific time. The same quality control processing that was conducted on the Delta-T tipping bucket could not be achieved for the EML tipping bucket, as no other high-resolution rain gauge was available. The differences in the relationship between the two tipping buckets were unlikely to be caused by issues in the FM at the RUAO as the FM located at CO was calibrated with respect to the RUAO FM. The relationships of the five rain gauges at CO all agree (within error) with the observations made

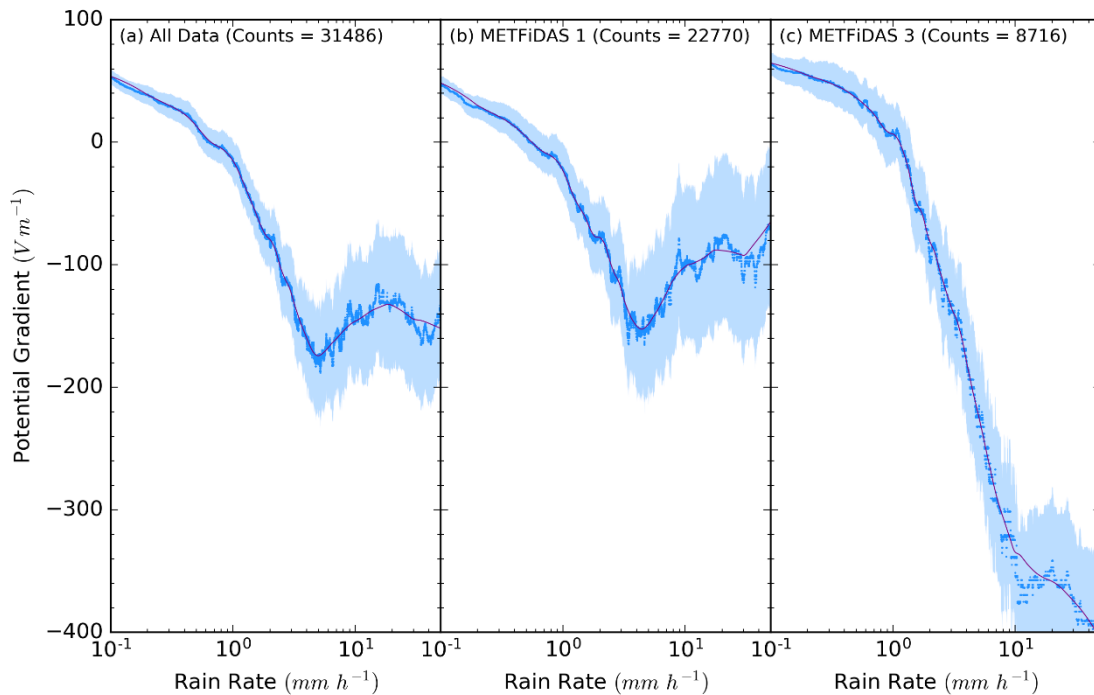


Figure 4-15: The median relationship between the PG and RR for the Delta-T tipping bucket (used during METFiDAS 1) and the EML tipping bucket (used during METFiDAS 3), located at the RUAO between 2006-2014 and 2014-present respectively. The 95% confidence limits (blue shading) and lowess function (purple solid lines) were calculated for each algorithm.

by the Delta-T tipping bucket. Therefore, the differences in the relationship between the *PG* and *RR* must be caused by the EML tipping bucket itself. As there were no practical solutions to fixing the EML rain gauge, the data was disregarded from any analysis. In the following sections, only the Delta-T tipping bucket (2006 – 2014) was used as it provided the longest dataset that would allow for the subsetting of its data. Due to the wide variability in the relationship between the *PG* and *RR*, the other rain gauges used would provide too much variance for any relationship to be observed.

4.5 Cloud Variations

The CI algorithm was calculated using the solar radiation data routinely measured at the RUAO alongside the FM and rain gauge measurements. The sunset and sunrise times (at an elevation angle of 8.3°) were calculated for each day and were used to mask the night-time cloud identification. A unique cloud type was associated with each calculated *RR* by finding the nearest timestamp. The *PG* and *RR* data were grouped by the associated cloud type and averaged together using the same methods used in §4.4.1.

Figure 4-16 shows the relationship between the *PG* and *RR* for the different cloud types. The masking of the night-time rain events reduced the dataset by 56.5% with 82.2% of the remaining data being classified as either clear, overcast or unclassified. All relationships showed a substantial negative *PG* perturbation for low *RRs* ($< 4 \text{ mm h}^{-1}$) and reached a maximum

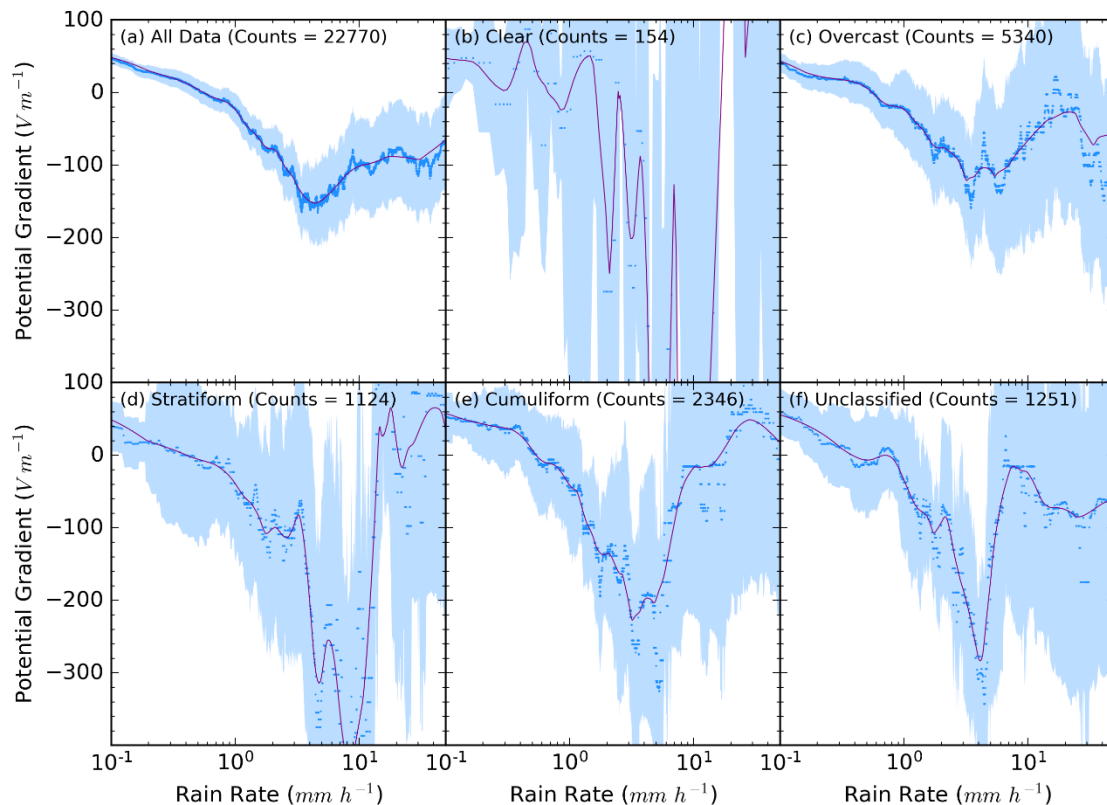


Figure 4-16: The median relationship between the PG and RR (blue points) at the RUAO between 2006 and 2014 decoupled by cloud type as identified using the Harrison (2008) algorithm. Each plot has a RR between 0- and 50- mm h^{-1} . The original relationship (a) before decoupling is plotted for reference. The clear (b), overcast (c), stratiform (d), cumuliform (e) and unclassified (f) cloud types are given. The 95% confidence limits (blue shading) and lowest (purple solid line) have been added to the data.

perturbation between 4- and 8- mm h^{-1} . For higher RRs, each relationship showed a weakening of the negative PG perturbation with no discernible differences outside the 95% confidence limits. The size of the confidence limits was directly correlated with the number of tips associated with each cloud type.

The clear and stratiform identifications (Figure 4-16b, d) were poorly defined caused by the small number of counts associated with these cloud types. A limitation of the CI algorithm was the identification of clear events even during rainfall. As the time resolution of the tipping bucket rain gauge is proportional to the rain intensity, the lower RRs are more susceptible to appreciable changes in the local meteorology. For example, for a small RR ($< 0.4 \text{ mm h}^{-1}$), the time between tips is long (> 30 minutes), but not long enough to be classified as a separate rain event. In the time between two tips, a series of clouds could pass overhead with clear skies in between. The clear classification can be assumed as rare cases when the RR was low, and the cloud cover was scattered.

The cumuliform cloud type (Figure 4-16e) was also poorly defined because of two reasons. First, the small number of counts associated with cumuliform clouds. Second, because of the

substantial perturbation of the PG caused by clouds which were charged (see §4.3.2 for a case study example). There was a small probability for the precipitation measured at the RUAO to be charged. For precipitation to be charged, the overhead cloud must also be substantially charged ($> 1 \text{ kV m}^{-1}$) increasing both the probability for charged rain and for the net charge on the drops to be appreciable (Bennett, 2018). It has been found by Bennett (2018) that the occurrence of charged rain was more likely for higher RR s. There was a 50% probability for appreciably charged rain ($> 1 \text{ pC s}^{-1}$) to occur for intensities above 10 mm h^{-1} . The mechanism for how charged rain is produced is still not fully understood. Some potential hypotheses for charged rain were discussed in §2.1.4 which looked at how the transport of charged ice could descend through the cloud and be precipitated. It was assumed in this study that cumuliform clouds were the only clouds that could produce charged rain, as active charge separation would be required to perturb the PG at the surface substantially. Stratiform clouds are charged inactively caused by the flow of charge towards the surface from the ionosphere, which collects at the edges of the cloud. Even for optically thick stratiform clouds, the amount of charge build-up would not be enough for charged rain without any turbulence or an updraught to increase the collision efficiency between the cloud drops and space charge (MacGorman and Rust, 1998).

Table 4-3 provides details of the relationship between the PG and RR for different cloud types. The PG at zero RR showed significant differences between cloud types varying by $(47.4 \pm 16.7) \text{ V m}^{-1}$; varying beyond the 95% confidence limits. At zero RR , the perturbation of the PG would be dominated by the cloud itself. Comparisons with the averaged fair-weather PG value measured at the RUAO ($(85.7 \pm 0.009) \text{ V m}^{-1}$), showed that only stratiform clouds were comparable with the fair-weather PG within the 95% confidence limits. Overcast, unclassified and cumuliform clouds showed an increase in PG at zero RR with overcast having the biggest difference. In overcast conditions, the flow of charge from the upper atmosphere would be restricted, causing a reduction of negative charge flowing to the surface. The reduction in negative charge would increase the PG at the surface and would account for the observations seen here.

The minimum PG for each cloud type was found to vary substantially between cloud types by $(688.8 \pm 546.0) \text{ V m}^{-1}$, but the difference was not significant outside the 95% confidence limits. The clear weather events had the largest perturbation of the PG but had the widest confidence limits. Both the clear and stratiform clouds are outliers in the minimum PG metric. Figure 4-16b shows how dispersed the relationship was even using a moving median to minimise the variation in the data. The RR at the minimum PG varied by $(3.3 \pm 0.1) \text{ mm h}^{-1}$ and was found to be significant for the 95% confidence limits. The error for the RR was calculated by finding the

Table 4-3: Details of the relationship between the PG and RR for the different cloud types at the RUAO and CO. The errors for each measurement are the 95% confidence limits.

Cloud Type	PG at 0 RR (V m ⁻¹)	Minimum PG (V m ⁻¹)	RR at Minimum PG (mm h ⁻¹)	Initial Rate of Change (< 5 mm h ⁻¹ ; V m ⁻¹ /mm h ⁻¹)	Final Rate of Change (> 5 mm h ⁻¹ ; V m ⁻¹ /mm h ⁻¹)
All	65.7 ± 6.0	-165.1 ± 55.5	4.6 ± 0.0	-51.9 ± 0.2	1.4 ± 0.3
Clear	102.7 ± 12.8	-956.4 ± 506.1	4.5 ± 0.3	-90 ± 8.8	6.3 ± 100.5
Overcast	113.1 ± 4.0	-176.1 ± 75.8	5.5 ± 0.0	-60.0 ± 0.4	1.2 ± 0.9
Stratiform	83.3 ± 6.8	-497.6 ± 274.5	7.7 ± 0.1	-77.6 ± 1.4	1.8 ± 11.0
Cumuliform	107.0 ± 4.1	-320.2 ± 201.9	5.1 ± 0.0	-88.3 ± 1.1	1.6 ± 4.9
Unclassified	101.1 ± 1.0	-342.5 ± 164.4	4.4 ± 0.0	-86.6 ± 1.6	-0.2 ± 2.3

difference between neighbouring RRs. Comparing the 'RR at minimum PG' result with the histogram of RRs measured at the RUAO (Figure 3-16), a transition of the slope was found at 10 mm h⁻¹ which can be interpreted as a threshold between stratiform and cumuliform precipitation types. The stratiform-cumuliform threshold does not overlap with the RR at minimum PG, which suggests the average relationship between the PG and RR is cloud type invariant.

The initial and final rate of change metrics were calculated using an ordinary least-squares linear regression for RRs less than and above 5 mm h⁻¹ respectively. The initial (< 5 mm h⁻¹) and final (> 5 mm h⁻¹) rate of change varied by (38.1 ± 9.1) V m⁻¹ / mm h⁻¹ and (6.5 ± 101.2) V m⁻¹ / mm h⁻¹ respectively. Only the initial rate of change showed significant differences between cloud types. The substantial differences between PG cloud types were dominated by the clear and stratiform cloud types, which were greatly under-sampled in this analysis. The remaining classifications showed strong agreement with each other within the 95% confidence limits. Only minor differences were observed for the RR at minimum PG and the initial rate of change metrics.

Due to the limitations of the CI algorithm, the differences between cloud types can only provide low confidence that any differences actually exist. Although there were some appreciable differences between cloud types (disregarding the clear and stratiform classification), these differences can only be observed for high RRs ($> 10 \text{ mm h}^{-1}$) when the confidence in the relationship between PG and RR reduces substantially. In the next section, the dependence of the surface conditions is explored by comparing the changes in the pressure, wind speed, wind direction, rain event length, and length between rainfall events.

4.6 Surface Conditions

As there exists an appreciable and robust relationship between PG and RR (for RR values $< 10 \text{ mm h}^{-1}$), it was important to understand whether changes in meteorology and surface conditions had any influence on the relationship. In the last section, the relationship between PG and RR was found to vary insignificantly (for $RRs < 10 \text{ mm h}^{-1}$) with respect to the type of cloud that produced the precipitation, with any differences in cloud type being low confidence. An invariance with cloud type suggests the negative PG perturbation during rainfall was not, on average, cloud dependent. Therefore, the invariance of cloud type on the PG during rainfall suggests that the drops themselves perturb the PG .

The dynamics of a drop falling through the atmosphere and their interaction with the surface was found to be dependent on the size of the drop, impact speed, pressure, wind speed, water level, ambient PG and drop impurities (discussed in §2.2). An analysis was performed to determine how changes in the pressure, wind speed, wind direction, rain event length, and length between rain events changed the relationship between the PG and RR . To undertake this analysis, the RR and PG data from the RUAO was grouped into rain events and the average meteorology and surface conditions were found for each event.

4.6.1 Definition of a Rain Event

In this chapter, a rain event is defined as a collection of tips when the length of time between successive tips was below a certain threshold. To determine a suitable threshold for the length of time between tips, four considerations were used. First, when drizzle occurs ($< 0.05 \text{ mm h}^{-1}$) the time between tips covers several hours. Second, the RR near the start and end of a rain event, especially for stratiform clouds, would plateau causing long times between successive tips. Third, as the tipping bucket requires 0.2 mm of precipitation to collect in the bucket, there was no way to determine whether precipitation was still reaching the surface until the next tip had occurred. Fourth, convective rainfall typically has sharp boundaries (e.g. showers). There were many occasions when several small cumulus clouds, each distinct from one another,

moved overhead causing a quick succession between raining and not raining. The quick succession was difficult to resolve in the tipping bucket rain gauge reliably. A sufficiently long-time length was used based on the considerations of when drizzle and stratiform clouds occurred. The threshold for defining a rain event was found for all clouds and for each major cloud type as defined in §4.2.

Figure 4-17 shows the histogram of RR s between 0- and 1- $mm\ h^{-1}$ for four different cases—all clouds, stratiform clouds, cumuliform clouds and unclassified clouds. The stratiform and cumuliform plots also contain the overcast and clear classification respectively. Without the addition of the overcast and clear classifications, the number of direct cumuliform and stratiform events was very low (< 10%). For a sufficient sample of each major cloud type, two assumptions were used. First, if precipitation is being measured at the surface but the cloud classification given is ‘clear’ the amount of cloud must be small and would suggest that cumuliform clouds were overhead. Second, when the cloud classification is given as ‘overcast’ the likely cause for the overcast conditions are stratiform clouds.

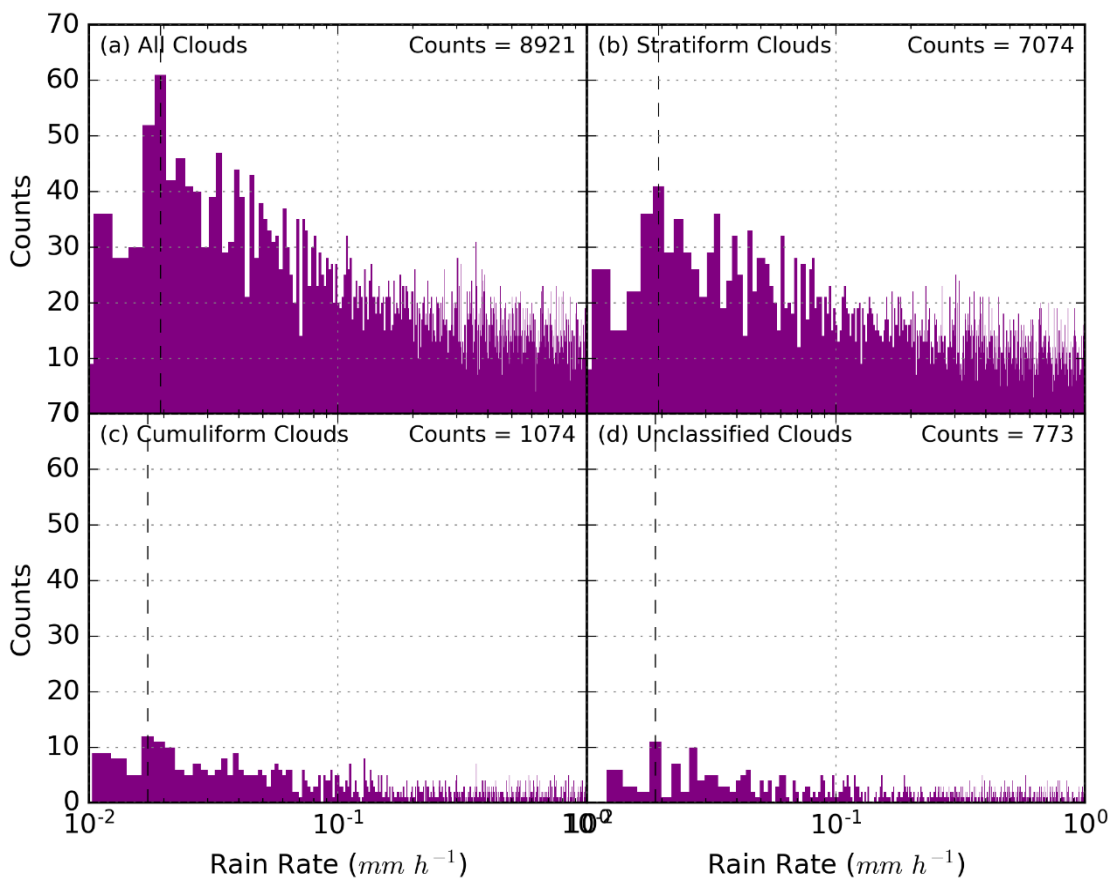


Figure 4-17: A histogram (purple) of rain rates measured at the RUAO between 2006 and 2014 for different cloud types as defined by Harrison (2008). (a) All clouds, (b) stratiform clouds, (c) cumuliform clouds and (d) unclassified cloud. The stratiform and cumuliform clouds also use the overcast and clear classification, respectively. The black dashed line indicated the maximum in the histogram (see text).

A lognormal distribution was observed for all clouds and stratiform clouds with a distinctive peak (kurtosis = 20.34 and 17.86 respectively), while the cumuliform and unclassified cases have a widespread and sporadic distribution (kurtosis = 26.39 and 16.15 respectively). The wide distribution of the cumuliform clouds (denoted by the high kurtosis) is likely caused by the large range of *RRs* that were observed with these cloud types, which are typically short-lived (Langer and Reimer, 2007). Stratiform clouds have a much narrower range of *RRs*, which are well defined in the low-intensity range ($< 7 \text{ mm h}^{-1}$). As stratiform rain can last for several hours at low intensity, the distribution is better defined.

The mean number of rain events per day was also calculated using the determined thresholds for each cloud type (Table 4-4). Stratiform clouds occur more frequently over Reading (59.9%) compared with the cumuliform (35.3%) and unclassified clouds (4.8%). The mean number of rain events to occur per day is surprisingly low. On average, a unique rain cloud occurs every 6.6 days, with cumuliform clouds being very rare, occurring once in 56.2 days. The low occurrence of cumuliform clouds highlights the limitation of the CI algorithm, which is an order of magnitude lower than a climatology of the area suggests (Costa-Surós et al., 2013). Despite the high cloud type amount (35.3%), the small size of the cumuliform clouds is often misidentified by the CI algorithm and occur too close together to be uniquely identified as separate rain events by the threshold applied in this study.

4.6.2 Determination of the Effect of Surface Splashing

From §2.2.3, the factors that could influence the splashing of liquid drops were discussed. The factors included the droplet size, impact speed, drop impurities, air pressure, ambient *PG*, and surface water content. Understanding whether these factors influence the relationship between the *PG* and *RR* was used to answer two questions. First, is the relationship between *PG* and *RR* dependent on the surface conditions or on the conditions of the overhead cloud? Second, does

Table 4-4: The commonality of cloud types over RUAO between 2006 and 2014. The rain event boundaries are also given and can be used to define the endpoint between rain events.

Statistics/Information	Stratiform	Cumuliform	Unclassified	All
Rain Event Boundary (mm h⁻¹)	0.018822	0.038938	0.018854	0.018822
Rain Event Boundary (s)	38253	18491	38188	38253
Mean Rain Events per Day	0.0413	0.0178	0.0921	0.1511
Cloud Type Amount (%)	59.9	35.3	4.8	100

the amount of water residing on the surface change the polarity of charge that is released from the splashing drop?

A method to evaluate how surface water influences the *PG* was used to analyse the effects of splashing. The method used the time between consecutive rain events as a proxy for how dry the surface was before the next rain event; the greater the time between rain events, the drier the surface. The relationship between the amount of water on the surface and the length of time since it last rained has a large degree of correlation (Magarey et al., 2005). Variations in the duration of surface wetness are dependent on the surface temperature, wind profiles, direct solar radiation, relative humidity, and the amount of water present on the surface from the previous rain event²⁷ (Magarey et al., 2005). In this study, the assumption that each rain event would saturate the surface with water was used. At the RUAO and CO, each instrument was surrounded by grasslands and after a rain event, the surface would begin to evaporate and flow through the subsurface through infiltration. The effect of surface temperature and wind were neglected with the assumption that averaging would minimise any variations and could be attributed to the relative errors of the results.

To understand how the relationship between the *PG* and *RR* depends on the surface conditions (pressure, wind speed, wind direction, rain event length and time between rain events), five methods were used to organise the data,

1. For each rain event, an average of each condition (e.g. pressure) was calculated,
2. The *PG* and *RR* for each rain event was grouped into equal divisions for each condition (e.g. 980-990 hPa, 990-1000 hPa),
3. For each group, the *PG* and *RR* were averaged together producing a unique relationship,
4. Four metrics were calculated to evaluate the change in the relationship between the *PG* and *RR* (Figure 4-18),
 - a. The 5th percentile of *PG* (PG_{5th}) and the associated *RR* (RR_{PGmin}),
 - b. The rate of decay in *PG* (PG') between zero *RR* and RR_{PGmin} ,
 - c. The median *PG* (PG_{Median}) for *RR*s greater than RR_{PGmin} ,
 - d. The standard error *PG* (PG_{SE}) for *RR*s greater than RR_{PGmin} ,
5. A moving median was used to improve the resolution of the data.

²⁷ As the surface conditions for each rain event varies in both time, space and magnitude, the amount of water present on the surface after each event can vary especially when comparing long rain events with short rain events (i.e. < 1 mm).

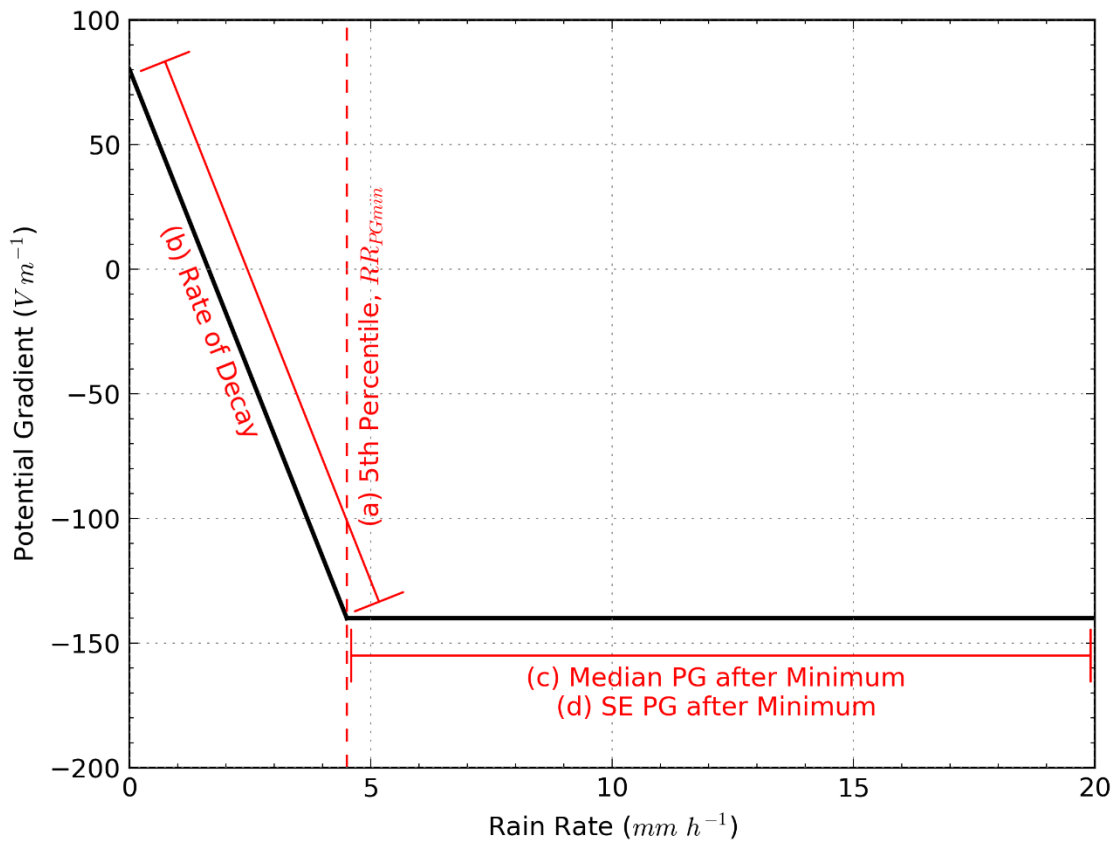


Figure 4-18: An example data (black line) showing the four metrics (see text) used to analyse the surface condition's influence on the relationship between the PG and RR.

The requirement for long-term, high-quality datasets was required to resolve the small variations of space charge being released from drop splashing. A moving average was used to increase the resolution of the relationship between the *PG* and *RR*. Using long-term data was necessary for analysing any embedded effects between the *PG* and *RR* such as drop splashing and drop charging.

4.6.3 Analysis of Meteorological Surface Conditions

The RUAO dataset (2006 – 2014) was grouped into rain events using the thresholds determined for each cloud type (Table 4-4). The mode cloud type for each rain event was then found, building up a list of rain events with a specific cloud type. Night-time rain events or rain events that crossed the day-night boundary were removed. The length of each rain event was also calculated to determine if rain event length influenced the relationship between *PG* and *RR*.

Over the 8 years of data collected at the RUAO, 1198 rain events were identified. Figure 4-19a-b shows the histogram of rain event length and time since the previous rain event. Both the length of each rain event and time since the previous rain event histograms is comparable to a lognormal distribution. The median (50%) events occur within 6 and 33 hours for the length of each rain event and time since the previous rain events respectively. The distribution of Figure

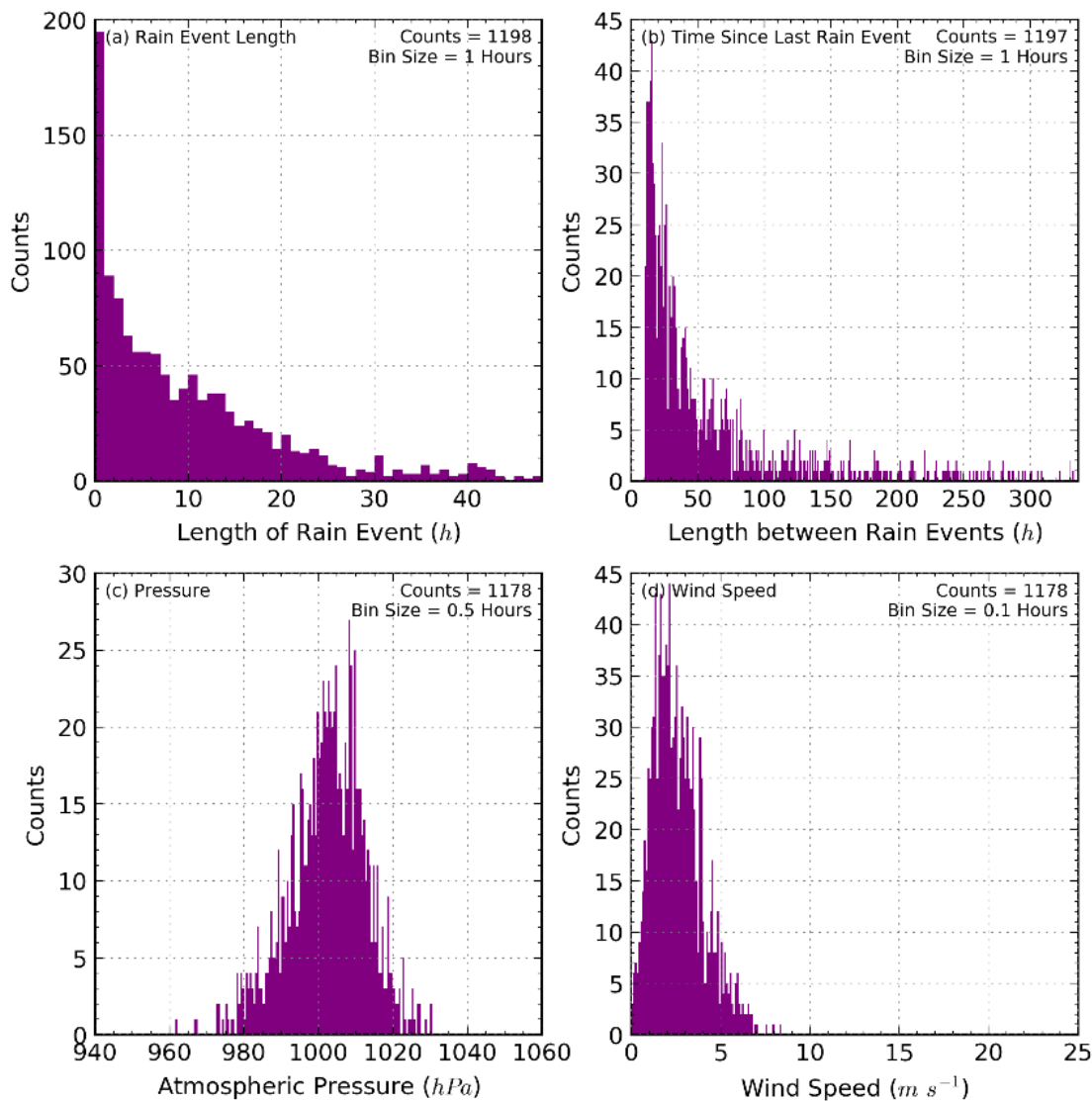


Figure 4-19: A histogram of rain event length (a), the time since the last rain event (b), atmospheric pressure (c) and wind speed (d). N.B. the time since the last rain event has one less count than the rain event length.

4-19b is substantially wider in time, covering several weeks in some circumstances, highlighting drought conditions at the RUAO (Tate and Gustard, 2000).

The histogram of atmospheric pressure (Figure 4-19c) was comparable to a Gaussian distribution with a mean pressure of 984 hPa and a median of 1000 hPa. There was a secondary peak in the distribution at 1008 hPa. The local minimum between peaks provides a distinction between low and high-pressure systems that move across Reading. The histogram for wind speed (Figure 4-19d) showed very few events were measured with a mean above 10 m s⁻¹. The distribution is narrow with wind speeds mostly below 5 m s⁻¹.

Pressure

The pressure was compared against the relationship between the *PG* and *RR* by grouping the rain events in pressure bins (0.5 hPa widths). The *PG'*, *PG*_{5th}, *PG*_{Median} and *PG*_{SE} metrics were

calculated for each pressure bin. There were no significant variations in pressure between 970 and 1025 hPa to the 95% confidence limits for any metric. The lack of variations with pressure suggests that the structure of a drop splash is not appreciably influenced by typical atmospheric pressures and much smaller pressures might be required to suppress a drop splash.

Wind Speed and Wind Direction

An examination of how the relationship between the PG and RR showed no significant variations for wind direction to the 95% confidence limit for the PG' , PG_{5th} and PG_{Median} metrics. The PG_{SE} metric showed a significant increase in variability for wind directions between 150 and 275° . The PG_{SE} reached zero for wind directions between 300 and 50° . For greater wind directions, PG_{SE} increased linearly until a plateau was reached at 100 V m^{-1} . The strong significance of the PG_{SE} metric might suggest different behaviours in precipitation between the ocean and land-originating cloud systems that pass Reading, assuming surface wind directions are, on average, equivalent to the cloud direction.

Figure 4-20 shows the changes in the relationship between the PG and RR as a function of the mean wind speed for each rain event. The PG' was greatest for wind speeds less than 0.5 m s^{-1} with a maximum PG' of -166.3 V m^{-1} . For wind speeds greater than 0.5 m s^{-1} the relationship plateaus, and any further increases in wind speed had little effect on the PG' . The PG_{5th} showed

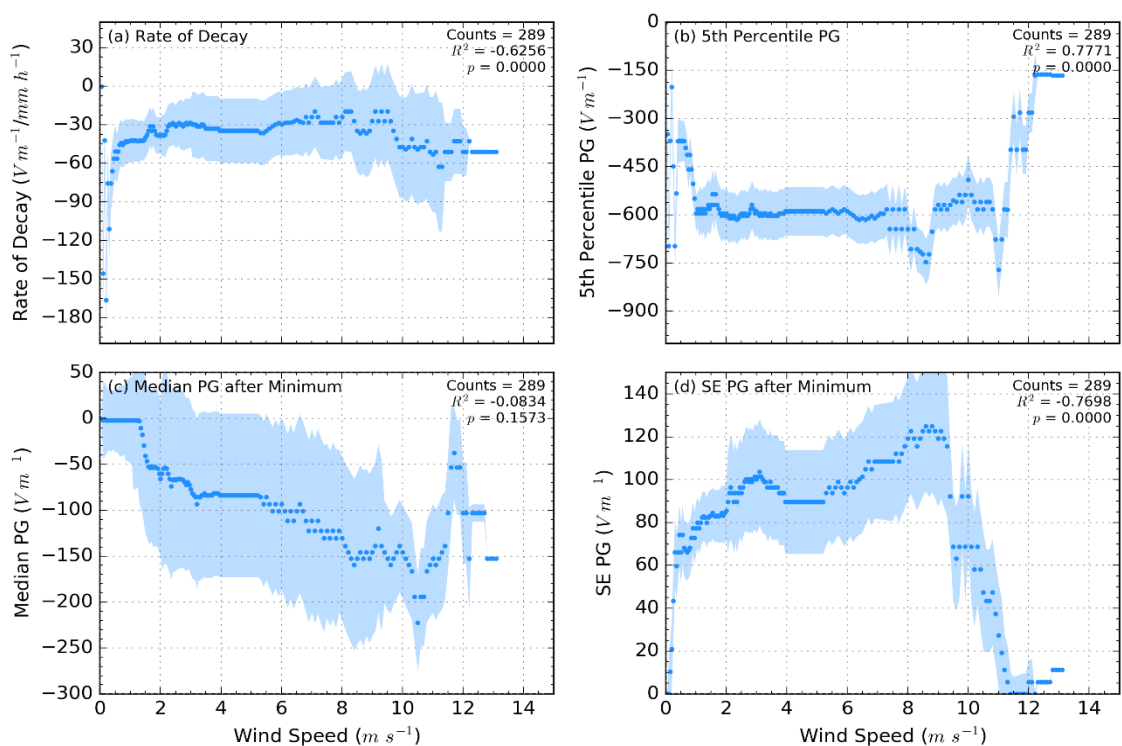


Figure 4-20: The change in the relationship between PG and RR as a function of the wind speed between 0 and 14 m s^{-1} . Four metrics were used to evaluate the change in the relationship between PG and RR were (a) the rate of decay, (b) 5^{th} percentile of PG , (c) median PG after 5^{th} percentile of PG and (d) Standard error of PG after 5^{th} percentile of PG . The 95^{th} per cent confidence intervals is shown as a blue shading.

a similar relationship. For wind speeds less than 1 m s^{-1} there was a sudden decrease in the PG_{5th} . Even though the PG' and PG_{5th} are not independent variables, a reduction in PG_{5th} would cause a reduction in PG' which should form a direct relationship. In Figure 4-20, an inverse relationship was seen for small wind speeds ($< 1 \text{ m s}^{-1}$) suggesting the RR at maximum perturbation varies with wind speed.

The PG_{Median} and PG_{SE} both showed significant changes for much greater wind speeds. The PG_{Median} had a weak negative relationship, while the PG_{SE} had a positive relationship until 10 m s^{-1} . There was a high likelihood that the variability in the relationship between PG and RR increased proportionally to windspeed as suggested by the PG_{SE} . The wide confidence intervals of the PG_{Median} also indicated an increase in variability as the median PG value was poorly defined, consistent with unstable atmospheric conditions. At higher wind speeds ($> 10 \text{ m s}^{-1}$) there was a reversal in the relationship for both PG_{Median} and PG_{SE} .

Rain Event Length and Time between Rain Events

An examination of how the relationship between the PG and RR showed no significant variations for rain event length to the 95% confidence limit. Some variation in the relationship between the PG and RR existed according to the PG_{SE} for very high rain event lengths ($> 40 \text{ h}$) but was insignificant. As the number of rain events above 40 hours was poorly sampled, the variation in the relationship between PG and RR has low confidence. Therefore, without the addition of more data, no relationship was found between the rain event length and the influence of rainfall on the local PG .

In Figure 4-21, the time between rain events showed significant relationships in three out of the four metrics (PG_{5th} , PG_{Median} and PG_{SE}). Increasing the time between rain events showed stronger perturbations of the PG up to 150 h according to the PG_{5th} . The PG_{5th} relationship was well defined with small confidence intervals. The PG' increased substantially within the first 10 hours and suggested a greater flux of negative ions were entering the atmosphere as the surface dried. Once the surface was dry, the relationship plateaus masked by the large 95% confidence limits. For short times between rain events ($< 20 \text{ h}$), the PG_{Median} increased in magnitude markedly. For longer times, the PG_{Median} reverses and begins to decrease in magnitude, until a maximum at 150 h. The time since rain events between 20 and 150 h was significant to the 95% confidence level. Above 20 hours, the surface could be classed as dry and any changes occur in the subsurface.

For grassland, the time between rain events had two effects. First, the time for the surface water to evaporate. Second, the time for the sub-surface water to evaporate which would harden the surface. Once the surface was devoid of water, the soil permeability would decrease, which

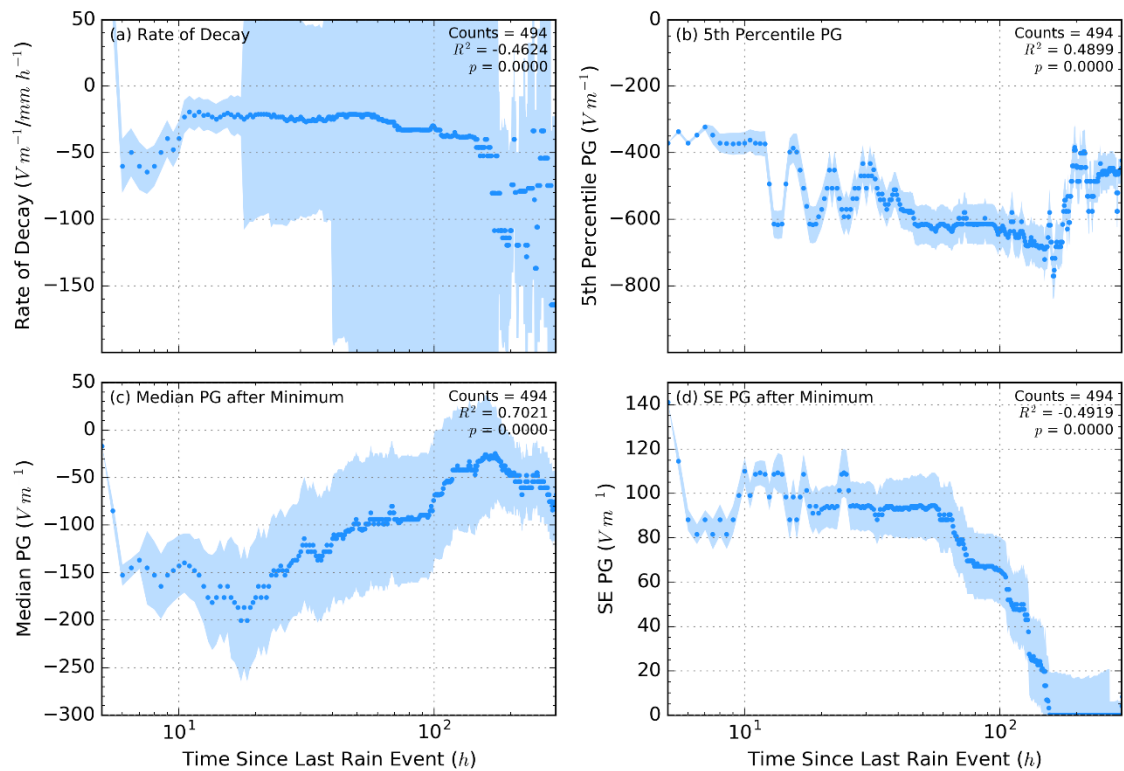


Figure 4-21: Same as Figure 4-20 but for time since last rain event.

could increase the build-up of water at the surface once a new rain event occurred. The stability of the relationship between the PG and RR increases with the time between rain events. The PG_{SE} shows a substantial increase in stability for rain events above 55 hours. After 150 h the relationship between the PG and RR had no variability between rain events. For shorter times between rain events, there was a well-defined negative relationship with time, plateauing at 95 V m^{-1} .

4.7 Discussion

In this chapter, seven rain gauges and two FMs located at the RUAO and CO were used to evaluate the relationship between the PG and RR (§4.4) using 13 years' worth of data (2006 – 2018). The type of rain gauges used in this study included three standard tipping bucket rain gauges, three drop counts and one disdrometer. As measuring RR accurately is complicated (Lanza et al., 2005; Goodison et al., 1998), this study focused on the quality control methods used to predict the RR accurately (§3.3). Three hypotheses were tested to understand the mechanisms responsible for the perturbation of the PG at the surface during rainfall (§4.1). The charge within the precipitating cloud (§4.5) and the charge released by the splashing of raindrops against the surface (§4.6) were compared to determine if they influenced the relationship between the PG and RR . Below summarises the results gained from each hypothesis tested within this study.

1 The rain rate has an inverse relationship with the potential gradient measured at the surface

- A substantial decrease in PG ($(250.8 \pm 55.5) \text{ V m}^{-1}$) was observed relative to the fair-weather state for all rain gauges and for all RR s measured (Figure 4-12).
- Six rain gauges (RUAO EML tipping bucket was the outlier) observed a plateau in the relationship between RR and PG around 4 mm h^{-1} with a weakening of the perturbation for greater RR s (Figure 4-12).
- The relationship between the PG and RR was sensitive to how well the rain gauge could measure rainfall. An RMSD between 30 and 50 V m^{-1} was found when changing the number of tips detected between 13% and 200% respectively (Figure 4-13).
- Which tip detection algorithm used significantly influenced the relationship between the PG and RR , for all RR s (Figure 4-14).
- For the RUAO EML tipping bucket, the PG had a linear relationship with RR . No plateauing effect was observed (Figure 4-15).

2 The cloud type has a negligible influence on the average relationship between rain rate and the potential gradient measured at the surface

- Although there were substantial variations in the relationship between the PG and RR for all cloud classifications, the wide 95% confidence intervals showed no significant differences for most RR s (Figure 4-16).

3 The relationship between rain rate and the potential gradient is dependent on the local meteorological and the dryness of the surface

- Only wind speed and length between rain events were found to have any appreciable influence on the relationship between the PG and RR (Figure 4-20 and Figure 4-21).
- The PG' and PG_{5th} metrics were found to be significant for small wind speeds ($< 2 \text{ m s}^{-1}$) and time between rain events ($< 10 \text{ h}$), (Figure 4-20a, b and Figure 4-21a, b).
- The PG_{Median} and PG_{SE} metrics were found to have a 95% statistical significance for higher wind speeds ($> 2 \text{ m s}^{-1}$) and length between rain events ($> 20 \text{ h}$), (Figure 4-20c, d and Figure 4-21c, d).

The hypotheses set out from this study, linking with previous research, suggested that negative ions were being released from raindrops that were polarised by the ambient PG (Smith, 1951; Lenard, 1892; Simpson, 1949). The raindrop interacts with the surface causing them to splash. Although not measured during this study, it was thought from previous research that a crown would form containing negative charge (Levin and Hobbs, 1971; Adkins, 1959). The negative

charge residing on the crown would be released into the atmosphere if the momentum on the drop were greater than its surface tension. This hypothesis was well established in the results presented in this study, as seen for low RRs ($< 4 \text{ mm h}^{-1}$) with the abundance of negative charge being measured, unanimously for all rain gauges.

For the first hypothesis, the agreement between all rain gauges (tipping buckets, drop counters, disdrometer) suggests an abundance of negative charge near the surface during rainfall. The relationship between the PG and RR was sensitive to changes in the instrumentation and the quality control procedures performed on the data. The sensitivity is consistent with the fast variability of precipitation which likely couples to external effects such as the charge in the cloud, charged rain, wind speed, and dryness of the surface. The fast variability highlights the close proximity of the charge that influences the local PG .

For the second hypothesis, the variations in the relationship between the PG and RR have low confidence due to the limitations of the CI algorithm. The broad classification used often misclassified the cloud type. Even using 7 years' worth of data (using the Delta-T tipping bucket at the RUAO), the low sample of clouds in each category made it difficult to resolve the relationship between the PG and RR , especially when comparing the differences in their relationships. Therefore, it is difficult to know, with any certainty, whether the cloud type influences the relationship between the PG and RR . The inclusion of charged rain increases the complexity of the relationship, which is also a function of RR (Bennett, 2018).

For the third hypothesis, the PG_{Median} and PG_{SE} metrics are related to the higher RRs ($> 5 \text{ mm h}^{-1}$) in the relationship between the PG and RR associated with cumuliform clouds. Meanwhile, the PG' and PG_{5th} metrics are associated with stratiform clouds. As a relationship was found between all metrics for both wind speed and time between rain events, suggest that surface splashing is an important mechanism for influencing the local PG . This result leads to the conclusions that the transport of charge is controlled by the surface winds and the magnitude and polarity of charge are influenced by the dryness of the surface.

The wind speed measured near the surface was hypothesised to increase the advection of ions entering the atmosphere from the splashing of drops. Without the aid of the wind, the ions released from splashing would have limited momentum, gained from the impact of the drop with the surface. The influence of rainfall through ion release was hypothesised to be short-lived without wind, as the negative ions would quickly reach the surface again. With the presence of wind, the ions can be transported and easily lifted higher into the atmosphere, capable of being detected by the FM, 3 metres above the surface. The causality of this relationship is not clear

though. As deep convective clouds can increase both PG and wind speed variability while producing a higher RR , the cause of the relationship in PG_{Median} and PG_{SE} is not clear. The relationship for PG' is clearer as the RR s used to define PG' are small ($< 5 \text{ mm h}^{-1}$) which are less influenced by the charge in the cloud which resides in cumuliform clouds. Further research would be required to test the results found in this chapter.

The results from comparing the relationship between the PG and RR have led to two hypotheses describing the mechanism causing the relationship between RR and PG above 4 mm h^{-1} . First, under a sufficient RR surface water would form, increasing in depth as a function of the RR . The depth of the surface water can change how a drop splashes against the surface. For a sufficient depth of surface water, a central jet can form alongside the crown during splashing (Levin and Hobbs, 1971). Similar to the crown, the central jet would break up due to the momentum of the drop. The central jet, under an ambient PG , can release positive ions into the atmosphere. The inclusion of positive ions would weaken the negative perturbation of the PG . Second, the washout of the negative charge could occur from successive raindrops capturing the negative charge shortly before reaching the surface. The successive raindrops would splash again releasing negative, and possibly positive, charge. The reduction of the PG perturbation is caused by lowering the amount of negative charge near the surface under a constant flux of precipitation. It is likely that both hypotheses would occur simultaneously as they both account for the increased variability in the PG for RR s greater than 4 mm h^{-1} . Nonetheless, there is substantial evidence that precipitation causes a negative perturbation of the surface PG , modulated by the wind speed and dryness of the surface at the time of the rain event.

5 Cloud Electrification Measured at the Surface

This chapter consists of six parts: first, a discussion of the cloud electrification hypotheses within this study are explored (§5.1); second, the cloud identification algorithm derived from radar and ceilometer data used for testing the hypotheses is discussed (§5.2); third, case study examples of different clouds measured at CO, highlighting the relationship between convection, cloud size, cloud optical thickness, turbulence and charge separation which relate to the hypotheses (§5.3); fourth, the classification of cumuliform clouds used as a basis for analysing the differences between clouds at different electrification stages (§5.4); fifth, testing the cloud electrification hypotheses (§5.5) using the classification of cumuliform clouds and the cloud identification algorithm; and sixth, a summary of all the results that have been shown (§5.6).

5.1 Introduction

In this chapter, the cloud electrification mechanisms of developing cumuliform clouds are analysed. For this study, the charge separation mechanisms discussed in §2.1 were used to form three hypotheses used to understand the electrification of cumuliform clouds in the UK. From these hypotheses, further understanding of the cloud-scale processes useful in the electrification of cumuliform clouds is achieved, extending the knowledge of the micro-scale processes thought to be responsible for charge separation to occur.

The processes responsible for cloud-scale electrification are examined by comparing measurements of overhead cumuliform clouds, which influence the surface potential gradient (PG), observed by ground-based electrical and radar instruments. Consistent with the previous chapter, the PG is used to measure the negative vertical component of the surface electric field. Cumuliform clouds are categorised objectively based on the associated strength of the PG , measured at the surface, as well as the detection of charged rain, corona and lightning (§5.3). Three hypotheses are developed to explore the cloud-scale electrification processes within developing cumuliform clouds:

- 1. High moisture content within the ice phase of the cloud increases the amount of charge that can be separated between two colliding ice hydrometeors.**

Laboratory (Saunders, 2008) and field experiments (Gunn, 1956) have shown that ice-ice and ice-liquid collisions in a chaotic environment can separate enough charge to initiate lightning. In the initial development stages of a cumuliform cloud, where only liquid water exists, the PG would usually not be strong enough to polarise liquid drops. Both the inductive and non-inductive charging mechanisms could not exist at this early

stage. Other methods such as the convective (Vonnegut and Moore, 1962) and unpolarised ion capture (Frenkel, 1947) mechanisms could generate a small amount of charge in the early stages of a cumuliform cloud but are unlikely to be detected by ground-based measurements. Therefore, by the time a cumuliform cloud has developed the inductive and non-inductive charge separation mechanisms would allow sufficient charge generation to be detected at the surface (Saunders, 2008).

2. The mean and standard deviation of hydrometeor size is directly proportional to the amount of charge within the cloud.

Within the ice phase of the cloud, the main electrification mechanism requires the collision between two hydrometeors of differing sizes (Saunders, 2008). According to the relative diffusional growth rate theory (Emersic and Saunders, 2010), an exchange of mass and charge occurs upon collision. If the hydrometeors are of equal size, no net charge would be exchanged between hydrometeors. Only when hydrometeors of differing sizes collide could a net charge be exchanged.

For the liquid phase of the cloud, coalescence and the breakup of drops is a significant limitation for charge separation. There are two main outcomes during a collision: first, the coalescence of the drop, especially for similarly sized drops; and second, rebounding drops, especially with differing sized drops. The size and density of drops would increase the optical density of the cloud, thereby increasing the probability for collisions to occur. The rapid growth and deformation of hydrometeors can provide a large distribution of sizes perfect for charge separation to occur.

The radar reflectivity (Z) is strongly dependent on the hydrometeor size (sixth power) and number concentration (first power) within a volume of space (Fabry, 2015a). Therefore, the total electrification of a cloud is hypothesised to be related to Z .

3. Turbulence within a cumuliform cloud increases the rate of collisions between hydrometeors and so increases the amount of charge within the cloud.

The most common method for charge separation involves the collision between hydrometeors of various sizes and phases. For a collision to occur, two hydrometeors must be travelling along intersecting trajectories. Previous evidence (Mareev and Demytyeva, 2017; Renzo and Urzay, 2018) has suggested that turbulence can increase the rate of collisions between hydrometeors, caused by the hydrometeors travelling in random directions. Smaller sized hydrometeors are thought to be preferentially

captured, weighted by the size of the most prominent eddy in the cloud. Larger sized hydrometeors would not be captured and instead gain momentum colliding with the captured hydrometeors (Renzo and Urzay, 2018). The preferential capture of the hydrometeors provides a simple way to form charge centres within the cloud of a single polarity. If the charge centres of different polarities were substantially separated in space, the PG would be enhanced, possibly enough for atmospheric breakdown allowing lightning to form.

Theoretical (Renzo and Urzay, 2018) and experimental (Cimarelli et al., 2014; Mareev and Dementyeva, 2017) observations of turbulent electrification showed many charge centres could exist within the cloud separated in both vertical and horizontal spatial directions. Observations by Cimarelli, et al. (2014) showed the number of electrical discharges increased as turbulence increased in artificially created volcanic plumes. Linking with cloud electrification, the particle size, number concentration, and turbulence within the volcanic plume was found to be positively correlated with the amount of charge that could be generated. Similar conclusions were found from theoretical modelling of cumuliform clouds by Mareev and Dementyeva (2017), particularly for the inductive mechanism. Therefore, turbulence within the ice phase is important for enhancing cloud electrification. Regions of higher turbulence within the cloud might also be co-located with charge centres within the cloud.

For this chapter, a JCI 131 electric Field Mill (FM) and a Biral Thunderstorm Detector (BTD) was installed at Chilbolton Observatory (CO) as part of a field campaign to investigate the processes required for cloud electrification. The FM measures the PG , while the BTD measures the electric current, j . These electrical instruments were compared with the 35 GHz Copernicus Doppler radar (henceforth 'radar') and a Vaisala CT75K ceilometer (henceforth 'ceilometer') to allow comparisons of the interior of charged cumuliform clouds. These instruments are discussed in further detail in §3 along with the data processing methods used prior to testing the hypotheses set out in this chapter.

The field campaign lasted for nearly two years (06/10/2016 – 19/06/2018) which allowed the identification of 653 charged cumuliform clouds (§5.2). The advantage of using a long dataset allowed the identified clouds to be grouped by the level of electrification (§5.3). A disadvantage of using surface and remote based instruments is that only an estimate of the charge and characteristics of a cloud could be made. Nevertheless, the data collected from this field campaign was capable of sampling clouds at all life stages with different synoptic conditions

throughout the year. The wide sampling of clouds has made it possible to provide a general overview of the main processes required for cloud electrification, along with confidence intervals of their importance. The next chapter aims to resolve the limitations of estimating the electrical and characteristics of the cloud by making in-situ measurements into charged cumuliform clouds using ten radiosondes (§6).

5.2 Cloud Identification Algorithm using Radar and Ceilometer Data

A cloud identification algorithm was designed in this thesis to identify cumuliform and frontal clouds in the radar situated at CO to test the hypotheses discussed in §5.1. The algorithm was designed to be as simple as possible, using two thresholds to identify a cumuliform cloud. This method was used to enable an objective method for the preliminary selection of cumuliform clouds as the radar is only capable of sampling a slice of a cloud that moves overhead of CO. In addition, data from the ceilometer was used, as it is a reliable instrument in detecting the presence of a cloud and provides cloud base information, typically not available from the radar. Overall, to identify a cloud using the radar and ceilometer data, five steps were used (see Figure 5-1 for a flow diagram of the algorithm):

1. Identify a cloud using the cloud base height data from the ceilometer.

When a cloud has not been detected by the ceilometer, no measurement of the cloud base height is given. The first criterion looks for contiguous cloud base heights, with missing values in the dataset acting as a natural divider between clouds. The second criterion looks for when a cloud base height was only detected for a short amount of time (< 7.5 minutes) to remove any anomalous measurements by the ceilometer and to focus on well-defined clouds, which have a large horizontal width.

2. Calculate the cloud top heights for each identified cloud.

The wavelength transmitted by the ceilometer is too small (905 ± 5 nm) to penetrate far into the cloud due to attenuation and cannot be used to detect the height of the cloud top. Therefore, Z is used to estimate the cloud top height. An issue occurs when multiple cloud layers exist and differentiating between clouds can be difficult, especially if the height difference between clouds is small. To overcome this issue, the cloud top height is defined as the lowest height when no cloud is measured by the radar for the entire width of the cloud. Therefore, if there is a single height layer with no measured Z , this height is used as the cloud top height.

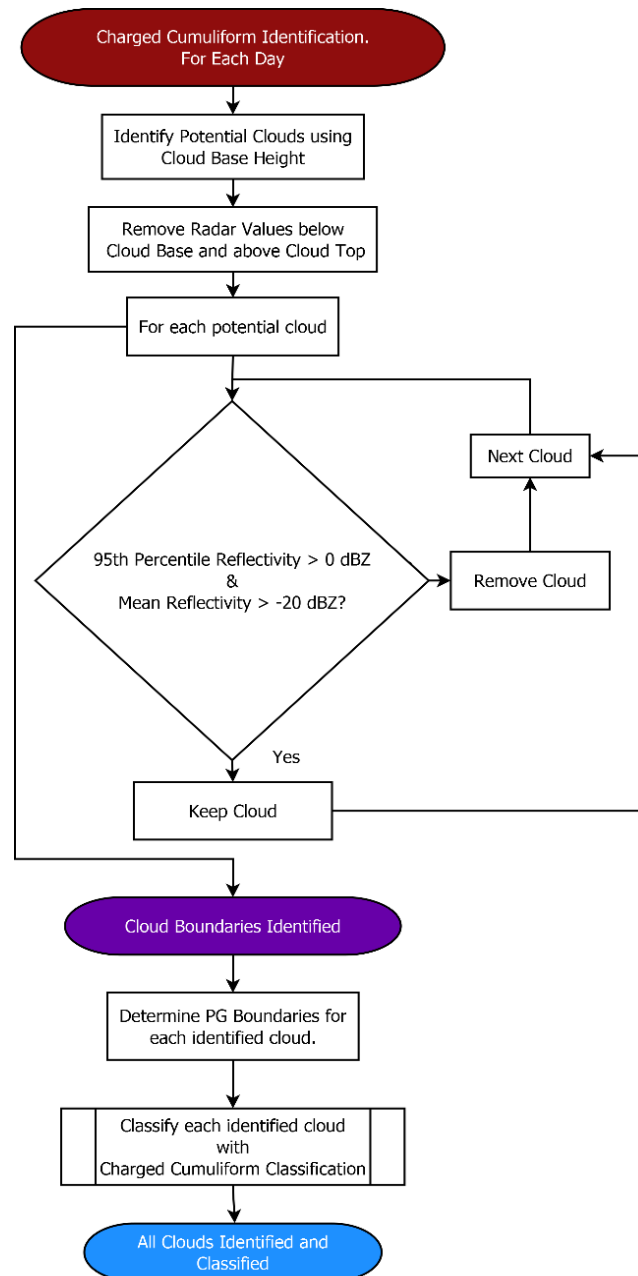


Figure 5-1: Flow diagram for the cloud identification algorithm (see text for description of each stage).

3. For each cloud identified, determine if the cloud satisfies two Z criteria.

The Z was used to test whether a cloud was cumuliform by looking at two parts of the Z distribution. First, the 95th percentile Z was used (> 0 dBZ), rather than the maximum Z, to avoid any extreme single values in the data. Second, the mean Z was used to define clouds with a consistently high Z. A low threshold of -20 dBZ was used to compensate for the low Z values near the cloud boundaries (around -40 dBZ) which would skew the average value. These criteria provide good segregation between cumuliform clouds and other cloud types, which are not actively separating charge (Dye et al., 2007).

4. Determine the *PG* boundaries for each identified cloud.

The charge residing in a convection cloud can perturb the *PG* substantially, in both magnitude and time. The length of time the *PG* is perturbed is often longer than the cloud can be identified with the radar. This means the time boundaries of the *PG* must also be identified separately to associate the influence of a cloud with the surface *PG*.

The *PG* perturbation caused by the charge within the cloud is proportional to the inverse square distance between the observer and the charge as stated by Coulomb's Law. Therefore, the size of the charge within the cloud is directly related to the width of the *PG* boundaries. An approximation for the charge within the cloud is to use the *PG* range (max-min). From the manual identification of 264 case studies, a relationship was found between the *PG* range and *PG* time length as measured by the FM (Figure 5-2). The relationship is poor, partially because the size of the *PG* perturbation is strongly related to the position, size, and velocity of the charge within the cloud. All of these variables are difficult to determine prior to the cloud being identified. If multiple charge centres exist within the cloud of opposite polarity, the magnitude of the *PG* range can be greatly suppressed depending on the charge centre's horizontal separation. Nevertheless, the weak relationship between the *PG* range and the *PG* width can be used to provide time boundaries for each identified cloud from the cloud identification algorithm as long as an overestimation is used to ensure the *PG* perturbation is fully captured.

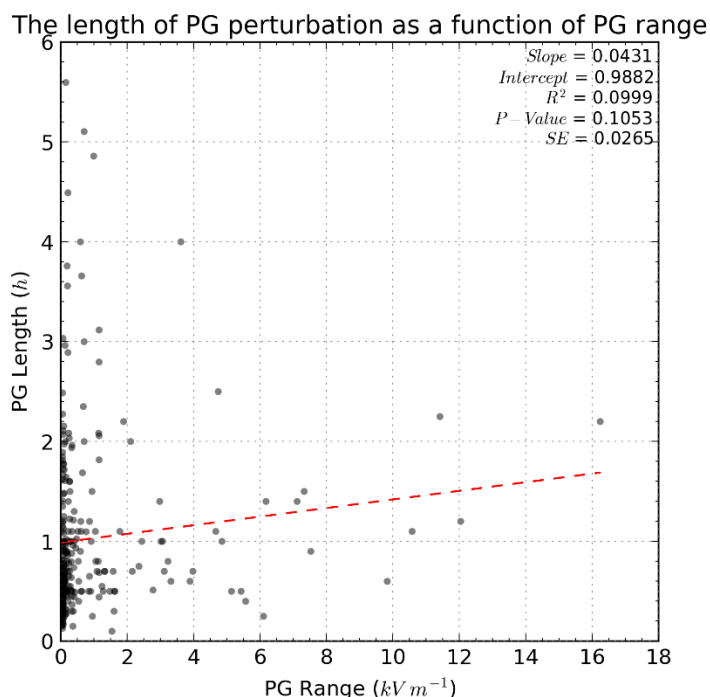


Figure 5-2: The *PG* time length as a function of *PG* range (max-min) for 264 manually identified clouds.

5. Calculate the Charged Cumuliform Cloud Classification for each identified cloud.

To help understand how a cumuliform cloud develops over time, a classification was created which groups the case studies into three categories depending on the level of electrification. This is known as the charged cumuliform cloud classification and is discussed in more detail in §5.3.

Figure 5-3 shows radar, ceilometer and FM measurements taken on 09/09/2017 and 31/01/2017 highlighting the cloud identification algorithms capabilities. Figure 5-3a provides an example of when a thunderstorm passed CO at 1330 UTC. All cumuliform clouds measured during this day were successfully identified by the cloud detection algorithm (highlighted by the red boxes). The cloud at 0330 UTC was originally detected as a cloud but did not satisfy the Z criteria. On 31/01/2017 (Figure 5-3b), the cloud detection algorithm identified a cloud that occurred for the entire 24 hours as there were no breaks in the cloud according to the ceilometer. As this chapter focuses on cumuliform clouds which influence the surface PG (e.g. Figure 5-3a), and less on clouds with a wide horizontal width (e.g. Figure 5-3b), a threshold was used remove extreme cloud cases (> 23 hours). Using this threshold is further justified as the cloud on 31/01/2017 had a negligible influence on the surface PG .

Overall, 689 clouds were identified from between 06/10/2016 and 19/06/2018. A histogram (Figure 5-4) of the cloud length shows that over 50% of the clouds had a cloud length less than 3 hours (50.76%) suggesting the majority of the clouds are inherently cumuliform. 36 clouds were detected having a cloud length longer than 23 hours and are substantial with respect to the neighbouring cloud lengths. A spike at the tail of a histogram provides a strong sign of data truncation, as the average counts over the previous 10 hours are less than 20 clouds per bin.

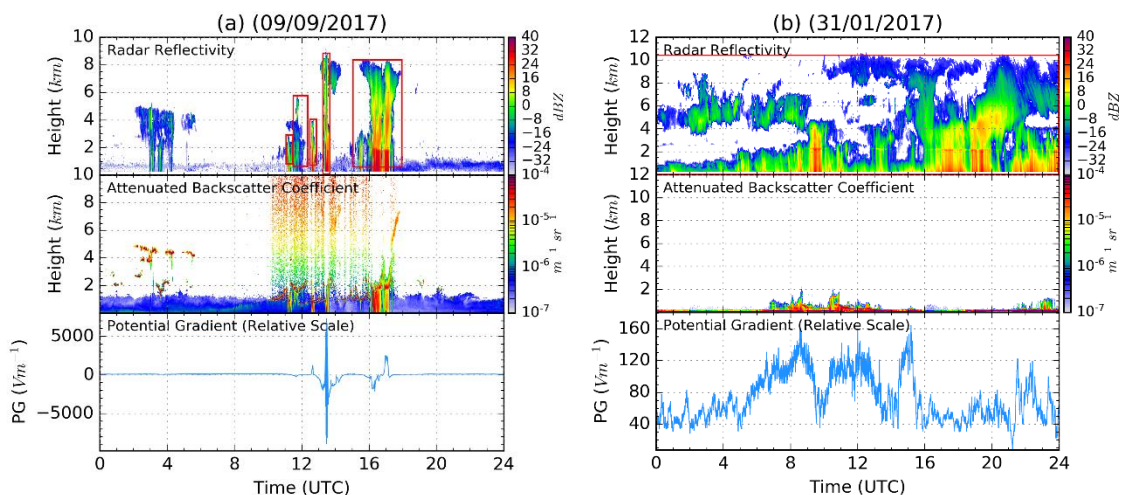


Figure 5-3: The cloud identification algorithm for two days showing (a) cumuliform clouds (2017/08/31) and (b) frontal clouds (31/01/2017). From top to bottom the plots show the radar reflectivity, terminal fall velocity, attenuate backscatter and the potential gradient. The red boxes are the bounding boxes for each cloud that has been identified.

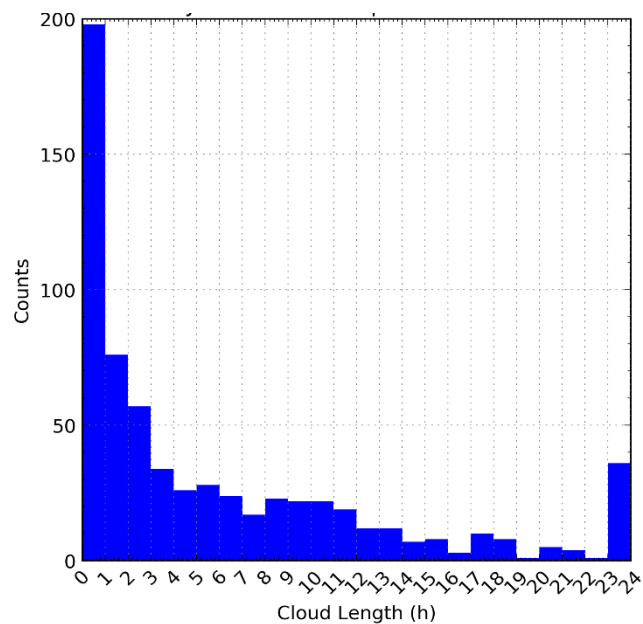


Figure 5-4: A histogram showing the cloud lengths for all 689 detected clouds from the cloud identification algorithm. Therefore, any clouds with a length longer than 23 hours were removed from further analysis, leaving 653 clouds for testing the hypotheses discussed in §5.1.

5.3 Classification of Convective Clouds at CO

To help test the three hypotheses defined in §5.1, an algorithm was designed to classify the amount of the charge inside the identified clouds. A charged cloud can be defined in two ways: first, the overall influence of the charge on the *PG*; or second, the sum of the net charges on each hydrometeor. The first description is easier to measure, as measurements of the *PG* were made using the BTM and FM at the surface. A problem with this approach requires a minimum charge to reside within the cloud before it can be detected at the surface, above the influence of space charge situated closer to the surface. This problem defines the upper limit of how far back in time a cumulonimbus cloud can be predicted to produce lightning. The exact time before a possible lightning flash would not be constant. Instead, the time depends on how fast the cloud generates charge in their development stage.

The second description (not used in the chapter) is complex to measure, especially without disturbing the environment which you are measuring (i.e. the cloud). This problem can be simplified by modelling the charge within the cloud. The modelling is achieved by inserting point charges into the cloud (used to represent the charge centres) and matching the model with the *PG* observations. The strength of the *PG* can be calculated by solving Coulomb's law for several point charges and optimising the position and magnitude of the charges by comparing with the measured *PG*. Calculating the approximate point charges has the additional benefit of determining the minimum charge threshold required to detect the charged cloud using surface-

based instrumentation. Determining this threshold can be used to resolve the problem from the first description.

The classification of charged clouds was achieved using the Z and PG (see Table 5-1 and Figure 5-5), with the criteria used for Z is consistent with §5.2. Figure 5-6 shows the distribution of Z measured for all 653 identified clouds between 06/10/2016 and 19/06/2018. The majority of Z measured was negative with a sharp decline at -30 dBZ. Using the distribution of Z , the thresholds for the mean and 95th percentile were defined around the central maximum at -5 dBZ to identify as many clouds as possible while removing the most non-cumuliform clouds (e.g. cirriform). As the clouds identified in the radar cover the entire life cycle of a cumuliform cloud, it was important to sample the full range of clouds. Using a low threshold for mean and 95th percentile Z allowed sampling of clouds even in their early growth stage. Using the PG range further helps to distinguish between cumuliform and non-cumuliform clouds, by increasing the contrast of the cloud characteristics important for charge separation.

The PG range and presence of either charged rain, corona or nearby lightning were used to help qualitatively classify the magnitude of the charge within the cloud. The PG naturally varies in time, caused by fluctuations in space charge and conductivity. If a cloud was measured by the radar, any variations greater than 75 V m^{-1} were associated with charge inside the cloud. A PG range of 75 V m^{-1} was used, as this range is typically greater than the noise in PG variability caused by space charge near the surface. A PG range threshold was not set higher to avoid missing any charged clouds in the exceedingly early stages of development. The warning flags provided by the BTM were used to see if any charged rain, corona or nearby lightning were measured to classify a cloud as highly charged (Group 3). The identification of warning flags from the BTM and a PG perturbation $> 75 \text{ V m}^{-1}$ were used as confirmation of a highly charged cloud.

Table 5-1: The criteria for the charged cumuliform cloud classification. The statistics for Z were calculated only for cloud regions above and below the cloud base and top, respectively. The PG range and identification of charged rain, corona or nearby lightning was calculated by subsetting the data when the cloud was identified to exist in the radar data.

Criteria	Group 1: No Charge	Group 2: Small Charge	Group 3: Large Charge
95 th Percentile Z (dBZ)	> 0		
Mean Z (dBZ)	> -20		
PG Range (Vm^{-1})	< 75	> 75	
Charged Rain, Corona or Nearby Lightning (< 18 km)?	No		Yes
Number of cases	129	314	210

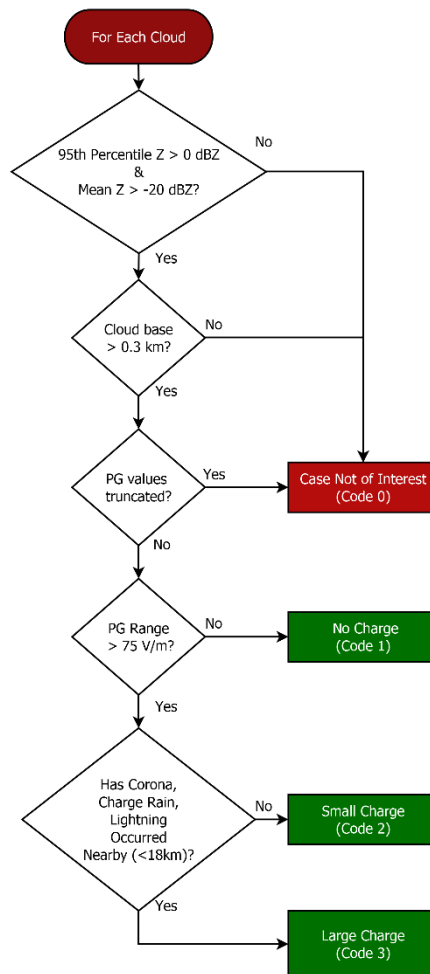


Figure 5-5: Flow diagram of the classification of convective clouds, used to highlight the electrification within.

A second classification was used to compare the differences between the liquid and ice phases. Figure 5-7 shows a conceptual diagram of a cloud which has been separated into the ice phase (blue) and liquid phase (purple) with the freezing level acting as a divider (dashed line). The purpose of considering the liquid and ice phases of the cloud separately was to understand whether the non-inductive or inductive charge separation mechanisms were important in the electrification of a cloud. The next section contains an analysis of four case studies, which measured cumuliform clouds with different electrical and cloud characteristics, used to highlight the main conditions required to electrify a cloud.

5.4 Case Study Analysis

Measurements of the surface *PG* can be used to detect the charge present inside overhead cumuliform clouds. The size of the *PG* perturbation caused by the charge inside the cloud can be compared with the cloud properties as measured by the radar. From analysing the case studies, the common and uncommon properties of clouds with different changes in *PG* can be evaluated. The cloud analysed in case study (1) is used as a baseline for a cloud, which can

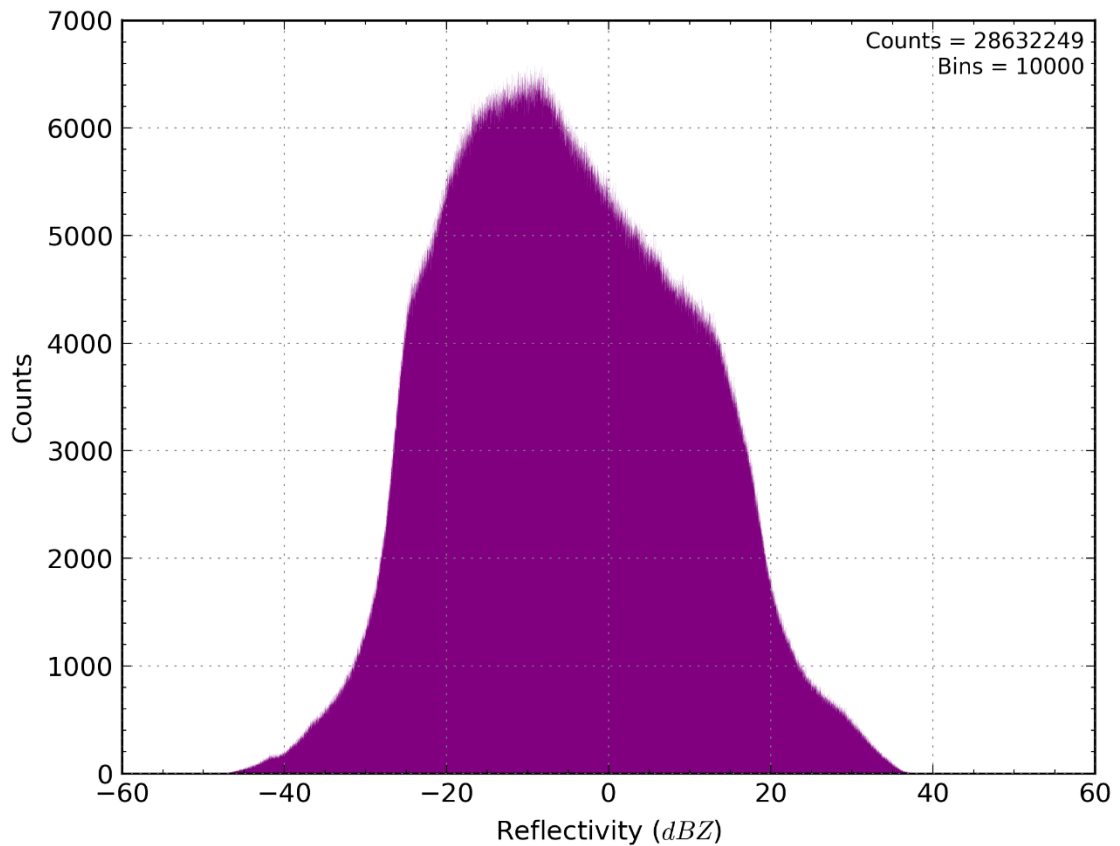


Figure 5-6: A histogram (10,000 bins) of the Z values (8,546,154) measured for all 653 identified clouds between 06/10/2016 and 19/06/2018. All Z values below the cloud base and above the cloud top were removed.

produce lightning. In case study (2), as the PG is negligibly perturbed but has appreciable cloud characteristics (e.g. high Z), hypotheses (1) and (2) are examined by comparing the importance of the ice phase with a high moisture content along with the hydrometeor size distribution for producing lightning. Case studies (3) and (4) are related to hypothesis (3) by comparing two clouds with a substantial PG , measured at the surface, with one cloud having appreciable turbulence (case study (3)) and one with negligible turbulence (case study (4)). Overall, understanding the processes which are necessary for electrification to occur (e.g. an ice phase, updraught, etc.) and which processes are more important can help in the prediction of lightning.

Many of the radar measurements used to characterise the condition of a cumuliform cloud are used throughout these case studies and are later used in the hypothesis testing section (§5.5). As the hydrometeor size has the biggest dependence on Z , an assumption was made that, on average, Z is directly related to the hydrometeor size. For most cumuliform clouds, Z usually decreased with height. There is often an appreciable reduction in Z above the freezing level as the typical shape of ice reduces the amount of radiation that can be reflected directly back to the radar. On average, there is a 7-dBZ difference between ice crystals and liquid drops of the same diameter (Fabry, 2015a). Once the Z discontinuity between liquid and ice phases becomes

negligible, the growth of ice (e.g. crystals, graupel, and hail) is substantial enough for the charge generated within the cloud to be easily measured at the surface. To analyse these case studies, several radar parameters are used, which include the Doppler velocity, \bar{v} , spectral width, σ_v , the standard deviation of the terminal fall velocity, σ_d , turbulent kinetic energy eddy dissipation rate, ε_r , and the cloud dimensions (e.g. cloud base). All these parameters are discussed in further detail in §3.4.1.

As discussed in §4, the variability of the *PG* perturbation is directly related to the proximity of the charge. Charge closer to the surface, such as space charge and rainfall, typically has higher variability than the charge within the cloud. The higher variability of space charge is caused by the velocity of the charge relative to the surface and the mixing of different polarities. The charge present within cumuliform clouds has a much greater distance to the surface and therefore, the FM. The charge distribution within a cumuliform cloud is typically more organised than space charge near the surface with separate charge centres containing mostly positive or negative charge. The combination of the distance between charge centres and the polarity residing in a finite region reduces the variability of the *PG* perturbation. The aim of these case studies is to explore the cloud structure and hydrometeor dynamics to understand why certain clouds become electrified. Table 5-2 provides descriptive statistics of the properties of the cloud that are thought to be important in understanding the development of charged cumuliform clouds.

Table 5-2: Descriptive statistics characterising the cloud conditions for all four case studies discussed in this section. The cloud has been subset into the liquid and ice phases.

Case Study	1			2			3			4		
	Whole Cloud	Liquid Phase	Ice Phase	Whole Cloud	Liquid Phase	Ice Phase	Whole Cloud	Liquid Phase	Ice Phase	Whole Cloud	Liquid Phase	Ice Phase
Cloud Region												
Maximum Reflectivity (dBZ)	39.9	39.9	36.8	39.0	39.0	22.3	16.2	10.4	16.2	33.9	33.9	24.4
Minimum Doppler velocity (m s⁻¹)	-10.45	-10.45	-7.97	-7.13	-7.13	-5.23	-3.85	-3.85	-2.45	-6.29	-6.29	-3.25
Maximum Doppler velocity (m s⁻¹)	5.34	3.20	5.34	1.72	1.72	0.18	2.56	2.17	2.56	0.75	-0.38	0.75
Maximum Spectral Width (m s⁻¹)	1.63	1.63	1.62	1.67	1.67	1.51	0.78	0.53	0.78	1.69	1.69	0.93
Maximum Eddy Dissipation Rate (ϵ_T) (m²s⁻³)	1.140	1.140	0.794	0.554	0.554	0.367	0.281	0.265	0.281	0.390	0.390	0.344
Maximum $\ddot{\epsilon}_T$ (m s⁻⁴)	0.032	0.032	0.022	0.010	0.010	0.010	0.010	0.010	0.009	0.012	0.012	0.011
Mean Standard Deviation of the Terminal Fall Velocity (m s⁻¹)	0.591	0.750	0.538	0.590	0.585	0.623	0.330	0.334	0.330	0.328	0.749	0.289
Maximum Cloud Depth (km)	3.85	1.08	3.60	3.0	2.15	0.93	1.60	0.06	1.41	3.35	0.53	3.03
Minimum Cloud Base Height (km)	0.87	-	-	0.37	-	-	0.79	-	-	0.33	-	-
Maximum Cloud Base Height (km)	2.37	-	-	2.47	-	-	1.54	-	-	2.42	-	-
Cloud Top Height (km)	5.55	-	-	3.48	-	-	2.79	-	-	3.90	-	-
Mean Freezing Level (km)	2.81	-	-	2.58	-	-	1.03	-	-	0.75	-	-
Maximum Rain Rate (mm h⁻¹)	28.1	-	-	11.0	-	-	0.0	-	-	2.7	-	-
Displacement Current Range (nA)	145.4	-	-	0.58	-	-	4.64	-	-	183.4	-	-
Potential Gradient Range (V m⁻¹)	7104.5	-	-	61.1	-	-	1351.5	-	-	9837.0	-	-

5.4.1 (1) Highly Electrified Cloud

Case study (1) examines a highly charged mature cumuliform cloud that was measured on 2017/08/31. The surface pressure analysis chart (Figure 5-8a) suggested the atmosphere was convectively unstable, with three troughs present in and around the UK. The passing of a long cold front (passing through France and Germany) brought in cooler air. The cooler air mixed with the surface heating during the day led to substantial convection. Despite a substantial amount of charge detected by the FM and BTM, the convective available potential energy (CAPE), convective inhibition (CIN) and lifting index²⁸ (LI) were fairly weak (CAPE = 69 J kg^{-1} , CIN = -23 J kg^{-1} , LI = $1 \text{ }^\circ\text{C}$) as measured by Larkhill radiosonde station (03743) at 1200 UTC (University of Wyoming, 2018). Satellite imagery of the UK (Figure 5-8b), one hour prior to the cloud pass, showed scattered clouds across most of the UK. The convection was unorganised over the mainland and is typically seen when LI and the surface wind speeds are low.

Figure 5-9 shows the radar (a-c), precipitation (d) and electrical (e-f) data measured during the passing of a highly charged mature cumuliform cloud at 1145 UTC. The cloud can be considered as a single-celled convective system with a maximum cloud top height of 5.6 km. A discussion of each measurement highlights the conditions required for substantial cloud electrification.

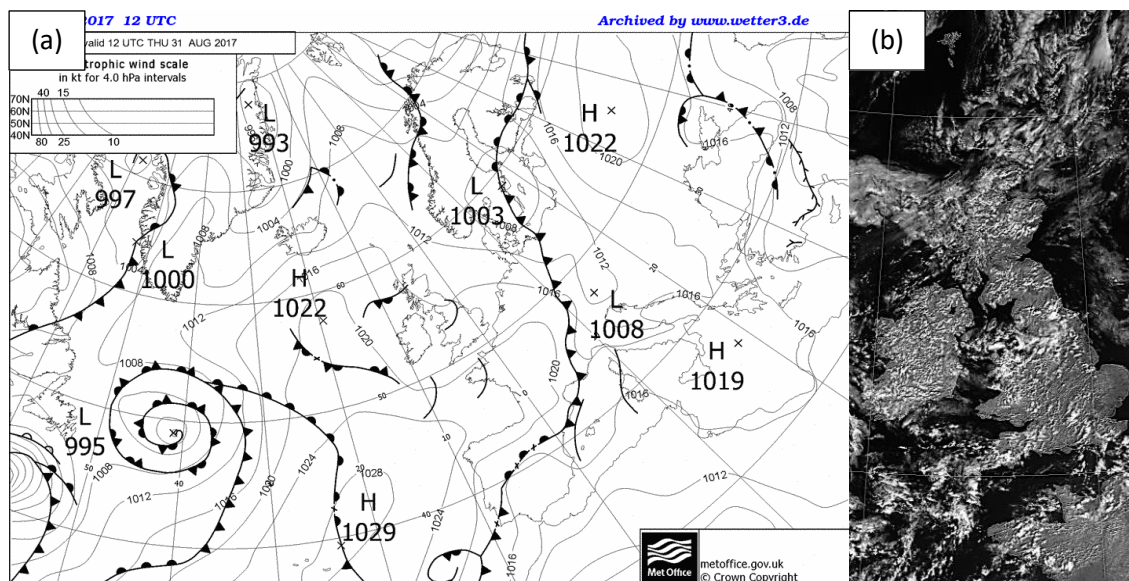


Figure 5-8: The synoptic conditions during the cases study on 2017/08/31. (a) The United Kingdom Met Office (UKMO) surface pressure analysis charts on 2017/08/31 1200 UTC (courtesy of www.wetter3.de/fax). (b) A near-infrared ($0.725\text{-}1.100 \mu\text{m}$) satellite image was taken at 2017/08/31 1043 UTC over the UK. The image was taken using the advanced very-high-resolution radiometer (AVHRR) aboard the NOAA-17 satellite (courtesy of NERC Satellite Receiving Station, Dundee University, Scotland (NEODAAS-Dundee, 2018)).

²⁸ The lifting index defines the atmospheric instability. It is calculated by finding the temperature difference between the environment and an air parcel lifted adiabatically from the surface to 500 hPa. Temperatures less than 0°C are considered unstable with colder temperatures increasing the probability for thunderstorms to occur.

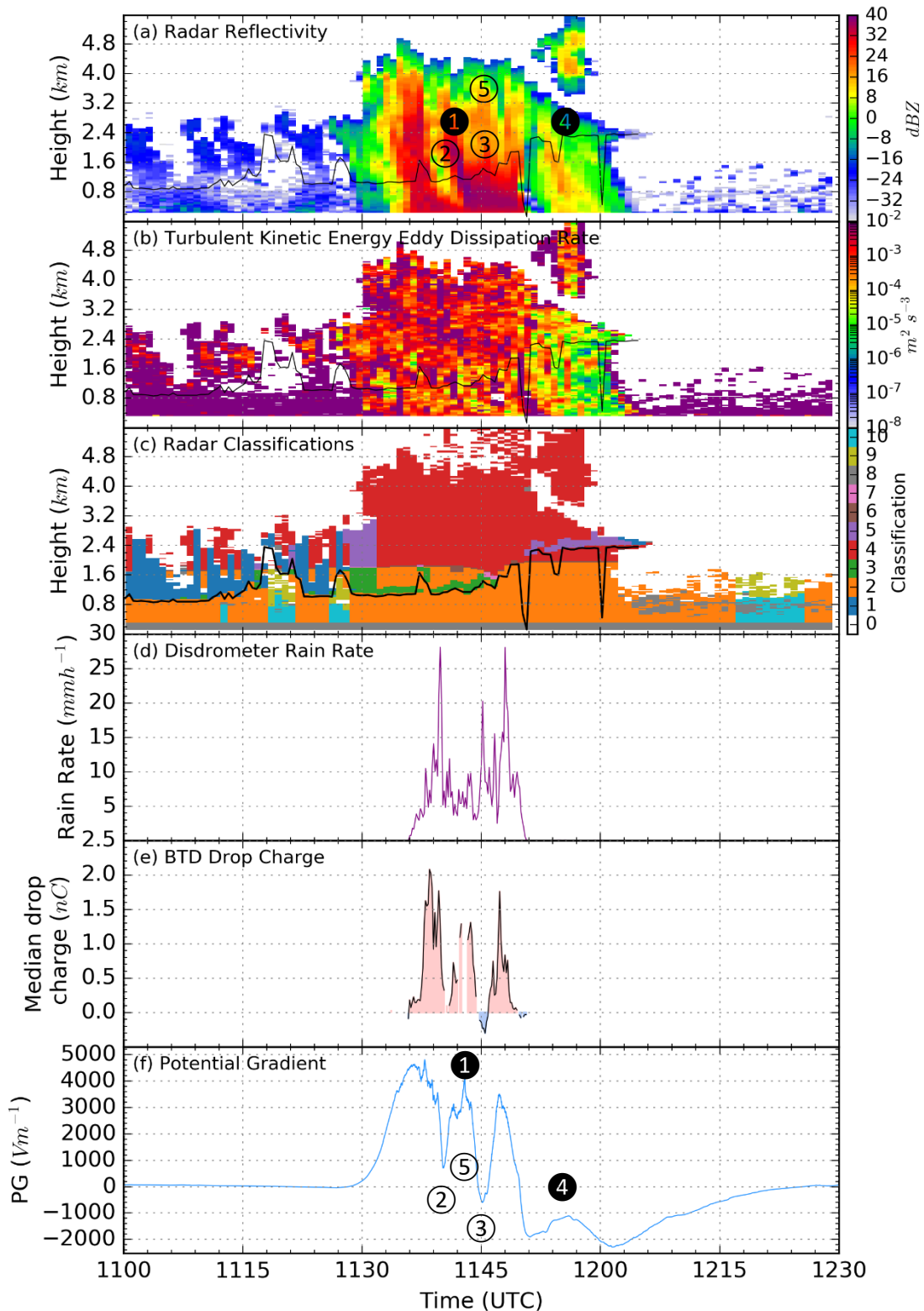


Figure 5-9: An example of a highly charged mature cloud that was measured at CO on 2017/08/31 between 1100 and 1230 UTC. The figure shows Z (a), ϵ_T (b), hydrometeor classification (c), RR measured by the disdrometer (d), median drop charge measured by the BTD-300 over a 10 second period, (e) and PG (f). The cloud base as measured by the Vaisala CT75K ceilometer is plotted on the radar subplots (a-c) (black line). The numbers ① – ⑤ represent the estimated positions of the positive (black numbers) and negative (white numbers) charge centres residing within the cloud (f). The legend for the radar classifications is given in Appendix C.

The PG shows five marked turning points that are labelled ① - ⑤ in Figure 5-9f. These turning points suggest at least five charge centres existed within the cloud. This is caused by the superposition of the PG produced by each charge centre forming the complex structure observed in the surface PG . The labels ① - ⑤ defines the location of the charge centres within the Z (Figure 5-9a) and PG (Figure 5-9f) plots. The low-frequency PG perturbations showed several turning points that were unlikely to be caused by any other charge source, other than from charge residing within the cloud. The frequency of the PG variations is proportional to the velocity and inversely proportional to the distance of the charge with respect to the surface. As the cloud can be assumed to be travelling at a uniform velocity throughout the cloud, the frequency of the PG variations is inversely proportional to the distance of the charge. The greater the distance of charge from the surface, the smaller the frequency (i.e. the wider the PG perturbation).

Another relationship can be seen between the drop charge (Figure 5-9e) and the PG (Figure 5-9f). The magnitude and polarity of both measurements are closely related. The close relationship is caused by the liquid drops being polarised by the enhanced PG . The charge within the drop is reorganised along PG lines with the lower half of the drop containing the same polarity of charge as the polarity of the PG . The spatial difference between charge polarities within the drop causes the charge at the bottom of the drop to be detected with greater influence.

There was a substantial Z (Figure 5-9a) near and below the cloud base (max. 39.9 dBZ). In this case study, the maximum Z in the ice phase was 36.8 dBZ compared to the liquid phase of 39.9 dBZ. The Z was not uniform throughout the cloud with noticeable vertical bands extending into the ice phase of the cloud. As discussed previously, the Z also decreases with height, but a high Z (> 30 dBZ) can still be observed in the lower regions of the ice phase (2 km) which is a common observation in mature charged cumuliform clouds.

Figure 5-9b shows a substantial ϵ_T throughout most of the cloud ($> 10^{-3} \text{ m}^2\text{s}^{-3}$) with a maximum ϵ_T of $1.140 \text{ m}^2\text{s}^{-3}$. The variability of the turbulence, $\ddot{\epsilon}_T$ was also quite substantial at 0.032 m s^{-4} . The variability in ϵ_T might have resulted in the formation of multiple charge centres within the cloud, resulting in the complex PG structure observed. The hydrometeor classification (Figure 5-9c) shows both ice (code 4, red) and liquid (code 2-3, orange/green) phases existed in this cloud. The ice phase had greater depth than the liquid phase for the entire width of the cloud. The liquid phase only existed for the lower cloud base region. No supercooled liquid water was detected for the left-hand side of the cloud coinciding with the positive PG perturbation. There

was a substantial increase in cloud base height (1.4 km) between 1145 and 1200 UTC (see Figure 5-9c) which suggests that both updraughts and downdraughts existed; downdraught in the left-hand side of the cloud, updraught in the right-hand side of the cloud. The asymmetry of the cloud base can also be seen in the *PG* perturbation. The maximum *PG* perturbation occurred at 1140 UTC when the cloud base was lowest²⁹.

The *RR* (Figure 5-9d) was substantial during this case study (max. 28 mm h⁻¹) matching the close relationship between drop size and *Z* (Marshall and Palmer, 1948). The precipitation was also found to be highly charged (Figure 5-9e) which is common for the *RR*s observed in this study (Bennett, 2018). Over 2 nC of charge was measured peaking at 1138 UTC associated with a substantial *PG* perturbation exceeding 1 kV m⁻¹; this is much greater than the *PG* perturbations observed by uncharged precipitation at the RUAO (§4). Like the case study discussed in §4.3.2, the influence of precipitation can be observed near the turning points of the low-frequency *PG* perturbations. At these turning points, there was a substantial increase in the *PG* variability. From Figure 5-9d-e, the greater intensity and the charge on the precipitation coincide with the faster *PG* perturbations. The detection of charged rain might be related to the reduction of the cloud base. The melting ice charge separation hypothesis (§2.1.4) suggests that charged ice can descend through the cloud and melt below the freezing level, retaining its charge. The radar and ceilometer data show evidence for a downdraught in this region, near the location of three charge centres (①-③). It is quite possible that the charged rain originated from the ice phase that was precipitated through a downdraught out of the cloud.

After the cloud passed over CO, several lightning discharges were detected by the BTM (Figure 5-10). The time and location of the lightning flashes match up with the trajectory of the cloud. Using the steering level (700 hPa) wind direction (270°) and the wind speed (24.1 km h⁻¹) measured at Larkhill, the cloud coincides with two lightning flashes detected by the BTM (see the red-dashed box in Figure 5-10). This suggests that the observations of this highly charged cloud were representative of the conditions observed before (~30 mins) lightning was initiated.

The cloud described in this case study was one of three substantially charged clouds that were measured during the day (Figure 5-11). Clouds (A) and (C) are almost identical in shape, *Z* and *PG*. Cloud (C) showed evidence of being a cloud in an earlier development stage with a lower *Z* and a weaker *PG* perturbation with only two charge centres. The similarities of the shape of the

²⁹ There are anomalous measurements in the cloud base (spikes, see black line in Figure 5-9c). For example, the cloud base is anomalous at 1151, 1154, 1200 UTC and are disregarded from this analysis in this case study.

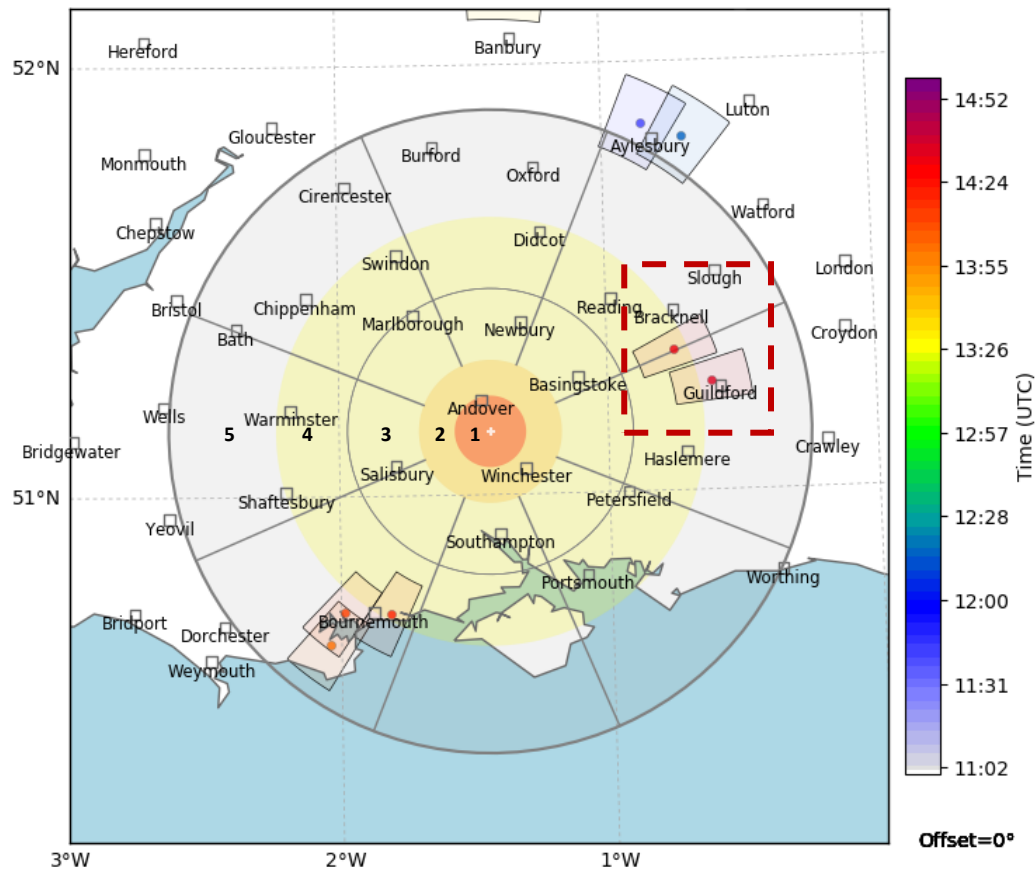


Figure 5-10: The location of lightning flashes (solid points) and the 95% confidence limits (shaded boxes) detected by the BTD in the south of England on 2017/08/31 between 1100 and 1500 UTC. The circles represent the distances from CO (white crosshair) and are used for various warning flags. The distance between each sector 1, 2, 3, 4, 5 and CO are 9.26, 18.52, 37.04, 55.56, 83.34 km respectively. The red-dashed box represents the lightning flashes of interest (see text).

PG perturbation between clouds (A) and (C) are comparable: both showed a skewed negative dipole in the *PG*.

5.4.2 (2) Developed Cloud with no Measurable Electrification

Case study (2) examines a substantially developed cloud, as described by Z, without any substantially *PG* perturbations that occurred on 2017/07/27. Case study (1) provided a benchmark for a mature cumuliform cloud with the right synoptic conditions for lightning to be produced, at least in the vicinity. For this case study, a comparison with the case study (1) was used to understand which cloud properties (e.g. Z, ϵ_T) is important for charge electrification. The surface pressure analysis (Figure 5-12a) shows similar conditions to case study (1) with an elongated cold front passing over the UK leading to several troughs residing over the UK. The large spacing between isobars, suggests surface winds were also weak. The thermal-infrared AVHRR satellite image taken over the UK (Figure 5-12b) shows scattered clouds over the south of the UK. The image also suggests cloud top heights were particularly low (dark cloud features) across the south of the UK. The convective parameters measured from radiosonde flights at

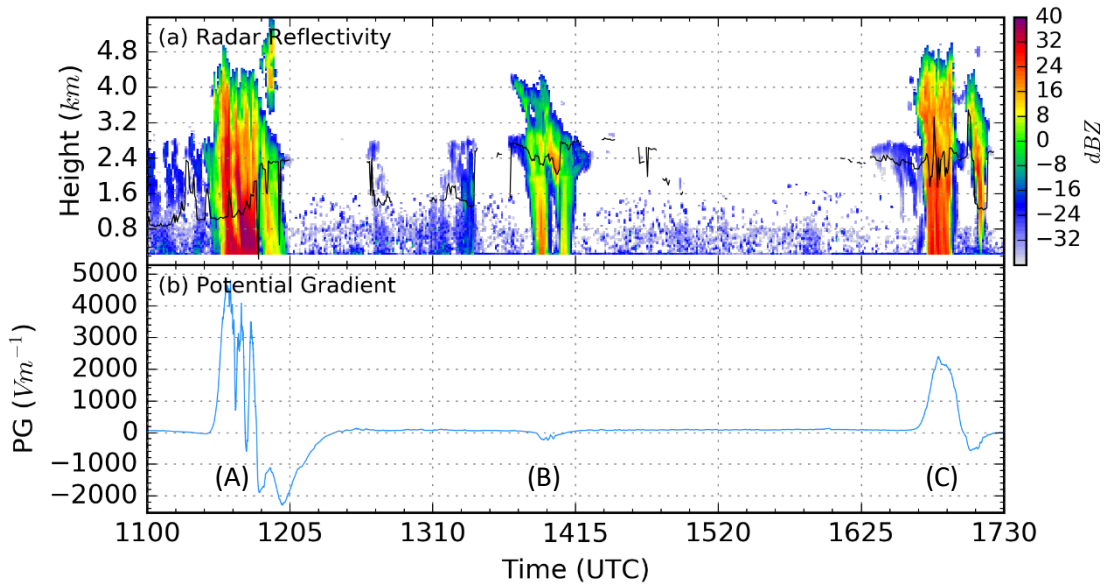


Figure 5-11: Time-series of three charged convective clouds ((A) – (C)) showing Z (a) and PG (b) on 2017/08/31 between 1100 and 1730 UTC. The cloud base height defined by the ceilometer is shown as a black line in (a). Cloud (A) is the same cloud discussed in this case study (Figure 5-9).

Camborne (03808) and Larkhill (03743) showed CAPE to be very weak at 19 and 5 J kg^{-1} measured at 0 and 6 UTC respectively. Although the convective parameters were weak measured at both Camborne and Larkhill, a substantially charged cloud (PG range = 5.9 kV m^{-1}) was measured at 1600 UTC with charged rain being measured by the BTM. The estimated CAPE measured by the radiosondes launched from Camborne and Larkhill was inconsistent with the convective activity observed during the day. This inconsistency was also present in case study (1), suggesting that for a cloud to become substantially electrified the strength of the convective instability at the synoptic-scale is less important in comparison to the dynamics that occur within the cloud.

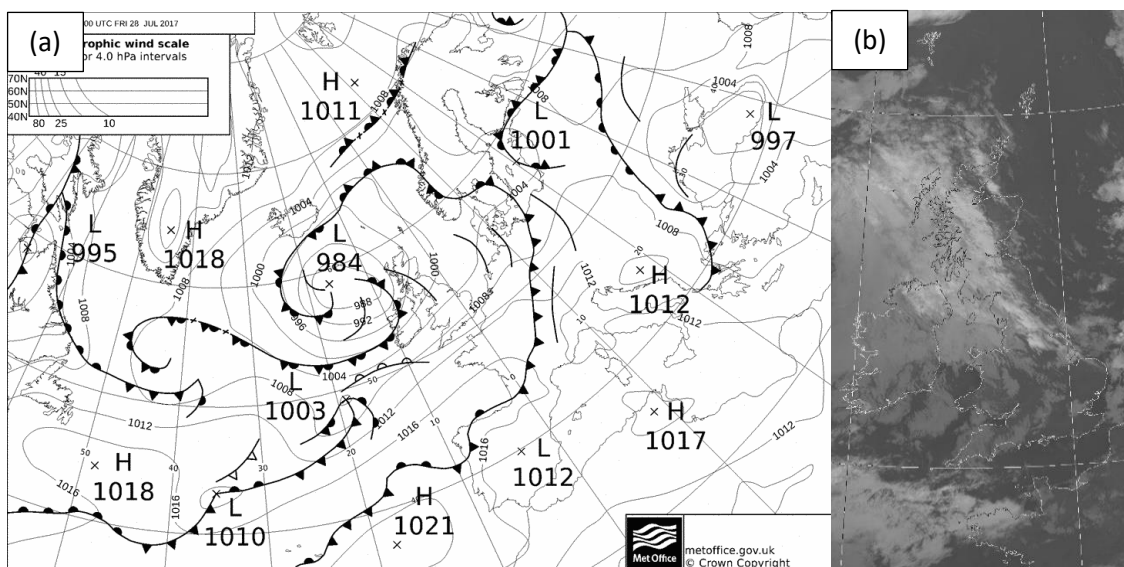


Figure 5-12: As for Figure 5-8 but for (a) 28/07/2017 0000 UTC and (b) a thermal-infrared (10.3 - 11.3 μm) satellite image on 2017/07/27 2058 UTC.

Figure 5-13 shows the radar (a-c), precipitation (d) and electrical (e) data during the passing of a negligibly charged cumuliform cloud at 2100 UTC. Overall, this case study describes another single-celled cumulus cloud with a cloud top height of 3.5 km. The Z (Figure 5-13a) measured from this cloud was comparable to case study (1) in the liquid phase. In the ice and liquid phases, the maximum Z was measured as 22.3 and 39.0 dBZ respectively. In case study (1), the maximum Z was 39.9 dBZ and was higher in both phases of the cloud (see Table 5-2 for descriptive statistics).

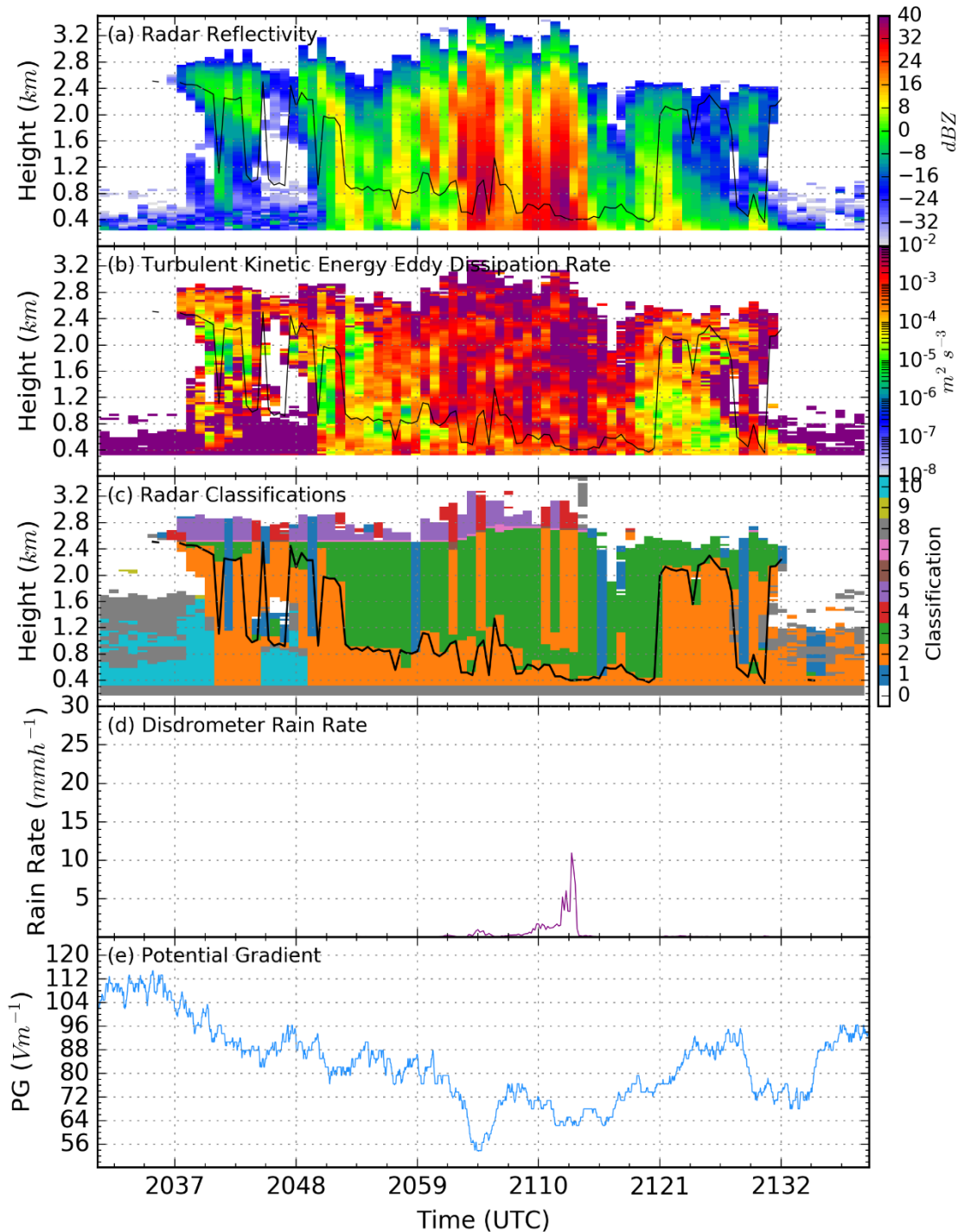


Figure 5-13: As for Figure 5-9 but for 2017/07/27 between 2030 and 2140 UTC.

Visually, ε_T (Figure 5-13b) was very similar between case studies (1) and (2), particularly for the central cloud region with ε_T above $10^{-3} \text{ m}^2\text{s}^{-3}$. The maximum ε_T though was substantially different between case studies (1) and (2), especially in the ice phase with a 74% reduction in (2). The comparison between case studies (1) and (2) showed that $\ddot{\varepsilon}_T$ was lower for both liquid and ice phases (104% and 75% difference respectively). An appreciable reduction in ε_T and $\ddot{\varepsilon}_T$ suggest the hydrometeor collision efficiency was reduced with less hydrometeor mixing occurring within the ice phase of the cloud, inhibiting the enhancement of the PG .

A stark difference between case studies (1) and (2) can be seen in the depth of the ice phase. In this case study, the ice phase depth had a mean of 0.43 km while in the case study (1) a depth of 1.57 km was measured. As other researchers (Stolzenburg and Marshall, 2008; Saunders, 2008) have suggested, charge generation is more important within the ice phase of the cloud. The lack of perturbation of the surface PG suggests a cloud must contain an ice phase with a depth greater than 0.43 km in order for a cloud to become substantially charged. Another appreciable difference between case studies (1) and (2) was the velocity of the hydrometeors. For \bar{v} , the ice phase had a smaller maximum velocity of 0.18 m s^{-1} ; a difference of 97% with respect to case study (1). In case study (1), \bar{v} was most likely limited by the design of the radar, which has a maximum velocity range of around $\pm 10 \text{ m s}^{-1}$, so the percentage difference might be even higher. As the maximum \bar{v} was very low (0.18 m s^{-1}) it can be assumed that no substantial updraught existed within this cloud.

The spectral width, σ_v was the only property similar between case studies (1) and (2) with σ_v in the liquid phase greater for this case study. As discussed in §3.4.1, σ_v can be decomposed into three terms. As the amount of turbulence decreased and the beam broadening can be assumed constant, most of the difference between case studies (1) and (2) can be associated with an increase in σ_d . Having a wide hydrometeor distribution is thought to be a requirement for sufficient electrification to occur in most cumuliform clouds (Emersic and Saunders, 2010). Therefore, the depth of the ice phase might have a stronger relationship with the electrification of the cloud, masking the benefits of increasing the hydrometeor distribution, at least for this cloud system.

The disdrometer measured precipitation during the cloud pass with a maximum RR of 11.0 mm h^{-1} . Despite the high RR , typically associated with cumuliform clouds, there was negligible perturbation in the PG , due to the precipitation, with no charged rain being detected by the BTD . According to the averaged relationship between the PG and RR measured by the disdrometer (see Figure 4-12), the PG should be below 0 V m^{-1} for all RR s above 1 mm h^{-1} if no

other substantial charge perturbs the PG (e.g. charge within the cloud). Figure 5-13e shows the PG was always above 0 V m^{-1} , suggesting precipitation had little effect on the PG during this event. No lightning discharges were measured by the BTM near CO for any cloud measured on the 2017/07/27. The high RR , Z , and \bar{v} suggest this cloud was in the mature life stage. The lack of PG perturbation also suggests that this cloud would not become substantially charged, unable to produce lightning.

The variability of the PG also decreased when the cloud was overhead as measured by the BTM. The current, j_{tot} , measured by the primary sensor of the BTM (Figure 5-14a) shows a smaller variation when the cloud was overhead and was found to be statistically significant using Levene's equality of variance test (W statistic = 46117, In Cloud Sample Size = 332617, No Cloud Sample Size = 1108283, $p < 0.001$). The suppression of the PG variability can be observed in the Fourier transform of j_{tot} (Figure 5-14b). Between 2110 and 2120 UTC there was a marked reduction in amplitude for all frequencies. A variability of less than 2 Hz can be associated with space charge variability, near the surface, and is often the main source of charge variability during fair-weather. Space charge near the surface is observed as a continuous red band at the bottom of Figure 5-14b.

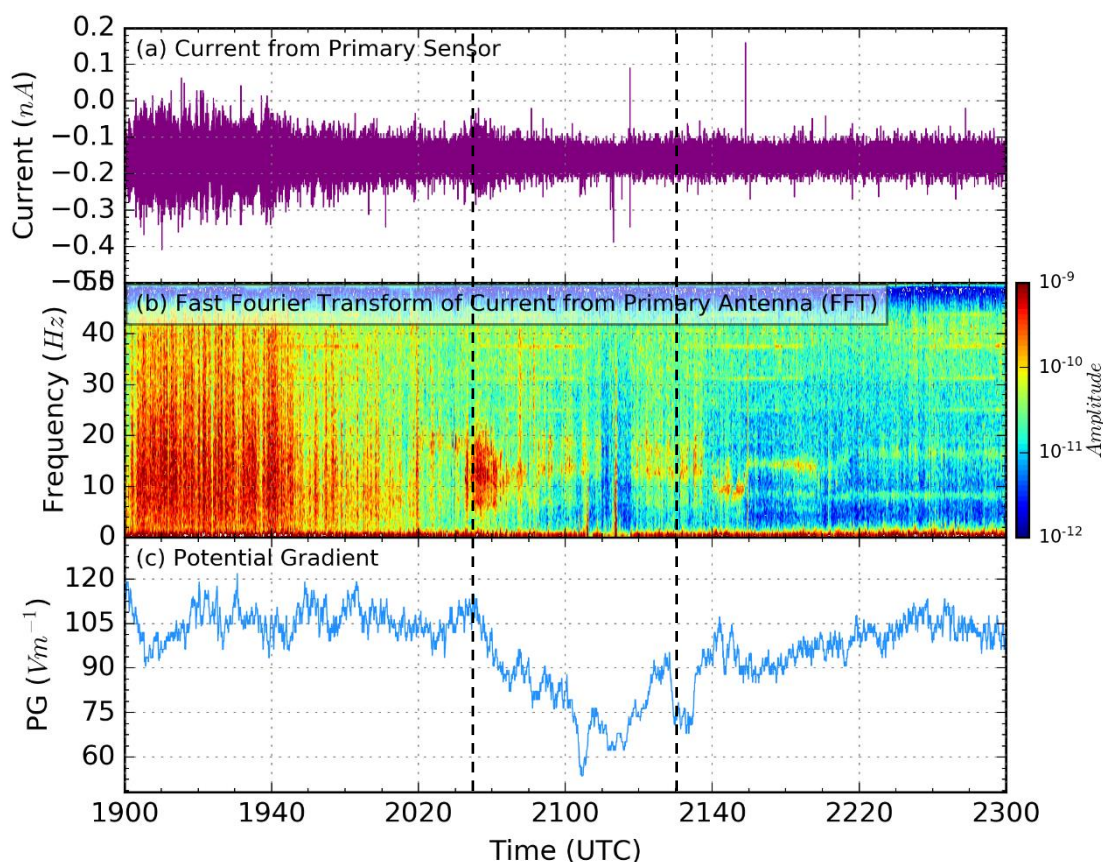


Figure 5-14: The measurements of the PG on 2017/07/27 between 1900 and 2300 UTC. The plot shows the current (a), current FFT (b) and potential gradient (c). The start and end times of the cloud pass are shown using the vertical black dashed lines.

For case studies (3) and (4), how ε_T can influence the electrification of a cumuliform cloud is investigated. Two cases are examined, one with substantial turbulence (3) and one with negligible turbulence (4). These two cases have similar PG perturbations that allow an assessment of turbulence on cloud electrification. Similarly, the first two case studies had comparable Z , which allowed the variations in PG to be investigated.

5.4.3 (3) Cloud Turbulence and Appreciable PG Perturbation

Case study (3) examines a cloud with appreciable ε_T , and with an appreciable negative perturbation of the PG measured on 2017/03/21. The surface pressure analysis (Figure 5-15a) at 0 UTC on 22/07/2018 showed an extratropical cyclone to the immediate west of the UK which crosses the UK during the same day. The pressure analysis agrees well with the thermal-infrared AVHRR satellite image (Figure 5-15b) capturing the cyclonic behaviour over the Irish Sea. A long band of cloud stretched over the west of the UK with cloud tops being heterogeneous and high (> 8 km). On the 2017/03/21, five scattered clouds were observed prior to the arrival of the cyclone at CO at 0445 UTC on the 22nd. All scattered clouds were appreciably charged, perturbing the PG above ± 1 kV m⁻¹.

For this case study, the last scattered cloud (2150 UTC) prior to the arrival of the cyclone provides an example of a small (cloud top = 2.8 km) single-celled cumulus cloud in its developing stages with an appreciable amount of turbulence and charge detected from the surface (Figure 5-16). This case study examines the conditions measured in the cloud, which were likely to lead to substantial electrification, relating back to case studies (1) and (2). A list of descriptive statistics describing the cloud can be found in Table 5-2 in relation to the case studies (1) and (2).

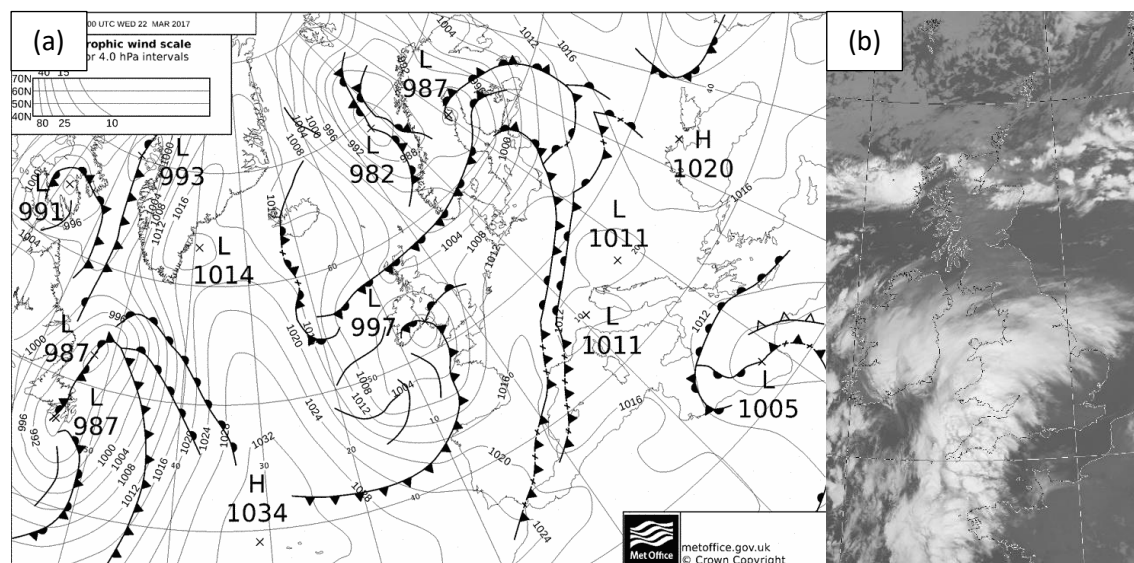


Figure 5-15: As for Figure 5-12 but for (a) 22/03/2017 0000 UTC and (b) 2017/03/21 2147 UTC.

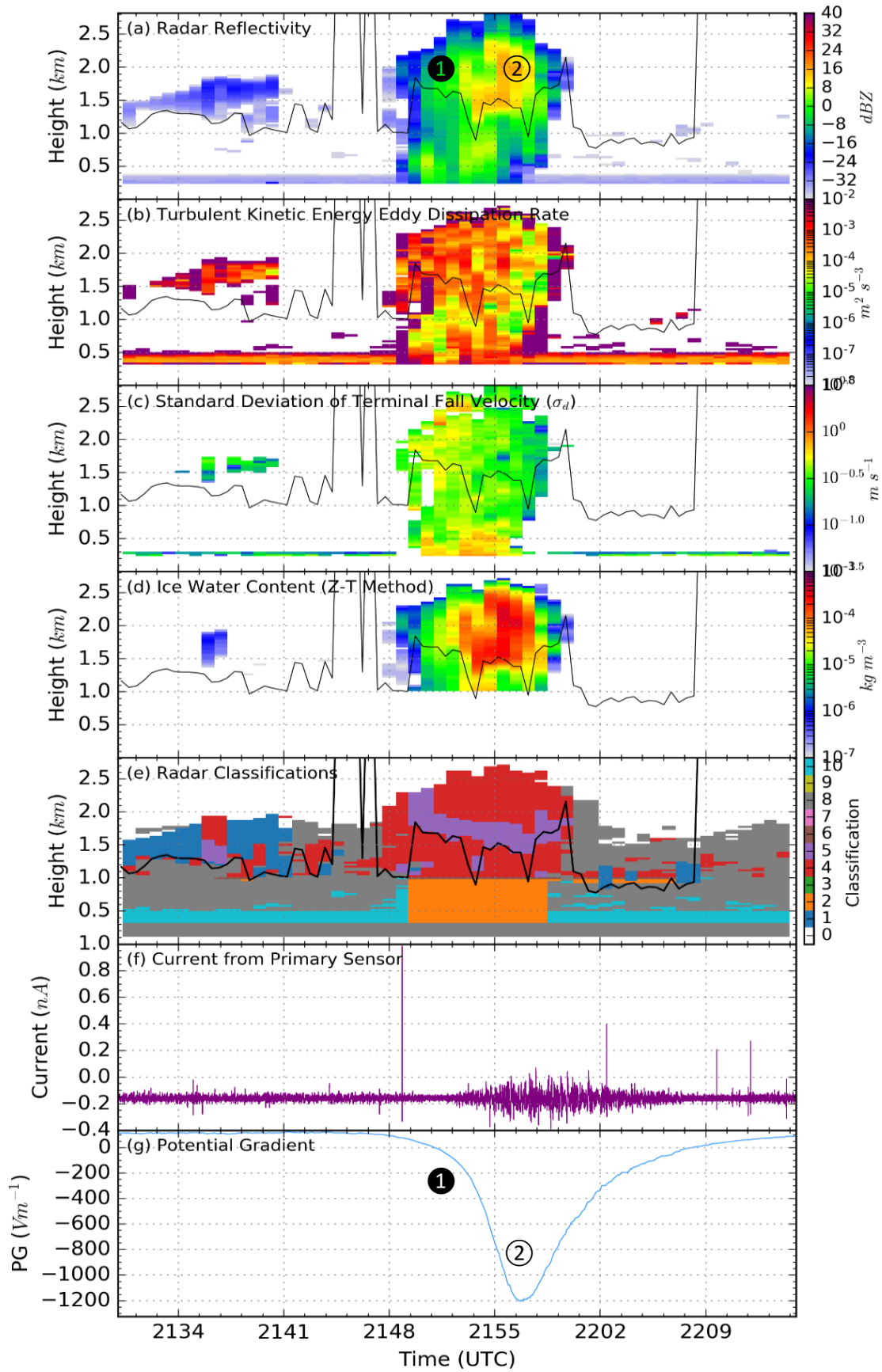


Figure 5-16: As for Figure 5-9 but for 2017/03/21 between 2130 and 2215 UTC with some exceptions. The standard deviation of the terminal fall velocity (c), ice water content (d) and electrical current measured by the primary sensor of the BT-D-300.

The PG (Figure 5-16g) shows a negative charge structure dominated by negative charge existed within the cloud. As the PG perturbation is not symmetrical, the positive charge centre ① resides within the left-hand side of the cloud, while the negative charge centre ② resides within the right-hand side of the cloud. The small perturbation of the positive charge on the PG suggests the positive charge was either poorly organised (i.e. resides over a wider area than the negative charge centre) or mixed with negative charge. In comparison to the case study (2), the electrical current, j_{tot} (Figure 5-16f) measured at the surface saw a substantial increase in the variability of the PG , which coincides with the negative PG perturbation (2153 – 2208 UTC; $j_{tot} = (1.807 \pm 0.008)$ nA). During the positive PG perturbation (2148 – 2153 UTC), the PG variability decreased ($j_{tot} = (0.148 \pm 0.001)$ nA) compared to the non-cloudy conditions (2130 – 2148 UTC and 2208 – 2215 UTC, $\sigma^2 = (0.164 \pm 0.001)$ nA). Using Levene's equality of variance test, the variability of j_{tot} between positive and negative PG perturbations compared with non-cloudy weather (2130 – 2148 UTC and 2208 – 2215 UTC) was found to be statistically significant (Levene's Test = 49453, Positive Charge Sample Size = 25301, Negative Charge Sample = 94853, No Cloud Sample Size = 150356, $p < 0.001$).

The Z measured in this cloud (Figure 5-16a) was substantially lower than in the case study (2), particularly for the ice phase of the cloud (16.2 dBZ, 78% difference). The Z was greater in the ice phase of the cloud, which is uncommon for cumuliform clouds. The greater Z in the ice phase was a result of the small liquid phase (0.06 km). A noticeable feature of Z in this cloud was the horizontal asymmetry. The right-hand side of the cloud had a higher Z than the left-hand side of the cloud. As no precipitation was measured by the disdrometer, it was likely that the cloud was not in the mature stage. The asymmetry in Z coincides with the asymmetry in the PG and current measurements at the surface, suggesting larger hydrometeors contained negative charge.

For this case study, ε_T (Figure 5-16b) was also found to be asymmetrical. The left-hand side of the cloud had a higher ε_T compared to the right-hand side. The ε_T within this cloud was appreciably smaller than for case study (1), between 10^{-2} and 10^{-3} m^2s^{-3} throughout the cloud. The influence of turbulence in the left-hand side of the cloud suggests mixing of the hydrometeors occurred which might be the main reason for the weak positive PG perturbation. In contrast to the right-hand side of the cloud, where ε_T was weaker, ε_T also adds some certainty to the grouping of the negative charge centre for the larger sized hydrometeors. $\ddot{\varepsilon}_T$ was much smaller than for case study (1). As $\ddot{\varepsilon}_T$ is weighted by the magnitude of ε_T , $\ddot{\varepsilon}_T$ needs to be normalised for comparison. Normalising $\ddot{\varepsilon}_T$ by the maximum ε_T measured in the ice phase, saw a 15.6% increase in $\ddot{\varepsilon}_T$ compared with case study (1). The increased normalised $\ddot{\varepsilon}_T$ can be attributed to the asymmetry in the turbulence between the left and right sides of the cloud.

Having a high variation of ε_T is also thought to be beneficial for the electrification of a cumuliform cloud as the hydrometeor collision efficiency is increased. An asymmetry of ε_T can help form charge centres within the cloud (Renzo and Urzay, 2018).

The σ_d suggests a possible cause for the monopole structure in the PG (Figure 5-16c). The negative charge centre resided in a low σ_d region (right-hand side of the cloud). The low σ_d suggests small variations in hydrometeor sizes existed. The positively charged hydrometeors resided in the higher σ_d region (left-hand side of cloud) suggesting a wide distribution of hydrometeor sizes. The wide distribution also suggested the hydrometeors were spread over a wide area. If most of the hydrometeors in the left-hand side of the cloud were positively charged, the wide size distribution might suggest that the magnitude of charge also had a wide distribution. This interpretation conforms to several non-inductive charge separation hypotheses (e.g. relative diffusional growth rate theory (Emersic and Saunders, 2010)).

The approximate positions of the positive, ① and negative, ② charge centres were situated near the high and low regions of Z , respectively, which suggest the type of hydrometeors that resided at these locations. The positively charged hydrometeors mainly consisted of smaller ice crystals, while the negatively charged hydrometeors mainly consisted of larger ice crystals, perhaps as large as graupel. The ice water content (IWC, Figure 5-16d), which was calculated using a Z -temperature relationship (Hogan et al., 2006), is consistent with these observations. The hydrometeor classification (Figure 5-16e) suggests supercooled liquid water mixed with ice (code 5, purple) was appreciable in the left-hand side of the cloud. The abundance of supercooled liquid water and ice highlights a prime region for ice crystal growth and adds to the possible reasons for the high σ_d and the small positive PG perturbation.

Almost every descriptive statistic measured in Table 5-2 was lower in magnitude compared with case study (1). For example, \bar{v} was much greater than case study (2), especially for the ice phase. The higher \bar{v} suggests an updraught and possibly a downdraught were active in this cloud, potentially enhancing the PG by transporting the charged hydrometeors around the cloud through gravitational separation.

The influence of wind shear can be seen acting on the cloud as the shape of the cloud was forward tilted in time (see any radar plot in Figure 5-16). The cloud top passes overhead before the cloud base. Wind shear might suggest why the position of the positive and negative charge centres was horizontally separated inside the cloud. A localised region of σ_v was likely caused by turbulence, increasing the likelihood for charge separation as long as there was another process to transport the charges away from the region (Saunders, 2008). The cloud base height was

lower than case study (1), but the overall depth saw a 41.6% difference. Most of the cloud was in the ice phase according to the ceilometer measurements. The variability of the cloud base saw at times a liquid phase appearing. The strong variability of the cloud base suggests updraught and downdraught regions, like the variability of the cloud base in case study (1). Another consequence of the cloud base variability is consistent with the low optical thickness for the cloud (low Z), causing the ceilometer to struggle at identifying the height of the cloud base.

Similar to the previous case studies, the convective parameters measured by the radiosondes launched at Camborne (03808) and Larkhill (03743) suggested little to no convection was possible near the time of this case study ($CAPE = 5.47 \text{ J kg}^{-1}$, $CIN = -0.25 \text{ J kg}^{-1}$, $LI = 1.42^\circ\text{C}$). No lightning discharges were measured by the BTM near CO for any cloud measured on the 2017/03/21 consistent with weak convective instability. This suggests that although the cloud was electrified enough to be detected at the surface, the properties of the cloud were substantially different from case study (1). The high normalised $\bar{\epsilon}_T$, large ice phase, the presence of supercooled liquid water and high \bar{v} were the main reasons for any charge separation to have taken place. The lack of any substantial liquid phase can be assumed to plateau any charge generation over time caused by the lack of formation of new ice hydrometeors within the ice phase of the cloud. This assumption is consistent with the low Z measured in the cloud.

5.4.4 (4) Negligible Turbulence and Appreciable PG Perturbation

Case study (4) examines a cloud with no appreciable ϵ_T , but with an appreciable perturbation of the PG . From the surface pressure analysis (Figure 5-17a), northerly winds provided a different cloud steering level compared with westerlies which are most common for the UK, consistent with the trajectory of the jet stream. Two extratropical cyclones over Iceland and two anticyclones over the mid-Atlantic and Spain provided uncommon synoptic conditions observed throughout the case studies discussed. The tight isobars in the surface pressure analysis suggest wind speeds were higher compared with case studies (1) – (3). The thermal-infrared AVHRR satellite image taken over the UK (Figure 5-17b) showed scattered clouds over the south of the UK. The cloud tops were very low according to the thermal-infrared, which is consistent with the radar observations at CO. As this cloud occurred early in the morning, $CAPE$ was also low. This case study focuses on a single-celled cumulus cloud (Figure 5-18) with a cloud top height of 3.8 km. The cloud characteristics (Table 5-2) that were likely to cause the electrification observed, are compared with case study (3).

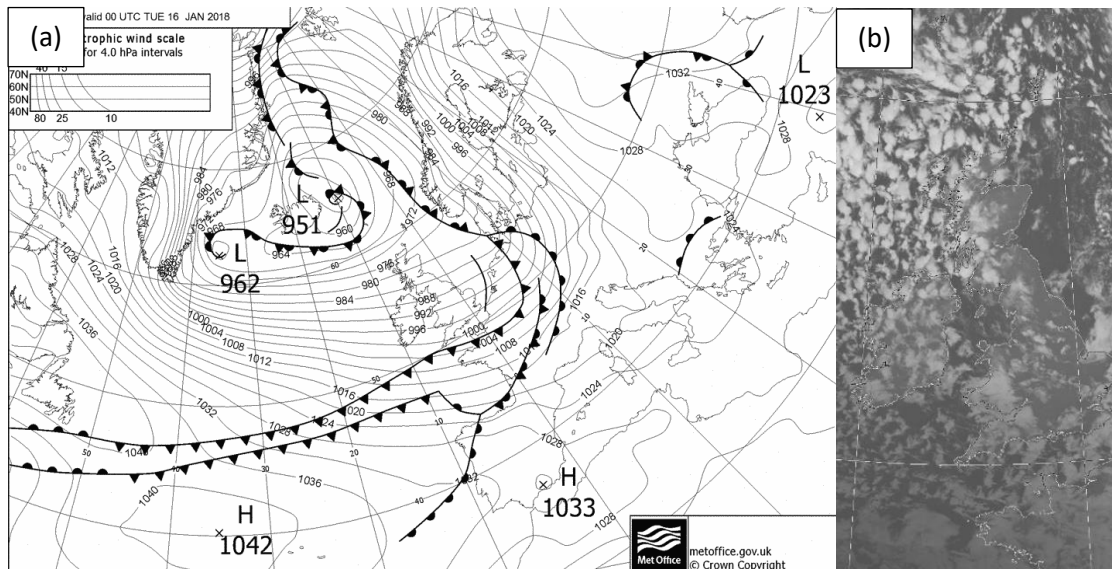


Figure 5-17: As for Figure 5-12 but for (a) 2018/01/16 0000 UTC and (b) 2018/01/16 0443 UTC.

There were two main perturbations observed in the PG (Figure 5-18g), noted by the ① and ②, which formed a skewed negative vertical dipole. The higher variability of the PG observed near the turning points was similar to the observations seen in the previous chapter (§4) caused by uncharged precipitation and charged precipitation (§5.4.1). The higher variability has a secondary effect of suppressing the perturbation caused by the charge residing in the overhead cloud, due to the superposition of various charges; hence, the PG structure looks truncated near the extreme points. The variability of the current (Figure 5-18f) is substantial, especially during the negative PG perturbation, greater than for any other case study discussed in §5.4. The greater variability during the negative PG perturbation also coincides with the detection of corona.

The Z was homogeneous for the ice and liquid phases (Figure 5-18a). The liquid phase, on average, was 8.2 dBZ greater than the ice phase showing once again the asymmetry between the two phases. The Z difference suggests the hydrometeors were of comparable size in the two phases (as also found for the first case study). The σ_d was also homogenous across the entire cloud consistent with the observations seen in Z (Figure 5-18c). The Doppler velocity, \bar{v} (see Table 5-2) showed appreciable differences compared with case study (3). The maximum velocity was very small (0.75 m s^{-1}), particularly in the liquid phase (-0.38 m s^{-1}) where no positive velocities were detected, suggesting no updraught was present within this cloud. The minimum \bar{v} (-6.29 m s^{-1}) was much larger in comparison with the case study (3) (48% difference), showing a strong tendency for the hydrometeors to fall. The combination of \bar{v} and the substantial PG perturbation suggests this case study is unique for cumuliform clouds observed at CO during this study.

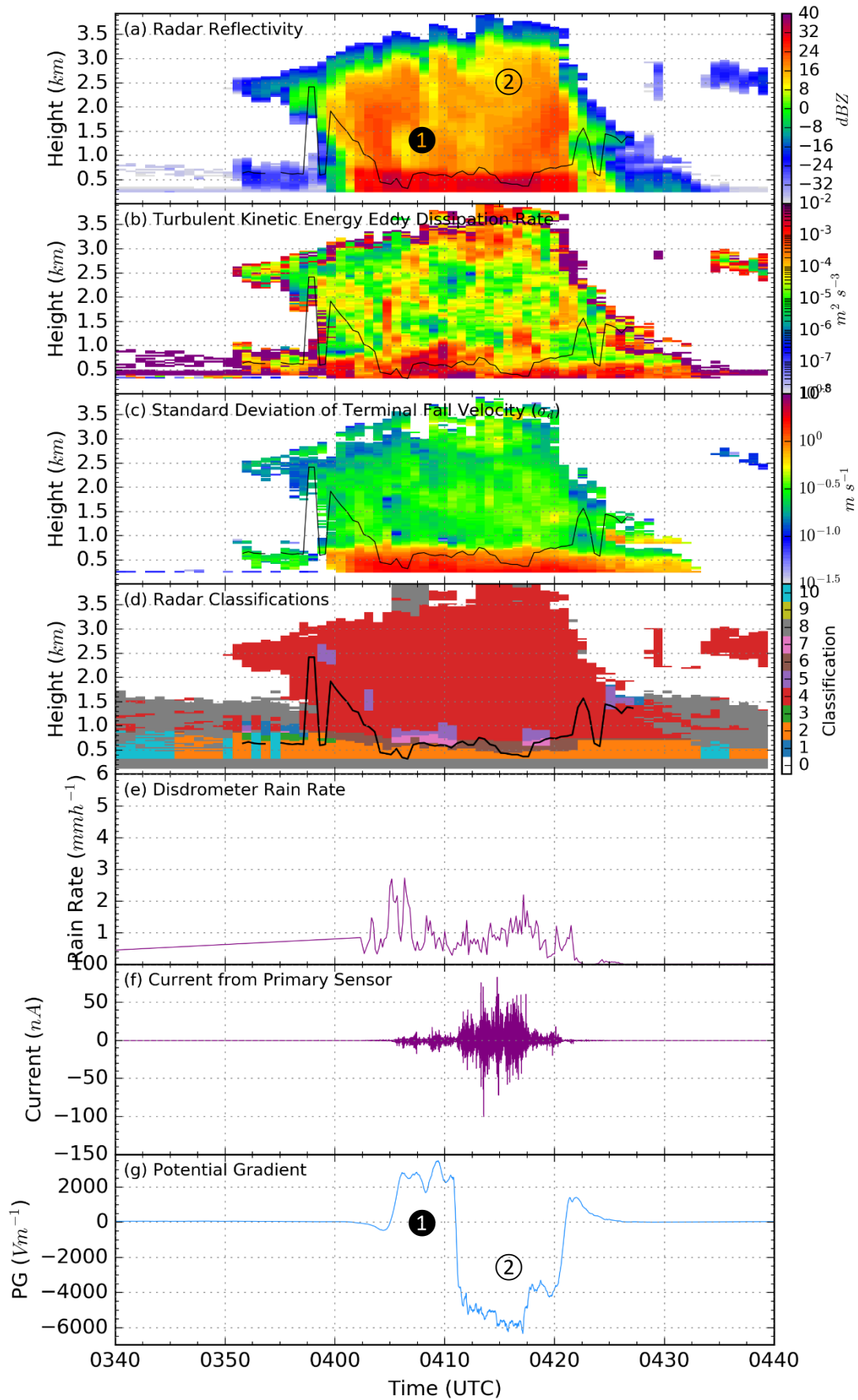


Figure 5-18: As for Figure 5-9 but for 2018/01/16 between 0340 and 0440 UTC.

For this case, ε_T was appreciably small throughout the cloud (mean = $1.3 \times 10^{-3} \text{ m}^2 \text{ s}^{-3}$) and was one of the only examples of a cumuliform cloud with a consistently low ε_T observed at CO during this field campaign (Figure 5-18b). The mean ε_T was below the 15th percentile for all cumuliform clouds observed in this study. Despite the low average ε_T , there was less difference to previous cases when considering the maximum ε_T . The $\ddot{\varepsilon}_T$ was also fairly homogenous across the entire cloud, suggesting that the hydrometeor collision efficiency was low at this stage of the cloud's lifetime. Normalising $\ddot{\varepsilon}_T$ with respect to the maximum ε_T , showed a weaker variability compared to case study (3).

The hydrometeor classification (Figure 5-18d) showed a substantial ice phase existed within the cloud with a depth of 3.03 km (91% depth of the entire cloud). The ice phase contained mostly ice with very little supercooled liquid water being detected by CloudNet. The lack of supercooled liquid water suggests the reduction of charge separation within the cloud, consistent with the assessment that this cloud is in the dissipating phase. The classification shows melting ice near the cloud base (code 6, brown). The detection of melting ice supports the theory of Dinger and Gunn (1946) who suggested charged rain was the result of charged ice hydrometeors melting and later precipitated. The disdrometer (Figure 5-18e) measured exceptionally low RRs ($< 3 \text{ mm h}^{-1}$) as this cloud passed overhead, lower than case studies (1) – (3) discussed. The low RR is consistent with RRs typically measured by stratiform clouds and is consistent with the hypothesis that this cloud was within the dissipating life phase.

The current measured at the surface (Figure 5-18f) was over an order of magnitude bigger than any other cases discussed (5-95th range = 4.3 nA, 53% difference from case study (1). A noticeable difference with case studies (1) – (3) discussed was the detection of both charged rain and corona (Figure 5-19). The detection of corona (warning flag 1) only occurs during the negative PG perturbation. This is related to the greater PG observed during the negative perturbation with the corona onset voltage likely coinciding between 2.5 and 4.0 kV m^{-1} . The presence of corona is rarely observed, even in the most electrified of clouds; no corona was detected for case study (1) on 2017/08/31 despite later producing lightning. As pointed out by Bennett (2018), the detection of corona before the onset of lightning is not mutually exclusive. Corona can be detected without any lightning occurring and vice versa. Nonetheless, the detection of corona is, on average, an important indicator that lightning might occur within the next thirty minutes. Like charged rain, corona can have a considerable influence on the local PG , typically of several kVs. It is therefore not surprising that the PG perturbation was complex in form.

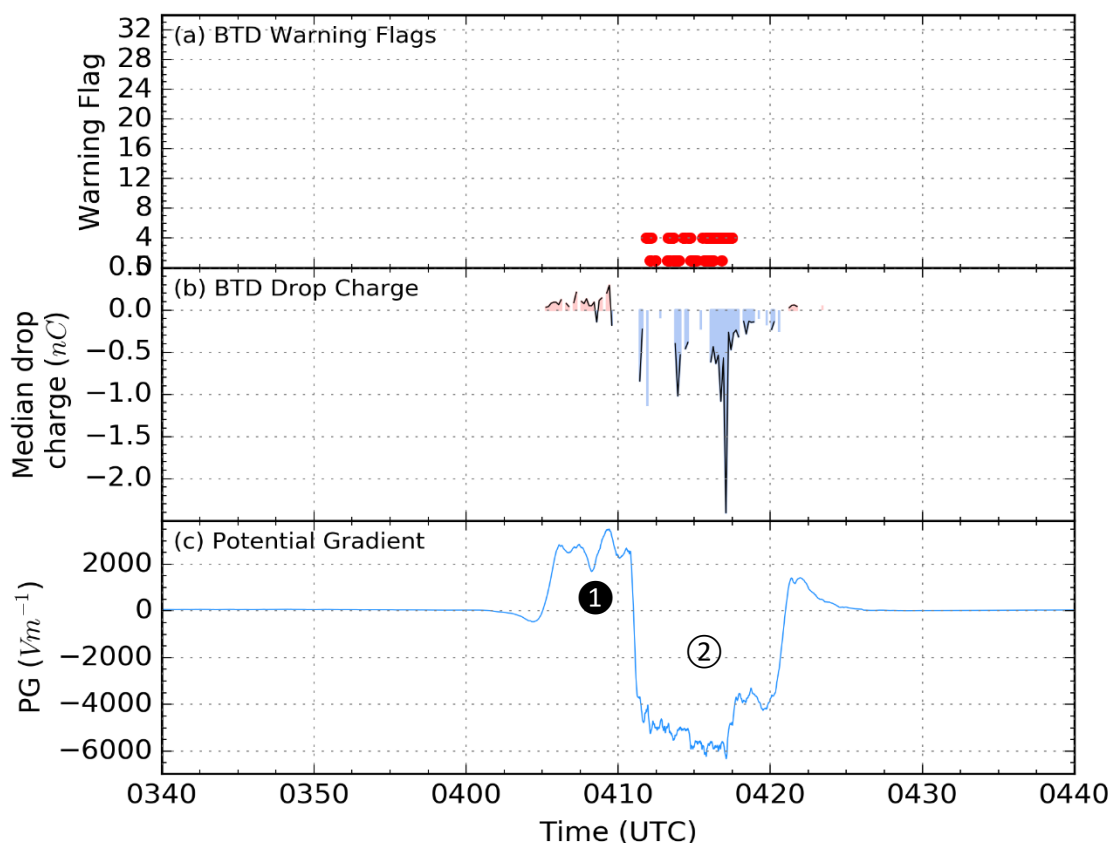


Figure 5-19: A time-series of the warning flags provided by the BTD (a), the median 10-second drop charge (b) and the PG (c). The warning flags show corona (1) and charged rain with corona (4). A minimum threshold of 50 pC is given before a charge rain flag is given. The numbers ① and ② represent the approximate positions of the positive and negative charge centres residing within the cloud respectively.

Similar to case studies (1) – (3), the radiosonde flights at Camborne (03808) and Larkhill (03743) showed very weak conditions for convection ($CAPE = 7.16 \text{ J kg}^{-1}$, $CIN = -2.44 \text{ J kg}^{-1}$, $LI = 15.04^\circ\text{C}$). The weak conditions would be the dominant cause for the low cloud top seen, limiting the vertical growth of any cumuliform cloud and the amount of charge that could be separated. The lifting index particularly highlights the stability of the atmosphere at CO. For a cloud which has produced such a substantial PG perturbation³⁰ (9.8 kV m^{-1}), it was surprising that the measurements of Z , \bar{v} , σ_v , ε_T and σ_d were much smaller in comparison to the other case studies (particularly case study (1)). The descriptive statistics of the cloud (Table 5-2) suggest that the cloud was in its dissipating phase. A hypothesis for why this cloud did not produce lightning was the limitation in the cloud's depth. Other clouds that typically produce lightning have much higher cloud tops ($> 6 \text{ km}$). Although a substantial amount of charge was measured from the surface, its lack of vertical growth would reduce its potential for further ice hydrometeors to

³⁰ As discussed earlier, the PG perturbation caused by the charge within the cloud would be much greater without the influence of corona near the surface.

form, suppressing the electrification of the cloud before the breakdown voltage could be reached for lightning to be initiated.

5.4.5 Summary of Case Studies

Four case studies with different electrical and cloud characteristics were analysed and were chosen based on the hypotheses set out in §5.1. There were several bulk properties observed in the cases including high Z , large ice phase, high ε_T , high minimum and maximum mean \bar{v} and a high σ_d . As there are many properties observed to occur within highly charged clouds, it was important to compare clouds with similar characteristics.

Case study (1) measured a cloud with sufficient electrification for lightning to occur and provided a benchmark for all other case studies. Case study (2) had no measurable electrification but the Z was comparable to case study (1). The most noticeable difference between cases was the depth of the ice phase followed by the strength of the vertical velocity. The Z and ε_T were still substantial and similar in both case studies.

Case study (3) and (4) were used to contrast the influence of turbulence within the cloud. Case study (3) showed moderate turbulence, but only on the left-hand side of the cloud. Despite the substantial PG perturbation (1.35 kV m^{-1}), the maximum Z was low in comparison to case study (1) (16.2 dBZ). As well, \bar{v} and ε_T were much smaller than for all other case studies discussed. The noticeable exception was the normalised $\ddot{\varepsilon}_T$ within the cloud, which was greater than all the other case studies. Regions of higher ε_T coincided with low Z and lower ε_T coincided with high Z . This observation is consistent with the turbulence electrification mechanism hypothesised by Renzo and Urzay (2018).

The case study (4) provided one of the few examples observed, throughout the field campaign at CO, with consistently low turbulence throughout the cloud. The case study also had the greatest PG perturbation (9.84 kV m^{-1}) for all case studies discussed and was above the corona activation limit at the surface. In comparison with the case study (1), all observed cloud characteristics had smaller values. The lack of supercooled liquid water, low mean ε_T , low Z (in comparison to the case study (1) and (2)) and no mean positive velocities (i.e. no updraught) suggests that this cloud was in the dissipating phase and any further charge separation would be unlikely. There were many cloud characteristics with values much smaller than the case study (1), making it difficult to identify which were the most important characteristic for charge separation from these case studies alone. Therefore, it was necessary to identify a large sample of cumuliform clouds at various stages of convective and electrical development to determine the importance of each cloud characteristic for cloud electrification. The next section tests the

hypotheses discussed in §5.1 using the identified clouds (§5.2) grouped by the level of electrification (§5.3) to emphasise the relationship with the cloud characteristics.

5.5 Hypothesis Testing

This section tested the three hypotheses discussed in §5.1 to understand how the structure and characteristics of the cloud are related to cloud electrification as measured at the surface. The electrification of a cloud can be defined as the magnitude of either the PG or j_{tot} measured by the FM and BTM, respectively.

5.5.1 The relationship between cloud electrification and cloud phase and cloud depth

To test whether the ice phase of a cloud is important for cloud electrification, the presence of ice and the size of the ice phase was examined with the hypothesis that,

High moisture content within the ice phase of the cloud increases the amount of charge that can be separated between two colliding ice hydrometeors.

To increase the robustness of the hypothesis test, the size of the liquid phase was also compared. The liquid phase is important to supply moisture into the ice phase of the cloud. As concluded in §2.1.6, the most important charge separation mechanism requires ice hydrometeors to grow through riming (deposition of liquid water) for a build-up of negative charge on the outer shell of the ice. Upon the collision between two different sized ice hydrometeors, net exchange of liquid mass leads to a net exchange of charge, resulting in positively and negatively charged hydrometeors after they collide.

Presence of ice and a high moisture content

The first method to test the hypothesis looked at whether any of the 653 identified cumuliform clouds contained ice. The determination of ice was found using the target classification data derived from CloudNet (Hogan and O'Connor, 2004). The presence of high moisture content within the ice phase of the cloud is important to determine whether the growth of the hydrometeors increase the amount of charge separation. The presence of high moisture content was identified when CloudNet identified supercooled liquid water within the ice phase of the cloud. Three CloudNet classifications (Donovan et al., 2002) were used for the identification of ice and one classification was used for identifying regions of high moisture content (Table 5-3). To identify regions of high moisture content, the classification of ice coexisting with supercooled liquid water (Code 05) was used.

In Table 5-4, the 653 identified clouds are grouped by the presence of either ice or supercooled liquid water. Most of the identified clouds (92.2%; 602 clouds) contained an ice phase with

Table 5-3: The classification codes defined by the CloudNet target classification used for identifying the presence of ice and high moisture content.

Classification Code	Description	Used to Identify
04	Ice particles	Ice
05	Ice coexisting with supercooled liquid droplets	High Moisture Content
06	Melting ice particles	Ice
07	Melting ice particles coexisting with cloud liquid droplets	Ice

supercooled liquid water. This suggests that an ice phase is a common feature found in a cumuliform cloud’s development. In comparison, only 3.2% (21 clouds) and 4.6% (30 clouds) of the identified clouds had no supercooled liquid water and no ice phase, respectively. No clouds were found with supercooled liquid water without the measurement of ice.

A back-to-back histogram of the PG range, j_{tot} range and 95th percentile of the Z between clouds with and without an ice phase shows a marked reduction in all three parameters when the ice phase is missing (Figure 5-20). This suggests that the presence of ice and supercooled liquid water is causally related to the electrification of the cloud. The reduction of Z for clouds without an ice phase suggests the importance of the hydrometeor size for charge separation to occur.

As the number of clouds found to have either no ice or supercooled liquid water was low (7.8%), the sample size might be too small to represent the true relationship of the ice phase. Cross-comparison of the electrical measurements (Table 5-5), shows a substantial decrease, going from both ice and supercooled water to ice only to no ice nor supercooled water, in all measurements of the PG , even between the poorly sampled clouds. The decrease of the PG also suggests that the presence of high moisture content in the ice phase is appreciably more important than the ice phase alone. The reduction of the PG range is substantially greater between ice and supercooled liquid water and ice only clouds compared with the change between ice only and no ice nor supercooled liquid water.

Table 5-4: A contingency table of clouds that contain either ice or supercooled liquid water for 653 identified clouds.

		Supercooled Liquid Water	
		Yes	No
Ice	Yes	602	21
	No	0	30

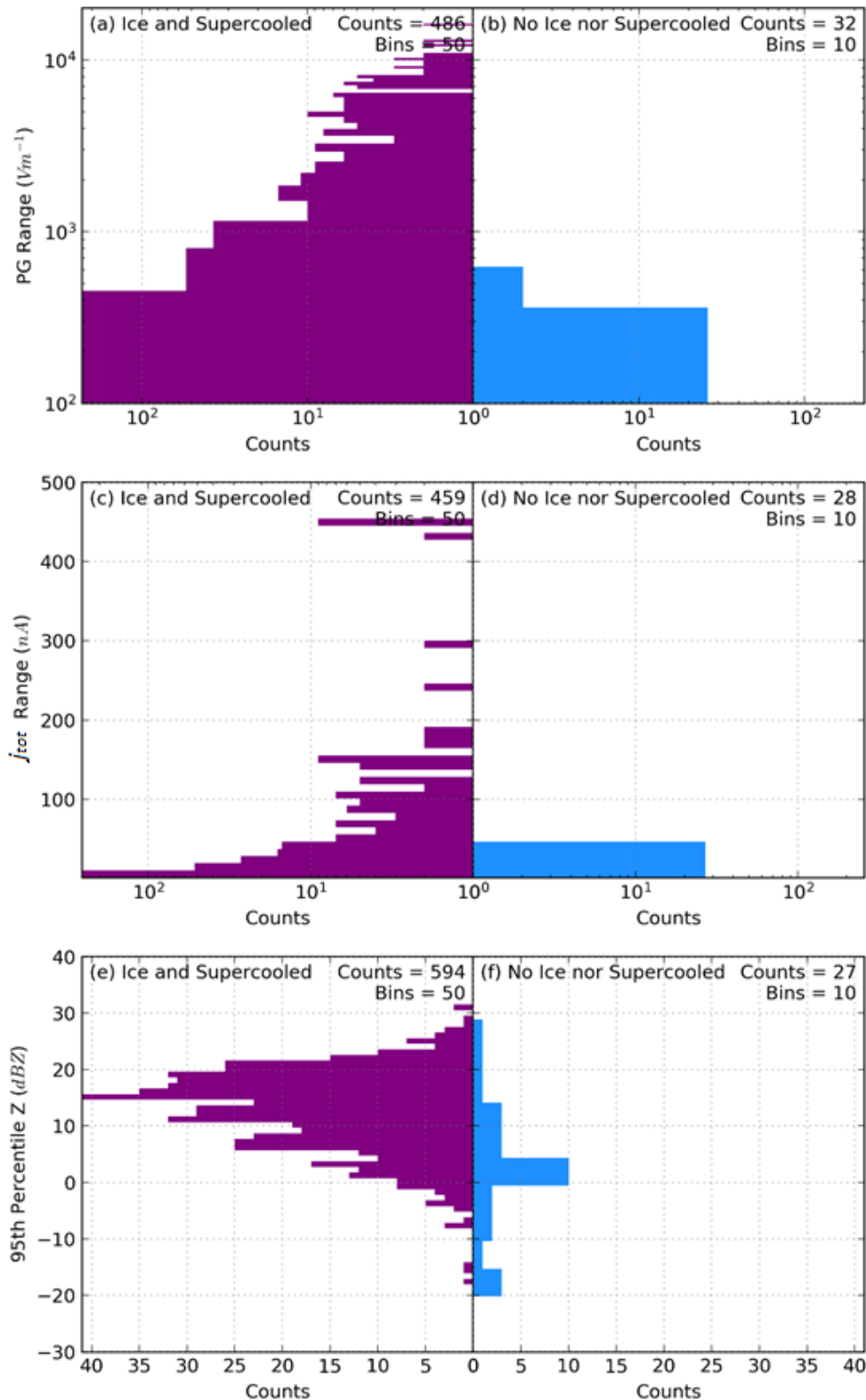


Figure 5-20: Back-to-back histograms of the PG range (a,b), j_{tot} range (c,d) and 95th percentile of Z (e,f) for clouds that contained both ice and supercooled liquid water (a,c,e) and no ice phase (b,d,f).

The depth of the ice and liquid phases

The second method to test hypothesis (1) involved looking at the structure of the cloud to see whether the depth of the cloud changed with electrification. The depth of the cloud is important

Table 5-5: The mean and 95th percentile statistics for the PG range and j_{tot} range for clouds with ice and supercooled liquid water, only ice and no ice nor supercooled liquid water. The numbers in the brackets are the percentage value compared to the value for clouds with ice and supercooled liquid water.

	Ice and Supercooled Liquid Water	Ice Only	No Ice nor Supercooled Liquid Water
Mean PG Range (Vm^{-1})	1669 (100%)	621 (37.2%)	203 (12.2%)
95th Percentile PG Range (Vm^{-1})	7954 (100%)	2728 (34.3%)	601 (7.5%)
Mean j_{tot} Range (nA)	35 (100%)	28 (80.0%)	3 (8.6%)
95th Percentile j_{tot} Range (nA)	178 (100%)	65 (36.5%)	11 (6.2%)

for two reasons. First, as the size of the cloud is proportional to the number of hydrometeors, on average, there is a greater probability for charge separation to occur through collisions. Second, the ratio of the liquid and ice phases is hypothesised to be related to the amount of moisture within the ice phase of the cloud. A liquid phase along with an updraught can feed the ice phase with liquid water, used to grow ice hydrometeors, required for non-inductive electrification. Once the PG increases, the polarisation of the liquid drops can occur leading to further electrification within the liquid phase of the cloud.

Figure 5-21 shows six parameters of the cloud (cloud base height, cloud top height, freezing level, liquid phase depth, ice phase depth, and ice-liquid phase ratio), for the three classification groups (see §5.3) to compare the electrification of the cloud. The cloud base and cloud top heights show an appreciable decrease and increase occur from group 1 to 3 respectively, highlighting the transition from cumulus to cumulonimbus. The changes in the cloud base height (Anderson-Darling Test³¹ (AD) = 25.36, p-value < 0.0001) and cloud top height (AD = 31.71, p-value < 0.0001) were found to be statistically significant when comparing the means between all three distributions. The cloud top height had the greatest difference compared to the cloud base height, as the surface acts as a hard limit for the cloud base. In contrast, the cloud top is typically limited by the tropopause where a substantial temperature inversion occurs. The depth of the cloud is already well established to increase as the cloud becomes more charged (e.g. thunderstorms are associated with cumulonimbus clouds which have a cloud depth of > 5 km), but the association between the depth of the ice and liquid phases with electrification is less established (Chylek et al., 2004). The freezing level height of the cloud (Figure 5-21c) shows no

³¹ The Anderson-Darling test is a non-parametric goodness-of-fit test. It has the null hypothesis that two samples are drawn for the same distribution (i.e. comparable). The greater the value of the AD statistic, the greater the mean difference between distributions.

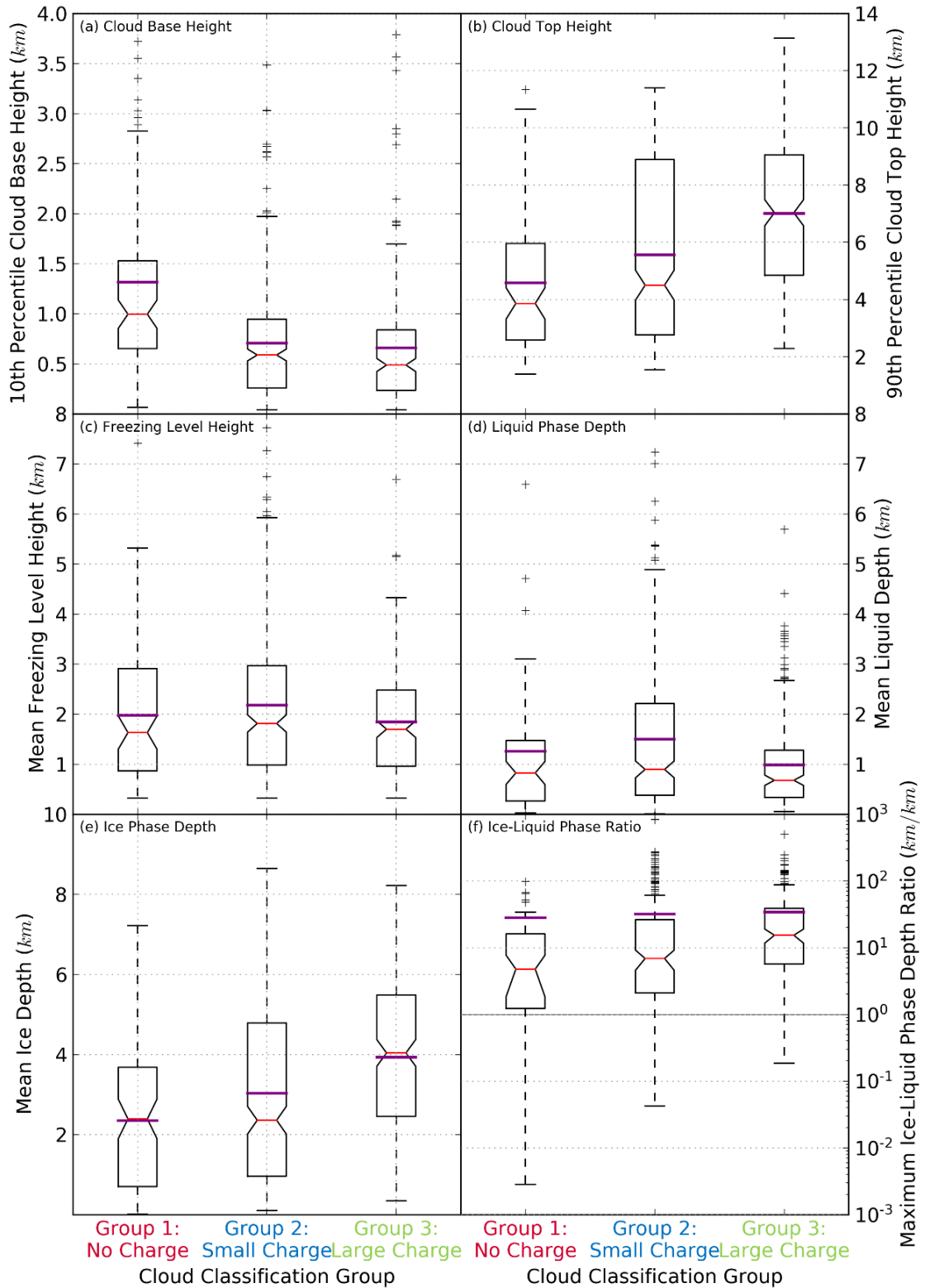


Figure 5-21: Boxplots showing the distributions of the cloud base height (a), cloud top height (b), freezing level height (c), liquid phase depth (d), ice phase depth (e) and ice-liquid phase ratio (f). The median (red line) and mean (purple) is given.

appreciable changes with the electrification of the cloud. Similarly, there is no statistically significant relationship at the 99% confidence interval (AD Test = 2.52, $p = 0.0267$).

There is an appreciable difference between the changes of the liquid and ice phase depths with respect to the electrification of the cloud. The liquid phase depth increases from group 1 to 2 and decreases from group 2 to 3. The change in liquid phase depth was also found to be statistically significant (AD Test = 5.85, $p = 0.0007$). The ice phase shows a substantial increase with electrification with over 4-sigma confidence (AD Test = 22.46, $p < 0.0001$). The minimum ice phase depth also increases with electrification increasing the probability that a cloud requires an ice phase for lightning to be produced.

The ratio between the ice and liquid phases (Figure 5-21f) also increases with electrification, but as the range of ratios is not exclusively above one for group 3 (ice phase always bigger than liquid phase depth), we cannot reject the hypothesis that mixed phased clouds are important for the electrification of a cumuliform cloud (i.e. a positive result). Most clouds have a larger ice phase than the liquid phase, increasing in probability as the cloud becomes more charged. There is a statistically significant increase in the ice-liquid phase ratio (AD Test = 14.08, $p < 0.0001$). The distribution of the ice-liquid phase ratio is heavily skewed with 50% of clouds having an ice phase depth at least 10 times greater than the liquid phase depth.

Overall, there is a clear indication that most charge generation occurs within the ice phase of the cloud. The presence of ice has been shown to be associated with an increase in the charge separation within the cloud as measured at the surface by two separate electrical instruments. Detection of supercooled liquid water, used to identify high moisture content within the ice phase, has a greater benefit for charge separation than ice alone. The benefit of increasing the moisture content is hypothesised to increase the growth of the ice hydrometeors, which can share their liquid outer shells upon collisions between two different sized hydrometeors.

5.5.2 The relationship between cloud electrification and hydrometeor size distribution

To test whether the hydrometeor size distribution within a cumuliform cloud is important for cloud electrification, the PG and j_{tot} measured at the surface were used to represent the charge within the cloud with the hypothesis that:

The mean and standard deviation of hydrometeor size is directly proportional to the amount of charge within the cloud.

As with the first hypothesis, the liquid and ice phases of the cloud were considered separately when testing this hypothesis. Two properties of the cloud were used to test this hypothesis. First, Z was used to estimate the size of the hydrometeors. Second, σ_d was used as it is closely related to the width of the hydrometeor size distribution. All 653 identified clouds were used

for testing the hypothesis that the mean and standard deviation of hydrometeor sizes is directly proportional to the electrification of a cloud.

Hydrometeor Average Size using Radar Reflectivity

The 653 identified clouds were grouped into the charged classification groups (§5.3). To increase the comparability of different clouds, a single statistic was used to characterise the cloud. The 95th percentile of Z was calculated for all identified clouds and showed to increase between groups (Figure 5-22). The 95th percentile was chosen to minimise any extreme values of Z that can occur on certain occasions, typically caused by errors in the radar echoes.

Each cloud was split into the liquid and ice phases to compare how Z changed for each phase. The liquid phase was found to have the widest Z distribution (emphasised by the highest number of outliers) compared to the ice phase with the smallest Z distribution. On average, Z was greatest in the liquid phase for most classification groups. The increase in Z for the different groups was found to be statistically significant for both the liquid (AD test = 104.0, $p < 0.0001$) and ice (AD test = 93.9, $p < 0.0001$) phases. The AD test has the null hypothesis that the

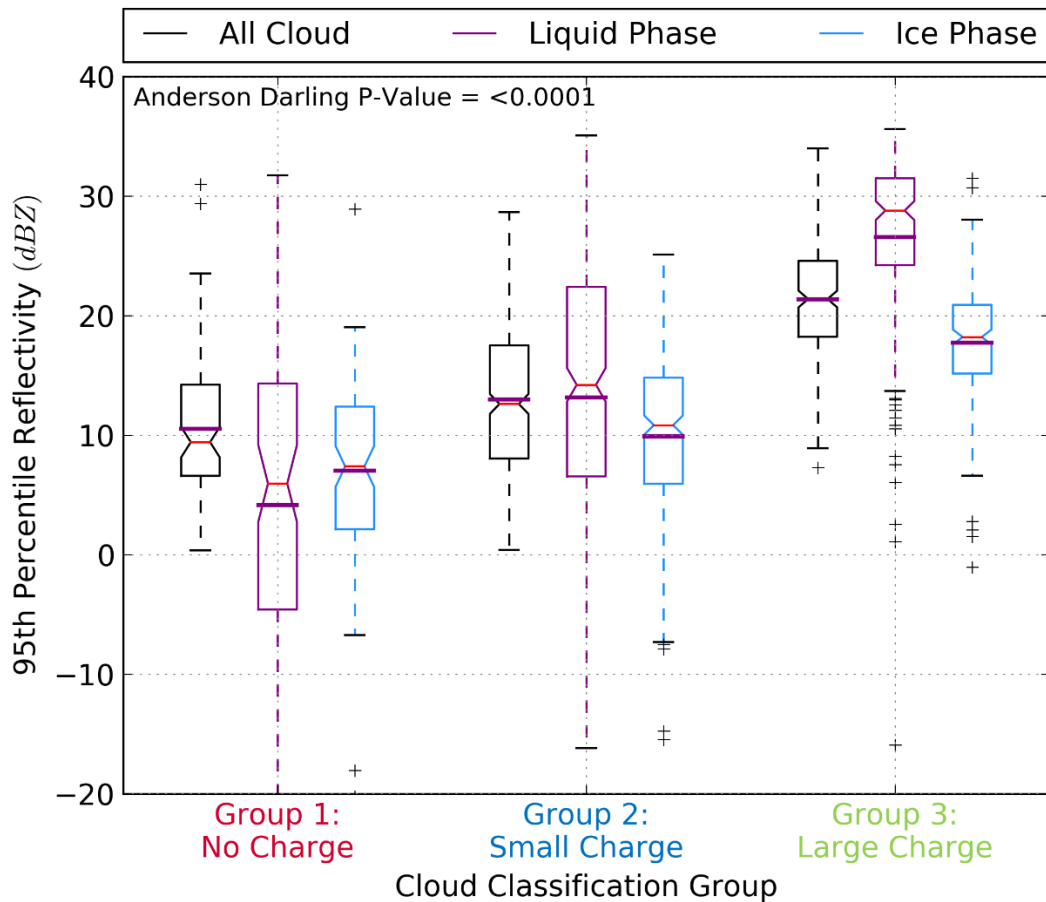


Figure 5-22: A boxplot of the 95th percentile Z for 653 identified clouds (black box) classified into no charge, small charge and large charge groups. The cloud was also decoupled into the liquid (purple box) and ice (blue box) phases. The box-plot shows the mean (purple bar), median (red bar), upper and lower quartiles (upper and lower limits of the box) and the 10th and 90th percentiles (limit of dashed tails).

distributions of the 95th percentile Z for all three-classification groups came from the same population using the mean statistic.

A relationship can also be seen when comparing the 95th percentile Z directly with the PG and j_{tot} range (Figure 5-23). A 65-cloud moving average was used to reduce the variations between cloud systems. The purpose of using a moving average was to emphasise the mean changes for each phase of the cloud with an estimation of the 95% confidence intervals (shaded regions in Figure 5-23). The Z measured in the ice phase had a stronger relationship for both the PG range and j_{tot} range than that measured in the liquid phase. The stronger relationship observed for the ice phase suggests charge separation is more important in this region. Changes in Z in the liquid phase are less sensitive to changes in PG and j_{tot} measured at the surface suggesting the mean size of liquid hydrometeors are less important for charge generation using the inductive mechanism.

A limitation of the radar was the maximum Z (~ 40 dBZ) that could be measured, causing a logarithmic relationship to form as the Z begins to plateau at its maxima. Looking at the individual clouds, another conclusion can be made between the 95th percentile Z and PG Range. As the PG - Z relationship is logarithmic, a few clouds fall outside the 95% confidence intervals (Figure 5-24). In this study, 20 clouds which were positioned above the 95% confidence interval

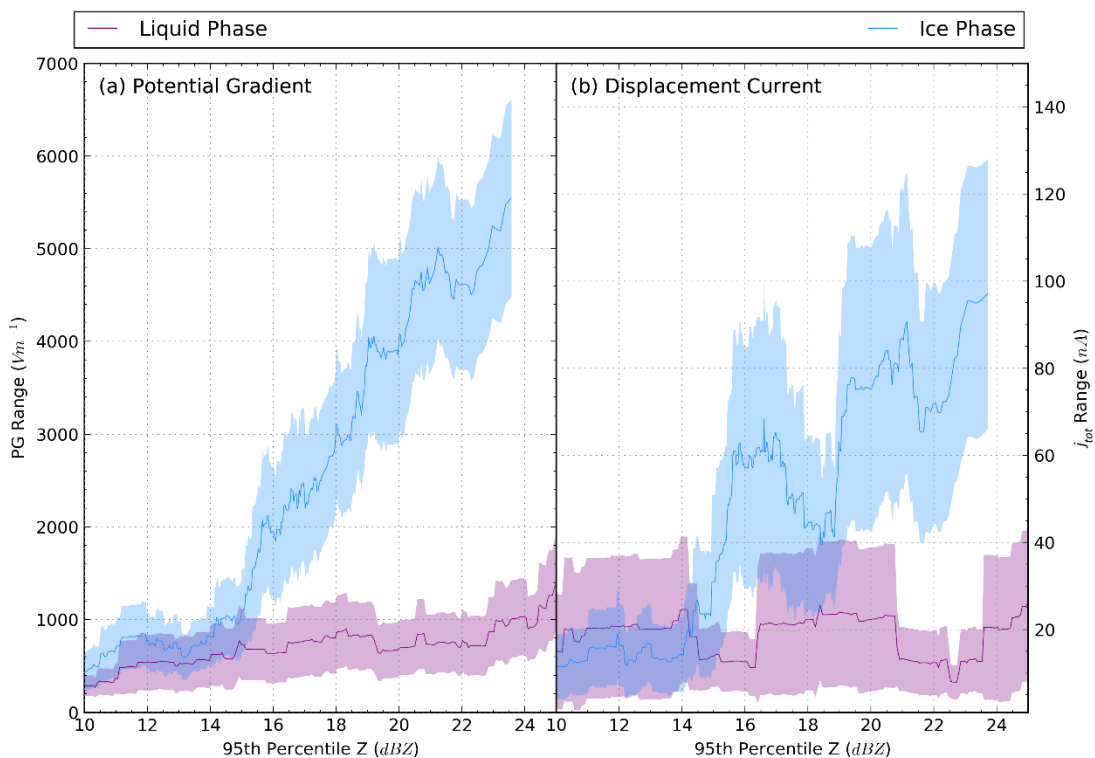


Figure 5-23: The moving-mean relationship between the 95th percentile of Z and the PG range (a) and j_{tot} range (b) for both liquid and ice phases of each identified cloud. The shading represents the 95% confidence intervals. N.B. the 95th percentile Z -axis limits are kept constant between subplots and the number of clouds averaged per bin was 65.

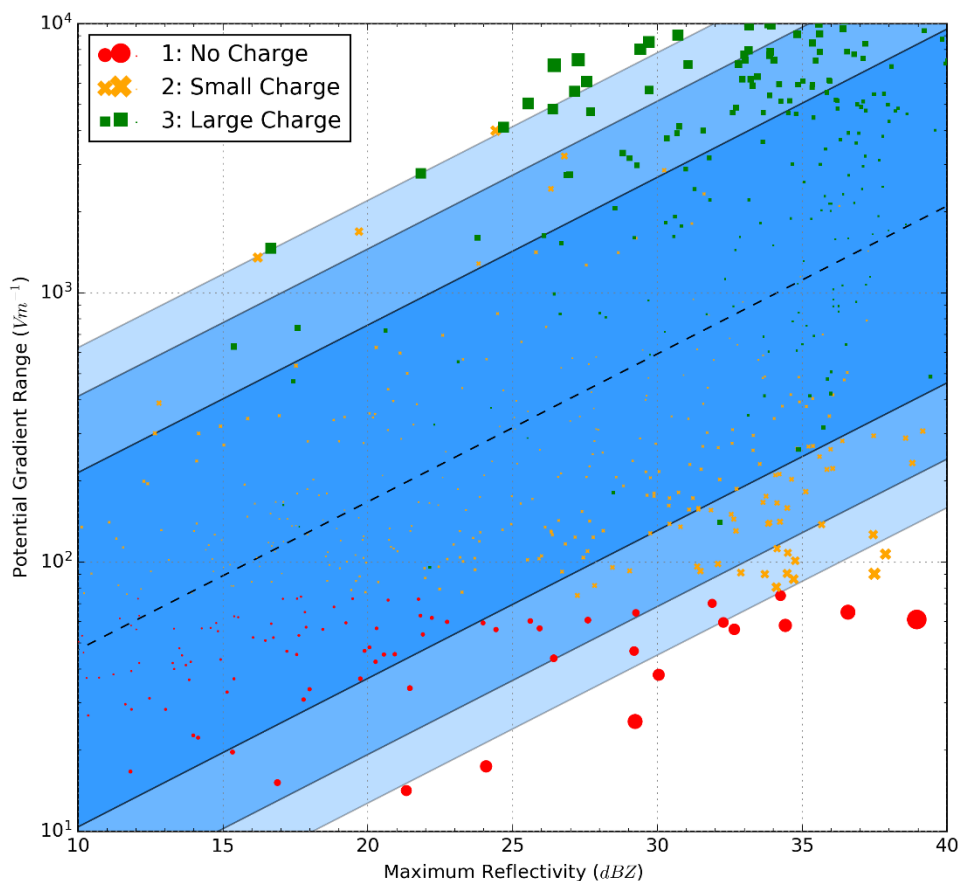


Figure 5-24: The PG range and maximum Z for all 653 identified clouds grouped into the three charge cloud classification groups, no charge (red circles), small charge (orange crosses), large charge (green squares). A log-transformed linear regression model (black dashed line) and the 95th, 90th and 75th confidence limits (blue shading) show the main trend in the relationship. The size of the points is proportional to the distance from the linear regression model to emphasise the outliers in the data.

have a higher than average PG compared to Z , which suggests that these clouds are separating charge at a faster than average rate. In comparison, 14 clouds which were below the 95% confidence interval have a lower than average PG compared to Z , which suggests that these clouds were generating charge at a slower than average rate. For 20% (4) of the clouds above the 95% confidence interval, lightning was detected within 70 km of CO within three hours of the cloud passage. For 7% (1) of clouds below the 95% confidence interval, lightning was detected within 70 km of CO within three hours of the cloud passage.

The higher probability for lightning to occur for clouds above the 95% confidence intervals might be a useful predictor for lightning, which can be used for forecasting purposes. One of the issues with this predictor was related to the type of clouds that exist above the 95% confidence interval. Observations have shown clouds in their dissipating phase often have a higher PG compared to the measurement of Z , \bar{v} and ε_T (see §5.4.4 for an example). A reduction of Z in the dissipating phase would cause many clouds to move above the 95% confidence intervals, increasing the number of false positives when using the PG - Z relationship as a predictor for

lightning. Although the number of clouds identified beyond the 95% confidence interval was small, the $PG-Z$ relationship provides a potentially viable predictor for lightning once a better detection of a dissipating cloud can be made. For future studies, the removal of clouds, which later produced lightning, would provide an unbiased predictor for the $PG-Z$ relationship providing a better prediction for lightning.

Hydrometeor Size Variance using the Standard Deviation of the Terminal Fall Velocity

The width of the hydrometeor distribution was also hypothesised to increase the electrification of a cumuliform cloud. The same methods used in the previous section were applied to σ_d .

The 95th percentile σ_d also shows a positive relationship between classification groups for all identified clouds (Figure 5-25). The ice phase, on average, has a smaller σ_d compared to the liquid phase. Like the 95th percentile Z , the ice phase has a much narrower distribution which is also more symmetrical (i.e. median = mean). The wide variations of σ_d in the liquid phase are caused by the faster rate of growth of liquid hydrometeors through coalescence, a process which

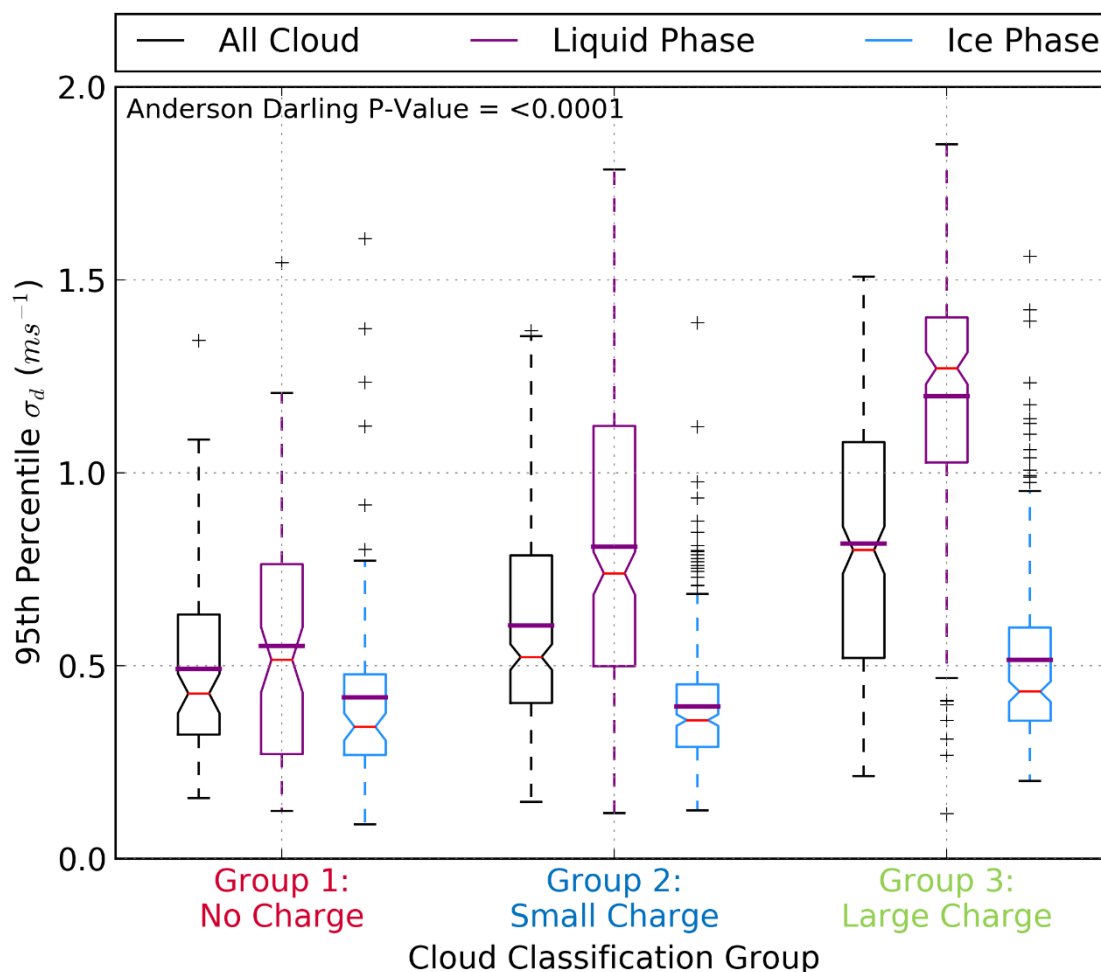


Figure 5-25: A boxplot of the 95th percentile σ_d for 653 identified clouds (black box) classified into no charge, small charge and large charge groups. The cloud was also decoupled into the liquid (purple box) and ice (blue box) phases. The box-plot shows the mean (purple bar), median (red bar), upper and lower quartiles (upper and lower limits of the box) and the 10th and 90th percentiles (limit of dashed tails).

can also occur for ice hydrometeors forming hail, but at a slower rate (MacGorman and Rust, 1998). The increase in σ_d with electrification was found to be statistically significant for both the liquid (AD test = 84.1, $p < 0.0001$) and ice (AD test = 24.0, $p < 0.0001$) phases.

A comparison of the 95th percentile σ_d with respect to the PG and j_{tot} range showed an appreciable relationship, especially for the ice phase (Figure 5-26). A 65-cloud moving average was used to reduce the variations between cloud systems. Figure 5-26 shows an appreciable increase in the PG range and j_{tot} range with σ_d for both phases of the cloud. The terminal fall speeds measured in the ice phase had a stronger relationship for both PG range and j_{tot} range. In contrast to Figure 5-23, the confidence intervals are much wider despite using the same maximum number of clouds per bin. The wider confidence intervals suggest a substantial variation between cloud systems and indicate the variance of hydrometeors sizes is less important for charge generation.

5.5.3 The relationship between cloud electrification and turbulence

To test whether turbulence is important for cloud electrification, the PG and j_{tot} were used to represent the charge within a cumuliform cloud, with the hypothesis that:

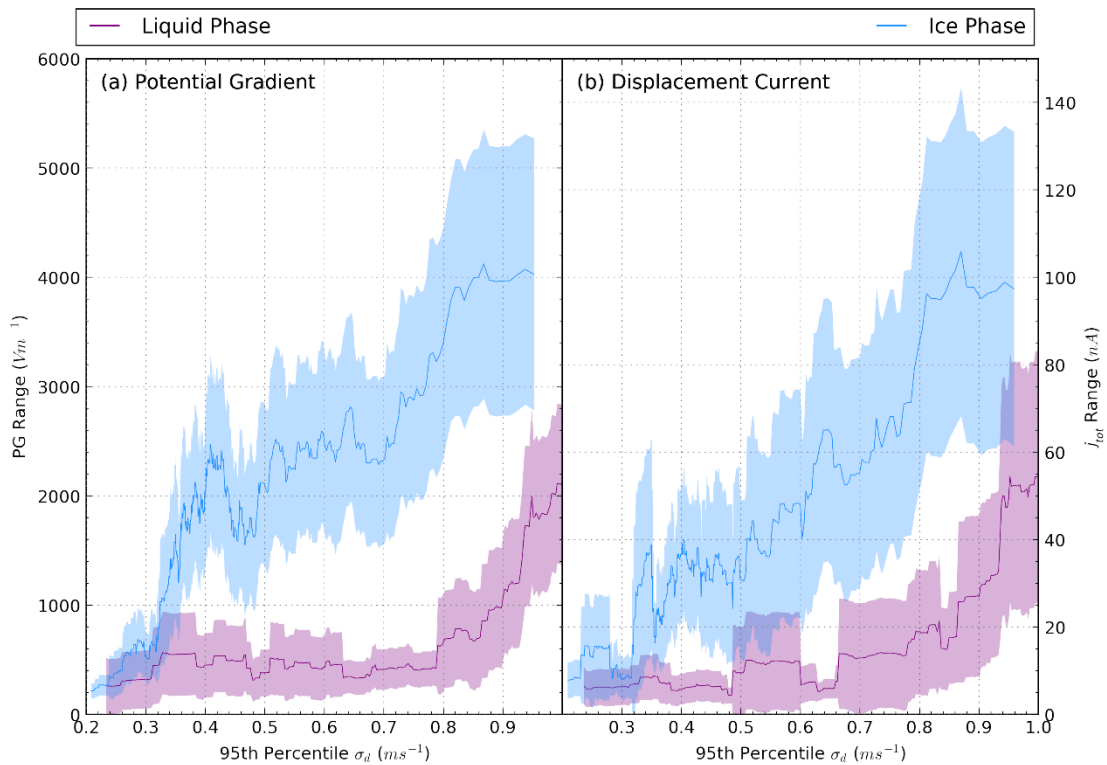


Figure 5-26: The moving-mean relationship (using the advanced averaging technique) between the 95th percentile σ_d and the PG range (a) and j_{tot} range (b) for both liquid and ice phases of each identified cloud. The shading represents the 95% confidence intervals. N.B. the 95th percentile σ_d axis is kept constant between subplots and the number of clouds averaged per bin was 65.

Turbulence within a cumuliform cloud increases the rate of collisions between hydrometeors and so increases the amount of charge within the cloud.

As with the previous two hypotheses, the liquid and ice phases were considered separately to understand whether one phase was more important for the electrification of a cumuliform cloud. From the earlier hypotheses tested, the ice phase of a cumuliform cloud was shown to have a stronger relationship with cloud electrification compared to the liquid phase. Turbulence is hypothesised to be an important process to increase the rate of charge separation within the ice phase of the cloud. As the depth of the ice phase and the hydrometeor size was also found to be important for the charge separation, it was necessary to try to decouple these characteristics from turbulence. As the radar pulse is Z-weighted, an independent relationship with turbulence was difficult to decouple. The following sections determine the relationship of $\sigma_{\bar{v}}$ and ε_T with respect PG and j_{tot} measured at the surface, followed by an attempt to decouple turbulence from the Z-weighting, integral to radar measurements.

Influence of Turbulence on Cloud Electrification

Two derived properties of the cloud were used to test the importance of turbulence on cloud electrification. First, $\sigma_{\bar{v}}$ was used as it provides a measure of the vertical component of turbulence under the assumption that variations in the microphysics are negligible. Second, ε_T was used adding the horizontal component of turbulence by combining the zonal and meridional wind speeds from the ECMWF ensemble forecast system with $\sigma_{\bar{v}}$ (Bouniol et al., 2003). Using both $\sigma_{\bar{v}}$ and ε_T enables one to differentiate between vertical and horizontal dimensions of turbulence, to see if one dimension is more important for cloud electrification.

As the turbulence within the cloud can occur on many scales ranging from sub-grid (of the radar) to scales larger than the grid spacing of the radar, the range of eddy sizes cannot be resolved³². Consistent with the earlier hypotheses tested, a statistic of the turbulence parameters was compared with a statistic of the electrical parameters measured at the surface. The sum of $\sigma_{\bar{v}}$ and ε_T over the entire cloud was used to test the importance for cloud electrification allowing the entire cloud to be sampled, under the hypothesis that a cloud with more turbulence allows more charge generation. All 653 identified clouds were grouped using the classification of cumuliform clouds (§5.3).

³² The smallest scale of turbulence that can be measured by the radar is proportional to half of the radar wavelength (Bouniol et al., 2003). For the 35 GHz radar the smallest scales of turbulence that can be resolved is 4.3 mm.

For both phases of the cloud, $\sigma_{\bar{v}}$ and ε_T were found to increase significantly (see Table 5-6) with electrification (Figure 5-27). For the ice phase, $\sigma_{\bar{v}}$ and ε_T were found to have the strongest relationship with electrification, particularly for ε_T with a 41% difference in AD test between ice phases. The liquid phase increased between group 1 and group 2 for both $\sigma_{\bar{v}}$ and ε_T but did not increase significantly from group 2 to group 3 clouds. In comparison with Figure 5-22, turbulence plateaus with electrification, unlike Z , in the liquid phase. This suggests that the plateau is not caused by the hydrometeor size plateauing. Instead, it can be inferred that the turbulence is similar between groups 2 and 3 for the liquid phase of a cloud.

From Table 5-6, the AD test quantifies the mean difference between all three electrification groups. The difference between the ice and liquid phases is greater for ε_T and suggests the horizontal component of turbulence is important for charge separation. The importance of the horizontal wind speeds might also suggest the importance of wind shear which was hypothesised for transporting charge horizontally in direct competition with the updraught and downdraughts present within the cloud. Overall, the magnitude of turbulence increased relative to the charge residing within the cloud as measured at the surface.

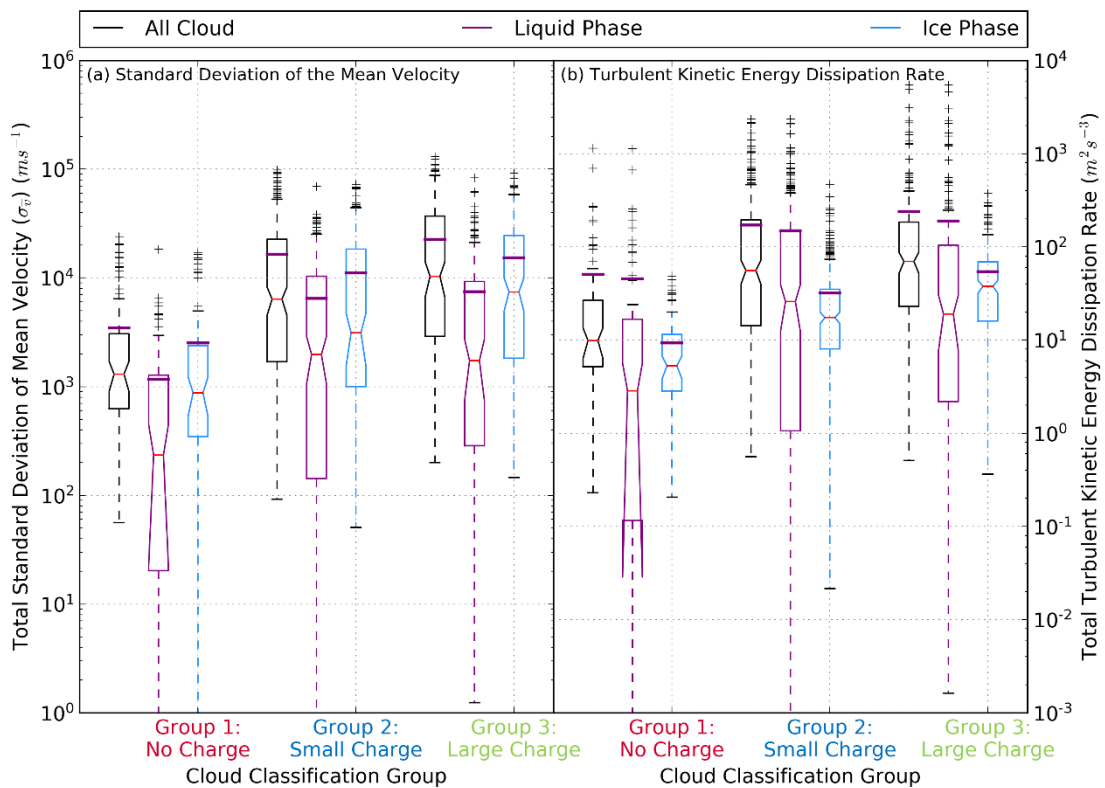


Figure 5-27: A boxplot of the total standard deviation of the mean velocity (a) and turbulent kinetic energy eddy dissipation rate (b) for 653 identified clouds (black box) classified into no charge, small charge and large charge groups. The cloud was also decoupled into the liquid (purple box) and ice (blue box) phases. The box-plot shows the mean (purple line), median (red line) and upper and lower quartiles (upper and lower limits of the box).

Table 5-6: AD statistical test data comparing the mean difference between each charge classification grouped by the cloud phase and turbulence parameter. All relationships were statistically significant ($p < 0.0001$). The higher the AD statistic, the greater the mean difference between distributions

Turbulence Parameter	Cloud Phase	AD Statistic
Standard Deviation of the Mean Velocity ($\sigma_{\bar{v}}$)	Both	38.67
	Liquid	21.31
	Ice	39.39
Turbulent Kinetic Energy Dissipation Rate (ϵ_T)	Both	34.32
	Liquid	13.24
	Ice	59.71

Flow of charge

This section compares the electrical current measured at the surface with the turbulence measured within the cloud. The electrical current, j , can be derived from a microscopic principle by taking into account the number of charged particles, n with an average charge, q spread over an area, A with average velocity, v ,

$$j = nqAv. \quad 5-1$$

The components of equation 5-1 can be related to the properties measured by the radar. Using the fundamental property measured by the radar, Z ,

$$Z \propto nD^6, \quad 5-2$$

along with a measure of the velocity of the hydrometeors, such as \bar{v} , or turbulence of the hydrometeors,

$$j \propto v, \quad 5-3$$

a relationship of the properties of the cloud can be related to the current measured at the surface. As the properties measured by the radar are Z -weighted, as defined by equation 5-2, the velocity of the hydrometeors is also a function of its size,

$$j \propto nD^6vA. \quad 5-4$$

As the hydrometeors are confined within the area of the cloud, A , a relationship can be found between equation 5-4 and equation 5-1. The only terms not represented between equations is q and D . Therefore, to make equation 5-4 comparable to equation 5-1, the charge on the hydrometeors can be related to its size as,

$$q \propto D^6. \quad 5-5$$

As the sixth power is just an artefact of the radar, a more accurate relationship between q and D can be found by using a power-law regression model between the current measured at the surface with the cloud properties measured by the radar. A power-law model is a common relationship used when comparing radar measurements with other properties, such as the relationship between Z and RR (Marshall and Palmer, 1948). Therefore, a semi-empirical relationship can be found relating the electrical current with the cloud properties,

$$j = a(v \cdot A)^b + c, \quad 5-6$$

where a , b and c are coefficients to be optimised using an ordinary least-squares regression model and v is a velocity term used to represent the movement of the hydrometeors (e.g. \bar{v} , σ_v , $\sigma_{\bar{v}}$).

To determine whether a relationship exists between turbulence and current, $\sigma_{\bar{v}}$ and the area of the cloud was compared with j_{tot} (Figure 5-28). The sum of j_{tot} and $\sigma_{\bar{v}}$ is defined over the region where the cloud was identified using the methods described in §5.2. The data used in Figure 5-28 was fitted using an ordinary least squares approach defined in equation 5-6. As the radar only observes a slice of the cloud, only two dimensions of the cloud structure were known. Since the magnitude of the PG is related to the distance between the FM and the charge squared, the size of the cloud base provides a better estimate of the cloud area compared with the depth of the cloud as the cloud base has a shorter distance to the surface. Specifically, the area used in equation 5-6 represents the cloud as a cylinder with a cloud base represented as a circle:

$$A_{base} = \pi r^2, \quad 5-7$$

where r is the half the width of the cloud at its base.

The data was split into the three classification groups (§5.3) to consider the importance of the charge within the cloud with respect to the j_{tot} . The ‘no charge’ group, had the smallest j_{tot} with a maximum of 608.0 μA compared with the ‘small charge’ and ‘large charge’ groups which had a maximum of 1406.4 μA and 1396.8 μA respectively. There is a noticeable asymmetry for the ‘large charge’ clouds above and below the regression line, with the majority of the ‘large charge’ clouds being below the regression line (74.8%). This asymmetry might be related to ‘large charge’ clouds having greater depth and therefore greater cloud area. The greater depth of the cloud means charge can be transported into the higher regions of the cloud increasing the distance of the charge centre from the surface. The increased distance from the surface would

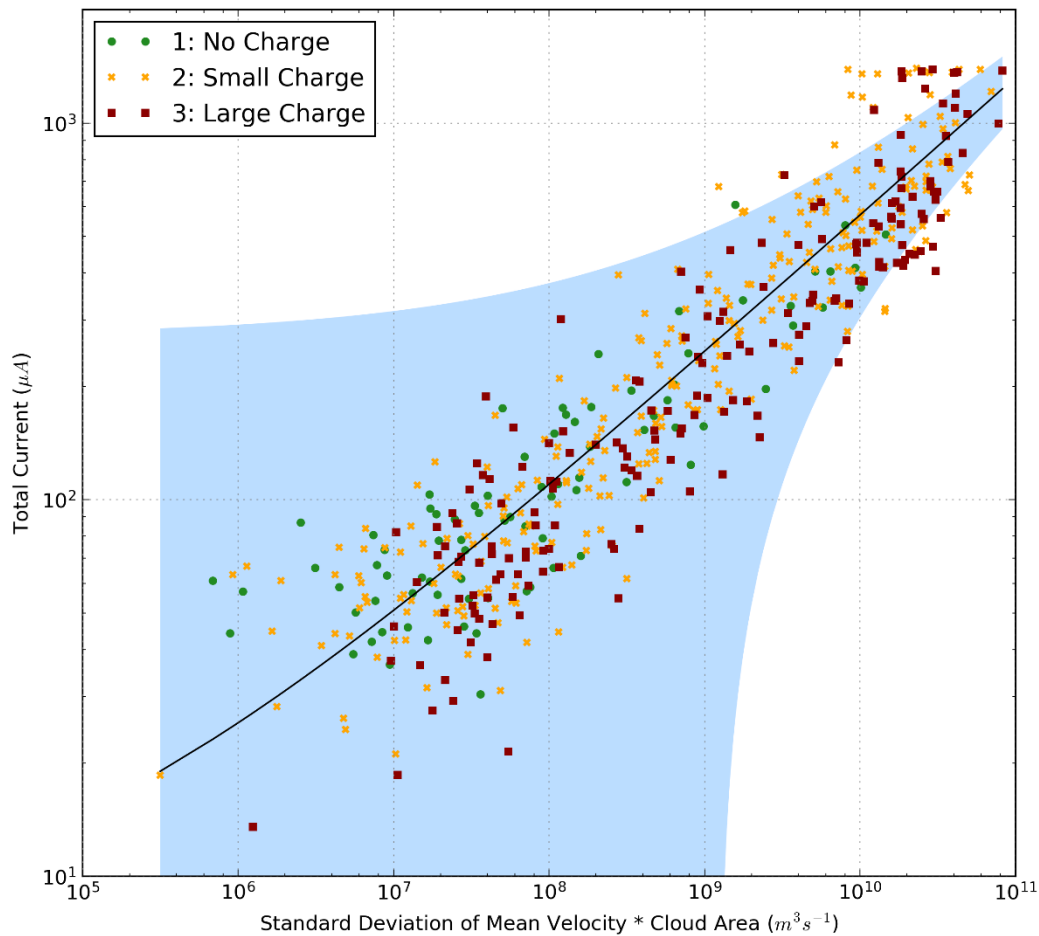


Figure 5-28: A scatter-plot relationship between the sum of j_{tot} and the total standard deviation of the mean velocity multiplied by cloud area as defined by equation 5-6. A power regression model (black line) and 95th confidence intervals (blue shading) was fitted to the data.

have an apparent decrease in the electrical strength caused by the inverse square law on distance for electrical charges.

The first row in Table 5-7 shows the statistical information for the power regression model defined by equation 5-6. A statistically significant relationship ($p < 0.001$) was found for all coefficients with $\sigma_{\bar{v}} \cdot A_{base}$ providing one of the strongest relationships with j_{tot} (Pearson $R^2 = 0.754$ and Spearman $R^2 = 0.8647$). Under a log-log scale, there was a substantial linear relationship with the variations in the relationship being constant for all measurements of j_{tot} . The Akaike Information Criterion (AIC) was used to estimate model quality with a smaller AIC indicating a better model.

For comparison, Z , \bar{v} , σ_v , $\sigma_{\bar{v}}$, σ_D , A_{face} and A_{base} were also compared against the sum of j_{tot} . A_{face} is a separate method to define the area of the cloud. A_{face} is the height multiplied by the width of the cloud, as measured by the radar. The remaining rows in Table 5-7 shows the statistical information for all cloud characteristics mentioned. Overall, A_{base} had the strongest relationship

Table 5-7: Statistical diagnostics for a power regression model (equation 5-6) as shown in Figure 5-28 (first row). The statistical diagnostics of other cloud characteristics being compared against the sum of j_{tot} is also shown for comparison (other rows). The Akaike Information Criterion (AIC) is used to estimate model quality and can be used in conjunction with the standard coefficient of determination (R^2). All coefficients were statistically significant ($p < 0.0001$).

Cloud Characteristics	a (unitless)	b (m)	c (A)	Pearson R^2	Spearman R^2	AIC	$q \propto D^?$
$\sigma_{\bar{v}} \cdot A_{base}$	0.117 ± 0.003	0.369 ± 0.037	- 6.643 ± 10.305	0.754	0.865	7011	2
Z	3.719 ± 0.104	0.404 ± 0.050	-44.13 ± 14.92	0.686	0.763	8047	2
\bar{v}	9.228 ± 0.247	0.389 ± 0.055	-68.50 ± 14.93	0.703	0.771	8015	2
σ_v	9.332 ± 0.213	0.443 ± 0.042	-68.78 ± 12.91	0.765	0.823	7875	2
$\sigma_{\bar{v}}$	3.038 ± 0.067	0.532 ± 0.056	-50.46 ± 12.20	0.777	0.832	7844	3
σ_d	13.79 ± - 74.91	0.208 ± 0.020	-74.92 ± 13.24	0.760	0.821	7848	1
A_{face}	1.972 ± 0.066	0.282 ± 0.049	-126.0 ± 19.9	0.603	0.718	8130	2
A_{base}	0.044 ± 0.010	0.560 ± 0.051	-68.50 ± 12.54	0.777	0.871	7804	3

with j_{tot} (highest R^2) while $\sigma_{\bar{v}} \cdot A_{base}$ had the best modelled quality (lowest AIC). In terms of velocity characteristics (\bar{v} , σ_v , $\sigma_{\bar{v}}$, σ_d), $\sigma_{\bar{v}}$ provided the best relationship, but only marginally.

The charge-diameter approximation (equation 5-5) is dominated by the radar measurements. As a power law provides the best relationship between j_{tot} and the radar measurements, the estimated power coefficient (see Table 5-7) can be used to estimate the direct relationship

between q and size of the hydrometeor. Using coefficient b , the relationship can be calculated as $D^x = (D^6)^b$, giving,

$$q = D^{2.214 \pm 0.037} \approx D^2. \quad 5-8$$

Out of all cloud characteristics compared with j_{tot} , 63% observed a square law between q and D . This suggests the charge is related to the size of the surface area of the hydrometeors within the cloud and is consistent with the relative diffusional growth rate theory (Emersic and Saunders, 2010). The theory involves the exchange of negatively charged liquid water from riming ice hydrometeors (typically between graupel and ice crystals) upon collision. The difference in surface areas between the two colliding hydrometeors is causally related to the amount of charge transported. A net difference in surface area results in a net charge on the hydrometeors after a collision.

5.6 Discussion

A field campaign was set-up at Chilbolton Observatory (CO) to understand the cloud characteristics important for the electrification of a cumuliform cloud. Two instruments were installed to measure the changes in the surface PG ; an electric field mill (FM) and an electrostatic Biral thunderstorm detector (BTD). Continuous electrical measurements of the atmosphere overhead were taken and compared against measurements taken by a 35 GHz radar and a Vaisala CT75K ceilometer to resolve the structure and properties of passing overhead clouds. Nearly two years' worth of data was collected between October 2016 and June 2018. Using a bespoke algorithm (see §5.2), 653 cumuliform clouds were identified throughout the nearly two years of data collected. A wide distribution of cumuliform clouds was measured at various convective and electrical developmental stages, sampled throughout the entire year. The text below summarises the results gained from each hypothesis tested within this study.

1 High moisture content within the ice phase of the cloud increases the amount of charge that can be separated between two colliding ice hydrometeors.

- For all 653 cumuliform clouds which were identified, 92.2% contained both ice and supercooled liquid water as classified by CloudNet. In comparison, only 3.2% (21 clouds) and 4.6% (30 clouds) of identified clouds had no supercooled liquid water and no ice phase respectively (Table 5-4).
- The charge detected within the clouds, measured by the potential gradient (PG) and (total current) j_{tot} range, was substantially lower in clouds without supercooled liquid water or ice (Table 5-5).

- The ice phase depth was found to be related to the amount of charge detected within the cloud. In contrast, the liquid phase depth had no significant relationship with the charge of the cloud (Figure 5-21).

2 The mean and standard deviation of hydrometeor size is directly proportional to the amount of charge within the cloud.

- Using the classification of cumuliform clouds (§5.3) a statistically significant relationship was found between how charged the cloud was and the radar reflectivity (Z) and standard deviation of terminal fall velocity (σ_d), (Figure 5-22 and Figure 5-25).
- The PG and j_{tot} were more sensitive to changes in Z and σ_d for the ice phase compared to the liquid phase of the cloud (Figure 5-23 and Figure 5-26).
- A comparison of the 95th, 90th and 75th confidence limit outliers found clouds with a greater potential gradient (PG) over Z were more likely to later produce lightning in comparison to clouds with a smaller PG over Z (Figure 5-24).

3 Turbulence within a cumuliform cloud increases the rate of collisions between hydrometeors and so increases the amount of charge within the cloud.

- The standard deviation of the mean velocity ($\sigma_{\bar{v}}$) and the turbulent kinetic energy eddy dissipation rate (ε_T) were both shown to substantially increase with cloud electrification. The increase in turbulence was found to be statistically significant ($p < 0.0001$), (Figure 5-27).
- In the liquid phase of the cloud, the turbulence plateaued with electrification (from group 2 to 3. In the ice phase, no plateau was observed with electrification (Figure 5-27).
- The current, j_{tot} measured by the BTD showed the amount of turbulence and the area of the cloud base had the strongest relationship according to the R^2 and AIC diagnostics (Table 5-7).
- The current, j_{tot} was found to be related to the hydrometeor's surface area, consistent with the relative diffusional growth rate theory (Equation 5-8).

For the first hypothesis, the structure of the cloud, particularly the ratio between the liquid phase and ice phase depth, was shown to be related to the strength (PG) and current (j_{tot}) of the PG . The depth of the cloud (particularly the ice phase) is important for electrification. As the depth of the cloud is important for cloud electrification, the cloud characteristics are important for both inductive and non-inductive charge separation mechanisms to generate charge. The

amount of moisture in the ice phase was found to be particularly useful for the electrification of a cumuliform cloud.

For the second hypothesis, Z and σ_d were used to estimate the distribution of hydrometeor sizes within a cloud. Clouds with a substantial variety of hydrometeor sizes were hypothesised to increase the rate of charge separation. As laboratory experiments (Emersic and Saunders, 2010) have suggested that for sufficient charge separation to occur, hydrometeors of differing sizes must collide to transfer a net mass and charge upon collision. The evidence presented in this study (Figure 5-22 and Figure 5-25) agrees with the second hypothesis.

For the third hypothesis, the measurement of turbulence is not an independent variable and is weighted by the size and number of hydrometeors in the cloud. Decoupling turbulence was conducted by comparing the relationship of Z , \bar{v} , σ_v , σ_d , $\sigma_{\bar{v}}$, A_{base} and A_{face} with the sum of the total current measured at the surface. The comparison between $\sigma_{\bar{v}}$ and ε_T provides an indication of the importance for horizontal turbulence and wind shear. The results suggest that the horizontal component of turbulence would increase the charge generation within cumuliform clouds and suggests why the horizontal charge structures are so common in charged cumuliform clouds observed at CO.

Overall, this study has highlighted the importance of both hydrometeor size distribution and turbulence within the cloud. The PG and j_{tot} were most sensitive to different cloud characteristics measured in the ice phase of the cloud. Therefore, it can be concluded that the non-inductive charge mechanism is more important for the electrification of a cumuliform cloud. Table 5-8 provides a qualitative summary of the factors that were observed to be related to cloud electrification in no particular order.

Table 5-8: A qualitative summary of the cloud characteristics found to be important for cloud electrification of a cumuliform cloud.

Radar Parameter	Physical Description
High Moisture Content in the Ice Phase	The amount of water vapour (moisture) in the ice phase was found to increase the PG and j_{tot} measured at the surface significantly.
Cloud Base Area and Cloud Depth	The overall size of the cloud, both in width and depth, was found to increase the PG and j_{tot} measured at the surface. The depth of the ice phase was particularly sensitive to the electrical parameters measured at the surface.
Radar Reflectivity	The electrification of a cumuliform cloud was most sensitive to the size and number concentration of hydrometeors within the liquid phase; although a positive relationship was also found, less sensitive, in the ice phase of the cloud.
Standard Deviation of Mean Velocity	The width of hydrometeors sizes was found to increase with the electrification of a cloud but was less sensitive than the radar reflectivity. Consistently, the standard deviation of mean velocity within the liquid phase was most sensitive to the electrical parameters measured at the surface.
Standard Deviation of Terminal Fall Velocity	The PG and j_{tot} were most sensitive to the vertical velocity fluctuation of the hydrometeors measured in the ice phase of the cloud. The vertical velocity fluctuation in the liquid phase was found to plateau for highly electrified clouds (between group 2 and group 3).
Turbulent Kinetic Energy Eddy Dissipation Rate	The PG and j_{tot} were most sensitive to the eddy dissipation rate for both phases of the cloud, particularly the ice phase. The eddy dissipation rate in the liquid phase was found to plateau for highly electrified clouds (between groups 2 and group 3). The importance of the velocity fluctuations of hydrometeors is therefore important in both vertical and horizontal directions.

6 Cloud Electrification Measured In Situ

This chapter consists of six parts. First, the four cloud electrification hypotheses addressed in this chapter are explored along with details of the radiosondes used (§6.1). Second, the launch criteria used to best measure charged cumuliform clouds from the Reading University Atmospheric Observatory (RUAO) is discussed (§6.2). Third, the cloud identification algorithm derived from the radiosonde data, used for testing the hypotheses is discussed (§6.3). Fourth, an overview of all the radiosonde ascents is given along with a detailed discussion of a single ascent flown through a highly charged cloud. This discussion forms a case study showing the relationship between charge, cloud size, cloud backscatter and supercooled liquid water content (§6.4). Fifth, the four cloud electrification hypotheses are tested (§6.5). Sixth, a summary of all the results in this chapter is presented (§6.6).

6.1 Introduction

In this chapter, the electrification of cumuliform clouds is examined by taking measurements in situ on board ten radiosonde ascents that were launched at the RUAO. This chapter complements the previous chapter, which made similar observations of cumuliform clouds from the surface. The importance of this chapter is two-fold. First, an agreement of the relationships found in both studies should increase the robustness of the results; provided the same conclusions were found by multiple independent instruments. Second, the measurements taken in situ are more representative of the conditions of the cloud and should be more accurate, in comparison to the approximations made in the previous chapter using surface instruments (e.g. Field Mill (FM), 35 GHz Doppler radar (henceforth 'radar')). In this chapter, additional measurements of the cloud were made in-situ such as cloud temperature, wind speed, wind direction, and supercooled liquid water content (SLWC). Overall, four hypotheses were developed to explore the electrification of cumuliform clouds:

1 The magnitude of electric charge and hydrometeor backscatter within a cumuliform cloud are dependent on the phase of the cloud.

This chapter aims to highlight the importance of the liquid phase of the cloud, which complements the charge generation that occurs within the ice phase. Using the updraught that develops within a cumuliform cloud, liquid water can increase the relative humidity (RH), allowing for both the riming of existing ice hydrometeors and the growth of new ice hydrometeors from crystallisation (Saunders et al., 2001).

The charge separation between ice hydrometeor collisions has been shown to provide a potential gradient (PG) strong enough to initiate lightning (Saunders, 1992; MacGorman and Rust, 1998). In contrast, the amount of charge separated during collisions between polarised liquid hydrometeors have been shown to plateau before the electrical breakdown of the atmosphere can occur (Helsdon et al., 2002).

In §5, a strong relationship was found between the surface PG and clouds with ice and high moisture content (see Table 5-5). Only the ice phase of a cloud was found to increase in depth as the cloud became more charged, in contrast with the liquid phase of the cloud, which decreased in depth slightly (see Figure 5-21). These two results provided confidence that the charge separation occurs most proficiently within the ice phase of the cloud. In this chapter, the testing of this hypothesis is extended by directly measuring the position and magnitude of the charge within the cloud.

2 The amount of charge present within a cumuliform cloud has a positive correlation with the hydrometeor backscatter.

As discussed in the previous chapter, the most important cloud electrification mechanism is caused by the collision between differing sized hydrometeors, which are typically riming (Saunders, 1992; Emersic and Saunders, 2010). Riming hydrometeors contain a layer of liquid water on their edge, which has been observed to be negatively charged (Dash et al., 2001). Upon collision, the liquid water containing a net negative charge is shared between hydrometeors. A net mass of liquid water can be transferred when there is a difference in hydrometeor size, allowing a net transfer of charge. Therefore, the hydrometeor number concentration and the distribution of sizes are important for charge separation, particularly for the non-inductive mechanism. Backscatter is related to both hydrometeor number concentration and size (see §3.5.3).

In the previous chapter, a statistically significant relationship was found between the radar reflectivity (Z), the standard deviation of the terminal fall velocities (σ_d) and the PG for both phases of the cloud. In this chapter, the backscatter from the hydrometeors is measured on the radiosonde using two independent sensors at two distinct wavelengths (§3.5.3). Using two distinct wavelength measurements of the hydrometeors within the cloud allows independent sampling of the hydrometeor size distribution and number concentration.

3 Areas of turbulence increase the amount of charge separation within a cumuliform cloud.

Theoretical (Mareev and Dementyeva, 2017; Renzo and Urzay, 2018) and experimental (Cimarelli et al., 2014) observations of turbulent electrification have shown many charge

centres could exist within the cloud, separated in both vertical and horizontal directions. Renzo and Urzay (2018) proposed a hypothesis that smaller hydrometeors would be captured in a finite region of the cloud, with the size of the hydrometeors directly related to the mean eddy size. Larger hydrometeors would gain momentum and would increase the collision rate. As this method allows for increased collisions between differing sized hydrometeors, the amount of charge that could be separated would also increase as discussed earlier. A benefit of the Renzo and Urzay (2018) hypothesis was the built-in formation of charge centres caused by the capture of smaller hydrometeors. Therefore, this chapter hypothesises that turbulence coexists with regions of charge in the cloud.

In the previous chapter, the sum of the total current, j_{tot} measured at the surface was found to be positively correlated to the hydrometeor size; velocity and area of the cloud (see Table 5-7). For the different velocity measurements derived from the radar data (e.g. Doppler velocity, \bar{v} , spectral width, σ_v), turbulence was found to have the strongest positive statistical relationship with the sum of j_{tot} . The main limitation of the previous chapter was how convolved³³ the measurement of turbulence was with other cloud characteristics, particularly Z . In this chapter, turbulence and charge can be independently measured and compared, improving the confidence in any relationship found.

4 The charge present within a cumuliform cloud is proportional to the change in surface PG during the time the cloud passes overhead

The surface PG is often substantially perturbed at the same time as a cumuliform cloud is overhead (§5), greater than for any other cloud type. Furthermore, when a charged cumuliform cloud was overhead, the high frequency (> 0.1 Hz) variability of the PG would often be greatly reduced. This reduction of the PG variability is a strong indicator of charge centres within the cloud caused by the appreciable distance of the charge and the organisation of the charge into similar polarities. The FM's sensitivity to the charge inside the cloud is poorly understood as the FM measures charge in 4-dimensions while the radiosonde can only provide a snapshot of the atmosphere. Knowing how well the surface PG can represent the charge in the cloud can allow for improved estimates of the charge within the cloud using only remote electrical measurements.

The organisation of the charge within the cloud is important for defining the strength of the PG measured by the FM. The organisation of the charge within the cloud is a fundamental

³³ A number of assumptions were made to estimate the turbulence within the cloud, based on the distribution in the Doppler velocity profile, such as assuming the microphysics within the cloud were negligible. A description of the limitations of the radar are discussed in §3.4.1.

process to enhance the PG strong enough to cause an atmospheric breakdown, allowing lightning to form. Therefore, determining how organised the charge was within the cloud is useful to understand the evolution of a cumuliform cloud.

For this chapter, ten standard Vaisala RS92 radiosondes (henceforth 'radiosonde') (Vaisala, 2013) were fitted with additional bespoke instruments used for measuring charged cumuliform clouds. The bespoke instruments were added to the radiosondes to observe the relationships between electrical charge, cloud backscatter, turbulence and SLWC. For the electrical charge instrument, two sensors were used, known as the linear and logarithmic charge sensors. The two-charge sensors are used to derive space charge densities, ρ with high precision for small amounts of charge (linear sensor $< \pm 50 \text{ pC m}^{-3}$) but could sample much greater charges at a lower precision (logarithmic sensor $< \pm 150 \text{ nC m}^{-3}$). For the cloud backscatter instrument, the cloud is measured using two LEDs of differing wavelengths (Infrared and Cyan). The infrared LED is brightest and therefore provides a larger signal-to-noise ratio, therefore the cyan sensor is only used to support the results using the infrared sensor. These instruments are discussed in further detail in §3.5 along with the data processing methods used.

This chapter has the advantage of measuring the conditions of the cloud in situ, providing a greater understanding of the cloud structure using many different instruments. A disadvantage of this chapter is the small amount of data that was collected compared to the previous chapter (§5), which collected two years' worth of data. The next section discusses the launch criteria used to measure charged cumuliform clouds along with an overview of the meteorological conditions observed during all ten ascents.

6.2 Launch Criteria

The aim of this chapter was to take measurements within charged cumuliform clouds at various stages of development, from small cumulus clouds to cumulonimbus thunderstorms. Observations of cumuliform clouds at various stages of development provide a broad sample of measurements from the limited number of radiosondes (10) that could be launched. Launching a radiosonde into developing cumuliform clouds, particularly in the UK, is challenging both from a forecasting and logistical perspective (Köhler, 2005). The probability for a charged cumuliform cloud to pass overhead of the launch site (RUAO) is relatively low (1 – 10%) depending on time and day of the year (Hand, 2006). The probability for deep convection that could lead to lightning is even rarer with an average of 24 – 40 fl yr⁻¹ observed over the Reading area (61 km²) according to Anderson and Klugmann (2014).

Logistical constraints included the limited amount of time available for launching a radiosonde from the RUAO. At the RUAO, a radiosonde could only be launched within standard working hours (0900 – 1700 local time, Monday – Friday). Therefore, a maximum of 24% of the week was available for launching radiosondes. Furthermore, most cumuliform clouds occur within the late afternoon (after 1500 local time) with many clouds occurring later into the evening, past the 1700 launch window (Hand, 2006). Along with staff availability, required to help launch the radiosonde, many potential cumuliform clouds were missed.

Along with the standard forecast by the UK's Met Office (UKMO) providing precipitation information, a series of forecast metrics from the Global Forecast System (GFS) were used in the identification of cumuliform clouds suitable for launching a radiosonde. These metrics included the convective available potential energy ($CAPE > 100 \text{ J kg}^{-1}$) and the lifting index ($LI < 0 \text{ }^\circ\text{C}$)³⁴. The GFS thresholds are appropriate for cumuliform clouds within the summer months (June-July-August), while the criteria are substantially relaxed for cumuliform clouds within the winter months (December-January-February).

On the day of a potential radiosonde launch, four meteorological observations were used to characterise the weather conditions as close to real time as possible. First, reports from the European STOrms Forecast EXperiment (ESTOFEX, 2019). Second, observations from the radar at Chilbolton Observatory (CO). Third, the UKMO rain radar. Fourth, *PG* measured from both CO and the RUAO. The *PG* measurements were particularly useful when a radiosonde was ready for launch, to observe any appreciable perturbations caused by the charge residing within the cloud overhead.

Due to the number of restrictions launching a radiosonde, the aim of launching into well-defined cumuliform clouds was revised after the first five flights. Frontal systems, particularly cold fronts, have also been observed to be substantially charged (see §5), less charged on average than single-celled cumuliform clouds. As frontal systems are much larger than single-celled cumuliform clouds and are substantially easier to forecast using synoptic charts, half the radiosondes were launched into frontal clouds. The *PG* measured at the RUAO was then used as an indicator when the frontal cloud was charged. If the trajectory of the front was from the south-west, the *PG* measurements from CO along with estimates of the frontal speed could be used as an early warning indicator, providing up to an hour lead time.

³⁴ The lifting index is defined as the temperature difference between an air parcel and the environment at 500 hPa. The air parcel is lifted adiabatically from 500 m above the surface to 500 hPa. $LI < 0 \text{ }^\circ\text{C}$ is considered unstable with colder temperatures increasing the probability for thunderstorm to occur.

Table 6-1: The configuration of the radiosonde packages flown from the RUAO, showing the flight date, no. of channels, bits per channel and the sensors on each channel.

No.	Flight Date (UTC)	No. of Channels	Bits	Ch. 1	Ch. 2	Ch. 3	Ch. 4	Ch. 5
1	2018-03-02 1543	5	12	Linear Charge	Log Charge	Cyan Cloud and SLWC	IR Cloud	N/A
2	2018-03-02 1716	5	12	Linear Charge	Log Charge	Cyan Cloud and SLWC	IR Cloud	N/A
3	2018-05-24 1510	5	12	Linear Charge	Log Charge	Cyan Cloud and SLWC	IR Cloud	N/A
4	2018-05-31 1538	5	12	Linear Charge	Log Charge	Cyan Cloud and SLWC	IR Cloud	N/A
5	2018-07-27 1539	5	12	Linear Charge	Log Charge	Cyan Cloud and SLWC	IR Cloud	N/A
6	2018-12-05 0922	5	12	Linear Charge	Log Charge	Cyan Cloud	IR Cloud	Turbulence
7	2018-12-05 1612	5	12	Linear Charge	Log Charge	Cyan Cloud	IR Cloud	Turbulence
8	2019-01-29 1720	4	16	Linear Charge	Log Charge and Turbulence	Cyan Cloud	IR Cloud	N/A
9	2019-03-06 1253	4	16	Linear Charge	Log Charge and Turbulence	Cyan Cloud	IR Cloud	N/A
10	2019-04-04 1146	4	16	Linear Charge	Log Charge and Turbulence	Cyan Cloud	IR Cloud	N/A

Table 6-1 provides a full configuration of all ten radiosonde packages that were flown from the RUAO. Various changes to the radiosondes were implemented over the course of this research to provide better resolution for instruments and to focus on the turbulence sensor, which replaced the supercooled liquid water (SLW) sensor, in the later radiosondes flown. An understanding of the bespoke instruments and a careful examination of the forecast meteorological conditions were required to increase the probability for measuring charged clouds successfully. The next section discusses the method used to find the position of clouds within the ascent data using relative humidity with respect to ice.

6.3 Cloud Identification in One Dimensional Ascent Data

The relative humidity with respect to water (RH_w) is measured by the radiosonde (Vaisala, 2013). For sub-zero temperatures, liquid water can become supercooled contributing to the RH_w (Korolev and Isaac, 2006). As the phase transition between liquid and ice occurs, the RH in sub-zero temperatures falls. The amount of water vapour and liquid water in the atmosphere decreases as temperature decreases (Korolev and Isaac, 2008). The RH_w is, therefore a useful quantity to estimate the amount of supercooled water vapour that exists within the cloud for sub-zero temperatures.

Many studies have shown the non-inductive mechanism, which involves the collision between ice hydrometeors, can separate enough charge within the cloud for lightning to be initiated (e.g. Saunders, 1992). The non-inductive mechanism has been suggested to be the most efficient mechanism for charge generation (MacGorman and Rust, 1998). Therefore, the relative humidity with respect to ice (RH_i) must be calculated for comparison with charge measured within the cloud.

There are several formulations for calculating RH_i (Vömel, 2011). The majority of the methods to calculate RH_i are empirical equations using RH_w and the dry-bulb temperature (Wexler, 1976; Buck, 1981; Sonntag, 1994; Hardy, 1998; Goff and Gratch, 1946). For this chapter, the Hardy equation was used as it provides an accurate estimate of the RH_i and conforms to the International Temperature Scale of 1990. RH_i is defined as the ratio of the saturated vapour pressure with respect to liquid water, e_w , and ice, e_i :

$$RH_i = RH_w \frac{e_w}{e_i}. \quad 6-1$$

The main purpose of calculating RH_i was to identify cloud layers within the ascent. The cloud identification algorithm by Zhang et al. (2010) was used for this chapter as the algorithm was specifically designed for the Vaisala RS92 radiosondes using RH_i for all sub-zero temperatures.

Although the Zhang et al. (2010) algorithm has a low accuracy when compared against a ceilometer (500 m), the algorithm was used to objectively identify cloud layers. This is consistent with the cloud identification algorithm designed for use with the radar at CO (see §5.2). Although the Zhang et al. (2010) algorithm might not identify the precise boundaries of the cloud top and base, the algorithm can identify the most optically thick parts of the cloud. As charge separation has previously been found to be related to optically thick regions of the cloud (§5), the testing of the hypotheses in this chapter would not be greatly affected by the limitations of the Zhang et al. (2010) algorithm.

6.4 Case Studies

Measurements of charge, cloud backscatter, turbulence, and SLW are important to understand the processes involved in the development of a charged cumuliform cloud prior to lightning being formed. This section presents the data from a single radiosonde flight launched at the RUAO to demonstrate the type of information available from the bespoke sensors on board the radiosonde. The following sections provide an overview of all the radiosondes flown into charged cumuliform clouds (§6.4.1), followed by an in-depth analysis of a single highly charged cloud (§6.4.2).

6.4.1 Overview of Ascents

A broad range of clouds were targeted with different amounts of charge, ranging from newly developed cumulus clouds to near-lightning producing cumulonimbus clouds. The field campaign lasted for 12 months and provided a sample of clouds across a single year. Table 6-2 provides an overview of each radiosonde flight along with the synoptic and weather conditions. Not all radiosonde flights were successful (most noticeably flight No.1), with some flights having instrument failures. These instrument failures were mostly caused by data logging and software issues within the bespoke instruments. Comments are provided for each ascent providing specific reasons for choosing the charged cumuliform clouds flown through.

The surface *PG* measurements at the RUAO for each radiosonde flight are shown in Figure 6-1. There was an appreciable difference in the *PG* perturbation measured at the RUAO between radiosonde flights highlighting the range of cumuliform clouds that were targeted. The clouds targeted during ascents 5, 8 and 10 (Figure 6-1e, h and j) both contained enough charge to saturate the FM (maximum range $\sim \pm 1 \text{ kV m}^{-1}$). Particularly for ascents 5 and 10, the range of the *PG* can only be estimated, but the rapid change in polarity can still be used to determine the number of charge centres within the cumuliform cloud.

Table 6-2: The configuration of the radiosonde packages flown from the RUAO, showing the flight date, no. of channels, bits per channel and the sensors on each channel. Lightning nearby is for lightning observed by the BT-D-300 instrument installed at CO within 50 km.

#	Flight Date	Synoptic Information	Weather Conditions (°C, m s ⁻¹ , V m ⁻¹)	Is Lightning Nearby?	Instrument Failure	Comments
1	2018-03-02 15:43:00	A low-pressure system over SE England with an occluded and upper-level warm front residing over the UK for most of the day. The stability of the low-pressure system allowed cool air to travel over the UK.	Precipitation: Freezing Rain Temperature: -1.66 Wind: 2.2 PG: -79.1	No	Charge, Cloud, Liquid- Water	High chance for snow with a stationary front. Little signs for convection and instability. A chance to observe charge within winter clouds.
2	2018-03-02 17:16:00		Precipitation: Snow Temperature: -1.59 Wind: 3.8 PG: 21.9	No	Charge, Cloud	High chance for snow with a stationary front. Little signs for convection and instability. A chance to observe charge within winter clouds.
3	2018-05-24 15:10:00	Developing occluded front stationary above the RUAO with convection over the RUAO.	Precipitation: None Temperature: 15.2 Wind: 1.1 PG: 48.1	Yes	None	Good signs for convection and instability (CAPE > 500 J kg ⁻¹ , LI = -1.0 °C). High probability of single-celled charged clouds.
4	2018-05-31 15:38:30	A poorly developed low-pressure system moving NW over the UK. A series of troughs reside over the RUAO. Convection is likely for summertime conditions.	Precipitation: Drizzle Temperature: 19.5 Wind: 0.3 PG: 32.1	Yes	None	Good signs for convection and instability (CAPE > 1000 J kg ⁻¹ , LI = -1.0 °C). High probability of thunderstorms. ESTOFEX suggest severe thunderstorms likely.
5	2018-07-27 15:39:00	Three low-pressure systems surrounding the Atlantic, France, and Spain. Their configuration is similar to a Spanish Plume type event.	Precipitation: Heavy (10 mm h ⁻¹) Temperature: 24.9 Wind: 3.6 PG: > 1000	Yes	Cloud	High potential for convection but low convective instability (CAPE > 800 J kg ⁻¹ , LI > 0.0 °C). The moderate probability for thunderstorms. ESTOFEX suggest severe thunderstorms likely.

#	Flight Date	Synoptic Information	Weather Conditions (°C, m s ⁻¹ , V m ⁻¹)	Is Lightning Nearby?	Instrument Failure	Comments
6	2018-12-05 09:22:30	Well defined cold front moving over the UK as part of a low-pressure system. Moist air brought in over the Atlantic Ocean.	Precipitation: None Temperature: 9.39 Wind: 0.8 PG: 127.9	No	Turbulence Cloud	A substantial cold front moving across the UK from the SW with high stratiform rain rates forecast. The charged front could be observed at CO two hours before arrival at the RUAO.
			Precipitation: Light Rain Temperature: 11.7 Wind: 3.2 PG: -16.4	No	Turbulence	
8	2019-01-29 17:20:00	Well defined cold front moving over the UK as part of a low-pressure system. Moist air brought in over the Atlantic Ocean.	Precipitation: Drizzle Temperature: 3.5 Wind: 2.6 PG: -49.0	No	None	A substantial cold front moving across the UK from the SW with high stratiform rain rates forecast. The charged front could be observed at CO two hours before arrival at the RUAO
9	2019-03-06 12:53:00	A low-pressure system moving slowly over the UK. After the passing of a cold front, continental air from west France, allows a squall line to form passing over Reading.	Precipitation: Heavy (10 mm h ⁻¹) Temperature: 11.40 Wind: 5.2 PG: -352.2	No	None	Well-defined multi-cell convection was forecast and observed over an hour in advance. Lightning predicted by ESTOFEX. Low stability predicted by GFS forecasts (CAPE < 100 J kg ⁻¹ , LI < 0 °C)
			Precipitation: Light (< 3 mm h ⁻¹) Temperature: 6.07 Wind: 4.3 PG: -477.7	Yes	None	An occluded front with substantial RR was expected. The charged front could be observed at CO around one hour before arriving at the RUAO
10	2019-04-04 11:46:27	A low-pressure system moving slowly over the Southern UK. A trough followed by an occluded brought in a band of high rain rates (RR) moving over Reading.				

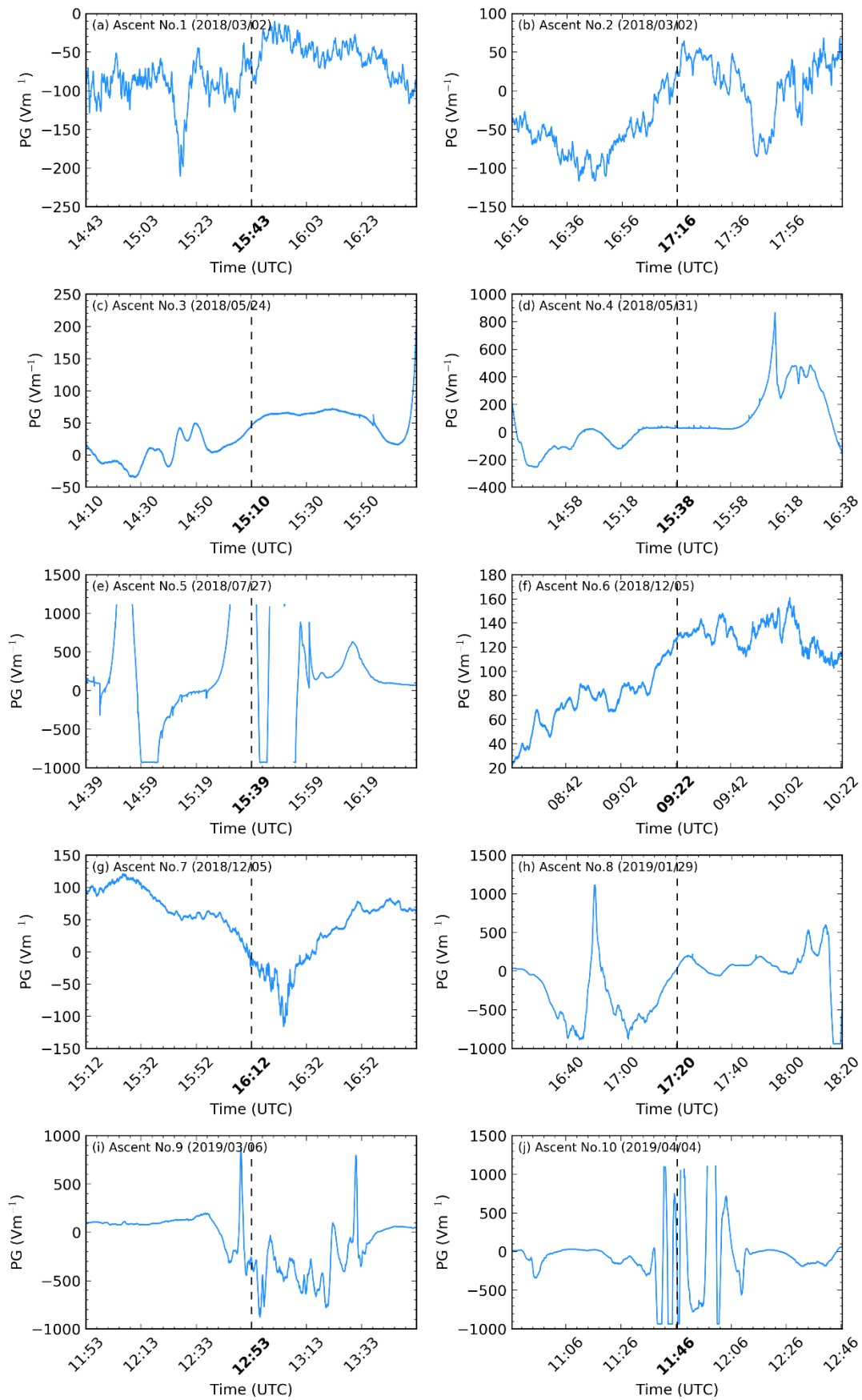


Figure 6-1: The PG time series for all ten-radiosonde ascents ± 1 hour around the time of launch. The launch time of each ascent is highlighted by the bold tick and vertical dashed black line. Note the large variations in y-axis values, particularly the truncated values near $\pm 1 \text{ kV m}^{-1}$.

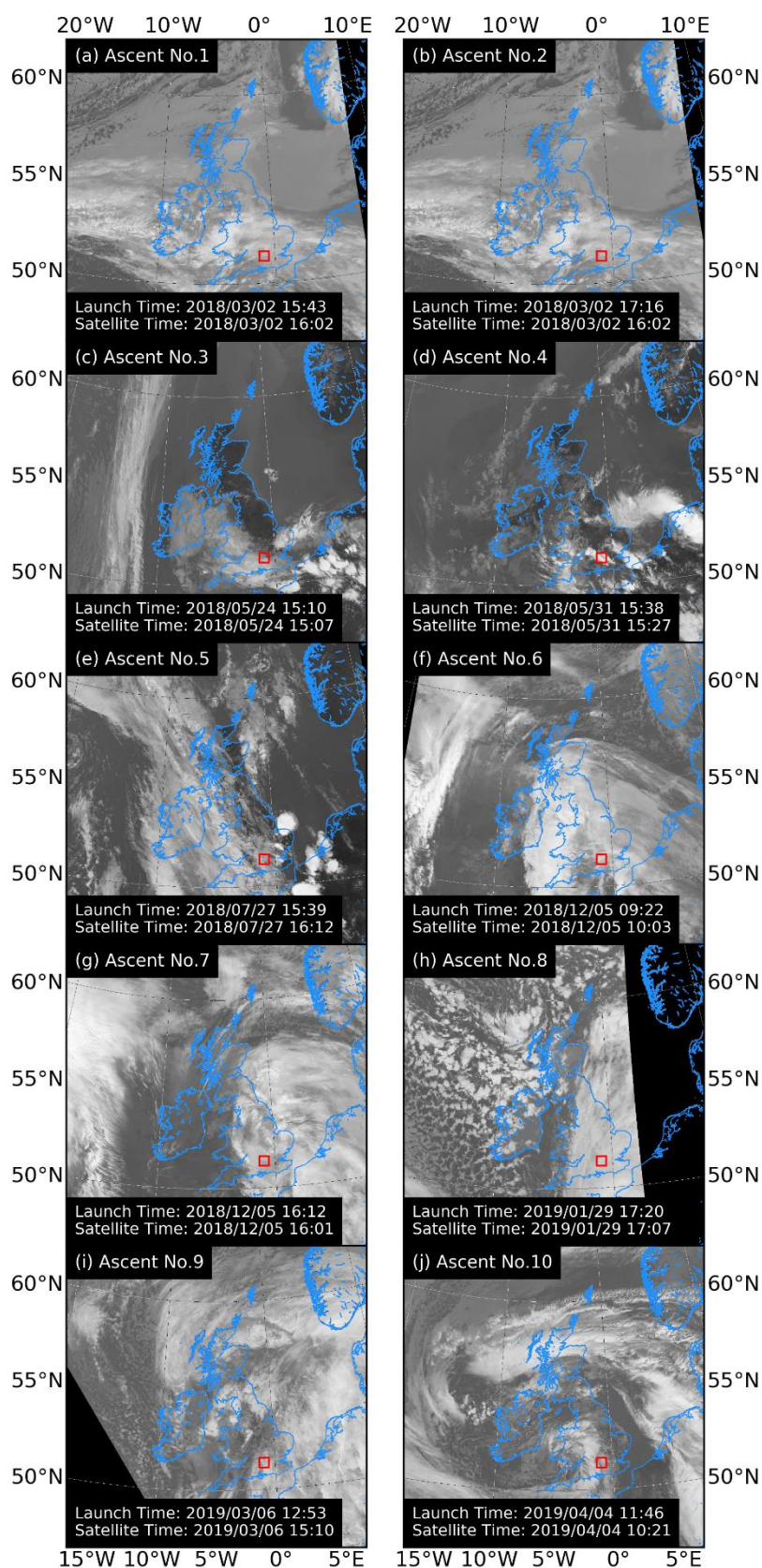


Figure 6-2: The closest (in time) near infrared (0.725-1.100 μm) satellite image taken over the UK for all ten radiosonde flights. The image was taken using the advanced very-high-resolution radiometer (AVHRR) aboard the MetOp-B satellite. The outlines show the sea-land and latitude-longitude boundaries (grey line). The RUAO launch site is defined by the red box and the coastlines are in blue [courtesy of NERC Satellite Receiving Station, Dundee University, Scotland (NEODAAS-Dundee, 2018)].

An overview of the cloud structure over the UK, for each of the successful flights, is shown in Figure 6-2 using the nearest, near infrared (0.725-1.100 μm) satellite image. The variations in cloud structure are substantial between convective plumes (Figure 6-2d) and well-defined fronts (Figure 6-2i). In Figure 6-2e, a band of mesoscale convective systems (MCS) can be seen over northern France and eastern England indicated by the bright white pixels within the satellite image.

6.4.2 Highly Electrified Cloud

This case study examines an ascent (No.4), which targeted two highly charged cumulus clouds on 2018/05/31, launched at 1538 UTC. The surface pressure analysis chart (Figure 6-3) shows four low-pressure systems co-existed over Europe. A trough line propagating north-west over Southern England highlights the chance for convection, bringing in warm dry air from central Europe and moist air from Spain, allowing for steep lapse rates to form. The trajectory of the trough line coincides with the trajectory of lightning strikes detected across the day (Blitzortung, 2019). The instability of the atmosphere can be observed during this ascent with very high values of CAPE (949 J kg^{-1}) and CIN (15 J kg^{-1}).

During the launch, drizzle was manually observed but was not measured by the automatic tipping bucket rain gauge at the site due to its low intensity. From the findings in §4, precipitation at this *RR* would have a negligible influence on the *PG* measured at the surface. The wind speed was very calm (one-minute average = 0.3 m s^{-1}) with an average temperature of $19.5 \text{ }^\circ\text{C}$. The state of the atmosphere at the RUAO can be seen in Figure 6-4. Deep convection was noticed west of the launch site, with thunder heard during launch. Lightning was confirmed

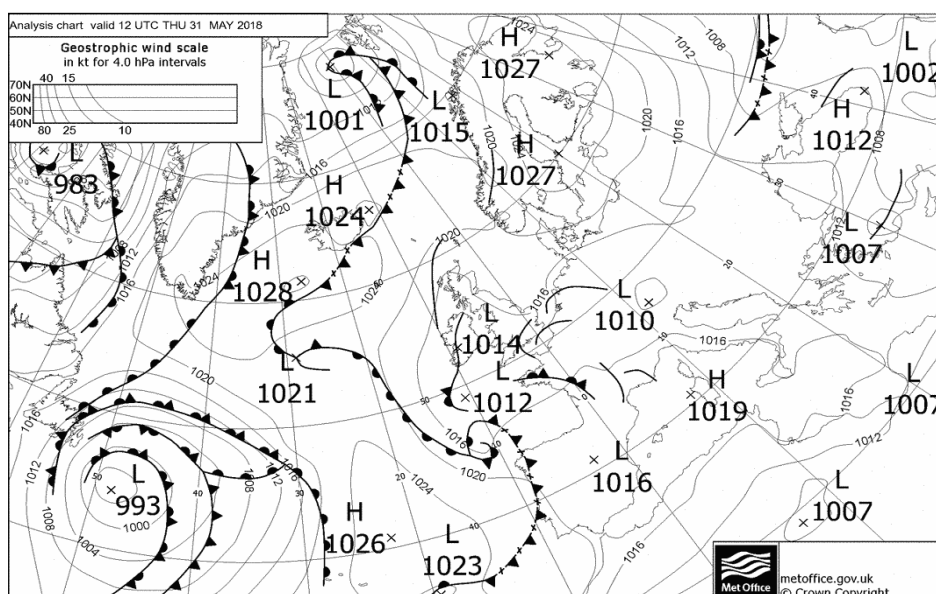


Figure 6-3: The United Kingdom Met Office (UKMO) surface pressure analysis charts on 2018/05/31 1200 UTC [courtesy of www.wetter3.de/fax].



Figure 6-4: Panorama of the cloud conditions at the launch site (RUAO) taken on 2018/05/31 1534 UTC with an azimuth between 130° (left edge of image) to 300° (right edge of image).

from the Biral Thunderstorm Detector (BTD) located at CO (Figure 6-5). A substantial amount of lightning was detected during this event across Southern England highlighting good synoptic and meteorological conditions for thunderstorms.

Overall, four cloud layers were identified within ascent No.4 using the Zhang et al. (2010) algorithm (Figure 6-6). Cloud layers ② and ③ were very thin layers (230 and 160 m respectively) and was not detectable by any bespoke instrument. A substantial amount of charge

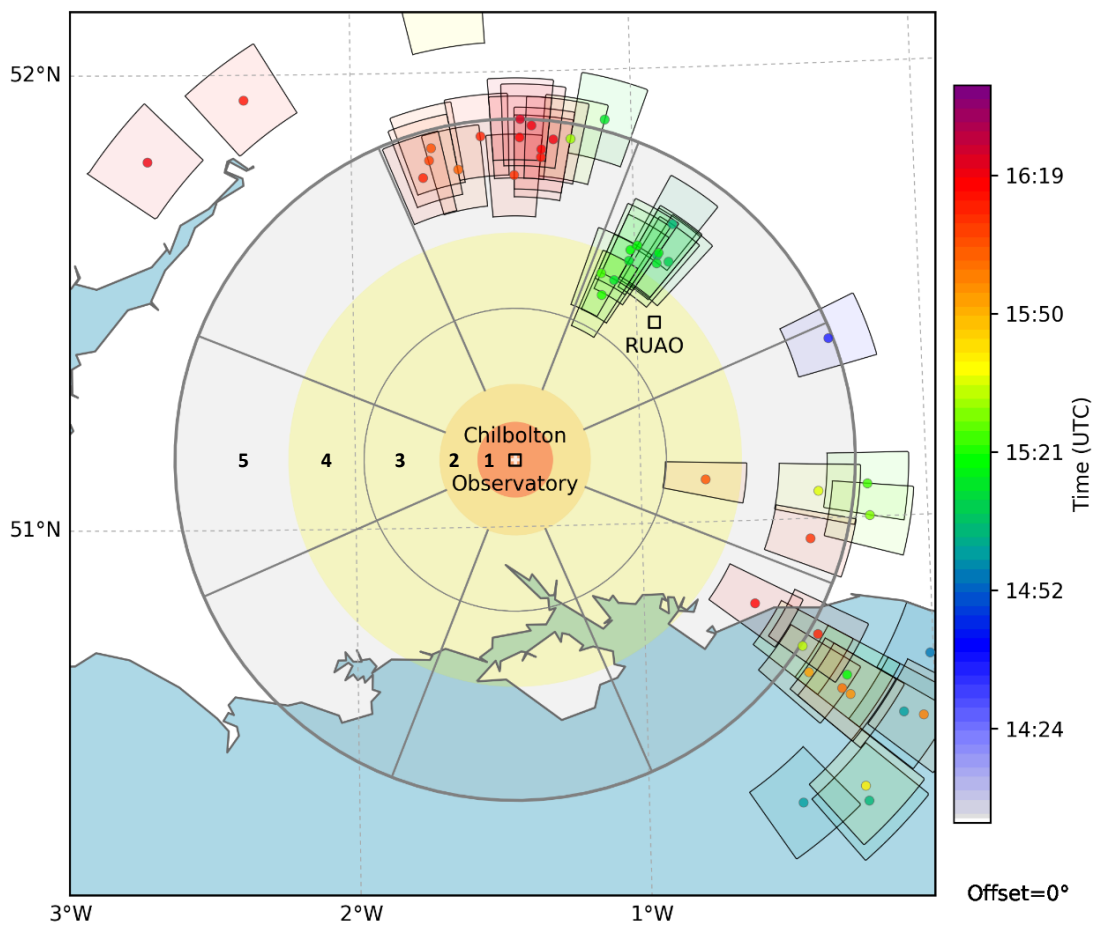


Figure 6-5: The location of lightning strikes detected by the BTD in the south of England on 2018/05/31 between 1438 and 1638 UTC. The circles represent the distances from Chilbolton Observatory (CO; white crosshair) and are used for various warning flags. The distance between each sector 1, 2, 3, 4, 5 and CO are 9.26, 18.52, 37.04, 55.56, 83.34 km respectively.

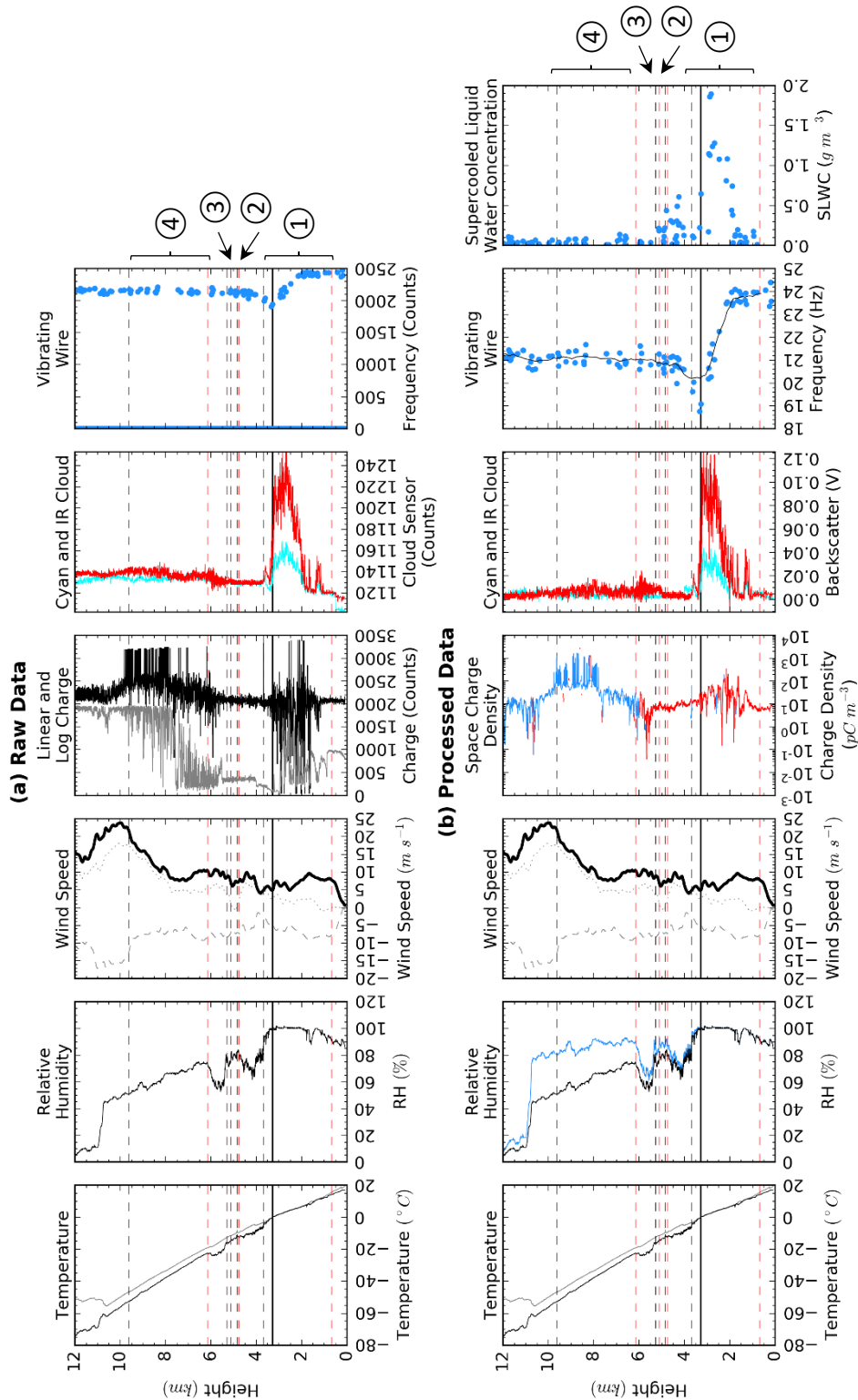


Figure 6-6: The raw (a) and processed (b) ascent profiles of a radiosonde (No.4) launched on 2018/05/31 1538 UTC. The dry-bulb (grey line) and dew-point (black line) temperature; relative humidity with respect to water (black line) and ice (blue line); meridional (dotted line), zonal (dashed line) and total (black line) wind speeds; linear (black line) and logarithmic (grey line) charge; cyan (cyan line) and infrared (red line) cloud; vibrating frequency (blue dots), SLWC (blue dots) and the 11-point moving average of the frequency (black line) of the SLW instrument are used to characterise the properties of the atmosphere. The space charge density shows the positive (red) and negative (blue) absolute values on a log scale to emphasise the wide range of charge measured. The cloud base (red horizontal dashed line) and cloud top (black horizontal dashed line) define the four cloud layers identified within the ascent, which are labelled ① - ④. The freezing level within the ascent is shown by the thick black horizontal line.

was observed in cloud layers ① and ④. Cloud ① contained mainly positive charge (95th percentile = 60 pC m⁻³), while cloud ④ contained mainly negative charge (95th percentile = -357 pC m⁻³).

The *PG* was also measured at the RUAO at the same time as the radiosonde launch (Figure 6-7). A large amount of charge was measured during the ascent and was expected to perturb the *PG* at the surface, but no appreciable perturbation of the *PG* could be observed. Some observations were made to understand why the *PG* was unperturbed. The variation of the *PG* was much smaller than during fair weather, suggesting space charge near the surface was being suppressed (MacGorman and Rust, 1998). The absolute *PG* at this time of day was smaller than the average at the RUAO (85.7 ± 0.009 V m⁻¹), plateauing around 30 V m⁻¹. A reduction in *PG* is consistent with charge being detected along the cloud base, a common observation in stratiform clouds (Harrison et al., 2017). Despite cloud ④ having an altitude 5 km greater than cloud ①, the amount of negative charge residing within ④ could mask the positive charge from ①. Several lightning strikes (and thunder) were observed during the launch which was measured by the FM (highlighted by the red circles in Figure 6-7a). The charge inside the thunderstorm, located less than 20.0 km away from the RUAO, could mask the charge from the cloud measured during this ascent, causing no substantial perturbations in the *PG*. The superposition of multiple charges on the *PG* can become complicated when coupled with other clouds, as discovered in §6.5.4.

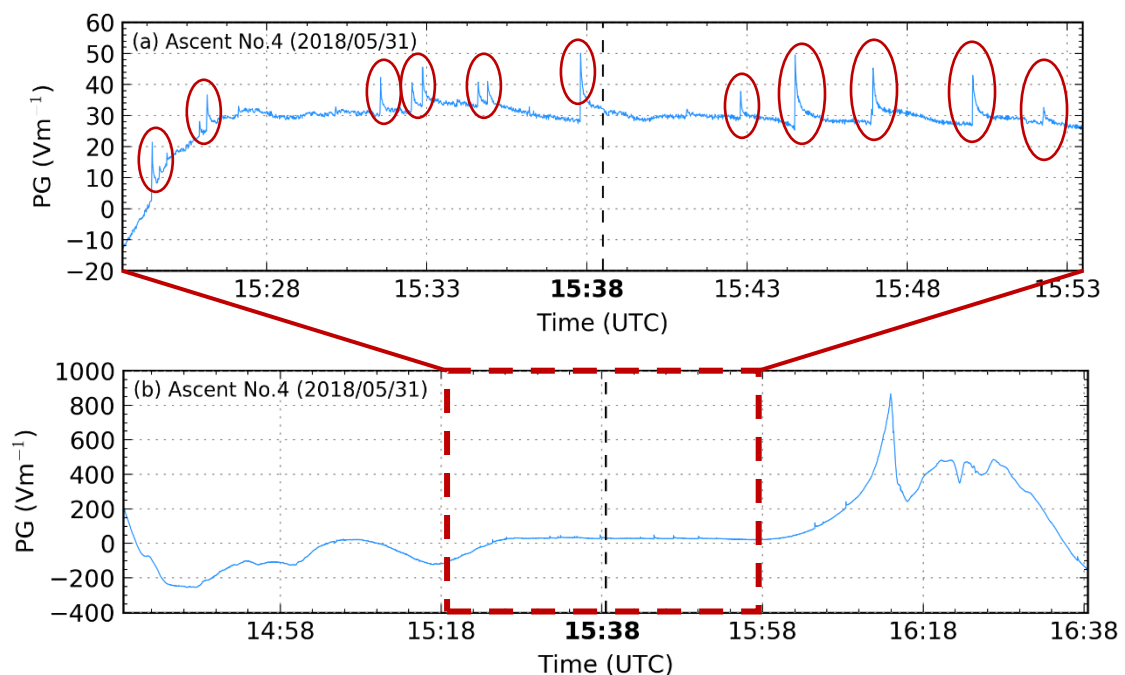


Figure 6-7: The *PG* measured at the RUAO between (a) 1523 and 1554 and (b) 1438 and 1638 UTC on 2018/05/31. The launch time of the radiosonde for this case study is highlighted by the bold tick and the vertical dashed black line. The red circles in (a) represent lightning strikes that were observed within the *PG*.

This radiosonde flight (Figure 6-6) was one of two ascents where the SLW instrument measured any appreciable changes in the vibrational frequency of the wire sensor. In cloud layer ①, the vibrating wire showed an appreciable change in frequency (5 Hz), equivalent to an SLWC of nearly 2.0 g m^{-3} . As the change in frequency occurred within the liquid phase of the cloud, SLW could not be the cause. Instead, the high backscatter voltage, V_B measured suggests that liquid drops colliding with the vibrating wire were more likely to cause a reduction in frequency.

The cloud layer closest to the surface ① was a mixed-phase cloud, marginally reaching into sub-zero temperatures (ice phase depth = 390 m). This cloud layer was very similar to the case study discussed in §5.4.2 which also existed with a small ice phase (maximum ice phase depth = 930 m). The case study in §5.4.2 was found to perturb the PG negligibly from the fair-weather state, but a substantial amount of charge was measured during this flight with $\rho > \pm 2 \text{ nC m}^{-3}$. Considering the measurements from the cloud backscatter instrument, only cloud layer ① had any noticeable perturbations with V_B up to 0.12 V and 0.04 V according to the infrared and cyan sensors respectively, the greatest perturbation from all ten ascents flown.

A noticeable correlation between V_B and ρ can be observed for cloud layer ①. V_B peaks just below the freezing level (3.0 km) and then sharply drops off as the radiosonde moves into sub-zero temperatures. Furthermore, the SLWC also peaks at the same height level, just below the freezing level. Above the freezing level, the frequency of the SLW instrument marginally increases but does not return to its original frequency (24 Hz), suggesting two processes were occurring simultaneously. First, the crystallisation of the liquid water forming ice started to occur. Second, the removal of the liquid water started occurring at a faster rate than the collection of liquid water as suggested by the substantial reduction in V_B .

A substantial amount of ρ was also detected within cloud layer ④ with up to 4 nC m^{-3} measured in the centre of the layer. As the temperature of the cloud was below $-20 \text{ }^\circ\text{C}$, no SLW was observed. The backscatter of the cloud was low in comparison to cloud layer ①. Both cloud sensors observed a low V_B ($< 0.02 \text{ V}$) which was consistent with the relatively low RH_i ($< 95\%$). The low RH_i and V_B , but high ρ has been observed before at CO. The case study described in §5.4.4 was a rare cloud event which consisted of a low Z (95th percentile = 22.7 dBZ) and low ϵ_T (median = $3.64 \times 10^{-5} \text{ m}^2\text{s}^{-3}$), relative to the mean sample of clouds identified, but a substantially larger PG was measured during its passing (range = 9.8 kV m^{-1}). The conclusion from that case study was that the cloud was in its dissipating stage. Similar observations have been observed at CO where Z would decay before the charge inside the cloud. The similarity between §5.4.4 and this case study is striking. The number of active thunderstorms that occurred around the

launch of this radiosonde along with the high CAPE and low LI calculated suggests that cloud layer ① was in its development phase, while cloud layer ④ was in its dissipating phase.

Summary statistics of all working radiosonde ascents (3 – 10) are given in Table 6-3. In comparison with other ascents, ascent No.4 had the smallest surface PG range, but not the smallest amount of ρ . For context, the ascent profile of all ten radiosondes is given in Appendix D consistent with Figure 6-6. The next section tests all the hypotheses discussed in §6.1, and are based only on the flights shown in Table 6-3. Ascents No.1 and 2 does not have any reliable measurements and to avoid bias, they were not used for any hypothesis testing.

6.5 Hypothesis Testing

This section tests the four hypotheses discussed in §6.1 relating to how the structure and kinematics of the cloud are important for cloud electrification, using the in-situ measurements from eight radiosondes (No.3 – 10). The following sections test each hypothesis in turn.

Table 6-3: Summary statistics of radiosonde flights 3 – 10 flown from the RUAO. The height of the cloud layers is based on the Zhang et al. (2010) algorithm with very thin clouds (< 400 m depth) being disregarded. The PG range is calculated using a time window of ± 10 minutes around the flight time. Radiosonde flights 1 – 2 are not given as these flights did not record any useful data and are not used in the testing of the hypotheses. The (L), (M) and (I) markers represent either a liquid, mixed or ice phase cloud respectively.

Flight Num.	Cloud Base (km)	Cloud Top (km)	Cloud Ice Depth (km)	Mean ρ ($\mu\text{C m}^{-3}$)	95 th Percentile ρ ($\mu\text{C m}^{-3}$)	Surface PG range (V m^{-1})
3	0.83	8.03	5.35 (M)	37	81	53
4	0.48	3.67	0.39 (M)	18	60	25
	6.14	9.62	3.48 (I)	-47	2	
5	3.44	8.24	4.53 (M)	303	451	> 2000
	10.62	11.87	1.25 (I)	-3	6	
6	0.15	0.98	0.00 (L)	43	85	62
	1.46	1.90	0.01 (M)	33	59	
	5.73	12.17	6.44 (I)	-15	26	
7	0.09	0.73	0.00 (L)	46	553	119
	1.95	8.84	6.63 (M)	223	106	
	9.21	10.18	0.98 (I)	17	25	
8	0.12	8.91	8.78 (M)	37	141	747
9	0.07	4.84	3.12 (M)	64	293	1755
	5.97	7.79	1.81 (I)	3	12	
10	0.21	6.94	6.23 (M)	85	257	> 2000

6.5.1 Relationship between cloud electrification and cloud phase and backscatter

To test whether the phase of the cloud is important for cloud electrification, ρ derived from the linear and log charge sensors (§3.5.2) and hydrometeor backscatter (§3.5.3) are compared with temperature with the hypothesis that,

The magnitude of electric charge and hydrometeor backscatter within a cumuliform cloud are dependent on the phase of the cloud.

The following sections test the hypothesis using the data collected from the radiosonde flights, highlighting the relationship between ρ and V_B is dependent on the phase of the cloud and is split into two parts.

The space charge density of a cumuliform cloud

To test the first hypothesis, the algorithm by Zhang et al. (2010) was used to identify layers of cloud within each ascent profile. Using the temperature data, three categories were used to group each cloud layer (Table 6-4). All measurements of ρ were then used as a sample for the distribution of charge typically observed within these three cloud types. To test this hypothesis, the magnitude of charge, $|\rho|$ is considered, as the polarity of the charge is not important here, only that charge was present.

Figure 6-8 shows a histogram of $|\rho|$ grouped by the cloud type as defined in Table 6-4. There is a substantial increase in $|\rho|$ between liquid and ice cloud layers, which was found to be statistically significant (first row in Table 6-5). A Mann-Whitney (MW) test was used as it provides a robust measure of the median difference between two distributions with no assumption about the distribution type (i.e. non-parametric). Despite the number of samples available for liquid cloud layers (388) being around an order of magnitude smaller than both ice (6074) and mixed (6531) cloud layers, a statistically significant relationship still holds using the more reliable Wilcoxon signed-rank test (last column in Table 6-5). The Wilcoxon signed-rank test assumes the two distributions are related and requires both distributions to be of equal length. Therefore, a random sample was taken from ice- or mixed-phase clouds to compare against the liquid-phase cloud layers making the statistical test fairer.

Table 6-4: Criteria used to classify all cloud layers within each ascent profile.

Cloud Group	Criteria
Liquid Clouds	Entire cloud $> 0\text{ }^{\circ}\text{C}$
Mixed Clouds	Bottom of cloud $> 0\text{ }^{\circ}\text{C}$, Top of cloud $< 0\text{ }^{\circ}\text{C}$
Ice Clouds	Entire cloud $< 0\text{ }^{\circ}\text{C}$

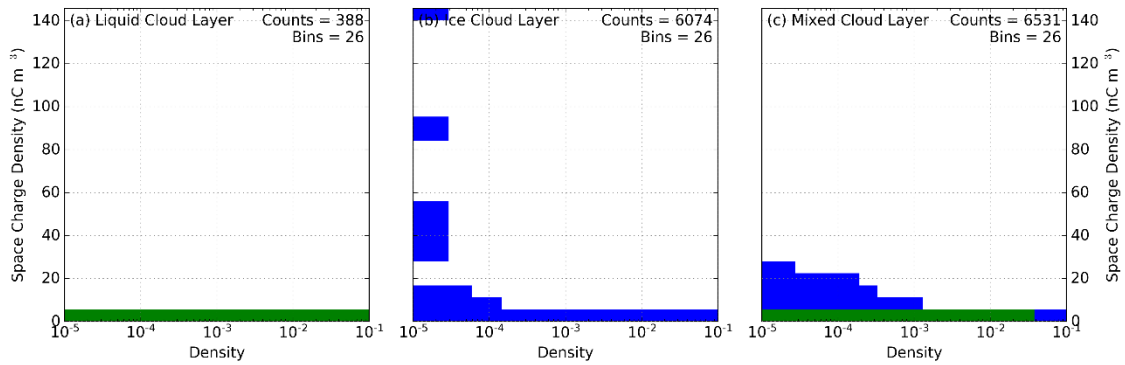


Figure 6-8: A normalised histogram of the absolute space charge density for (a) liquid cloud layers, (b) ice cloud layers and (c) mixed cloud layers using data from all ten radiosonde ascents. The colouring of each histogram shows the liquid (green) and ice (blue) components of the cloud layers. The histogram uses 26 bins (5.5 nC m^{-3} width) for each cloud type. A stacked histogram is used for (c) where green and blue represent the liquid and ice phase of the cloud respectively.

Ice-phase cloud layers have the greatest distribution of $|\rho|$ with values reaching over 140 nC m^{-3} . Looking at the density structure of the ice-phase cloud layers, $|\rho| > 20 \text{ nC m}^{-3}$ can be considered outliers. Conversely, mixed-phase cloud layers have the highest mean and median $|\rho|$ in comparison to liquid- and ice-phase layers with a strong statistical difference between ice- and mixed-phase cloud layers (second row in Table 6-5). On average, the greater amount of charge that has been measured in mixed-phase cloud layers suggests the important coupling between the liquid and ice phases of a cloud in the development of a thunderstorm. The outliers in ice-phase clouds might be a result of dissipating deep cumuliform clouds, which at their mature stage would be classified as a mixed-phase cloud, as concluded in §6.4.2.

Table 6-5: Results from testing the distributions of $|\rho|$ for liquid, ice and mixed-phase clouds using the Mann-Whitney U and Wilcoxon T statistics. All tests are statistically significant ($p < 0.001$), unless stated with *. The higher the value of the statistic, the greater the difference between cloud layers.

Test	Mann-Whitney U Statistic	Wilcoxon T Statistic
$ \rho $ between liquid- and ice-phase cloud layers	1382049	30372
$ \rho $ between mixed- and ice-phase cloud layers	10115599	4215829
$ \rho $ between liquid-phase clouds and the liquid component of mixed-phase clouds	225846	31463*
$ \rho $ between ice-phase clouds and ice component of mixed-phase clouds	7950350	3902587
$ \rho $ between liquid and ice components of mixed-phase layers	3047760	357888

The ice and liquid phase components of mixed-phase cloud layers contain a substantially higher $|\rho|$, on average, relative to liquid and ice only cloud layers respectively, highlighting directly the importance of liquid water for the non-inductive charge separation mechanism. The difference between cloud variants was also found to be statistically significant (third and fourth row in Table 6-5). The difference in the $|\rho|$ distribution between the ice and liquid phase components of mixed-phase cloud layers are also statistically significant. Although not explicitly shown in this analysis, the results from Figure 6-8 appear to agree with the relative diffusional growth rate theory, which requires ice crystal and graupel to rime in an atmosphere of high water vapour (Emersic and Saunders, 2010; Saunders et al., 2001).

The variability in synoptic and meteorology conditions observed during each radiosonde ascent provided a generic overview of the relationship found between $|\rho|$ and the phase of the cloud. Subsetting the ascents for cumuliform clouds, identified by strong perturbations of the surface PG^{35} , a comparable relationship was observed, consistent with Figure 6-8 (not shown). The difference between mixed cloud layers and ice cloud layers increased, with liquid layers being indistinguishable from ice cloud layers. The upper quartile of $|\rho|$ found in mixed-phase cloud layers in Figure 6-8 occurred only for cumuliform clouds subset as would be expected, capable of perturbing the PG substantially at the surface.

Hydrometeor backscatter and cloud phase

As the mean and width of the hydrometeor size distribution have been shown to play a vital role in increasing the probability for charge separation to occur (see §5.5.2), a test can be performed using the in-situ data from the eight radiosonde ascents (No.3 – 10). By subsetting³⁶ the cloud sensor data by cloud phase as described by Table 6-4, the dependence of V_B on the cloud phase can be evaluated.

Figure 6-9 shows the V_B distribution for the three cloud phases using data from the infrared backscatter sensor. The V_B for mixed-phase cloud layers has a substantially wider distribution than for liquid and ice-phase cloud layers, statistically significant using the MW test ($p < 0.0001$). The difference in the distribution of V_B was not statistically significant between liquid-mixed and ice-mixed cloud layers (MW = 1316983, $p = 0.1481$) suggesting liquid and ice hydrometeors increase in size and number concentration at comparable rates. As mixed-phase clouds were

³⁵ Ascents No.4, 5, 6, 9 and 10 were used for the cumuliform cloud subset.

³⁶ The subset of clouds was derived from the infrared and cyan cloud sensors from the radiosonde ascents when the cloud instrument was functioning correctly.

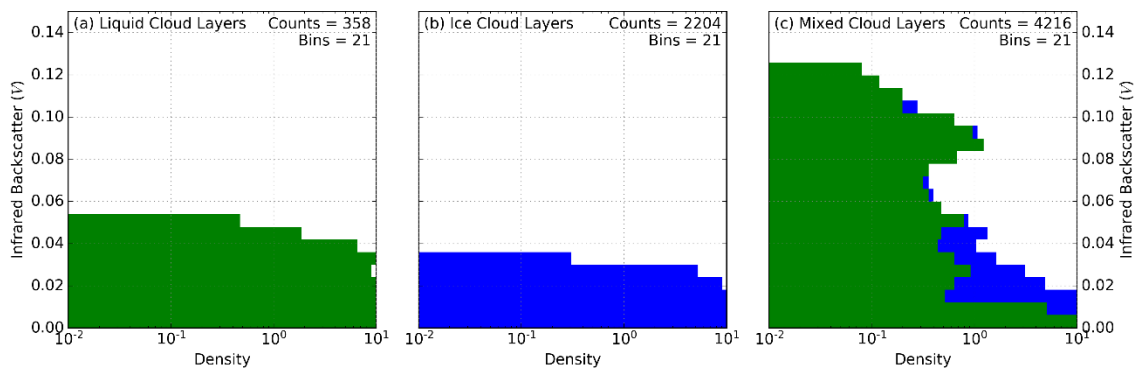


Figure 6-9: A histogram of the hydrometeor backscatter measured by the infrared cloud sensor for (a) liquid phase clouds, (b) ice phase clouds and (c) mixed phase clouds using data from radiosonde ascents 3, 4, 8, 9 and 10. The histogram uses 21 bins (7 mV width) for each cloud type. A stacked histogram is used for (c) where green and blue represent the liquid and ice phase of the cloud respectively.

found to contain more ρ than liquid- or ice-phase clouds (Figure 6-8), it can be inferred that both liquid and ice hydrometeors are equally important for charge separation.

6.5.2 Relationship between cloud charge and droplet properties

To test whether V_B is important for cloud electrification, V_B was compared with ρ , with the hypothesis that,

The amount of charge present within a cumuliform cloud has a positive correlation with the hydrometeor backscatter.

Linking with the second hypothesis in the previous chapter (§5.5.2), the electrification of a cumuliform cloud is directly related to the hydrometeor size distribution; a similar positive correlation was hypothesised to exist here with the hydrometeor backscatter. This requires the assumption that V_B is comparable to Z , and ρ is comparable to the surface PG ³⁷. Due to the number of issues with the cloud instrument, only five radiosonde flights were used (3, 4, 8, 9, and 10). The measurements of ρ are highly variable caused by the proximity of the charge with respect to the instrument (see §6.4.1). Therefore, to determine whether a relationship exists between the highly variable charge and hydrometeor backscatter, V_B and $|\rho|$ were grouped into 15 bins and median averaged.

Figure 6-10 shows the median relationship between V_B and $|\rho|$ using the data from radiosonde flights 3, 4, 8, 9, and 10. There is an appreciable positive correlation when $|\rho| > 20 \text{ pC m}^{-3}$ observed in both infrared and cyan sensors, while for $|\rho| < 20 \text{ pC m}^{-3}$, there is no appreciable change in V_B with $|\rho|$. Both infrared ($p < 0.0001$, $r = 0.865$) and cyan ($p < 0.0001$, $r = 0.836$) has a statistically significant relationship (for $|\rho| > 20 \text{ pC m}^{-3}$) using a 1.96σ inverse weighted least-squares linear regression. The threshold $|\rho|$ of 20 pC m^{-3} suggests a transition point occurs

³⁷ See §6.5.4 for a discussion on how comparable PG is with respect to the ρ measured within the cloud.

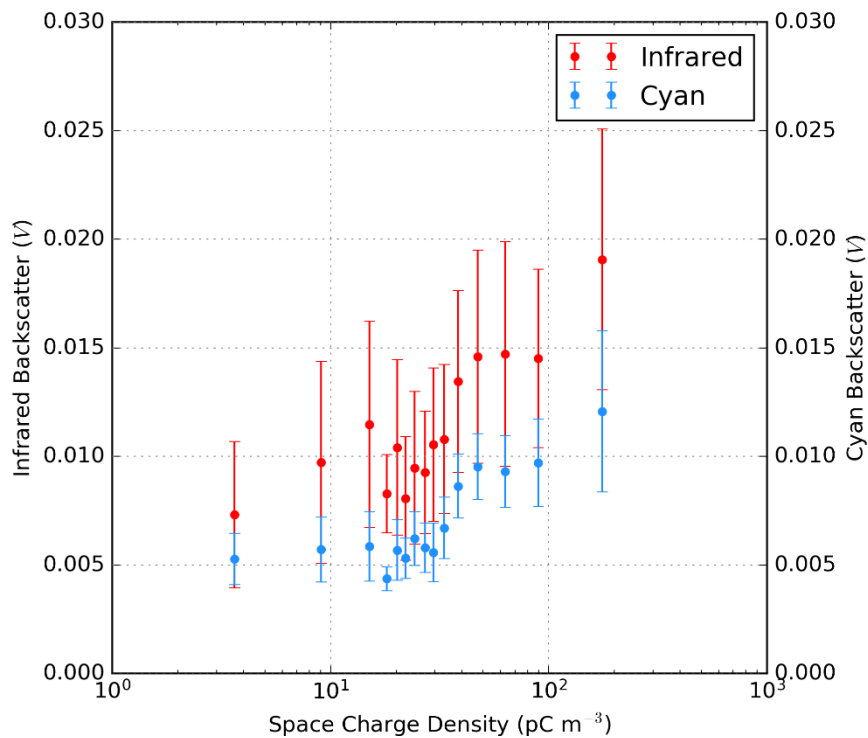


Figure 6-10: The median relationship (using 15 equal element unique bins) between number concentration derived from both infrared (left axis) and cyan (right axis) cloud sensors against absolute space charge density. A subset of radiosonde flights (3, 4, 8, 9, 10) was used for this figure of flights when the cloud instrument was working correctly.

between passively charging clouds (e.g. stratiform clouds) through conduction currents in fair weather towards actively charging clouds (e.g. cumuliform clouds) where the size of the hydrometeors is important for charge separation. The similarity between the relationship of the infrared and cyan sensor with ρ was found to be statistically significant ($p < 0.0001$, $r = 0.9623$) and that the transition point at $|\rho|$ of 20 pC m^{-3} suggests both sensors are responding similarly to the atmosphere.

6.5.3 Relationship between cloud electrification and turbulence

To understand whether turbulence is important for the electrification of cumuliform clouds, the eddy dissipation rate, ε_T was compared with ρ with the hypothesis that,

Areas of turbulence increase the amount of charge separation within a cumuliform cloud.

In the previous chapter (see §5.5.3), turbulence was found to be strongly related to the sum of the total current, j_{tot} measured at the surface (see Figure 5-31). This chapter aims to use the in-situ measurements to provide independent observations of both turbulence and charge within cumuliform clouds.

To determine if a relationship exists between ε_T and ρ , the data were averaged into 15 equal element bins using three ascents for which both turbulence and charge instruments were installed and working correctly (Figure 6-11). A strong inverse relationship was found between

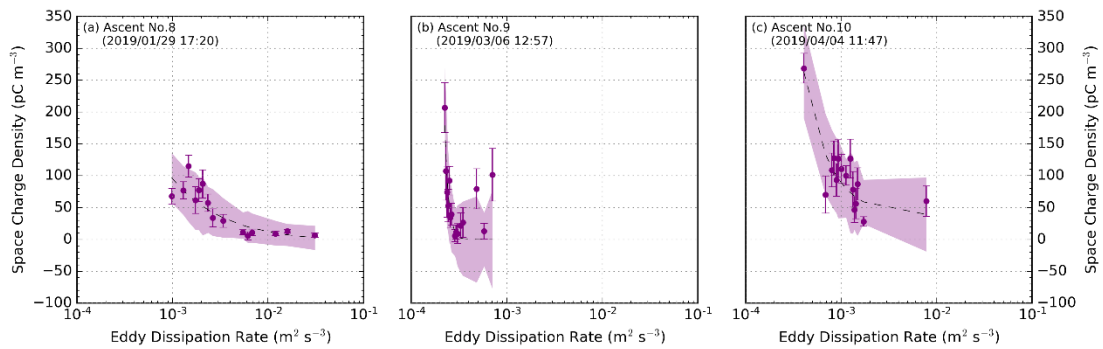


Figure 6-11: The relationship between ρ (measured by linear sensor) and ε_T averaged in 15 equal element bins for cloud layers (purple points) for ascents (a) No.8, (b) No.9 and (c) No.10 along with the 95% confidence limits (purple error bars). An ordinary least-squares power-law regression model ($y = ax^b + c$) was calculated for each ascent (black dashed line) and 95% confidence limits were calculated (purple shading).

ρ and ε_T for all ascents. Using a power regression model, weighted by inverse 1.96σ , ascents 8 ($p < 0.01$, $r = 0.881$), 9 ($p < 0.001$, $r = 0.733$) and 10 ($p < 0.001$, $r = 0.876$) were statistically significant. Although all ascents in Figure 6-11 have an inverse relationship, ascent 9 has an appreciable turning point at $3 \times 10^{-4} \text{ m}^2 \text{ s}^{-3}$, which is not consistent with ascent 8 and 10, which converges towards zero. As only three ascents could be used for this analysis, it is difficult to determine whether the differences in the relationship were caused by the difference in cloud type, a natural variation observed in ε_T , or something else. Ascent 8 measured a deep (8 km cloud top) cold front in which the turbulence profile was remarkably similar to that expected for an updraught: turbulence increased with height, reaching a maximum at the cloud top. Ascent 9 was part of a multicellular squall line with a substantial amount of charge measured, greater than ascent 8.

Finally, all ascents have an asymmetry in ρ , with a relatively small amount of negative ρ being measured on average. The relationship between ρ and ε_T supports recent theoretical modelling observations that turbulence enhances the charge separation process (Mareev and Dementyeva, 2017). Further measurements are vital to understand how turbulence influences charge separation and increase the reliability of the results shown in this chapter.

6.5.4 Relationship between space charge and potential gradient

To understand how the charge measured within the cloud is related to the surface PG , an estimate of the PG was calculated using ρ and was compared with the measured surface PG with the hypothesis that,

The charge present within a cumuliform cloud is proportional to the change in surface PG during the time the cloud passes overhead

An estimate of the PG can be found by using the in-situ measured ρ to represent charge centres within the cloud. Once the position of the charge centres has been estimated, the organisation of the charge within cumuliform clouds can be investigated to determine its importance in the development of a thunderstorm. This is achieved by comparing the results with other researchers' in-situ measurements of thunderstorms.

Estimating the Potential Gradient

As a radiosonde ascent only provides a single snapshot of a cumuliform cloud, a simple assumption was used to integrate ρ measured by the radiosonde to determine whether this is comparable to the surface PG . A simple assumption was required as there are numerous charges residing within the atmosphere that can contribute to the PG (MacGorman and Rust, 1998). Therefore, when estimating the PG using ρ , a finite time window around the launch time must be used for comparison. For example, the PG measured 10 hours prior to a charged cloud passing overhead is not related to the charge within the cloud.

To calculate the PG using the integrated ρ , a series of point charges were placed into the cloud. As the ρ measured by the charge sensors is dependent on the relative velocity of the charges within the cloud³⁸, placing point charges at every measurement position would not provide an accurate description of the charge within the cloud (i.e. this would be classed as oversampling). Therefore, an unbiased approach involved placing point charges during every polarity inversion. Figure 6-12 shows the method used to place the point charges within the ρ dataset. Once the polarity of ρ has been segregated, the charge, Q , was calculated using,

$$Q = \begin{cases} \text{percentile}(\rho, 5) \cdot \frac{4}{3}\pi\omega^3 & \{\rho: \rho < 0\} \\ \text{percentile}(\rho, 95) \cdot \frac{4}{3}\pi\omega^3 & \{\rho: \rho > 0\} \end{cases}, \quad 6-2$$

where ω is half the distance (units = m) covered by the radiosonde while within a single polarity of charge (see Figure 6-12 for visual example). A sphere ($\frac{4}{3}\pi\omega^3$) was used to represent the charge as larger charges have a greater influence on the surface PG and the influence of charge acts radially in 3 dimensions. The 95th percentile was used to minimise the effects of any anomalous values within the data. From equation 6-2, the PG can be estimated using Coulomb's law,

³⁸ Positive charge moving towards the sensor induces a positive current, positive charge moving away from the sensor induces a negative current. The opposite occurs for negative charge, making charge polarities difficult to decompose. The same condition applies whether the radiosonde or charge is moving.

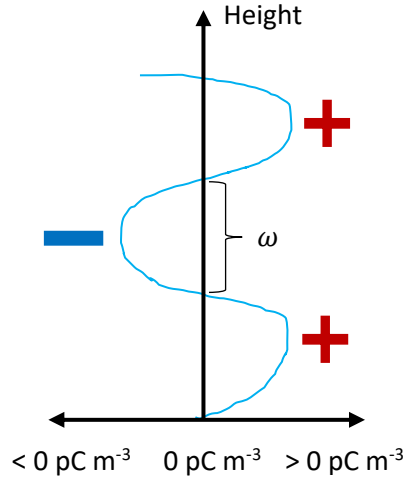


Figure 6-12: Diagram depicting the placing of negative (blue rectangle) and positive (red crosses) point charges within the space charge density data (blue line). ω is defined as ascent distance covered during a single polarity.

$$PG = PG_0 + \sum_i^n \frac{Q_i}{4\pi\epsilon_0 r_i^2} \cdot \hat{r}_i \quad 6-3$$

$$\hat{r}_i = \cos\left(\arctan\left[\frac{w_i(t + \Delta t_i)}{r_i}\right]\right) \quad 6-4$$

where PG_0 is the background PG , Q is the point charge, ϵ_0 the permittivity of free space, t is the time of the first point charge, Δt is the time difference of point charges with respect to the first point charge, r is the height of the point charge and w is the velocity of the cloud at its height level. For this chapter, PG_0 was set to 0 V m^{-1} as determining PG_0 with other charged clouds nearby, changing the PG , can be difficult to estimate and adds further uncertainty to the results. The temporal and horizontal spatial positions of the point charges were kept constant ($\Delta t_i = 0$), while the vertical spatial position was defined as the height, h measured by the radiosonde ($r_i = h$). The velocity, w of the point charge was defined as the total wind speed using the zonal, u and meridional, v vector wind components measured by the radiosonde,

$$w = \sqrt{u^2 + v^2}, \quad 6-5$$

Figure 6-13 shows a comparison of the estimated and measured PG for radiosonde ascents 3, 4, 6 and 7. Only the radiosonde ascent when neither the FM nor the charge sensor saturated was selected. The estimated and measured PG is substantially different from each other. As the point charges are vertically stacked and exist at a single time (launch time of the radiosonde), the shape of the estimated PG can only take two forms: a monopole or a vertical dipole. Ascents 4 and 7 are within the same order of magnitude, but ascent 3 is substantially different.

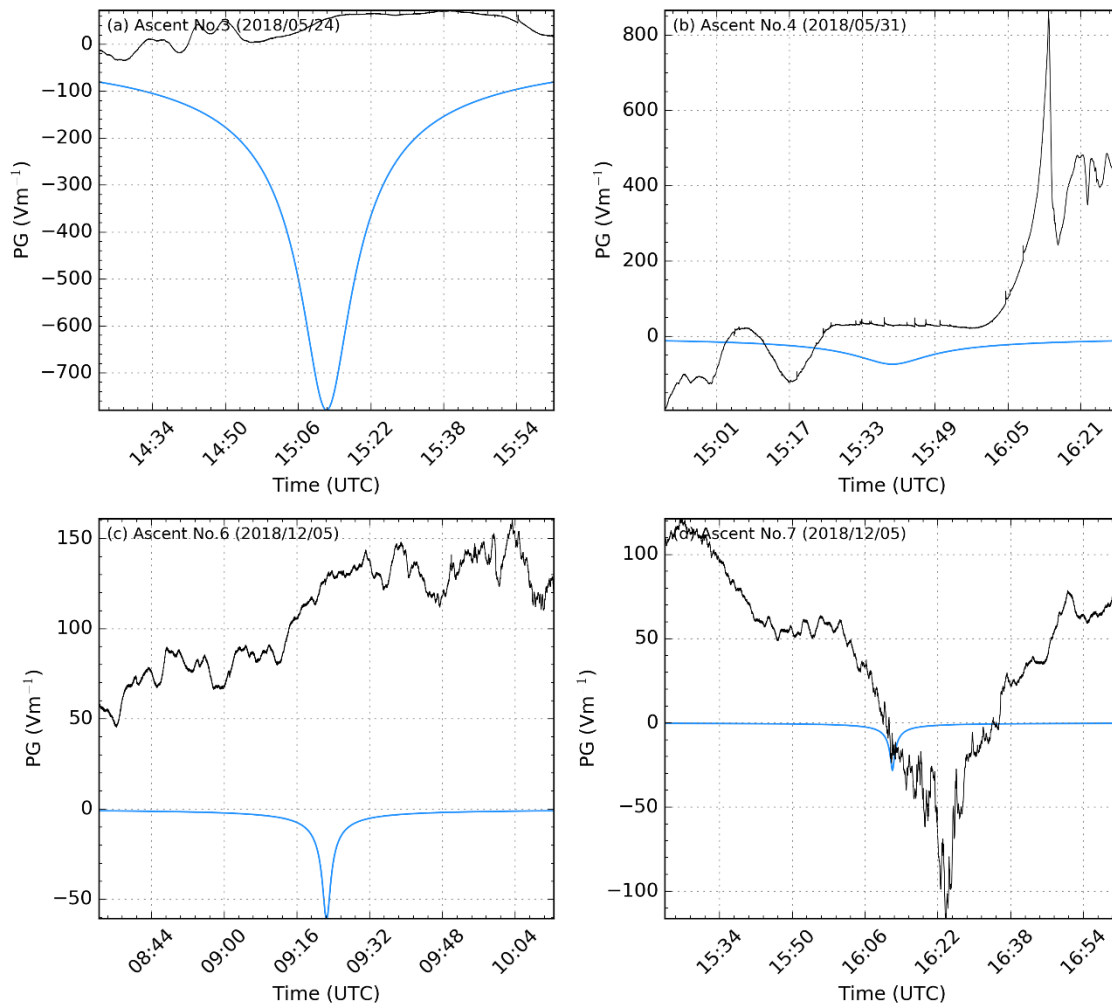


Figure 6-13: The measured (black) and estimated PG (blue) time series for radiosonde ascents 3, 5, 6 and 7, ± 1 hour around the time of launch. N.B The background PG was set to 0 Vm^{-1} for the estimated PG .

As the magnitude of the surface PG is weighted by the distance of the charge, and as the charge measured by the radiosonde only covers a small volume of the atmosphere, any relationship is difficult to identify. An alternative approach to compare the relationship between the cloud charge and the surface PG was to compare the statistics of each ascent. The sum of $|\rho|$ and the PG range (max-min) were used using the assumption that the more charge within the cloud would increase the PG perturbation. To understand how much of the surface PG was comparable to the charge in the cloud, the length of PG data around the time of launch was varied. As the four flights in Figure 6-13 all have small PG ranges ($< 80 \text{ V m}^{-1}$), additional flights were used when the PG was saturated. Only one extra flight (No.10) could be used as the remaining flights contained saturated or invalid values of ρ .

Figure 6-14 shows the relationship between the sum of $|\rho|$ and the surface PG range using ± 5 minutes' worth of data around the time of launch. Despite using a flight that saturated the FM, the FM was not saturated at the time of launch. A positive relationship was found using a 1.96

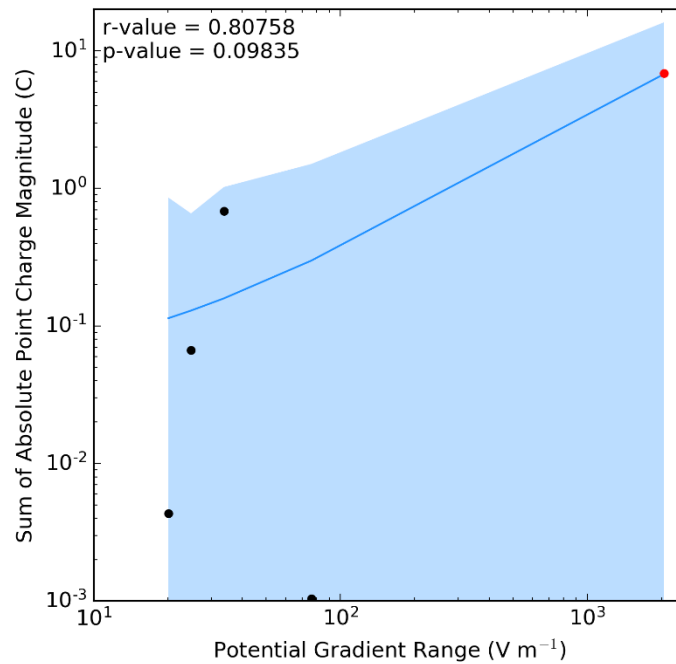


Figure 6-14: Relationship between the integrated $|\rho|$ and the PG range (max – min) using ± 5 minutes of PG data around the launch time. An ordinary least-square linear regression model was fitted to the data (blue line) with the 95% confidence limits estimated (blue shading). Saturated PG values are highlighted by the red data points.

σ inverse weighted least-squares linear regression model ($r = 0.8076$, $p = 0.0984$), but was only significant to the 90% confidence interval. Despite the causal link between charge within the cloud and its influence on the surface PG in the literature (MacGorman and Rust, 1998), the relationship between the sum of $|\rho|$ and the surface PG range is weak. There are many reasons why the relationship between the PG and the space charge within the cloud was so weak. First and most importantly, only having five flights with useable data requires an extremely high correlation ($r > 0.87834$) for the relationship to be statistically significant to 95%. Second, the charge instrument would contain an error associated with measuring the charge within the cloud. Third, there are numerous other charges within the atmosphere changing the PG (e.g. space charge, precipitation, and charge from other cumuliform clouds). Fourth, four of the five ascents used in this analysis contain weakly charged clouds, relative to other ascents in this dataset, barely capable of influencing the PG. Fifth, as multiple flights contain several cloud layers, the charge could be masked. As seen in flight No.4 (§6.4.2), there was a substantial amount of negative charge 5 km above a smaller amount of positive charge closer to the surface at 2.0 km. Sixth, the radiosonde itself is not measuring the vertical profile of the atmosphere, rather the profile of the cloud as the radiosonde moves both vertically and horizontally. During the radiosondes ascent, the dynamics within the cloud could greatly influence the magnitude and organisation of the charge during the radiosondes ascent through the cloud.

Space Charge Organisation

Using the polarity changes within ρ to locate the position of point charges can also be used to analyse the organisation of the charge within a cumuliform cloud. Previous observations of charged cumuliform clouds (§5), observed well-defined charge structures within the PG measured at the surface. A dipole was the most common charge structure observed which can be associated with the main charge centres within the cloud (MacGorman and Rust, 1998). For lightning to be initiated, a substantial PG is required to breakdown the atmosphere ($> 50 \text{ kV m}^{-1}$). Therefore, the distribution of the charge within a cloud must be sufficiently organised to allow a strong enough PG to be created to increase the probability for lightning to be initiated.

A comparison between ρ and the height between polarity changes can provide an indication of how organised the charge exists within the cumuliform cloud. Figure 6-15 shows the relationship between the 95th percentiles of $|\rho|$ with respect to the height between polarity changes. A strong positive correlation was found for cloud layers, which was found to be statistically significant ($p < 0.0001$) using an ordinary least-squares power-law regression model using the un-averaged data (black crosses in Figure 6-15). The correlation is emphasised when the data is averaged using 10 unique, equal element bins (solid circles in Figure 6-15). Only ρ derived from the logarithmic charge sensor was used rather than the combination of ρ derived from the linear and log charge sensors, as the time response of both instruments is different and reduced the relationship observed in Figure 6-15. This caused discontinuities in the data that were not

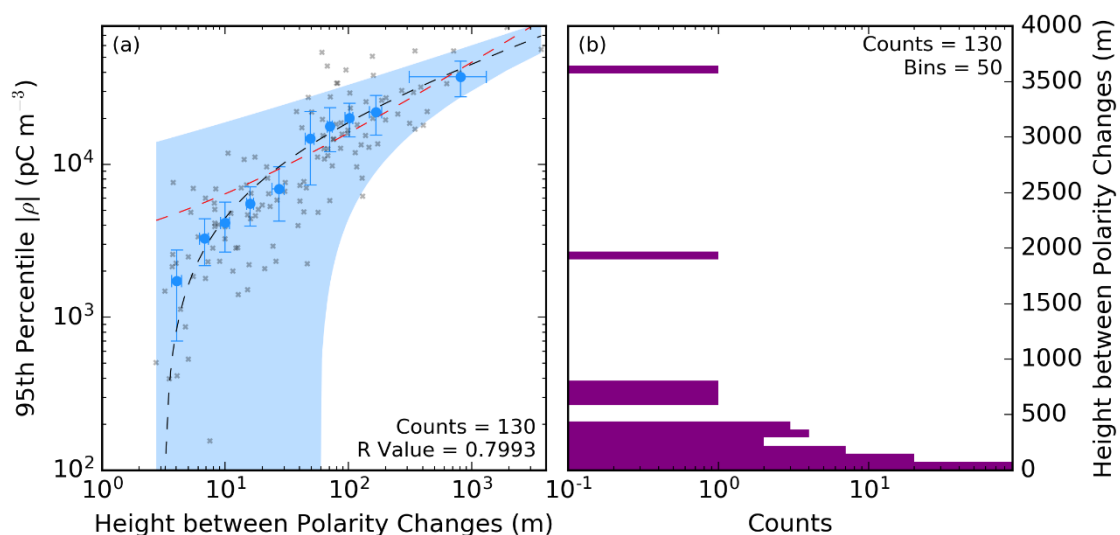


Figure 6-15: (a) The relationship between the 95th percentile absolute space charge density (using logarithmic sensor) and height between polarity changes for cloud layers. The data (black crosses) has been averaged (full circles) using 10 equal element bins with the 95% confidence level shown as error bars. An ordinary least-squares power-law regression model (black dashed line) was calculated using the un-averaged data with the shading representing the 95% confidence levels. The red dashed line is the same power-law regression model, but with the power coefficient fixed to 0.5 (see text for discussion). (b) A histogram of the height between polarity changes. Only flights number 3, 4, 5, 6, 7, and 10 were used, removing flights when saturation of the charge sensor occurred.

negligible when analysing the data at this resolution. Nevertheless, the same relationship was found using ρ derived from the linear sensor.

Table 6-6 provides the coefficients and model accuracy for the ordinary least squares power-law regression models used in Figure 6-15. The R^2 coefficient is appreciably high suggesting a strong relationship, matched by the small 95% confidence levels around all coefficients. As mentioned earlier, the charge sensors are sensitive to the movement of charge with respect to the sensing electrode (i.e. invariant to whether the radiosonde or the charge is moving), leading to false identifications of charge of a particular polarity.

To determine whether the relationship found in Figure 6-15 is directly proportional to the relative movement of charge, the electric force decay rate needs to be estimated. Using Coulomb's law, the strength of a point charge has an inverse-square proportionality with distance, meaning the greater the magnitude of charge, the longer in time and space that charge can be detected. Under this assumption, a relationship between $|\rho|$ and height between polarity changes should follow an inverse square law ($b = 0.5$) if the measurement of charge were proportional to the charges moving (see red dashed line in Figure 6-15). Using Table 6-6 (first row), the power-law coefficient (b) has a coefficient of 0.268 ± 0.103 , significantly smaller than the expected coefficient of 0.5 with the assumption that the movement of the charge within the cloud is the main reason for charges to be detected.

Further statistical testing can be achieved by using the Akaike Information Criterion (AIC). The AIC is used to estimate the model quality with a smaller AIC indicating a better model. The model quality of the relationship between $|\rho|$ and height between polarity changes is better (lowest AIC value) for a power coefficient of 0.268, compared to 0.5, emphasising the relationship is less caused by the charge moving relative to the radiosonde.

To increase the probability for lightning to be initiated, the charge needs to be organised into well-defined charge centres. Figure 6-15b shows a histogram of the height between polarity changes for cloud layers. The majority of the distribution has less than 1.0 km between polarity changes. Two events were recorded with substantially greater heights between polarity changes, both from radiosonde flight 10, with lightning detected within 50 km of the RUAO. The charge structure of the clouds measured in this chapter can be compared with the charge structure of known thunderstorms. Using six radiosonde flights, Marshall and Stolzenburg (1998) showed the vertical charge structure of thunderstorms has four main charge regions³⁹

³⁹ The main charge centres include the lower positive charge, main negative charge, upper positive charge, and upper negative charge.

Table 6-6: The results from four ordinary least-squares power-law regression model using the un-averaged data shown in Figure 6-15. The model has the form $y = a x^b + c$. All coefficients were found to be statistically significant ($p < 0.001$) and the 95% confidence levels are given. AIC is the Akaike information criterion used for model quality.

Model	R ²	a	b	c	AIC
Cloud $ \rho $ vs. Height between polarity changes (Variable power coeff.)	0.639	$(9.061 \pm 0.602) \times 10^3$	0.268 ± 0.103	$-(1.232 \pm 0.187) \times 10^4$	2727
Cloud $ \rho $ vs. Height between polarity changes (Fixed power coeff.)	0.593	$(1.408 \pm 0.103) \times 10^3$	0.5	$(1.960 \pm 1.156) \times 10^3$	2742

with other smaller charge regions interspersed. The height between polarity changes found by Marshall and Stolzenburg (1998) is greater than 0.2 km with at least one charge centre being greater than 1 km on average. The exact conditions (e.g. number, depth, width, the altitude of charge centres) required for lightning to be produced is unclear but is dependent on the microphysics and kinematic structure of the convective cloud (e.g. updraught speed) (Stolzenburg and Marshall, 2008).

The occurrence of thunderstorms in the UK is small relative to the occurrence of thunderstorms in other areas (e.g. mainland Europe, Africa, America). The results presented here suggest that most charged cumuliform clouds in the UK are capable of separating charge (high charge measured in many clouds both in situ and remotely), but most clouds are unable to organise the charge sufficiently (small difference in the height between polarity changes compared to known thunderstorms). The charge within the cloud needs to be organised into separate regions of polarity, forming charge centres, to help enhance the *PG* and to breakdown the atmosphere for lightning to be produced.

6.6 Discussion

In this chapter, ten radiosondes were launched at the RUAO into various cumuliform clouds with different meteorological conditions, providing a wide sampling range for studying the development of charged cumuliform clouds. Each radiosonde provided standard meteorological instrumentation (e.g. temperature, pressure, relative humidity, wind speed) along with bespoke instrumentation providing measurements of charge, backscatter, supercooled liquid water and turbulence (see Table 6-1 for instruments used on each radiosonde flight). Despite the much smaller dataset that was gathered for this chapter, in comparison to §5, the benefit of measuring the properties of the cloud in situ has provided a unique insight into the development of charged cumuliform clouds, particularly for the UK, aided by the wide sampling of cumuliform cloud

types (e.g. frontal, single-celled, squall lines). Therefore, this chapter provides independent measurements of charged cumuliform clouds, which can be used standalone and used to increase the robustness of the conclusions found in the previous chapter (§5). Below summarises the results gained from each hypothesis tested within this chapter.

1 The magnitude of electric charge and hydrometeor backscatter within a cumuliform cloud are dependent on the phase of the cloud.

- Mixed-phase cloud layers were found to contain significantly more charge ($p < 0.001$) than liquid and ice-phase cloud layers on average (Figure 6-8),
- Mixed-phase cloud layers had a higher hydrometeor backscatter than liquid and ice-phase cloud layers when observed using the infrared sensor (Figure 6-9).

2 The amount of charge present within a cumuliform cloud has a positive correlation with the hydrometeor backscatter

- For a hydrometeor backscatter voltage greater than 0.007 V, there was a statistically significant linear relationship with $|\rho|$. For a smaller backscatter, no relationship was found, but this is close to the lower limit of the instrument sensitivity (Figure 6-10).

3 Areas of turbulence increase the amount of charge separation within a cumuliform cloud.

- The ρ derived using the linear charge sensor, had a strong relationship ($p < 0.01$) with ε_T for cloud layers from three radiosonde ascents (Figure 6-11),
- An inverse relationship between ε_T and ρ was found but a statistically significant turning point only observed in ascent 9 suggesting key differences in either the charge separation process or the continuation of the relationship for different values of ε_T (Figure 6-11).

4 The charge present within a cumuliform cloud is proportional to the change in surface PG during the time the cloud passes overhead

- There is a strong correlation between the surface PG and ρ for ± 5 minutes around the launch time ($r = 0.8076$), but is statistically insignificant as only five ascents could be used (Figure 6-14),
- A strong power-law relationship was found between the height between polarity changes and the charge within the cloud ($r = 0.639$, $p < 0.0001$), (Figure 6-15a).
- The distribution of height between polarity changes is smaller than observed in thunderstorms measured by other researchers (Stolzenburg and Marshall, 2008). The lack of a charge centre greater than 1 km in depth is a good threshold between lightning and non-lightning producing storms (Figure 6-15b).

The results used to test hypothesis (1) of this chapter are consistent with those from the previous chapter (§5). In §5.5.1, 653 identified clouds were used to understand how the phase of the cloud influenced the surface PG . Overall, it was found that clouds perturbed the PG far less when no ice phase existed (see Table 5-5 and Figure 5-20). Clouds with both an ice phase and a high moisture content (presence of SLW) perturbed the PG greater compared with clouds with an ice phase, but no SLW present. The results presented here provide further evidence for the requirement of both liquid and ice phases for a cumuliform cloud to separate charge.

Recent theoretical modelling of thunderstorm electrification suggests the importance of turbulence for charge separation for both inductive and non-inductive mechanisms (Helsdon et al., 2002; Mareev and Dementyeva, 2017). Under a strong $\epsilon_T (> 10^{-2} \text{ m}^2 \text{ s}^{-3})$, the inductive mechanism was found to reach the breakdown voltage before the non-inductive mechanism, caused by the synchronisation between charge and relative velocity fluctuations providing an exponential growth for the inductive mechanism. Despite the small dataset acquired in this chapter, a strong relationship between ϵ_T and ρ was found for cloud layers. Further measurements would be advantageous to decouple the cloud by phase, velocity, and hydrometeor size and number concentration as these conditions have been found to be strongly related to the charge measured within the cloud.

The organisation of charge within cumuliform clouds is just as important as generating the charge itself. For example, all hydrometeors can be charged with an equal number being positively and negatively charged, but if the distribution of the charged hydrometeors is homogenous, no perturbation of the PG is possible. Therefore, the charge needs to be distributed by polarity, with enough charge to breakdown the atmosphere for lightning to occur. Measuring the charge, in situ, makes it possible to determine how organised the charge polarities are within the measured clouds. Comparisons with radiosonde launches conducted by Marshall and Stolzenburg (1998) showed well-defined charge regions with one region being greater than 1 km. Only one cloud measured in this chapter had a charge layer greater than 1 km. From an electrostatic modelling point of view, the amount of charge already separated would increase the number of thunderstorms if the charge were optimally organised, providing a PG strong enough to initiate lightning.

7 Conclusions and Future Work

7.1 Conclusions

The research presented in this thesis has investigated the processes required for cloud electrification prior to lightning occurring. The findings presented in this thesis can be used to improve the forecast of lightning, thereby reducing the hazards associated with thunderstorms, particular for human health. An electric field mill (FM) and two tipping bucket rain gauges were used to measure the potential gradient (PG) and rain rate (RR), respectively, at the Reading University Atmospheric Observatory (RUAO). A second FM and a thunderstorm detector (BTD), which measures the electrical current (j_{tot}), was installed at Chilbolton Observatory (CO) as part of a field campaign to take measurements of cumuliform clouds using the 35 GHz radar. Ten radiosondes were flown into charged cumuliform clouds from the RUAO, providing independent measurements of charge, cloud backscatter, turbulence and supercooled liquid water (SLW). Remote sensing (radar) and in-situ (radiosonde) measurements were made to measure the cloud characteristics allowing comparisons to be made with surface electrical measurements (FM and BTD). A tipping bucket, three drop counters and a disdrometer at CO and two rain gauges at the RUAO were used to investigate the influence of precipitation on the PG .

This research has also investigated the challenges involved in measuring the charge and characteristics of a cumuliform cloud. These challenges include the influence of precipitation on the surface PG , which can mask the charge residing within the overhead cloud, limiting the lead time of any lightning forecast. The accuracy of the cloud characteristics was investigated by making multiple independent measurements using in-situ observations of cumuliform clouds. The main research questions that have been investigated in this thesis are:

1. What are the effects of precipitation on the local potential gradient?
2. What are the main processes needed for appreciable electrification of a convective cloud that could lead to lightning?
3. How does charge within the cloud relate to the charge measured at the surface?

The last two questions provide context for considering the following open question:

- Why are most convective clouds charged, but rarely produce lightning?

This thesis has been presented as three work chapters. The following subsections summarise the main conclusions relating to each of the chapters, followed by the contributions this research has made to the knowledge of thunderstorm electrification. The remaining sections (§7.2 – 7.3) discuss the limitations of the instruments used to answer each research question,

followed by a discussion of the implications these results have for the scientific and wider community. Finally, a discussion is given on further improvements to this research and new lines of investigation based on the work conducted in this thesis (§7.4). Finally, a closing remark is given in §7.5.

7.1.1 The Effects of Precipitation on the Local Atmospheric Potential Gradient

The question of whether a relationship exists between the *PG* and *RR* is important for characterising the space charge that exists near the surface, particularly when using the *PG* when it is not raining. For example, using the FM to identify the charge within the cloud is limited by the magnitude and variability of the space charge near the surface. Previous research in understanding how precipitation influences the *PG* has struggled to conclude whether the change in *PG*, typically observed during rain events, is caused by the charge in the cloud (Ogawa, 1960; Simpson, 1949), the charge on the drops influencing the *PG* as it passes the FM (Scrase, 1938; Adkins, 1959), the washout of radon by precipitation (Takeychi and Katase, 1982) or the splashing of precipitation against the surface forming space charge (Lenard, 1892; Liu et al., 2010; Smith, 1955). What is consistent between previous researchers is an increase in negative charge during rainfall. This chapter attempted to understand the mechanism responsible for increasing the amount of charge near the surface during rainfall.

In this chapter, the *PG* was compared against the *RR* using two tipping buckets at the RUAO and one tipping bucket, three drop counters and one disdrometer at CO. The data was subset by cloud type (stratiform and cumuliform) (Harrison et al., 2008) to determine whether the relationship between the *PG* and *RR* changed, showing dependency on the charge within cumuliform clouds. The data was also subset by various surface conditions (pressure, wind speed, wind direction, rain event length and time between rain events) to evaluate whether rain splashing was the cause of increased negative charge near the surface. Overall, 13 years' worth of data was collected (2006-2018) to provide a robust relationship between the *PG* and *RR*, minimising any diurnal or seasonal variability.

A substantial decrease in the *PG* was observed for all *RR*s, consistent for all seven rain gauges used in this chapter. Six rain gauges observed a plateau in the relationship between the *PG* and *RR* around 4 mm h^{-1} with the *PG* perturbation weakening for greater *RR*s. No statistically significant variations were found when the relationship between the *PG* and *RR* was subset by cloud type to the 95% confidence interval. For changes in surface conditions, only changes in wind speed and time between rain events were found to influence the relationship between the *PG* and *RR* significantly (95% confidence interval). For small wind speeds ($< 2 \text{ m s}^{-1}$) and short

times between rain events (< 10 h), more negative charge was measured by the FM. For larger wind speeds ($> 2 \text{ m s}^{-1}$), the variability of the relationship increased significantly. For longer times between rain events (> 10 h), the amount of negative charge detected by the FM decreased. These findings suggest that the transport of charge is controlled by the surface winds and the magnitude and polarity of charge is influenced by the dryness of the surface. These findings are consistent with the splashing of rain against the surface.

7.1.2 Cloud Electrification Measured at the Surface

Now that a method has been established to determine the influence of precipitation on the surface PG , the relationship between the surface PG and charged cumuliform clouds was investigated. In this study, remote sensing data were used to evaluate the electrical and characteristics of cumuliform clouds. It was important to identify the position of a cumuliform cloud using radar and ceilometer data for comparisons to be made with the FM and BTM. The cloud base, cloud top and freezing level heights were identified, and the clouds were subset and compared. Overall, nearly 2 years' worth of data was collected at CO with 653 cumuliform clouds being identified using a bespoke algorithm designed to work with radar and ceilometer data (§5.2).

It was found that mixed-phase clouds contained the greatest amount of charge, measured by both FM and BTM. Liquid phase clouds had a substantially smaller amount of charge (87.8% reduction), and no clouds were identified with only an ice phase. This suggested that both liquid and ice phases are required for substantial electrification. It is inferred from the findings in this thesis, that the liquid phase of the cloud supplies moisture to the ice phase of the cloud, allowing riming of ice hydrometeors to occur, necessary for charge separation during collisions. Without a liquid phase, riming would be limited or cease altogether, halting charge separation. This inference is consistent with the relative diffusional growth rate theory, which requires riming ice hydrometeors to allow an exchange of mass and negative charge upon collision (Emersic and Saunders, 2010).

The size and density of hydrometeors within both liquid and ice phases of the cloud was found to be important for charge separation along with the width of the hydrometeor size distribution. For the 653 clouds identified at CO, a strong power law relationship was found between the PG range and 95th percentile reflectivity (Z) implying the hydrometeor size and density is positively correlated with cloud electrification. Linking back to the finding that mixed-phase clouds contained the greatest amount of charge, only 30 clouds identified (4.6% of total clouds identified) were found with only a liquid phase even though the Z threshold used to identify

cumuliform clouds was set very low (mean $Z > -20$ dBZ, 95th percentile > 0 dBZ). As a strong relationship was found between the cloud electrification and Z , it suggests that liquid phase clouds are weakly charged.

The clouds that lie above and below the 95% confidence limits could be used to identify clouds which had a high and low rate of electrification respectively. For example, in $PG-Z$ space, a cloud below the 95% confidence limit has a low rate of electrification as the hydrometeor size and density (inferred from Z) were increasing at a faster rate than the charge separation within the cloud. The opposite is true for clouds above the 95% confidence limit. Comparing these two groups of clouds found that clouds with a high rate of electrification (above 95% confidence limits) were 285% more likely to produce lightning (as detected by the BTM) than clouds with a low rate of electrification.

The velocity of the hydrometeors was also found to be important for cloud electrification, particularly when measuring j_{tot} by the BTM. The vertical component of turbulence, $\sigma_{\bar{v}}$, had the strongest agreement with j_{tot} measured at the surface ($r = 0.8814$) compared with all other cloud characteristics (e.g. Z , Doppler velocity (\bar{v}) and spectral width (σ_v)). Turbulence measured in both the vertical ($\sigma_{\bar{v}}$) and horizontal (eddy dissipation rate, ϵ_T) components were important for cloud electrification as observed by the FM. The horizontal component of turbulence is consistent with the horizontal dipole charge structures that have been commonly measured at CO. Comparisons between the velocity measurements of the cloud (σ_v , $\sigma_{\bar{v}}$, ϵ_T) and j_{tot} showed the surface area of the hydrometeors was important for cloud electrification, consistent with the relative diffusional growth rate theory (Table 5-7).

7.1.3 Cloud Electrification Measured In Situ

Now the cloud characteristics related to cloud electrification have been investigated, in-situ measurements of charged clouds were performed. In-situ measurements allow for independent measurements to be made, resolving some of the limitations of remotely measuring charge within clouds. The limitations that were resolved in this chapter involved the independent measurements of different cloud characteristics (e.g. space charge density (ρ), cloud backscatter, turbulence), which was previously Z -weighted and dependent on each other (see §3.4.1). Overall, ten⁴⁰ Vaisala RS92 radiosonde flights were launched from the RUAO which contained bespoke instruments measuring the charge, backscatter, SLW and turbulence within the atmosphere.

⁴⁰ Two of the ten flights contained mostly anomolous data and were not used in any analysis.

Overall, eight flights sampled a range of charged cumuliform clouds, ranging from frontal systems to squall lines. A consistent observation was found where mixed-phase clouds contained the widest charge and cloud backscatter distributions. The results derived from the in-situ turbulence measurements were not consistent with the study at CO, with an inverse relationship being found between ρ and ε_T for the three flights which measured turbulence successfully.

Secondary to separating charge within the cloud, the different polarities must be transported to separate regions of the cloud, forming charge centres, to enhance the PG by enough to breakdown the atmosphere allowing lightning to form. From six radiosonde flights, measurements of ρ for each ascent were used to identify how organised the charge was located within the cumuliform cloud. The height between polarity changes was used as a proxy for the organisation of charge within the cloud: the greater the height between polarity changes, the greater the depth of the charge centre. The organisation of charge into charge centres further enhances the PG , which can cause an atmospheric breakdown if the PG is strong enough. From six radiosonde flights, a strong relationship was found between $|\rho|$ and the height between polarity changes ($r = 0.639$) which was found to be independent of the relative velocity of the hydrometeors and the radiosonde. The maximum height between polarity changes was 3600 m, with 99% of events occurring with a height < 800 m. Marshall and Stolzenburg (1998) provides some comparison of the typical charge depths observed in thunderstorms. Marshall and Stolzenburg (1998) flew six radiosondes into six separate thunderstorms. They measured the height between polarity changes exceeded 1 km for at least one charge centre within the thunderstorm, consistent for all ascents. Therefore, one of the reasons identified by this research for why clouds rarely produce lightning in the UK is that there is an insufficient organisation of its charge.

7.1.4 Contributions

The research in this thesis has made several contributions to further understanding the cloud characteristics required for cumuliform clouds in the UK to separate charge prior to the onset of any lightning. Furthermore, measurements of the influence of precipitation on the surface PG have been analysed, providing insight into the mechanism involved. The key contributions for this work are grouped by each thesis research question and are summarised below:

What are the effects of precipitation on the local potential gradient?

- 1) During a rain event, an increase in negative charge exists, near the surface, causing the PG to be negative for all RRs above 1 mm h^{-1} .

- 2) The cloud type (i.e. stratiform, cumuliform) has little to no effect on the influence of precipitation on the PG near the surface.
- 3) The surface conditions including the wind speed and dryness of the surface (using the time between rain events) change how precipitation influences the PG near the surface. Greater wind speed increases the amount of negative charge near the surface, while the drier the surface decreases the amount of negative charge.
- 4) The increase of negative charge during rainfall, dependent on wind speed and surface dryness, is consistent with drop splashing against the surface. The release of negative charge by drop splashing is consistent with other researchers (Levin and Hobbs, 1971; Smith, 1955). This research provides a robust conclusion that drop splashing causes negative charge to be released at the surface.

What are the main processes needed for appreciable electrification of a convective cloud that could lead to lightning?

- 5) Mixed-phase clouds with a high vapour pressure in their ice phase provide the strongest electrification as measured by the surface PG . Substantial electrification ($> 1 \text{ kV m}^{-1}$) was only observed for clouds with an ice phase and when supercooled liquid water was detected. No substantially charged clouds were observed without a liquid phase.
- 6) Several cloud characteristics (Z , σ_d , $\sigma_{\bar{v}}$ and ϵ_T) were found to have a strong relationship with cloud electrification, consistent for both phases of a cumuliform cloud. The ice phase had the greatest sensitivity with surface electrical measurements (PG and j_{tot}).
- 7) Turbulence ($\sigma_{\bar{v}}$ and ϵ_T) has a strong correlation with cloud electrification, particularly for the liquid phase of a cumuliform cloud. This is consistent with the findings by Mareev and Dementyeva (2017) who found turbulence in the liquid phase can cause exponential growth of the PG using the inductive electrification mechanism.

How does charge within the cloud relate to the charge measured at the surface?

- 8) In-situ measurements showed that the charge within a cumuliform cloud can be measured at the surface, using the PG , for short time windows (± 5 minutes). The relationship between cloud charge and surface PG substantially weakens with the arrival of new charged cumuliform clouds.

Why are most convective clouds charged, but rarely produce lightning?

- 9) PG and Z have the strongest relationship out of all cloud characteristics. Clouds outside the 95% confidence limits of the relationship can represent clouds that either has a high

or low rate of electrification. Clouds with a higher rate of electrification have a greater probability of producing lightning compared to the lower rate of electrification clouds. The relationship between PG and Z has not been observed in the literature and provides a new method for detecting charged clouds using remote sensing observations.

- 10) The organisation of charge within cumuliform clouds in the UK are more disorganised than thunderstorms measured by other researchers (Marshall and Stolzenburg, 1998). A minimum threshold for at least one charge centre having a vertical depth greater than 1 km is required for lightning to occur.

These contributions have implications for experimental research and lightning forecast communities which are discussed in further detail in §7.3. Figure 7-1 shows all of the cloud characteristics discussed in Figure 1-6 that have been tested (green text) in this thesis. The conditions not tested are shown in black text. Additional cloud characteristics not explicitly defined have been appended to the figure. Overall, this figure highlights the complex cloud characteristics needed for sufficient cloud electrification.

7.2 Limitations

The following discusses the limitations of the instruments and data processing techniques employed for this thesis. Methods are highlighted on how these limitations were mitigated, to increase the robustness of the findings in this thesis.

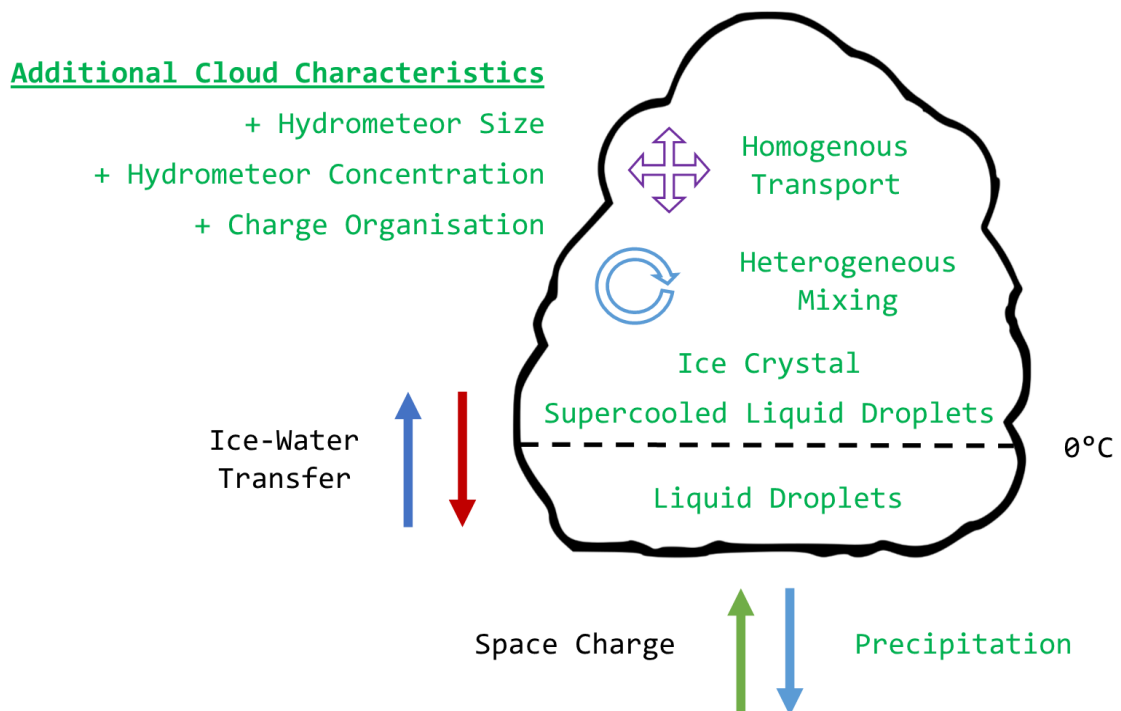


Figure 7-1: A conceptual diagram showing the cloud characteristics found to be related to cumuliform electrification within this thesis. Green text represents the cloud characteristics identified in this thesis. Black text represents cloud characteristics not tested within this thesis [adapted from Figure 1-6].

7.2.1 The Cloud Identification Algorithms

Three algorithms were used within this thesis to identify and categorise the types of clouds that existed at the RUAO and CO. A brief summary of the three algorithms are as follows:

- The Harrison, et al. (2008) algorithm uses solar radiation measurements to identify stratiform and cumuliform clouds. This was used in §4 to understand how the cloud influenced the relationship between the *PG* and *RR*.
- The radar-ceilometer cloud algorithm (§5.2) was designed for this thesis to identify the presence and location of cumuliform clouds. This was used in §5 to understand the important cloud characteristics needed for cloud electrification.
- The Zhang, et al. (2010) algorithm uses the relative humidity with respect to ice (RH_i) to identify cloud and moist layers within Vaisala RS92 radiosonde ascent data. This was used in §6 to provide a comparison between liquid, ice and mixed-phase clouds.

The Harrison, et al. (2008) algorithm can only identify clouds during the daytime once the sun has a direct line of sight with the solar radiation instruments. At the RUAO, due to tall trees along the horizon, the sun is required to be 8.28° above the horizon to allow correct measurement of the global and diffuse solar radiation. Due to this limitation, only 42.2% of the year can be used for cloud identification. This greatly limited the available data for subsetting the relationship between the *PG* and *RR* by cloud type. If the sky is overcast, then no identification of cloud type can be made (i.e. stratiform or cumuliform). As the time responses between the tipping bucket and cloud algorithm vary, it was difficult to gain a sufficient sample to determine the cloud type influence on the relationship between the *PG* and *RR*. Nevertheless, the findings show negligible variations between all cloud types within the 95% confidence limits, with any difference being low confidence.

The radar-ceilometer cloud algorithm has an unknown accuracy, as there are no known methods of identifying cumuliform clouds within the 35 GHz radar data. The purpose of the algorithm was to enable an objective method for the preliminary selection of cumuliform clouds within the dataset. The algorithm initially identified the cumuliform clouds and then human interpretation was used to remove false positives. The algorithm was kept as simple as possible to avoid over-processing the data. For each cloud identified, a series of statistics were calculated and were used to answer the second thesis question. Using a statistic to represent the entire cloud minimises the errors in the identification algorithm and the radar-ceilometer instruments.

Despite the Zhang, et al. (2010) algorithm being designed for the Vaisala RS92, its accuracy of identifying the base and top of a cloud can have an error of up to 500 m. This error is substantial

as many clouds can have a cloud depth smaller than 500 m and might not be identified by this algorithm. This error is caused by the low RH_i near the cloud boundaries, making it difficult to identify the position of a diffuse cloud base and top. As a consequence of this limitation, the areas of an ascent the algorithm identifies as a cloud can be considered with high confidence, as the cloud has a high RH_i . The cloud backscatter can also be used to identify regions of cloud in the ascent. As the data is also used for analysis (§6.5.1) an independent method was required and the cloud backscatter data was not used for cloud identification.

7.2.2 Instruments

The instruments used for this thesis all have varying degrees of capabilities when measuring their desired quantity. The limitations of these instruments increase the error associated with any finding in this thesis. A number of methods were used to address these issues.

Rain Gauges

The data retrieved from the Delta-T tipping bucket installed at the RUAO was recorded as an analogue voltage to represent the tips in the form of voltage steps. The data also varied substantially in time, which made identifying a voltage step difficult to locate. As the Delta-T tipping bucket contained the largest dataset (7 years), a bespoke algorithm (top-down tip detection) was designed to resolve this issue to retrieve the exact timing and number of tips recorded (see §3.3.1). As with all algorithms, false positives and negatives are an inevitable consequence that adds extra uncertainty into an otherwise complex relationship between the PG and RR . Extensive testing of the top-down tip detection algorithm and comparisons with six other rain gauges showed consistent results, but the extra uncertainty of having to process the data has increased the uncertainty in the relationships found in §4, particularly when decoupling the relationship by cloud type and surface conditions.

Electrical Instruments

The main limitations of the electrical instruments, particular the FM due to its one electrode, is the difficulty in identifying the origin of the charge (e.g. space charge, corona, precipitation, cloud charge, etc.). The timescales of variability can help to distinguish between different charge sources only if the distance between charges is large (e.g. cloud charge and surface charge). For example, the PG is a superposition of all charges within the atmosphere, a cumuliform cloud containing multiple charge centres with different polarities would produce a complex PG structure measured at the surface. The total charge that exists within the cloud is not easily found using the PG alone. Two clouds identified with the same PG structure, measured at the surface, can have substantially different charges within the cloud, depending on the orientation

of the charge within the cloud. Therefore, the *PG* only provides an estimate of the charge within the cloud. Electrostatic modelling is required to estimate the total charge within the cloud. An attempt was made to estimate the *PG* by placing point charges within the cloud which represented the charge centres of the cloud. This bespoke algorithm was eventually abandoned, due to issues in optimising multiple parameters that represented the point charges in spacetime. As there are multiple parameters that require optimising, many charge configurations are realistically possible. Therefore, it is difficult, if not impossible, to verify which charge configuration would be most accurate to the real world.

Radar

All the cloud characteristics measured by the radar are *Z*-weighted. Trying to decouple the influence of turbulence on the electrification of a cumuliform cloud is difficult. By cross-comparing the relationships of different cloud characteristics, an attempt can be made to partially decouple the *Z*-weighting (see §5.5.3 for an example of trying to decouple the *Z*-weighting issue). These limitations are one of the main reasons for the development of ten radiosondes that could measure many of the characteristics in situ, using different instruments, providing much more representative, uncoupled and independent measurements, in the attempt to increase the robustness of the findings of this thesis.

Radiosondes

There are two main limitations for comparing the cloud characteristics using the in-situ measurements.

First, the PANDORA interface with the Vaisala RS92 radiosonde provides a 64-bit data (four 16-bit variables) stream which greatly limits the number of sensors that can be recorded simultaneously. A compromise was made to limit the number of instruments to just three, with the SLW and turbulence sensors each being used in only half of the radiosondes. As the charge and cloud backscatter instruments were the most important instruments, each containing two sensors, the temporal resolution was decreased for a third instrument (either turbulence or SLW) to be used. As a consequence, certain instruments were recorded at 0.5 Hz in comparison to the standard 1 Hz resolution (i.e. two sensors would share the same data channel).

Second, the reliability of the bespoke instruments varies between and during ascents. As the bespoke instruments are research sensors⁴¹ (and therefore not commercially available), the amount of testing performed on them and the development time are limited. As the accuracy

⁴¹ Therefore, the instruments are still being developed, with some of the instruments being more reliable and accurate than others.

of each electronic component used to build each instrument has variability, the measuring range varies between instruments of the same type. This variation was mostly solved through laboratory calibrations (e.g. charge sensor), which saw appreciable differences between instruments. A radiosonde experiences a wide temperature difference between the surface and the stratosphere ($> 60\text{ }^{\circ}\text{C}$) with many instruments being prone to temperature drifts. Although a series of methods were used to accommodate any drift in the data, other atmospheric effects can also limit the instrument measuring capabilities. This includes rime that occurs on the instrumentation (e.g. on the charge electrodes) which reduces their sensitivity to measuring the atmosphere. The range of the instrument to which charge can be measured is unknown for the charge sensor and is assumed to be consistent, and thus comparable, throughout the ascent.

These limitations increase the error of any findings within this thesis. By quality controlling the data effectively (see §3), any results can still show significance if there is a difference beyond the 95% confidence limits.

7.3 Implications

The implications of the contributions presented in this thesis for the scientific and wider community are discussed and are separated by the three work chapters.

7.3.1 The Effects of Precipitation on the Local Atmospheric Potential Gradient

The implications of this work can be defined in two parts. The second implication is possible to implement (as have been performed in this thesis) but would likely have a minor impact on the wider community, likely to only be used in a small number of cases.

First, the release of negative charge during uncharged precipitation, caused by the splashing of drops against the surface, can be used to further characterise the *PG*. Other sources of charge are often masked during precipitation and a substantial source of charge (e.g. from a cumuloform cloud) is required before it can be distinguished in the *PG*. Secondary to the impact of precipitation on the *PG*, a minimum amount of charge residing within a cloud is required before this charge is detected at the surface. To gain a better understanding of the many factors which influence the surface *PG*, the minimum charge provides a threshold for how early in a charged cumuloform cloud's life stage the cloud charge can be detected using surface-based electrical instruments. A better understanding of the influences on the *PG* allows cloud charge studies to be analysed more effectively. As charged rain and corona have been observed to provide a much bigger influence on the surface *PG*, further research can provide a maximum threshold for identifying uncharged precipitation. Broader implications of the release of negative charge

during precipitation could be the benefit to human health as negative ions have been associated with the capture of particulate matter within the atmosphere (Jiang et al., 2018).

Second, the *PG* can now be used as an alternative quantitative method of determining the *RR* remotely without the need for a rain gauge. As the confidence limits increase substantially after 5 mm h^{-1} , the *PG* is only effective at measuring small *RRs*. Another caveat is that the *PG* can only be used to estimate precipitation from non-cumuliform clouds, as the charge residing within the cloud would break the relationship. As shown in the case study examples in §4.3, any charged clouds dramatically increase the variation in the relationship between the *PG* and *RR*. Despite the small benefits of using the *PG* to estimate the *RR*, observatories that only use manual rain gauges or only have access to a tipping bucket rain gauge can benefit from FM derived *RR*. For example, tipping bucket rain gauges have a low resolution for small *RRs* ($< 1 \text{ mm h}^{-1}$) and a FM can be used to increase the resolution for small *RRs*.

7.3.2 Cloud Electrification Measured at the Surface

The implications of this work can be defined in three parts.

First, the data collected from the field campaign at CO brings together a novel set of instruments (FM, BTD and radar) which has allowed the sampling of both the *PG* and j_{tot} in comparison to the cloud characteristics. The length of data collected allows the sampling of both summer and winter cumuliform clouds which were developed from a range of synoptic conditions. The subsetting and filtering of the data have allowed cumuliform clouds containing various amounts of charge to be identified, allowing one to focus on key meteorological conditions. The legacy of this dataset can allow future researchers to make new findings in how cumuliform clouds become electrified and how this can be related to lightning. As this data was recorded continuously, non-disturbed weather events were also sampled, and a variety of other atmospheric electrical research can be performed using other pre-installed instruments at CO, for example, aerosol - *PG* studies (Matthews et al., 2016).

Second, the findings from this chapter showed that mixed-phase clouds are capable of separating more charge than liquid or ice phase clouds. The importance of the liquid phase is to supply moisture into the ice phase of the cloud for the non-inductive charge separation mechanisms. This result is consistent with tropical thunderstorms, which often have a much greater liquid phase depth, and produce many lightning strikes (MacGorman and Rust, 1998; Lane-Smith, 1969; Peterson et al., 2017).

A third, but tentative implication is the relationship between *PG* and *Z* provides a simple example of using outlier clouds (95% confidence limits) as a method to forecast lightning. If a cumuliform

cloud has a higher PG compared to Z , compared to the mean relationship, a 285% increased chance for lightning to occur compared with clouds that have a lower PG compared to Z was found. A caveat of this was the inclusion of dissipating clouds. As the findings suggest, a dissipating cloud would decrease in Z at a faster rate than the charge within the cloud, causing a hysteresis effect. This inclusion of dissipating clouds weakened the $PG-Z$ metric to forecast lightning. With the identification of dissipating clouds, a formal probability function could be defined allowing for a robust prediction for lightning. For this metric to be viable for lightning nowcasting, especially over a wide area, a large cloud radar and FM network would be required which would produce difficulties in its practical implementation.

7.3.3 Cloud Electrification Measured In Situ

Although many clouds observed in both chapters 5 and 6 were substantially charged, suggesting charge separation occurs sufficiently, their poor organisation limits the enhancement of the PG . Under sufficient organisation of the charge within the cloud, it might be possible for the pre-existing charge to lead to lightning.

7.4 Future Work

In addition to the implications discussed in the previous section, there are other areas that this thesis has shown are worth examining in more detail. This section is separated into two key areas, focusing on the electrical effects of charged clouds (e.g. charged rain and corona) and on the importance of turbulence to organise and distribute charge within the cloud.

The use of charged rain and corona as a lightning forecasting metric

Charged rain and corona can have a substantial influence on the surface PG , especially the latter. The influence of corona can greatly interfere with measuring the charge within the overhead cumuliform cloud as seen in the case study in §5.4.4. Bennett (2018) has shown how charged rain and corona can be used as a metric in forecasting lightning, with a success ratio of 51 and 73% respectively, highlighting the effectiveness of surface-based observations for forecasting lightning. As there is a strong success rate using charged rain and corona, further research is vital for nowcasting of lightning. To understand how charged rain and corona can be used to predict the occurrence of lightning, and the lead time they give, the following questions can be answered:

- How does charged rain and corona influence the surface PG and what is the false alarm rate?
- How far in advance can charged rain and corona be used to forecast lightning?

- How does the predictive skill of charged rain and corona for lightning change with forecast lead time?

An approach to answering these questions is to use a composite analysis to measure the change in PG before and after the detection of corona and charged rain. Using many observations from many charged clouds, thresholds can be defined for the PG required to activate charged rain and corona along with the response time using these observations. The response time can be used to estimate the maximum lead time for lightning using these observations. The thresholds can be used to observe the common cloud characteristics when charged rain and corona has been detected, similar to what was conducted in this thesis (§5).

The importance of turbulence for cloud electrification

An important consideration that has been overlooked in the literature until recently is the role of turbulence on cloud electrification. Recent research has hypothesised that turbulence can help form charge centres, increase the rate of collisions and increase the importance of the inductive mechanism for cloud electrification (Cimarelli et al., 2014; Mareev and Dementyeva, 2017; Renzo and Urzay, 2018). Remote and in-situ measurements of turbulence using radar and radiosonde instruments used in this thesis are consistent with the importance of turbulence for cloud electrification (see §5 and 6). As the measurements of turbulence were highly convolved or were limited in the number of observations, it is important to investigate turbulence further, to determine whether cloud electrification is causally related to turbulence. Questions relating to this area that need to be considered include:

- Does turbulence coincide with the charge centres within the cloud?
- Does turbulence influence the vertical and horizontal charge structure within the cloud?
- What is the ideal charge structure within the cloud for lightning to occur, and what is the minimum charge depth required for lightning to occur?
- Looking at the evolution of a cumuliform cloud, what are the indicators for a cloud to continue to separate charge and what are the indicators for charge separation to be suppressed?

To address these questions, further in-situ measurements of turbulence and charge in cumuliform clouds are needed. Using remote measurements (i.e. radar) would be beneficial as a much larger dataset could be obtained, but better estimates of the turbulence would be needed to remove the Z -weighting. From both measurement methods, the charge structure of the cloud can be found directly (in the in-situ case) or from modelling of the charge in the cloud. Using non-vertically pointing radar measurements, which scan a cumuliform cloud multiple

times, would be vital in addressing the evolution of a cumuliform cloud more accurately. Multiple scans of the same cloud would be useful to determine how many of the cloud characteristics found in this thesis change over time, potentially increasing or inhibiting lightning production. Determining the life stage of the cumuliform cloud is also important to address these questions. Determining the minimum charge structure (i.e. number, size of the charge structure and the magnitude of charge inside each charge structure) required for lightning to occur can easily be related to the change of the surface PG . Therefore, it may be possible to use the structure and magnitude of the PG as a metric for lightning to occur.

7.5 Closing Remark

The processes involved in the electrification of cumuliform clouds prior to the first lightning strike are still an open area of research. Most importantly, the work conducted in this thesis was to provide a greater understanding of the important cloud characteristics for a cumuliform cloud to produce lightning, supported by environmental observations. The findings presented in this thesis have allowed the possibility to improve forecasting for lightning before its first strike. The importance of both the size, density and relative velocity of the hydrometeors within the cloud, in terms of cloud turbulence and the vapour pressure, particularly within the ice phase of the cloud are all important for the enhancement of the PG , required for the breakdown of the atmosphere to allow lightning to form. The main aim of this thesis was to understand why so many cumuliform clouds are charged but rarely produce lightning. The answer to this question, concluded in this thesis, is that although a sufficient amount of charge can be separated (causing the surface PG to change by $> 10 \text{ kV m}^{-1}$), the organisation of the charge into charge centres is often insufficient and unable to provide a strong enough PG for an electrical breakdown. Using numerical weather prediction (NWP) models, it may be possible using the findings in this thesis to improve the diagnostics used to forecast lightning. For example, looking only at cumuliform clouds with a high moisture content within the ice phase of mixed-clouds. Another example is to look at cumuliform clouds with a highly variable ϵ_T , suggesting the strong organisation of the cloud's charge (Renzo and Urzay, 2018). Implementation of the PG within NWP models can be used to test the effectiveness of these quantities. In an effort to increase the accuracy, precision and lead time of a lightning forecast, it is paramount to increase communication between the modelling and experimental research communities, particularly around the electrical quantities such as PG , as recognised by previous studies (Mareev and Dementyeva, 2017).

Appendices

Appendix A: Instrument Calibrations

The data collected from the JCI 131 Electrostatic Field Mill (FM) at the Reading University Atmospheric Observatory (RUAO), UK and Chilbolton Observatory (CO), UK is given as a voltage with a range of ± 5 V. Several calibration values were used throughout the lifetime of each instrument and is available in Table A-Error! Reference source not found.. The offset and multiplier values are used in the following form,

$$\text{Calibrated} = \text{Multiplier} \times \text{Uncalibrated} + \text{Offset},$$

Where the uncalibrated values are in V and the calibrated values are in the units of the instrument.

Table A-1: The calibration values used for all instruments at the RUAO and CO from 2006 until 2019.

Instrument	Location	Valid Date	Offset	Multiplier	Notes
JCI 131 Field Mill (FM)	RUAO	01/05/2005 – 16/01/2007	-0.031	0.002584	FM originally at a height of 2.0 m
		17/01/2007 – 21/05/2012	-1.02386	248.509	FM moved to a height of 3.0 m
		22/05/2012 – Present	-1.95032	215.983	
	CO	06/10/2016 1120 UTC – 11/01/2017 1104 UTC	17.0438	208.768	FM range was at ± 600 V m ⁻¹
		11/01/2017 1108 UTC – Present	17.0438	2087.68	FM range changed to ± 10 kV m ⁻¹
Delta-T Tipping Bucket	RUAO	01/05/2015 – 27/10/2006	0	20	To combat the noise issue, the voltage increments were increased twice
		27/10/2016 – 23/01/2007	0	10	
		24/01/2007 – 27/07/2014	0	5	
EML Tipping Bucket	RUAO	30/08/2014 – Present	0	1	No calibration need as output specifies tip time

Appendix B: Biral Thunderstorm Detector Warning Flags

The Biral Thunderstorm Detector (BTD) 300 is capable of detecting the presence of charged rain, corona, enhanced electric fields and lightning. The BTD uses three antennas to differentiate between the different properties causing an electrical perturbation. The BTD provides a warning of lightning when any of these properties have been identified. These warnings are available every two seconds. Table B-1 provides a list of the main warning flags used in the BTD-300.

Table B-1: A list of warning flags provide by the BTD-300 when the presence of charged rain, corona or lightning has been detected.

Warning Flag	Description
01	Corona
02	Charged Precipitation
04	Corona + Charged Precipitation
05	Corona + Charged Precipitation but Corona is strong
06	Corona + Charged Precipitation but Charged Precipitation is strong
08	Distant Lightning (< 30 nautical miles)
09	Distant Lightning + Corona
10	Distant Lightning + Charged Precipitation
12	Distant Lightning + Corona + Charged Precipitation
16	Vicinity Lightning (< 10 nautical miles)
32	Overhead Lightning (< 5 nautical miles)

Appendix C: CloudNet Classification Codes

CloudNet provides a useful target classification of the radar data measured at different sites around the world including Chilbolton Observatory (CO), UK (Hogan and O'Connor, 2004). The classification includes different phases of water, a combination of water phase and non-hydrometeor constituents (e.g. aerosols and insects). The figures given in this thesis use a classification code to represent the different targets determined by CloudNet and the definitions for each classification are given in (Table C-1).

Table C-1: A list of target classification codes used in radar data, [provided by CloudNet (2004)].

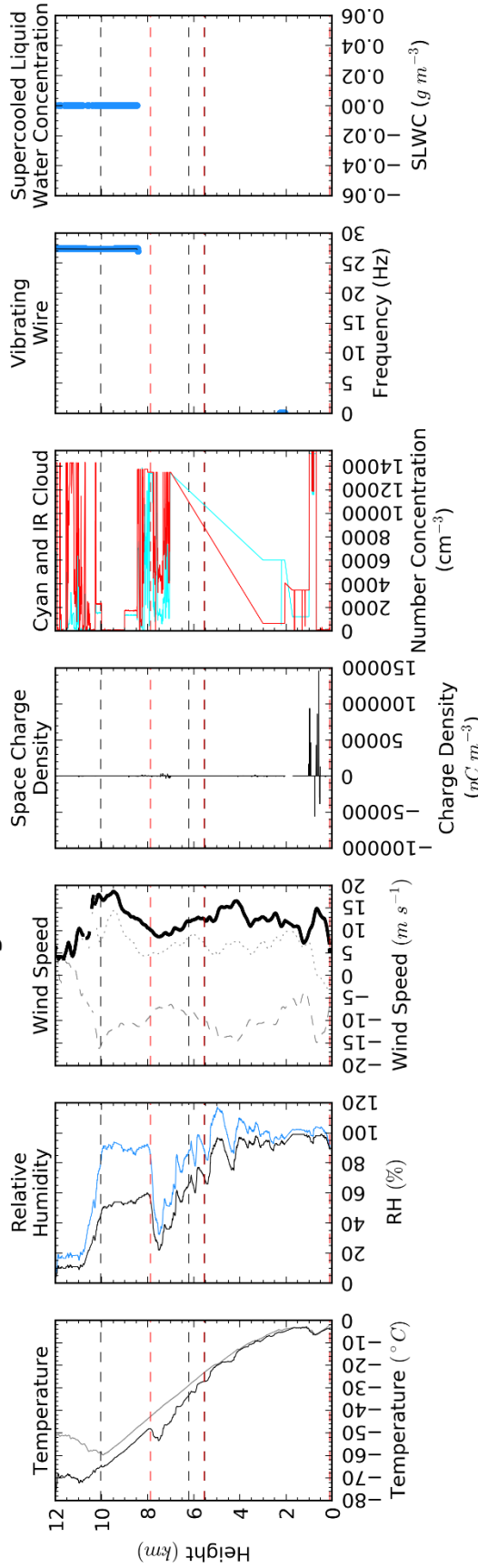
Classification Code	Description
00	Clear sky
01	Cloud liquid droplets only
02	Drizzle or rain
03	Drizzle or rain coexisting with cloud liquid droplets
04	Ice particles
05	Ice coexisting with supercooled liquid droplets
06	Melting ice particles
07	Melting ice particles coexisting with cloud liquid droplets
08	Aerosol particles, no cloud or precipitation
09	Insects, no cloud or precipitation
10	Aerosol coexisting with insects, no cloud or precipitation

Appendix D: Radiosonde Ascent Figures

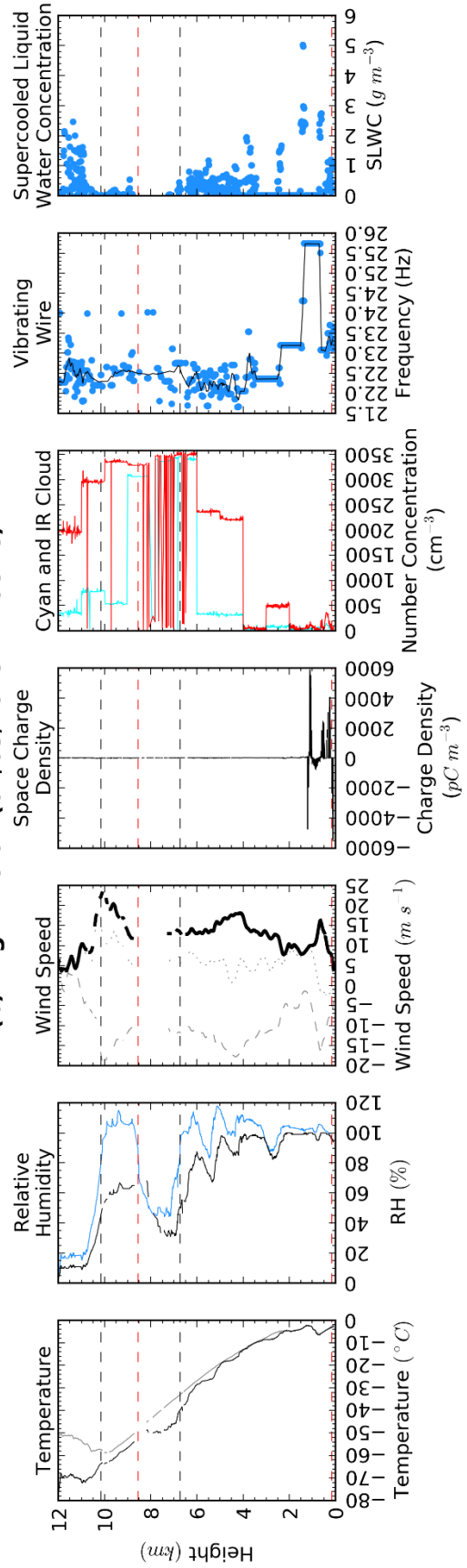
The temperature, humidity, wind, charge, cloud backscatter, turbulence and supercooled liquid water data from all ten radiosondes are presented on the following pages. As the dataset is small in comparison to §5, each ascent provides a unique observation into charged cumuliform clouds ranging from single-celled clouds to multi-cell squall lines to frontal systems. Further details of the radiosonde flights including launch times, synoptic and surface conditions are provided in Table 6-1.

Figure D-1: The profile of the atmosphere on (a) 2018-03-02 1543 UTC, (b) 2018-03-02 1716 UTC, (c) 2018-05-24 1510 UTC, (d) 2018-03-31 1338 UTC, (e) 2018-07-27 1539 UTC, (f) 2018-12-05 0922 UTC, (g) 2018-12-05 1612 UTC, (h) 2019-01-29 1720 UTC, (i) 2019-03-06 1253 UTC and (j) 2019-04-04 1146 UTC. The dry-bulb (grey line) and dew-point (black line) temperature; relative humidity with respect to water (black line) and ice (blue line); meridional (dotted line), zonal (dashed line) and total (black line) wind speeds; linear (black line) and logarithmic (grey line) charge; cyan (cyan line) and infrared (red line) cloud; vibrating frequency (blue dots), SLWC (blue dots), the 11-point moving average of the frequency (black line) of the SLW instrument, the z-axis acceleration and the eddy dissipation rate are used to characterise the properties of the atmosphere. The space charge density shows the positive (red) and negative (blue) absolute values on a log scale to emphasise the wide range of charge measured. The cloud base (red horizontal dashed line) and cloud top (black horizontal dashed line) define the cloud layers identified within the ascent. The freezing level within the ascent is shown by the thick black horizontal line.

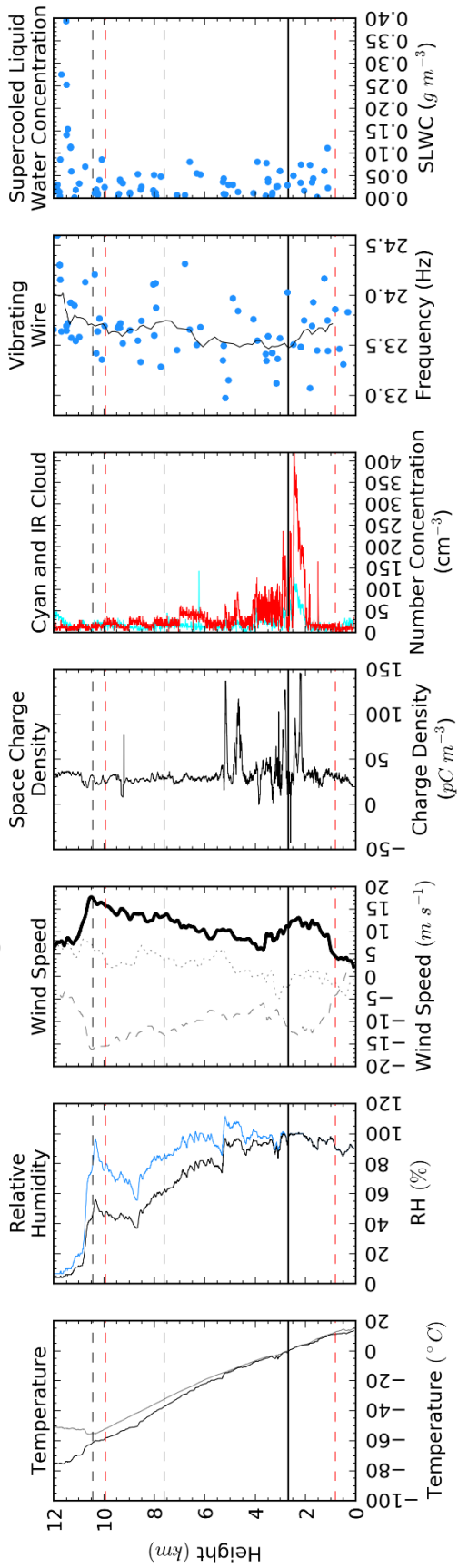
(a) Flight No.01 (02/03/2018 1543UTC)



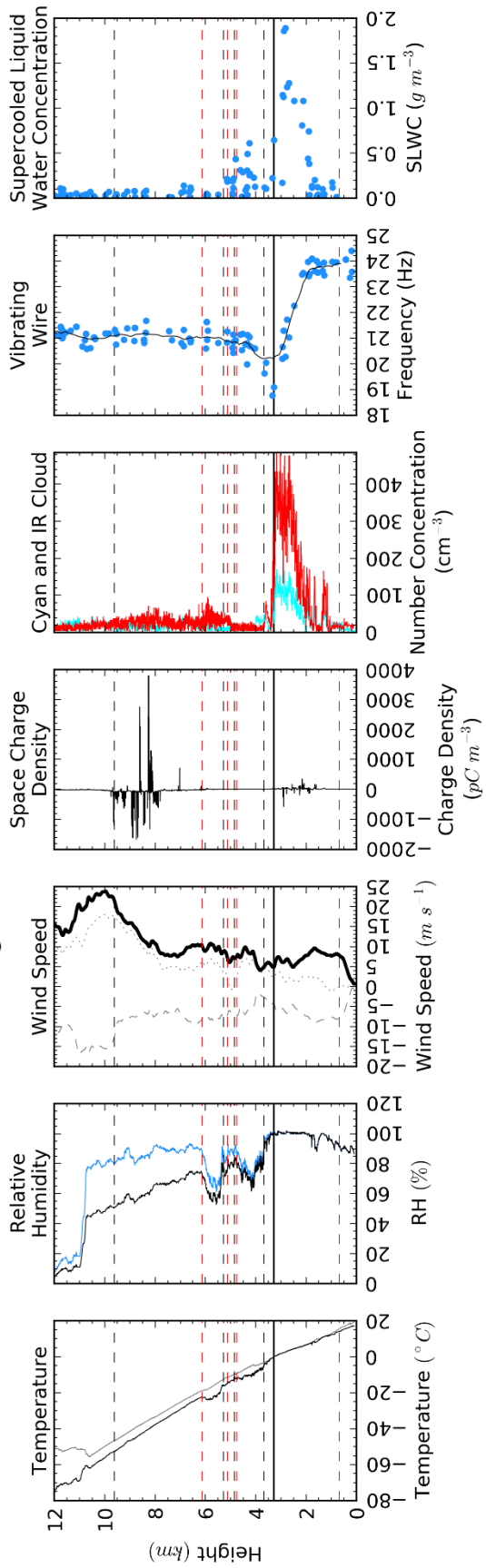
(b) Flight No.02 (02/03/2018 1716UTC)



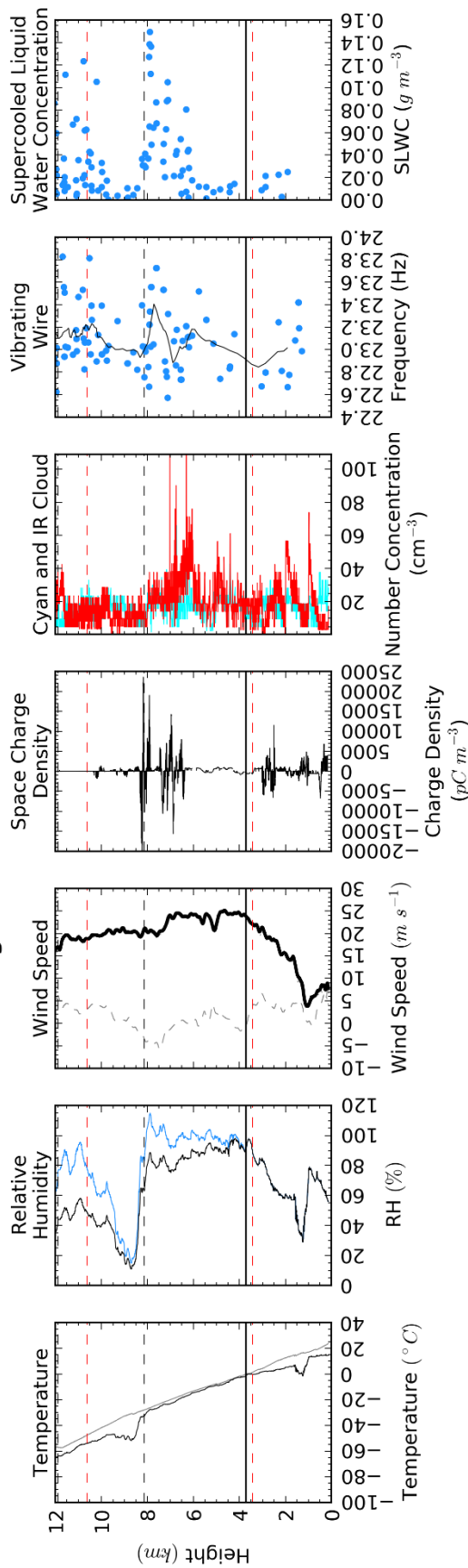
(c) Flight No.03 (24/05/2018 1510UTC)



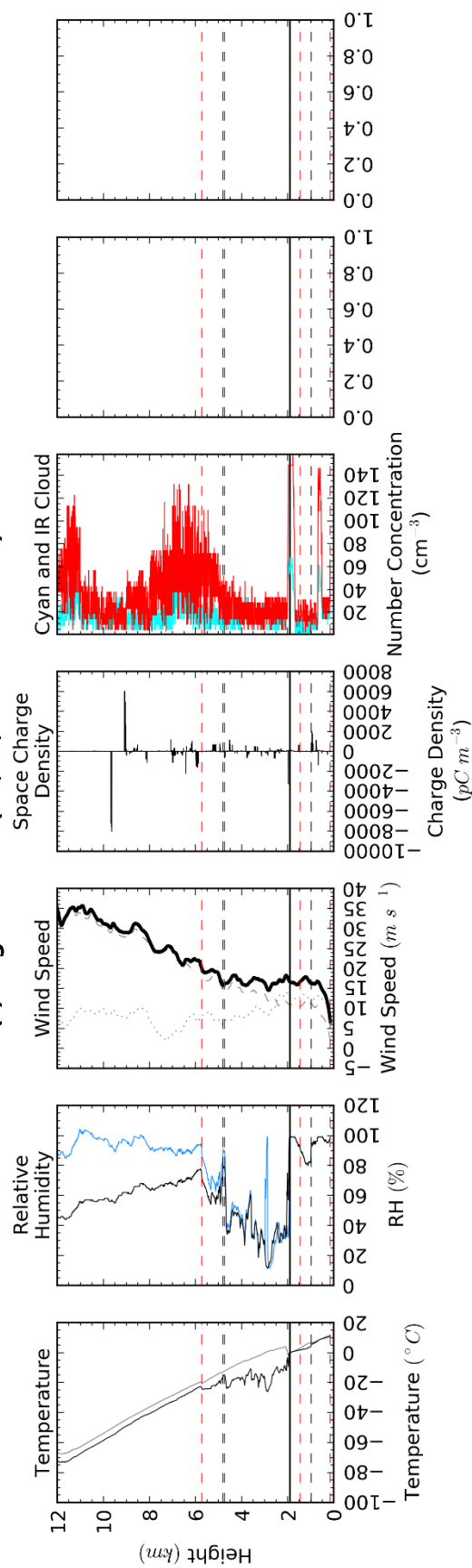
(d) Flight No.04 (31/05/2018 1538UTC)



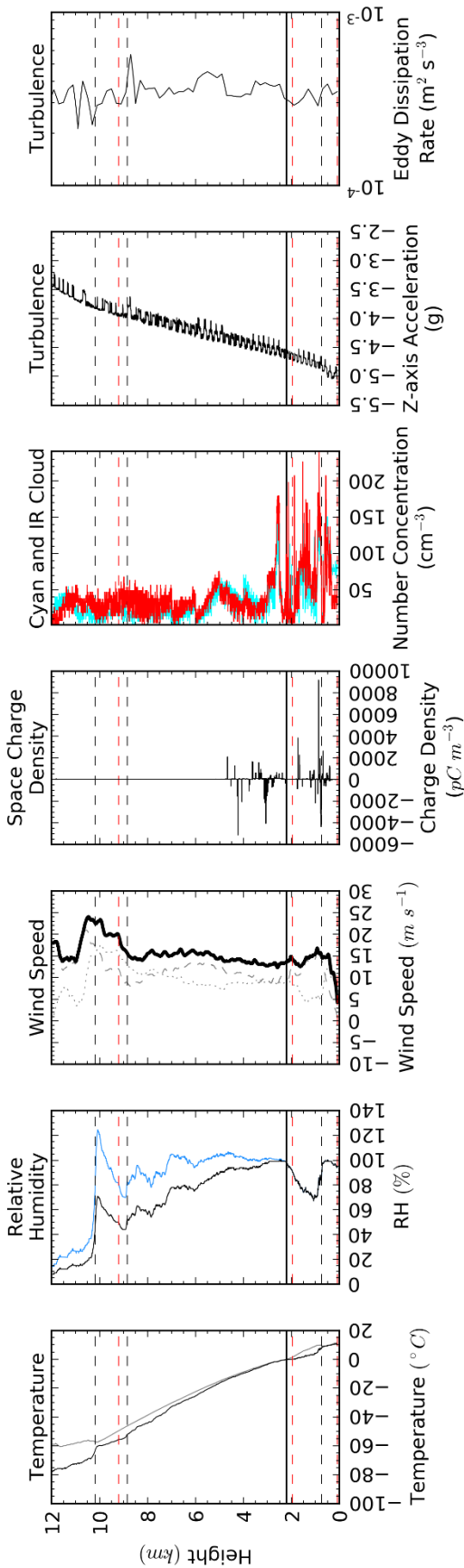
(e) Flight No.05 (27/07/2018 1539UTC)



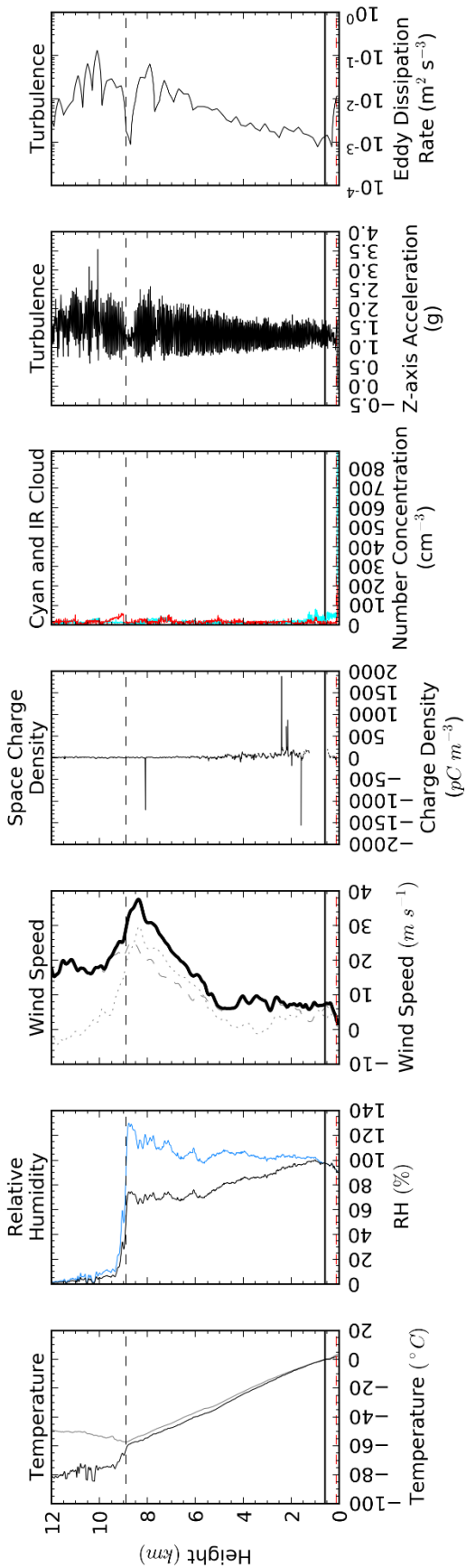
(f) Flight No.06 (05/12/2018 0922UTC)



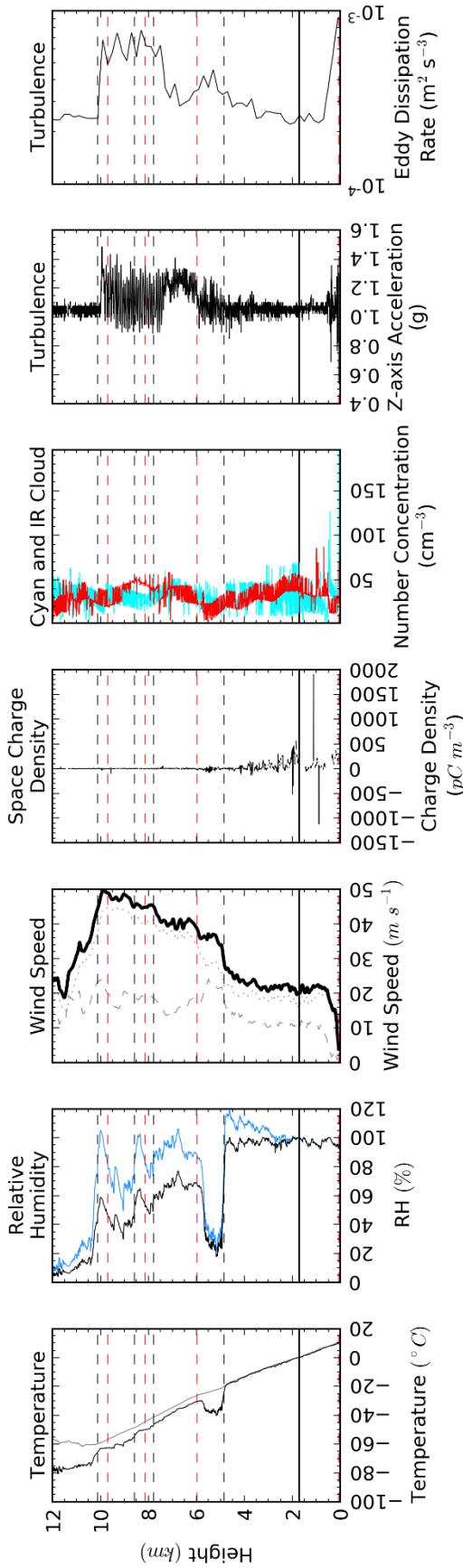
(g) Flight No.07 (05/12/2018 1612UTC)



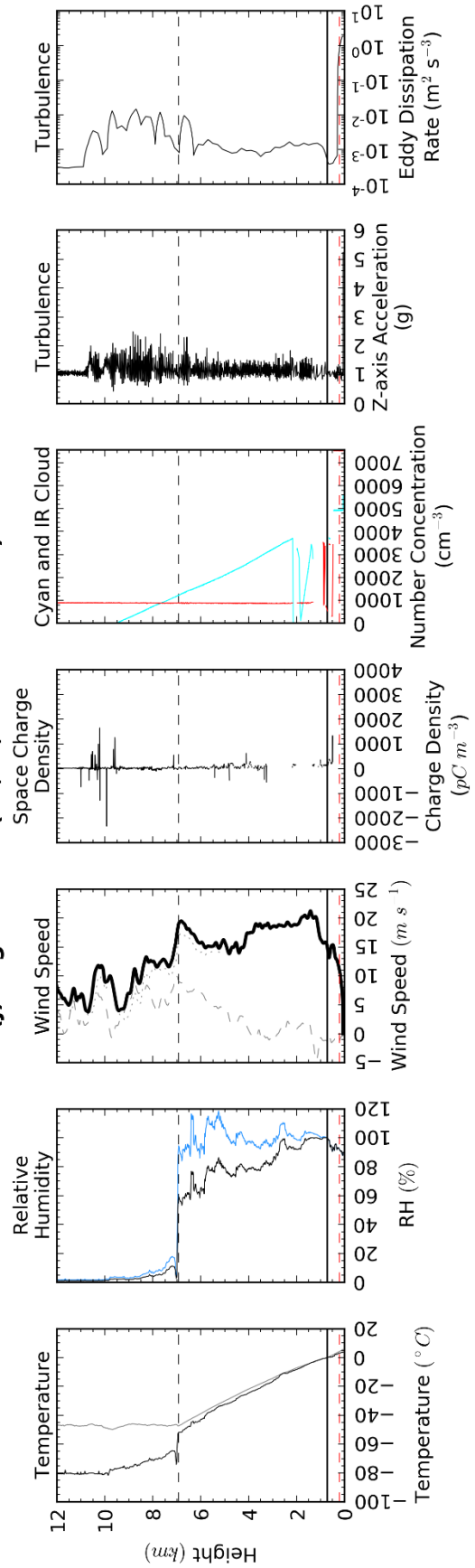
(h) Flight No.08 (29/01/2019 1720UTC)



(i) Flight No.09 (06/03/2019 1253UTC)



(j) Flight No.10 (04/04/2019 1146UTC)



References

- Abbas, M. A. & Latham, J., 1967. An experimental investigation of the selective ion-capture theory of cloud electrification. *Q.J.R. Meteorol. Soc.*, Volume 93, p. 474–482.
- Adkins, C. J., 1959. The small-ion concentration and space charge near the ground. *Q.J.R. Meteorol. Soc.*, 85(365), pp. 237-252.
- Airey, M. W. et al., 2017. Note: A miniature oscillating microbalance for sampling ice and volcanic ash from a small airborne platform. *Rev. Sci. Instrum.*, Volume 88, p. 086108.
- Ambaum, M. H. P., 2010. Water in the Atmosphere. In: *Thermal Physics of the Atmosphere*. Oxford: Wiley & Sons, pp. 93-109.
- Amplicon, 2018. *ADLINK PCI- 9812/ 9810*. [Online] Available at: <https://www.amplicon.com/MandC/product/PC-Analog-PCI-2215.cfm> [Accessed 4 September 2018].
- Analog Devices, 2009. *ADXL325*. [Online] Available at: <https://www.analog.com/media/en/technical-documentation/data-sheets/ADXL325.pdf> [Accessed 04 February 2019].
- Anderson, G. & Klugmann, D., 2014. A European lightning density analysis using 5 years of ATDnet data. *Nat. Hazards Earth Syst. Sci.*, Volume 14, pp. 815-829.
- Aplin, K. L. & Harrison, R. G., 2013. Lord Kelvin's atmospheric electricity measurements. *Hist. Geo Space. Sci.*, 4(2), pp. 83-95.
- Aufdermaur, A. N. & Johnson, D. A., 1972. charge separation due to riming in an electric field. *Q. J. Roy. Meteor. Soc.*, Volume 98, pp. 369-382.
- Baker, M. B. & Dash, J. G., 1994. Mechanism of charge transfer between colliding ice particles in thunderstorms. *J. Geophys. Res.*, 99(10), pp. 621-26.
- Beard, K. V. K., 1986. Charging Mechanisms in Clouds and Thunderstorms. In: *The Earth's Electrical Environment*. Washington D.C.: National Academy Press, pp. 114-130.
- Bennett, A. J., 2007. *Measurement of Atmospheric Electricity During Different Meteorological Conditions [Thesis]*, Reading: University of Reading.
- Bennett, A. J., 2016. *Differences between the BTD-300 and an electric field mill*, Portishead: Biral.

- Bennett, A. J., 2018. Warning of imminent lightning using single-site meteorological observations. *Weather*, 73(6), pp. 187-193.
- Bennett, A. J. & Harrison, R. G., 2006. In situ calibration of atmospheric air conductivity instruments. *Rev. Sci. Instrum.*, Volume 77, p. 016103.
- Bennett, A. J. & Harrison, R. G., 2007. Atmospheric electricity in different weather conditions. *Weather*, 62(10), pp. 277-283.
- Bennett, A. J. & Harrison, R. G., 2008. Surface measurement system for the atmospheric electrical vertical conduction current density, with displacement current density correction. *Journal of Atmospheric and Solar-Terrestrial*, 70(11-12), pp. 1373-1381.
- Bhatnagar, A. K. et al., 2003. Doppler radar – A detecting tool and measuring instrument in meteorology. *Current Science*, 85(3), pp. 256-264.
- Biral, 2018. *BTD-300 Thunderstorm Detector*. [Online] Available at: <https://www.biral.com/product/btd-300-thunderstorm-detector/> [Accessed 30 August 2018].
- Blanchard, D. C., 1948. *Observations on the behavior of water drops at terminal velocity in air*, Schenectady: Occasional Report 7, Project CIRRUUS, General Electric Research Laboratory.
- Blanchard, D. C., 1950. The Behavior of Water Drops at Terminal Velocity in Air. *Eos Trans. AGU*, 31(6), pp. 836-842.
- Blitzortung, 2019. *Lightning archive: Maps and animations*. [Online] Available at: https://www.lightningmaps.org/blitzortung/europe/index.php?bo_page=archive&bo_map=uk&lang=en&bo_year=2018&bo_month=05&bo_day=31&bo_hour_from=12&bo_hour_range=6&bo_animation=1#bo_arch_strikes_maps_form [Accessed 15 February 2019].
- Bouniol, D., Illingworth, A. J. & Hogan, R. J., 2003. *Deriving turbulent kinetic energy dissipation rate within clouds using ground-based 94 GHz radar*. Seattle, 31st International Conference on Radar Meteorology.
- Brazier-Smith, P. R., Jennings, S. G. & Latham, J., 1972. The interaction of falling water drops: coalescence. *Proc. R. Soc. Lond. A*, 326(1566), pp. 393-408.

Brugge, R. & Burt, S., 2015. *One hundred years of Reading Weather*. 1st ed. Reading: Climatological Observers Link.

Buck, A. L., 1981. New equations for computing vapor pressure and enhancement. *J. Appl. Meteor.*, Volume 20, p. 1527–1532.

Campbell Sci., 2018. *CR9000X: Datalogger Base System*. [Online] Available at: <https://www.campbellsci.co.uk/cr9000x> [Accessed 4 September 2018].

Campbell Sci., 2019a. *CR1000: Measurement and Control Datalogger*. [Online] Available at: <https://www.campbellsci.com/cr1000> [Accessed 16 May 2019].

Campbell Sci., 2019b. *CELL215: 4G LTE CAT1 Cellular Module for EMEA Countries*. [Online] Available at: <https://www.campbellsci.eu/cell215> [Accessed 16 May 2019].

Canton, J., 1753. A Letter to the Right Honourable the Earl of Macclesfield, President of the Royal Society, concerning Some New Electrical Experiments. *Phil. Trans.*, Volume 48, pp. 780-785.

Caranti, G. M., Avila, E. E. & Ré, M. A., 1991. Charge transfer during individual collisions in ice growing from vapor deposition. *J. Geophys. Res.*, 96(D8), p. 15365–15375.

Caranti, G. M. & Illingworth, A. J., 1980. Surface potentials of ice and thunderstorm charge separation. *Nature*, Volume 284, pp. 44-46.

Caranti, G. M. & Illingworth, A. J., 1983. Transient Workman-Reynolds freezing potentials. *J. Geophys. Res.*, 88(C13), pp. 8483-8489.

Chalmers, J. A., 1967. *Atmospheric electricity*. 2nd ed. Oxford: John Wiley & Sons.

Chilworth, 2016. *JCI 131 Adverse Conditions Fieldmeter*. [Online] Available at: <http://www.chilworth.co.uk/instruments/jci-electrostatic-instruments/jci-131-adverse-conditions-fieldmeter.aspx> [Accessed 18 July 2016].

Christian, H. J. et al., 2003. Global frequency and distribution of lightning as observed from space by the Optical Transient Detector. *J. Geophys. Res.*, 108(D1), p. 4005.

Chubb, J. N., 1990. Two New Designs of “Field Mill” Type Fieldmeters not Requiring Earthing of Rotating Chopper. *IEEE Trans. Ind. Appl.*, 26(6), pp. 1178-1181.

- Chubb, J. N. & Pavey, I. D., 2009. *Instrumentation for Measurement of Atmospheric Electric Fields, Environmental Electrostatics Meeting*. London, Institute of Physics.
- Chylek, P., Borel, C. & Klett, J., 2004. *Mixed Phase Clouds, Cloud Electrification and Remote Sensing*. United States, Los Alamos Workshop on Lightning Monitoring from Space.
- Cimarelli, C. et al., 2014. Experimental generation of volcanic lightning. *Geology*, 42(1), pp. 79-82.
- Cleveland, W. S., 1993. Bivariate Data. In: *Visualizing Data*. s.l.:Hobart Press, pp. 91-102.
- CloudNet, 2004. *Target classification and cloud boundaries*. [Online] Available at: <http://www.cloud-net.org/data/products/classification.html> [Accessed 18 October 2018].
- CloudNet, 2005. *Cloudnet products for release*. [Online] Available at: <http://www.cloud-net.org/data/products/> [Accessed 26 April 2019].
- Colgate, S. A., 1967. Enhanced Drop Coalescence by Electric Fields in Equilibrium with Turbulence. *J. Geophys. Res.*, 72(2), pp. 479-487.
- Costa-Surós, M., Calbó, J., González, J. A. & Martin-Vide, J., 2013. Behavior of cloud base height from ceilometer measurements. *Atmos. Res.*, Volume 127, pp. 64-76.
- Cotton, W. R. & Gokhale, N. R., 1967. Collision, Coalescence and Breakup of Large Water Drops in a Vertical Wind Tunnel. *J. Geo. Res.*, 72(16), pp. 4041-4049.
- Courtier, B. M. et al., 2019. Intensification of single cell storms prior to lightning onset. *Atmos Sci Lett.*
- D'Adderio, L. P., Porcù, F. & Tokay, A., 2015. Identification and Analysis of Collisional Breakup in Natural Rain. *J. Atmos. Sci.*, Volume 72, pp. 3404-3416.
- Dash, J. G., Mason, B. L. & Wettlaufer, J. S., 2001. Theory of charge and mass transfer in ice-ice collisions. *J. Geophys. Res.*, Volume 106, pp. 20395-20402.
- Delta-T, 2016. *RG1 BP-06 - Raingauge, aerodynamic pattern (6m cable), including baseplate*. [Online] Available at: <http://www.delta-t.co.uk/product-display.asp?id=665> [Accessed 01 May 2016].

Dementyeva, S. O. & Mareev, E. A., 2018. On the Contribution of Turbulence to the Electrification of Thunderclouds. *Izv. Atmos. Ocean. Phys.*, 54(1), p. 25–31.

Dinger, J. E. & Gunn, R., 1946. Electrical effects associated with a change of state of water. *Terr. Magn. Atmos. Electr.*, 51(4), pp. 477-494.

Distromet, 2012. *Description of the Disdrometer RD-80*. [Online] Available at: <http://distromet.com/94/product-description/disdrometer-rd-80> [Accessed 4 September 2018].

Dominguez, F., 2011. *Formation and Growth of Ice Crystals*, Arizona: University of Arizona.

Donovan, D. et al., 2002. *CloudNet: Development of retrieval algorithms (optimized algorithms and performance)*. [Online] Available at: <http://www.cloud-net.org/deliverables/documents/deliverable10.pdf> [Accessed 18 March 2019].

Dye, J. E. et al., 2007. Electric fields, cloud microphysics, and reflectivity in anvils of Florida thunderstorms. *J. Geophys. Res.*, Volume 112, p. D11215.

Eck, T. F., Bhartia, P. K., Hwang, P. H. & Stowe, L. L., 1987. Reflectivity of Earth's Surface and Clouds in Ultraviolet From Satellite Observations. *J. Geophys. Res.*, 92(D4), pp. 4287-4296.

Elsay, J., Coleman, M. D., Gardiner, T. & Shine, K. P., 2017. Can Measurements of the Near-Infrared Solar Spectral Irradiance be Reconciled? A New Ground-Based Assessment Between 4,000 and 10,000 cm^{-1} . *Geo. Phys. Res. Lett.*, Volume 44, pp. 10,071–10,080.

Elsom, D. M., 2015. The Science and Nature of Lightning. In: *Lightning*. London: Reaktion Books Ltd, pp. 109-118.

Elster, J. & Geitel, H., 1888. "Über eine Methode, die elektrische Natur der atmosphärischen Niederschläge zu bestimmen (About a method for determining the electric nature of atmospheric precipitation). *Meteor. Z.*, Volume 5, pp. 95-100.

Elster, J. & Geitel, H., 1913. Zur Influenztheorie der Niederschlagskejrutzat. *Phys. Z.*, pp. 1287-1292.

Emersic, C. & Saunders, C. P. R., 2010. Further laboratory investigations into the Relative Diffusional Growth Rate theory of thunderstorm electrification. *Atmos. Res.*, Volume 98, pp. 327-340.

Environmental Measurements Limited, 2018. *The SBS range of rain gauges from EML*. [Online] Available at: <http://www.emltd.net/sbs.html> [Accessed 4 September 2018].

Eow, J. S. & Ghadiri, M., 2003. Drop–drop coalescence in an electric field: the effects of applied electric field and electrode geometry. *Colloids and Surfaces A: Physicochemical and Engineering Aspects*, 219(1-3), pp. 253-279.

ESTOFEX, 2019. *European Storm Forecast Experiment*. [Online] Available at: <http://www.estofex.org/> [Accessed 04 February 2019].

Fabry, F., 2015a. Fundamentals of weather radar measurements. In: *Radar Meteorology*. Cambridge: Cambridge University Press, pp. 8-32.

Fabry, F., 2015b. Doppler Velocity Information. In: *Radar Meteorology*. Cambridge: Cambridge University Press, pp. 65-92.

Fox, J., 1991. Measuring Influence: Cook's Distance and Other Diagnostics. In: *Regression Diagnostics: An Introduction*. s.l.:Sage Publications, pp. 21-39.

Freier, G. D., 1960. The Coalescence of Water Drops in an Electric Field. *J. Geophys. Res.*, 65(12), pp. 3979-3985.

Frenkel, J., 1947. Atmospheric electricity and lightning. *J. Franklin Inst.*, 243(4), pp. 287-307.

Gaskell, W., 1981. A laboratory study of the inductive theory of thunderstorm electrification. *Q. J. Roy. Meteor. Soc.*, Volume 107, pp. 955-966.

Goff, J. A. & Gratch, S., 1946. *Low-pressure properties of water from -160 to 212 F*, New York: Transactions of the American society of heating and ventilating engineers.

Goodison, B. E., Louie, P. Y. T. & Yang, D., 1998. WMO Solid Precipitation Measurement. *Instruments and Observing Methods*, Volume 67, p. 318.

Grabowska, J., Kuffel, A. & Zielkiewicz, J., 2017. The accretion of the new ice layer on the surface of hexagonal ice crystal and the influence of the local electric field on this process. *J. Chem. Phys.*, Volume 147, p. 174502.

Grahame, D. C., 1947. The electrical double layer and the theory of electrocapillarity. *Chem. Rev.*, 41(3), pp. 441-501.

- Grenet, G., 1947. Essai d'explication de la charge électrique des nuages d'orage. *Ann. Geophys.*, Volume 3, pp. 306-307.
- Griffiths, D. J., 1999a. Potentials and Fields. In: *Introduction to Electrodynamics*. 4th ed. New Jersey: Pearson Education, pp. 436-466.
- Griffiths, D. J., 1999b. Multipole Expansion. In: *Introduction to Electrodynamics*. New Jersey: Pearson Education, pp. 146-160.
- Gunn, R., 1956. Initial Electrification Processes in Thunderstorms. *J. Meteor.*, Volume 13, pp. 21-29.
- Habib, E., Krajewski, W. F. & Kruger, A., 2001. Sampling Errors of Tipping-Bucket Rain Gauge Measurements. *Journal of Hydrologic Engineering*, 6(2), pp. 159-166.
- Hakim, G. & Patoux, J., 2018. Cloud Formation. In: *Weather: A Concise Introduction*. Washington: Cambridge University Press, pp. 90-117.
- Hallett, J. & Mossop, S. C., 1974. Production of secondary ice particles during the riming process. *Nature*, Volume 249, pp. 26-28.
- Hallett, J. & Saunders, C. P. R., 1979. Charge Separation Associated with Secondary Ice Crystal Production. *J. Atmos. Sci.*, Volume 36, p. 2230–2235.
- Hand, W. H., 2006. Climatology of shower frequency in the British Isles at 5 km resolution. *Weather*, Volume 60, pp. 153-158.
- Hao, J., 2017. Effect of surface roughness on droplet splashing. *Physics of Fluids*, Volume 29, p. 122105.
- Hardy, B., 1998. *ITS-90 Formulations for Vapor Pressure, Frostpoint Temperature, Dewpoint Temperature, and Enhancement Factors in the Range -100 to +100C*, London, England: The Proceedings of the Third International Symposium on Humidity & Moisture.
- Harikumar, R., Sampath, S. & Kumar, V. S., 2010. Variation of rain drop size distribution with rain rate at a few coastal and high altitude stations in southern peninsular India. *Advances in Space Research*, 45(4), pp. 576-586.
- Harrison, R. G., 2013. The Carnegie Curve. *Surv Geophys*, 34(2), pp. 209-232.
- Harrison, R. G., 2015. Temperature. In: *Meteorological Measurements and Instrumentation*. Chichester: John Wiley & Sons, pp. 77-103.

- Harrison, R. G. & Aplin, K. L., 2007. Water vapour changes and atmospheric cluster ions. *Atmospheric Research*, Volume 85, pp. 199-208.
- Harrison, R. G., Chalmers, N. & Hogan, R. J., 2008. Retrospective cloud determinations from surface solar radiation measurements. *Atmospheric Research*, Volume 90, pp. 54-62.
- Harrison, R. G. et al., 2017. Note: A self-calibrating wide range electrometer for in-cloud measurements. *Rev. Sci. Instrum.*, 88(12), p. 126109.
- Harrison, R. G. & Nicoll, K. A., 2014. Note: Active optical detection of cloud from a balloon platform. *Rev. Sci. Instrum.*, Volume 85, p. 066104.
- Harrison, R. G. & Nicoll, K. A., 2018. Fair weather criteria for atmospheric electricity measurements. *J. Atmos. Sol. Terr. Phys.*, Volume 179, pp. 239-250.
- Harrison, R. G., Nicoll, K. A. & Aplin, K. L., 2017. Evaluating stratiform cloud base charge remotely. *Geo. Res. Lett.*, 44(12), pp. 6407-6412.
- Harrison, R. G., Nicoll, K. A. & Aplin, K. L., 2017. *Remote sensing of cloud base charge*. University of Ottawa, Proceedings of the 2017 meeting of the Electrostatics Society of America.
- Harrison, R. G., Nicoll, K. A. & Lomas, A. G., 2012. Note: Programmable data acquisition system for research measurements from meteorological radiosondes. *Rev. Sci. Instrum.*, 83(3), p. 036106.
- Helsdon, J. H., Gattaleeradapan, S., Farley, R. D. & Waits, C. C., 2002. An examination of the convective charging hypothesis: Charge structure, electric fields, and Maxwell currents. *J. Geophys. Res.*, 107(D22), p. 4630.
- Hogan, R. J., Illingworth, A. J., O'Connor, E. J. & Baptista, J. P., 2003. Characteristics of mixed-phase clouds. II: A climatology from ground-based lidar. *Q.J.R. Meteorol. Soc.*, Volume 129, pp. 2117-2134.
- Hogan, R. J., Mittermaier, M. P. & Illingworth, A. J., 2006. The retrieval of ice water content from radar reflectivity factor and temperature and its use in the evaluation of a mesoscale model. *J. Appl. Meteor. Climatol.*, Volume 45, p. 301-317.
- Hogan, R. J. & O'Connor, E. J., 2004. *Facilitating cloud radar and lidar algorithms: the Cloudnet Instrument Synergy/Target Categorization product*, Reading: CloudNet.
- Holle, R. L., 2008. *Annual rates of lightning fatalities by country*. Tucson, 2nd International Lightning Meteorology Conference.

Huber, P. J., 1973. Robust Regression: Asymptotics, Conjectures and Monte Carlo. *Ann. Statist.*, 1(5), pp. 799-821.

Huber, P. J., 1984. Finite Sample Breakdown of M- and P-Estimators. *Ann. Statist.*, 12(1), pp. 119-126.

Illingworth, A. J., 1985. Charge separation in thunderstorms: Small-scale processes. *J. Geophys. Res.*, Volume 90, pp. 6026-32.

Illingworth, A. J. & Caranti, J. M., 1985. Ice conductivity restraints on the inductive theory of thunderstorm electrification. *J. Geophys. Res.*, 90(D4), p. 6033–6039.

Islam, T., Rico-Ramirez, M. A., Han, D. & Srivastava, P. K., 2012. A Joss–Waldvogel disdrometer derived rainfall estimation study by collocated tipping bucket and rapid response rain gauges. *Atmos. Sci. Let.*, Volume 13, pp. 139-150.

Jayarathne, E. R. & Saunders, C. P. R., 1984. The "Rain Gush", Lightning, and the Lower Positive Charge Centre in Thunderstorms. *J. Geophys. Res.*, 89(7), pp. 11816-11818.

JCI, 2006. *User Manual: JCI 131 Electrostatic Fieldmeter*. [Online] Available at: <http://www.infostatic.co.uk/UM/UMJCI131.pdf> [Accessed 30 August 2018].

Jennings, S. G., 1975. Electric Charging of Water Drops in Polarizing Electric Fields. *J. Electrostatics*, Volume 1, pp. 15-25.

Jiang, S., Ma, A. & Ramachandran, S., 2018. Negative Air Ions and Their Effects on Human Health and Air Quality Improvement. *Int J Mol Sci.*, 19(10), p. 2966.

Kahn, T., 2016. *Python algorithms for autonomous step detection in 1D data*. [Online] Available at: <https://github.com/thomasbkahn/step-detect> [Accessed 10 August 2016].

Keith, W. D. & Saunders, C. P. R., 1990. Further laboratory studies of the charging of graupel during ice crystal interactions. *Atmos. Res.*, Volume 25, pp. 445-464.

Kingsmill, D. E., Yuter, S. E., Nance, L. B. & Loffler-Mang, M., 2006. Observations of Precipitation Size and Fall Speed Characteristics within Coexisting Rain and Wet Snow. *J. Appl. Meteor. Climatol.*, Volume 45, pp. 1450-1464.

Kochin, A. V., 2001. Formation of Electric Charges in Melting Layer. *arXiv: Atmospheric and Oceanic Physics*, p. 4.

- Köhler, M., 2005. Improved prediction of boundary layer clouds. *ECMWF Newsletter*, Volume 104, pp. 18-22.
- Korolev, A. V. & Isaac, G. A., 2006. Relative Humidity in Liquid, Mixed-Phase, and Ice Clouds. *J. Atmos. Sci.*, Volume 63, p. 2865–2880.
- Korolev, A. V. & Isaac, G. A., 2008. *The effect of spatial averaging on the relative humidity and phase composition of clouds*. Cancun, Mexico, Int. Conf. on Clouds and Precip..
- Lane-Smith, D. R., 1969. *Electrical processes in heavy rain in the tropics [Thesis]*, Durham University: Durham theses.
- Langer, I. & Reimer, E., 2007. Separation of convective and stratiform precipitation for a precipitation analysis of the local model of the German Weather Service. *Adv. Geosci.*, Volume 10, pp. 159-165.
- Langmuir, I., 1951. Cloud Seeding by Means of Dry Ice, Silver Iodide and Sodium Chloride. *Transactions of the New York Academy of Sciences*, 14(1), pp. 40-44.
- Lanza, L. et al., 2005. *Laboratory Intercomparison of Rainfall Intensity Gauges*, Genoa : WMO.
- Latham, J. & Mason, B. J., 1961. Generation of Electric Charge Associated with the Formation of Soft Hail in Thunderclouds. *Proc. R. Soc. Lond. A*, Volume 260, pp. 537-549.
- Lenard, P., 1892. Ueber die Electricität der Wasserfälle. *Annalen der Physik*, 282(8), pp. 584-636.
- Lenard, P., 1904. Ueber Regen. *Met. Zs*, Volume 21, pp. 248-262.
- Levin, Z. & Hobbs, P. V., 1971. Splashing of Water Drops on Solid and Wetted Surfaces: Hydrodynamics and Charge Separation. *Phil. Trans. R. Soc.*, Volume 269, pp. 555-585.
- Levin, Z. & Machnes, B., 1977. Experimental Evaluation of the Coalescence Efficiencies of Colliding Water Drops. *B. PAGEOPH*, 115(4), pp. 845-867.
- Levin, Z. & Ziv, A., 1974. The electrification of thunderclouds and the rain gush. *J. Geophys. Res.*, 79(18), pp. 2699-2704.
- Lieberman, M. A. & Lichtenberg, A. J., 2005. Appendix B: The Collision Integral. In: *Principles of Plasma Discharges and Materials Processing*. s.l.:John Wiley & Sons, Inc., pp. 727-729.
- Liu, J. et al., 2010. Splashing Phenomena During Liquid Droplet Impact. *Atomisation and Sprays*, 20(4), pp. 297-310.

Lozowski, E. P., Stallabrass, J. R. & Hearty, P. F., 1983. The Icing of an Unheated, Nonrotating Cylinder Part I: A Simulation Model. *J. Clim. Appl. Meteorol.*, Volume 22, pp. 2053-2062.

Lüttgens, S. et al., 2015. Electrostatic Charge Measurements of Droplets of Various Liquids Falling over a Large Distance. *Chem. Eng. Technol.*, 38(7), pp. 1261-1268.

MacGorman, D. R. & Rust, D. W., 1998. *The Electrical Nature of Storms*. 1st ed. New York: Oxford University Press.

Magarey, R. D., Russo, J. M., Seem, R. C. & Gadoury, D. M., 2005. Surface wetness duration under controlled environmental conditions. *Agricultural and Forest Meteorology*, 128(1-2), pp. 111-122.

Mallat, S. & Zhong, S., 1992. Characterization of Signals from Multiscale Edges. *IEEE Transactions on Pattern Analysis and Machine Intelligence*, 14(7), pp. 710-732.

Mareev, E. A. & Demytyeva, S. O., 2017. The role of turbulence in thunderstorm, snowstorm, and dust storm electrification. *J. Geophys. Res. Atmos.*, Volume 122, p. 6976–6988.

Marlton, G. J., 2016. *On the development, characterisation and applications of a balloon-borne atmospheric turbulence sensor [Thesis]*, Reading: University of Reading.

Marlton, G. J., Harrison, R. G., Nicoll, K. A. & Williams, P. D., 2015. Note: A balloon-borne accelerometer technique for measuring atmospheric turbulence. *Rev. Sci. Instrum.*, Volume 86, p. 016109.

Marsalek, J., 1981. Calibration of the tipping-bucket raingage. *J. Hydrology*, 53(4), pp. 343-354.

Marshall, J. S. & Palmer, W. M., 1948. The distribution of rain drops with size. *J. Meteor.*, Volume 5, p. 165–166.

Marshall, T. C. & Stolzenburg, M., 1998. Estimates of cloud charge densities in thunderstorms. *J. Geophys. Res.*, 103(D16), p. 19769– 19775.

Mason, B. L. & Dash, J. G., 2000. Charge and mass transfer in ice–ice collisions: Experimental observations of a mechanism in thunderstorm electrification. *J. Geophys. Res.*, Volume 105, pp. 10185-10192.

Matthews, J. et al., 2016. *Relationship Between Aerosol Number Size Distribution and Atmospheric Electric Potential Gradient in an Urban Area*. Vienna, EGU General Assembly.

- McCaul, E. W., Goodman, S. J., LaCasse, K. M. & Cecil, D. J., 2009. Forecasting Lightning Threat Using Cloud-Resolving Model Simulations. *Wea. Forecasting*, Volume 24, pp. 709-729.
- Mezuman, K., Price, C. & Galanti, E., 2014. On the spatial and temporal distribution of global thunderstorm cells. *Environ. Res. Lett.*, Volume 9, p. 124023.
- Moncrieff, M. W. & Green, J. S. A., 1972. The propagation and transfer properties of steady convective. *Quart. J. R. Met. Soc.*, Volume 98, pp. 336-352.
- Moore, C. B., Vonnegut, B., Machado, J. A. & Survilas, H. J., 1962. Radar observations of rain gushes following overhead lightning strokes. *J. Geophys. Res.*, Volume 67, pp. 207-220.
- Munro Instruments, 2015. *Tipping Bucket Rain Gauge*. [Online] Available at: <https://munroinstruments.com/product/tipping-bucket-rain-gauge/> [Accessed 4 September 2018].
- Murray, B. J. et al., 2010. Kinetics of the homogeneous freezing of water. *Phys. Chem. Chem. Phys.*, Volume 12, p. 10380–10387.
- National Archives, 2017. *The Kite Experiment, 19 October 1752*. [Online] Available at: <https://founders.archives.gov/documents/Franklin/01-04-02-0135> [Accessed 31 January 2018].
- NEODAAS-Dundee, 2018. *NERC Satellite Receiving Station, Dundee University, Scotland*. [Online] Available at: <http://www.sat.dundee.ac.uk/> [Accessed 10 September 2018].
- NETPDTC, 2011. Principles of Doppler Radar. In: *Environmental Satellites and Weather Radar*. s.l.:CreateSpace Independent Publishing Platform, pp. 55-60.
- Nicoll, K. A., 2010. *Coupling Between the Global Atmospheric Electric Circuit and Clouds [Thesis]*, Reading: University of Reading.
- Nicoll, K. A., 2013. Note: A self-calibrating electrometer for atmospheric charge measurements from a balloon platform. *Rev. Sci. Instrum.*, Volume 84, p. 096107.
- Nicoll, K. A. & Harrison, R. G., 2016. Stratiform cloud electrification: comparison of theory with multiple in-cloud measurements. *Q.J.R. Meteorol. Soc.*, Volume 142, pp. 2679-2691.
- Nicoll, K. A. et al., 2018. Electrical sensing of the dynamical structure of the planetary boundary layer. *Atmos. Res.*, Volume 202, pp. 81-95.

NOAA, 2017. *Advanced Very High Resolution Radiometer - AVHRR*. [Online] Available at: <https://noaasis.noaa.gov/NOAASIS/ml/avhrr.html> [Accessed 10 September 2018].

Norbury, J. R. & White, W. J., 1971. A rapid-response rain gauge. *J. Phys. E: Sci. Instrum.*, Volume 4, pp. 601-602.

Ochou, A. D., Nzeukou, A. & Sauvageot, H., 2007. Parametrization of drop size distribution with rain rate. *Atmos. Res.*, 84(1), pp. 58-66.

O'Connor, E. J., Hogan, R. J. & Illingworth, A. J., 2005. Retrieving Stratocumulus Drizzle Parameters Using Doppler Radar and Lidar. *J. Appl. Meteor.*, Volume 44, pp. 14-27.

Ogawa, T., 1960. Electricity in Rain. *Geophysical Institute*, Volume 12, pp. 21-31.

Peterson, M. et al., 2017. A TRMM/GPM retrieval of the total mean generator current for the global electric circuit. *J. Geophys. Res. Atmos.*, Volume 122, pp. 10,025–10,049.

Phelps, C. T., Griffiths, R. F. & Vonnegut, B., 1973. Corona produced by splashing of water drops on a water surface in a strong electric field. *J. App. Phys.*, 44(7), pp. 3082-3086.

Pollock, M. D. et al., 2018. Quantifying and Mitigating Wind-Induced Undercatch in Rainfall Measurements. *Water Resources Research*, Volume 54, p. 3863–3875.

Priestley, J., 1767. *The History and Present State of Electricity, with Original Experiments*, London: The Royal Society II.

Protat, A., Bouniol, D. & Haeffelin, M., 2004. *Evaluation of vertical velocity and its distribution in four operational forecast models using continuous Doppler cloud measurements*. Bologna, 14th Int. Conf. on Clouds and Precipitation.

Protat, A., Lemaître, Y. & Bouniol, D., 2003. Terminal fall velocity and the FASTEX cyclones. *Q.J.R. Meteorol. Soc.*, Volume 129, pp. 1513-1535.

Pruppacher, H. R., 1963. The Effect of an External Electric Field on the Supercooling of Liquid Water Drops. *J. Geophys. Res.*, 68(15), pp. 4463-4474.

Rakov, V. A. & Uman, M. A., 2007. *Lightning: Physics and Effects*. Florida: Cambridge University Press.

Ramsay, M. W. & Chalmers, J. A., 1960. Measurements on the electricity of precipitation. *Q.J.R. Meteorol. Soc.*, Volume 86, pp. 530-539.

- Renzo, M. D. & Urzay, J., 2018. Aerodynamic generation of electric field in turbulence laden with charged inertial particles. *Nat. Comms.*, 9(1676).
- Reynolds, S. E., Brook, M. & Gourley, M. F., 1957. Thunderstorm charge separation. *J. Meteor.*, Volume 14, pp. 426-36.
- Riboux, G. & Gordillo, J. M., 2016. Maximum drop radius and critical Weber number for splashing in the dynamical Leidenfrost regime. *Journal of Fluid Mechanics*, Volume 803, pp. 516-527.
- Rust, W. D. & Moore, C. B., 1974. Electrical conditions near the bases of thunderclouds over New Mexico. *Q. J. Roy. Meteor. Soc.*, Volume 100, pp. 450-68.
- Rutherford Appleton Laboratory, 2002. *Chilbolton 905 nm CT75K lidar ceilometer data*. [Online] Available at: https://artefacts.ceda.ac.uk/badc_datadocs/chilbolton/vaisala_ceilometer.html [Accessed 22 May 2019].
- Rutherford Appleton Laboratory, 2016. *Copernicus radar*, Chilbolton: Science and Technology Facilities Council.
- Rycroft, M. J., Nicoll, K. A., Aplin, K. L. & Harrison, R. G., 2012. Recent advances in global electric circuit coupling between the space environment and the troposphere. *Journal of Atmospheric and Solar-Terrestrial Physics*, Volume 90-91, pp. 198-211.
- Sartor, J. D., 1954. A laboratory investigation of collision efficiencies, coalescence and electrical charging of simulated cloud droplets. *J. Meteor.*, Volume 11, p. 91.103.
- Sartor, J. D., 1960. Some Electrostatic Cloud-Droplet Collision Efficiencies. *J. Geophys. Res.*, 65(7), pp. 1953-1957.
- Saunders, C. P. R., 1992. A Review of Thunderstorm Electrification Processes. *J. App. Meteo.*, Volume 32, pp. 642-655.
- Saunders, C. P. R., 2008. Charge Separation Mechanisms in Clouds. *Space Sci. Rev.*, Volume 137, pp. 335-353.
- Saunders, C. P. R. et al., 2001. A laboratory study of the influence of water vapour and mixing on the charge transfer process during collisions between ice crystals and graupel. *Atmos. Res.*, Volume 58, pp. 187-203.
- Saunders, C. P. R., Wheeler, M. F. S., Jallo, N. & Jayaratne, E. R., 1985. Ice crystal interactions with a riming target: Charge transfer and collection efficiencies. *J. Geophys. Res.*, 90(D4), p. 6047–6050.

- Scrase, F. J., 1938. Electricity of Rain. *Geophys. Mem.*, 9(75), pp. 1-20.
- Serke, D. et al., 2014. Supercooled liquid water content profiling case studies with a new vibrating wire sonde compared to a ground-based microwave radiometer. *Atmos. Res.*, Volume 149, pp. 77-97.
- Shewchuk, S. R. & Iribarne, J. V., 1970. Electrification associated with drop splashing. *Trans. Faraday Soc.*, Volume 66, pp. 2092-2105.
- Simpson, G. C., 1909. On the Electricity of Rain and Its Origin in Thunderstorms. *Philosophical Transactions of the Royal Society of London*, Volume 209, pp. 379-413.
- Simpson, G. C., 1949. Atmospheric electricity during disturbed weather. *Terr. Magn. Atmos. Electr.*, 53(1), pp. 27-33.
- Singh, N. & Singh, D., 2004. Polarizability affecting nucleation of water vapour condensation and ice glaciation in presence of external electric field. *Indian J. Radio Space Phys.*, Volume 33, pp. 43-49.
- Slingo, J. et al., 2014. *The Recent Storms and Floods in the UK*, Exeter: UK Met Office.
- Smith, L. G., 1951. *Rain Electricity [Thesis]*, Cambridge: Cambridge University.
- Smith, L. G., 1955. The electric charge of raindrops. *Q.J.R. Meteorol. Soc.*, Volume 81, pp. 23-47.
- Sonntag, D., 1994. Advancements in the field of hygrometry. *Meteorol. Z.*, 3(2), pp. 51-66.
- Soula, S. & Chauzy, S., 1997. Charge transfer by precipitation between thundercloud and ground. *J. Geophys. Res.*, 192(10), pp. 11061-11069.
- Soul, K. M., Archibald, E. J., Hardaker, P. J. & Hounsell, A., 2002. Using the GANDOLF system as a tool to aid the forecasting of lightning strikes. *Meteorol. Appl.*, Volume 9, pp. 229-238.
- Squires, P., 1958. Penetrative Downdraughts in Cumuli. *Tellus*, 10(3), pp. 381-389.
- Sreenivasan, K. R., 1995. On the Universality of the Kolmogorov Constant.. *Phys. Fluids*, Volume 7, pp. 2778-2784.
- Standler, R. B. & Winn, W. P., 1979. Effects of corona on electric fields beneath thunderstorms. *Q. J. Roy. Meteor. Soc.*, Volume 105, pp. 285-302.
- Stojek, Z., 2010. The Electrical Double Layer and Its Structure. In: *Electroanalytical Methods*. Berlin: Springer, pp. 3-9.

- Stolzenburg, M. & Marshall, T. C., 2008. Charge Structure and Dynamics in Thunderstorms. *Space Sci. Rev.*, Volume 137, pp. 355-372.
- Stow, C. D. & Stainer, R. D., 1977. The physical products of a splashing water drop. *Met. Soc. of Japan*, Volume 55, pp. 518-532.
- Taflin, D. C., Ward, T. L. & Davis, J. E., 1989. Electrified Droplet Fission and the Rayleigh Limit. *American Chemical Society*, 5(2), pp. 376-384.
- Takahashi, T., 1984. Thunderstorm Electrification—A Numerical Study. *J. Atmos. Sci.*, Volume 41, p. 2541–2558.
- Takahashi, T. & Fullerton, C. M., 1972. Raindrop Charge-Size Measurements in Warm Rain. *J. Geophys. Res.*, 77(9), pp. 1630-1636.
- Takeychi, N. & Katase, A., 1982. Rainout-Washout Model for Variation of Environmental Gamma-Ray Intensity by Precipitation. *Journal of Nuclear Science and Technology*, 19(5), pp. 393-409.
- Tate, E. L. & Gustard, A., 2000. Drought Definition: A Hydrological Perspective. In: *Drought and Drought Mitigation in Europe*. Dordrecht: Springer, pp. 22-48.
- Taylor, F. W., 2005. Atmosphere and Climate. In: *Elementary Climate Physics*. Oxford: Oxford University Press, pp. 40-52.
- Thompson, W., 1872. Atmospheric Electricity. In: *Reprint of Papers on Electrostatics and Magnetism*. London: Macmillan, p. Section XVI.
- Tolman, R. C., 1949. The Effect of Droplet Size on Surface Tension. *J. Chem. Phys.*, 17(3), pp. 333-337.
- Twomey, S., 1956. Electric Charge Separation in Subfreezing Cumuli. *Tellus*, 9(3), pp. 384-393.
- Twomey, S. A., Piepgrass, M. & Wolfe, T. L., 1984. An assessment of the impact of pollution on global cloud albedo. *Tellus B*, Volume 36B, pp. 356-366.
- UKMO, 2018. *Reading climate*. [Online] Available at: <https://www.metoffice.gov.uk/public/weather/climate/gcck9yegm> [Accessed 24 September 2018].
- United Nations, 2018. *2018 Revision of World Urbanization Prospects*, s.l.: United Nations Department of Economic and Social Affairs.

References

University of Wyoming, 2018. *Atmospheric Soundings*. [Online] Available at: <http://weather.uwyo.edu/upperair/sounding.html> [Accessed 10 September 2018].

Vaisala, 2013. *Vaisala Radiosonde RS92-SGP*, s.l.: Vaisala.

Valentin, B. D., 2012. *Cloud classification*. [Online] Available at: https://commons.wikimedia.org/wiki/File:Cloud_types_en.svg [Accessed 9 May 2019].

Vömel, H., 2011. *Saturation vapor pressure formulations*. [Online] Available at: https://www.eas.ualberta.ca/jdwilson/EAS372_13/Vomel_CIRES_satvpformulae.html [Accessed 29 January 2019].

Vonnegut, B., 1953. Possible mechanism for the formation of thunderstorm electricity. *Bull. Amer. Meteor. Soc.*, Volume 34, p. 378.

Vonnegut, B. & Moore, C. B., 1962. Effect of Atmospheric Space Charge on Initial Electrification of Cumulus Clouds. *J. Geophys. Res.*, 67(10), pp. 3909-3922.

Wexler, A., 1976. Vapor Pressure Formulation for Water in Range 0 to 100C. A Revision. *J. Res. Nat. Bur. Stand. Sec. A: Phys. Ch.*, 80(5), pp. 775-785.

Whipple, F. J. W. & Chalmers, J. A., 1944. On Wilson's theory of the collection of charge by falling drops. *Q.J.R. Meteorol. Soc.*, Volume 70, p. 103–119.

Wilkinson, J. M., 2017. A Technique for Verification of Convection-Permitting NWP Model Deterministic Forecasts of Lightning Activity. *Wea. Forecasting*, Volume 32, pp. 97-115.

Wilkinson, J. M. & Bornemann, J. F., 2014. A lightning forecast for the London 2012 Olympics opening ceremony. *Weather*, Volume 69, pp. 16-19.

Williams, E. R., Zhang, R. & Rydock, R., 1991. Mixed Phase microphysics and cloud electrification. *J. Atmos. Sci.*, Volume 48, pp. 2195-2203.

Wilson, C. T., 1929. Some thundercloud problems. *J. Franklin. Inst.*, Volume 208, pp. 1-12.

Wilson, C. T. R., 1916. On some determination of the sign and magnitude of electric discharges in lightning flashes. *Proc. Roy. Soc. Lond. A.*, Volume 92, pp. 555-574.

- Wilson, C. T. R., 1920. Investigations on lightning discharges and the electric field of thunderstorms. *Philos. Trans. R. Soc. London*, Volume 221, pp. 73-115.
- WMO, 2017. General Classification of Meteors. In: *Internal Cloud Atlas Manual on the Observation of Clouds and Other Meteors*. Hong Kong: WMO, p. Section 1.2.
- Workman, E. J. & Reynolds, S. E., 1950. Electrical Phenomena Occurring during the Freezing of Dilute Aqueous Solutions and Their Possible Relationship to Thunderstorm Electricity. *Phys. Rev.*, Volume 78, pp. 254-259.
- Wormell, T. W., 1953. Atmospheric electricity; some recent trends and problems. *Q.J.R. Meteorol. Soc.*, Volume 79, pp. 3-38.
- Wu, Z. & Cao, Y., 2017. Dynamics of initial drop splashing on a dry smooth surface. *PLOS ONE*, 12(5), p. e0177390.
- Xu, L., Zhang, W. W. & Nagel, S. R., 2005. Drop Splashing on a Dry Smooth Surface. *Phys. Rev. Lett.*, Volume 94, p. 184505.
- Xu, L., Zhang, W. W. & Nagel, S. R., 2007. Liquid drop splashing on smooth, rough and textured surfaces. *Phys. Rev. E*, 75(5), pp. 26-28.
- Yano, J. et al., 2018. Scientific Challenges of Convective-Scale Numerical Weather Prediction. *Bull. Amer. Meteor. Soc.*, Volume 99, p. 699–710.
- Ying, W., Xiaoning, L. & Xiaohui, J., 2006. *Differences between Automatic and Manual Meteorological Observation*. Geneva, WMO.
- Zeleny, J., 1933. Variation with Temperature of the Electrification Produced in Air by the Disruption of Water Drops and Its Bearing on the Prevalence of Lightning. *Phys. Rev.*, 44(10), pp. 837-842.
- Zhang, J. et al., 2010. Analysis of cloud layer structure in Shouxian, China using RS92 radiosonde aided by 95 GHz cloud radar. *J. Geophys. Res.*, Volume 115, p. D00K30.
- Zilch, L. W. et al., 2008. Charge Separation in the Aerodynamic Breakup of Micrometer-Sized Water Droplets. *J. Phys. Chem. A*, 112(51), p. 13352–13363.